frontiers | Research Topics

Cell size regulation: Molecular mechanisms and physiological importance

Edited by
Evgeny Zatulovskiy and Jette Lengefeld

Published in
Frontiers in Cell and Developmental Biology

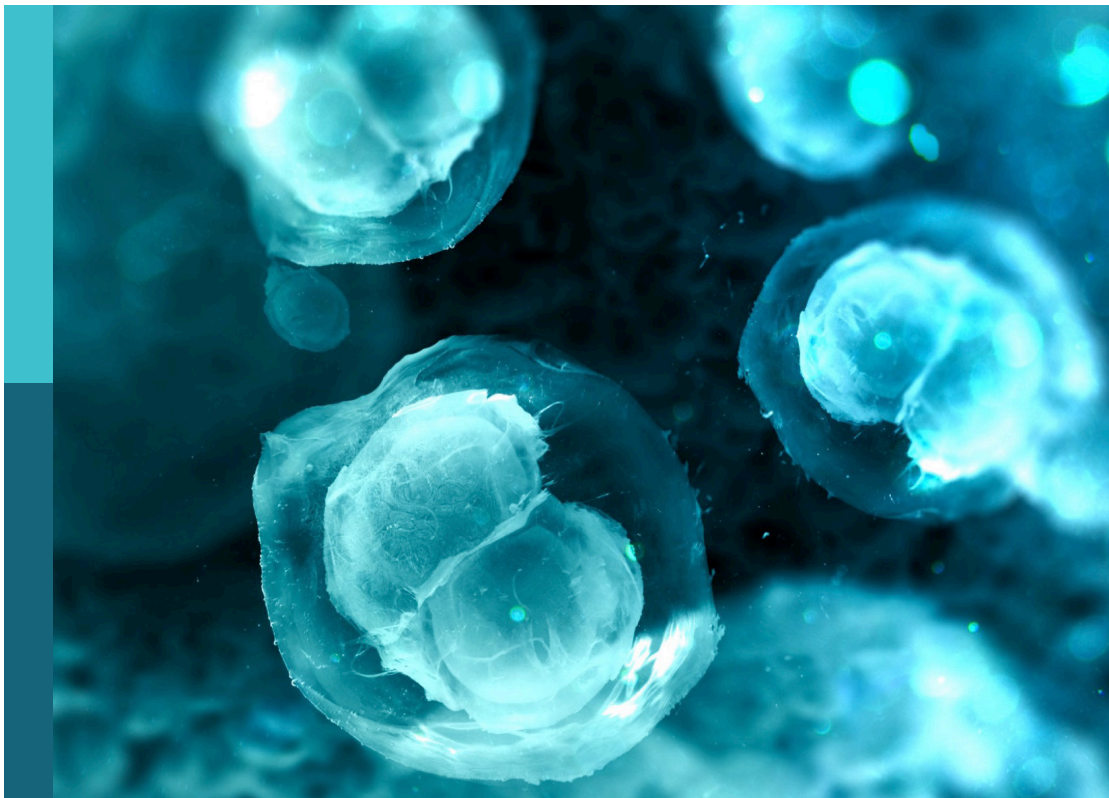

ISSN 1664-8714
ISBN 978-2-8325-2607-1
DOI 10.3389/978-2-8325-2607-1

About Frontiers

Frontiers is more than just an open access publisher of scholarly articles: it is a pioneering approach to the world of academia, radically improving the way scholarly research is managed. The grand vision of Frontiers is a world where all people have an equal opportunity to seek, share and generate knowledge. Frontiers provides immediate and permanent online open access to all its publications, but this alone is not enough to realize our grand goals.

Frontiers journal series

The Frontiers journal series is a multi-tier and interdisciplinary set of open-access, online journals, promising a paradigm shift from the current review, selection and dissemination processes in academic publishing. All Frontiers journals are driven by researchers for researchers; therefore, they constitute a service to the scholarly community. At the same time, the *Frontiers journal series* operates on a revolutionary invention, the tiered publishing system, initially addressing specific communities of scholars, and gradually climbing up to broader public understanding, thus serving the interests of the lay society, too.

Dedication to quality

Each Frontiers article is a landmark of the highest quality, thanks to genuinely collaborative interactions between authors and review editors, who include some of the world's best academicians. Research must be certified by peers before entering a stream of knowledge that may eventually reach the public - and shape society; therefore, Frontiers only applies the most rigorous and unbiased reviews. Frontiers revolutionizes research publishing by freely delivering the most outstanding research, evaluated with no bias from both the academic and social point of view. By applying the most advanced information technologies, Frontiers is catapulting scholarly publishing into a new generation.

What are Frontiers Research Topics?

Frontiers Research Topics are very popular trademarks of the *Frontiers journals series*: they are collections of at least ten articles, all centered on a particular subject. With their unique mix of varied contributions from Original Research to Review Articles, Frontiers Research Topics unify the most influential researchers, the latest key findings and historical advances in a hot research area.

Find out more on how to host your own Frontiers Research Topic or contribute to one as an author by contacting the Frontiers editorial office: frontiersin.org/about/contact

Cell size regulation: Molecular mechanisms and physiological importance

Topic editors

Evgeny Zatulovskiy — Stanford University, United States

Jette Lengefeld — University of Helsinki, Finland

Citation

Zatulovskiy, E., Lengefeld, J., eds. (2023). *Cell size regulation: Molecular mechanisms and physiological importance*. Lausanne: Frontiers Media SA.

doi: 10.3389/978-2-8325-2607-1

Table of contents

04 Editorial: Cell size regulation: molecular mechanisms and physiological importance
Jette Lengefeld and Evgeny Zatulovskiy

08 S6 kinase 1 at the central node of cell size and ageing
Stefano Fumagalli and Mario Pende

20 The cell cycle inhibitor RB is diluted in G1 and contributes to controlling cell size in the mouse liver
Shuyuan Zhang, Evgeny Zatulovskiy, Julia Arand, Julien Sage and Jan M. Skotheim

32 Delineation of proteome changes driven by cell size and growth rate
Evgeny Zatulovskiy, Michael C. Lanz, Shuyuan Zhang, Frank McCarthy, Joshua E. Elias and Jan M. Skotheim

46 Expansion of the Inguinal Adipose Tissue Depot Correlates With Systemic Insulin Resistance in C57BL/6J Mice
Claes Fryklund, Mathis Neuhaus, Björn Morén, Andrea Borreguero-Muñoz, Richard Lundmark and Karin G. Stenkula

58 The uniformity and stability of cellular mass density in mammalian cell culture
Xili Liu, Seungeun Oh and Marc W. Kirschner

82 Aberrant regulation of autophagy disturbs fibrotic liver regeneration after partial hepatectomy
Yuan-E. Lian, Yan-Nan Bai, Jian-Lin Lai and Ai-Min Huang

94 What programs the size of animal cells?
Shixuan Liu, Ceryl Tan, Mike Tyers, Anders Zetterberg and Ran Kafri

113 Cellular enlargement - A new hallmark of aging?
Daniel M. Davies, Kim van den Handel, Soham Bharadwaj and Jette Lengefeld

130 The environmental stress response regulates ribosome content in cell cycle-arrested *S. cerevisiae*
Allegra Terhorst, Arzu Sandikci, Charles A. Whittaker, Tamás Szórádi, Liam J. Holt, Gabriel E. Neurohr and Angelika Amon

frontiers | Frontiers in Cell and Developmental Biology

TYPE Editorial
PUBLISHED 18 May 2023
DOI 10.3389/fcell.2023.1219294

OPEN ACCESS

EDITED AND REVIEWED BY
Philipp Kaldis,
Lund University, Sweden

*CORRESPONDENCE
Jette Lengefeld,
jette.lengefeld@helsinki.fi
Evgeny Zatulovskiy,
evgeny@stanford.edu

†These authors contributed equally to this work

RECEIVED 08 May 2023
ACCEPTED 10 May 2023
PUBLISHED 18 May 2023

CITATION
Lengefeld J and Zatulovskiy E (2023), Editorial: Cell size regulation: molecular mechanisms and physiological importance.
Front. Cell Dev. Biol. 11:1219294.
doi: 10.3389/fcell.2023.1219294

Editorial: Cell size regulation: molecular mechanisms and physiological importance

Jette Lengefeld[1,2†]* and Evgeny Zatulovskiy[3†]*

[1]Helsinki Institute of Life Science, HiLIFE, Institute of Biotechnology, Faculty of Biological and Environmental Sciences, University of Helsinki, Helsinki, Finland, [2]Department of Medicine Huddinge, Center for Hematology and Regenerative Medicine, Karolinska Institutet, Stockholm, Sweden, [3]Department of Biology, Stanford University, Stanford, CA, United States

KEYWORDS

cell size, aging, cell cycle, cell growth, mTOR

Editorial on the Research Topic
Cell size regulation: molecular mechanisms and physiological importance

Cell size is an evident and universal property of all cells in nature, yet we still know surprisingly little about the molecular mechanisms controlling cell size. Even less is known about how changes in cell size affect cell physiology. Over the past decades, many studies have described that various genetic and chemical manipulations also alter cell size, but the significance of these size changes has often been overlooked when interpreting experimental results. Thus, we know very little of how cell size affects cellular processes. Now, it crystallizes that cell size is an indispensable cellular feature that globally affects cell physiology. In this Research Topic, we are presenting a collection of papers that provide an overview of the existing knowledge and new studies demonstrating how cell size is regulated and why cell size regulation is crucial for cell and tissue function (Figure 1).

How is cell size controlled?

Although cell size homeostasis has been studied for over a century, only with modern techniques are we able to gain more detailed and mechanistic insights into how cell size is regulated. The review by S. Liu et al. summarizes the historical findings and our current understanding of the molecular principles controlling cell size. An analogy of a 'room thermostat' is used to explain the two distinct modules of cell size regulation: one module sets the target average size for cells in a population, and another module senses cell size to ensure that cells do not deviate too far from the set size. Different types of mutations in size-related signaling pathways can either shift the mean size of the cells in the population or increase the size variation without changing the mean size (Liu et al., 2018; Tan et al., 2021). The review points out that a more comprehensive mechanistic understanding of what pathways sense and regulate cell size in a wild-type context still needs to be achieved in the future.

In global terms, cell size can be regulated in two possible ways: the cell can either adjust its biosynthesis rate (size-dependent growth) or its division rate (size-dependent cell cycle progression) (Cadart et al., 2018; Ginzberg et al., 2018; Zatulovskiy and Skotheim, 2020). To mechanistically understand how size affects cell cycle progression rates *in vivo*, the report by Zhang et al. followed up on the recent finding that size-dependent cell cycle progression in

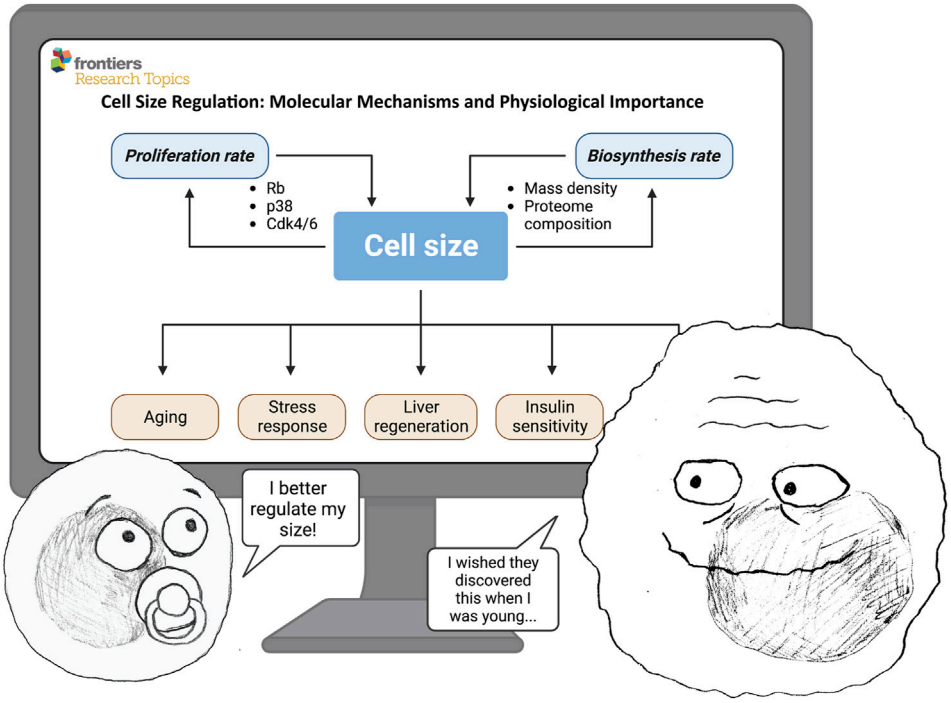

FIGURE 1
Cell size is determined by the balance between biosynthesis (cell mass accumulation rate) and proliferation (cell division rate). In turn, cell size can affect many important physiological processes—such as proliferation, growth rate, aging, stress response, regeneration, insulin sensitivity, and others. ©BioRender—biorender.com was used for image.

cultured cells is controlled by the dilution of a key cell cycle inhibitor - the retinoblastoma protein (RB) (Zatulovskiy et al., 2020). The authors demonstrate that RB dilution also plays an important role in controlling the size of mouse liver cells *in vivo*. This study confirms that growth-dependent dilution of cell cycle inhibitors is an evolutionary conserved mechanism that plays an important role in cell size regulation in different types of organisms (Schmoller et al., 2015; D'Ario et al., 2021).

The review by Fumagalli and Pende addresses the other branch of cell size control - the growth rate regulation. Specifically, the authors focus on one of the central nodes of mTOR signaling–the S6 kinase 1 (S6K1). They review proposed mechanisms underlying the effects of S6K1 on cell size and discuss the roles of S6K1 in connecting cell size with regeneration and aging. Evidence for a molecular program coordinating nucleic acid and protein synthesis, fat mass accumulation, retrograde control of insulin action, senescence program and cytoskeleton organization is revealed through the analysis of S6K1 targets.

While cell size is typically characterized either by the dry mass or by the volume of the cell these two parameters are regulated by different mechanisms and operate at different time scales (Cadart et al., 2019). The study by X. Liu et al. focuses on the biomass density dynamics in mammalian cells undergoing cell mass and cell volume changes. Using a novel technique that they developed and optimized - Normalized Raman Imaging (NoRI) - they demonstrate that besides the overall cell volume and mass, cells also very precisely control the intracellular mass density, which remains constant across many perturbations of cell biosynthesis and proliferation rates. Furthermore, they also observe that cellular senescence and starvation can alter the cell mass density, in agreement with previous reports (Neurohr et al., 2019; Neurohr and Amon, 2020; Oh et al., 2022). Thus, a stringent control of cell mass density is likely important for cell physiology.

Why is cell size regulation important for cell function?

Cell size is tightly regulated within tissues (Xie and Skotheim, 2020), indicating that cell size control is crucial for cellular function. Yet, we know very little about how cell size affects cellular physiology and how cell size deregulation contributes to cellular dysfunctions. Aging is a prime example of the connection between cell size alterations and cellular dysfunction. The review by Davies et al. takes a thorough look through the body of literature published over the past decades to provide an overview of the connections between cell size and aging-related diseases. First, the review discusses the implications of recent studies suggesting that cellular enlargement promotes aging (Demidenko and Blagosklonny, 2008; Neurohr et al., 2019; Lengefeld et al., 2021; Lanz et al., 2022), and then highlights connections between cell size and established aging factors. Then, the focus is placed on publications reporting a correlation between cell size and aging-related diseases, crystallizing the potential of cellular enlargement as a new hallmark of aging. In line with this

paper, the above-mentioned review by S. Liu et al. also highlights the connections between cell size, stemness, and lifespan/aging. These two papers underscore the need for future research to understand the correlative or causative links between cellular enlargement and function. Such research could affect other research areas that have so far overlooked the importance of cell size.

A related study by Zatulovskiy et al. sheds light on the mechanisms by which large cell size is connected to senescence and global proteome rearrangements. It was long assumed that senescent cells are large because they permanently exit the cell division cycle while continuing to grow in mass (Hernandez-Segura et al., 2018). However, using a quantitative proteomics approach, the authors demonstrated that the reversed causality also takes place–*i.e.*, large cell size itself leads to global proteome rearrangements that promote senescence (Lanz et al., 2022). Here, the authors show that an increase in cell size slows down cell growth, and this slowdown mediates many of the observed size-dependent changes in the cell proteome, including the senescence-related changes. These effects can be avoided if cell size increase is compensated by a corresponding increase in cell ploidy. These findings provide a possible rationale for why cells control their size: the further a cell gets from its size optimum, the more disbalanced its proteome becomes, which impairs cell fitness and function. For the same reason, cells that need to be large to perform their functions may become polyploid to avoid senescence and other negative consequences.

The slowdown of cell growth in large mammalian cells is accompanied by a selective reduction in the ribosome fraction. Terhorst et al. here demonstrate that selective downregulation of ribosomes also accompanies growth attenuation in cell-cycle-arrested budding yeast cells. Ribosome downregulation is orchestrated by a transcriptional program known as the Environmental Stress Response (ESR), which is activated in a size dependent manner. Interestingly, preventing downregulation of ribosome biogenesis did not rescue growth rates in large cells, suggesting that ribosomes are not rate limiting for protein synthesis in oversized cells.

A challenge in the cell size field is to understand how cell size affects the function of different organs *in vivo*. Two papers in this Research Topic approach this question by looking at cell size in the adipose tissue and in regenerating liver. The study by Lian et al. shows that liver regeneration after partial hepatectomy is impaired in fibrotic mouse livers. This reduction in tissue regeneration is accompanied by an increase in hepatocyte size and deregulated autophagy. However, the mechanistic and causal relationship between the fibrotic changes, cell size, autophagy, and regeneration remain to be elucidated.

The paper by Fryklund et al. demonstrates that diet-induced obesity in mice leads to inguinal adipocytes hypertrophy (increase in size), accompanied by an increased actin filamentation and reduced insulin-stimulated glucose uptake. Interestingly, when the animals were switched from 4 or 8 weeks of high-fat diet back to regular chow, those changes in cell size and insulin sensitivity reversed back to normal. However, if the animals were kept on a high-fat diet for 12 weeks, those changes could not be reversed anymore. Together with earlier observations that changes in pancreatic beta-cell sizes lead to reduced insulin production (Salans et al., 1968; Giordano et al., 1993), these findings point towards a possible contribution of cell size dysregulation to obesity-related diabetes.

Summary

Overall, the papers presented in this Research Topic demonstrate how latest technological developments–such as Raman spectroscopy (X. Liu et al.), quantitative proteomics (Zatulovskiy et al.; Terhorst et al.), chemical and genetic screens (S. Liu et al.; Fumagalli and Pende) - provide an excellent opportunity for moving forward from phenomenological towards mechanistic studies of cell size. Our progress in understanding the functional roles of cell size regulation in tissues will strongly depend on our ability to adopt tractable and analyzable *in vivo* models for cell size research (Davies et al.; Lian et al.; Fryklund et al.; Zhang et al.).

In memory of Angelika Amon - A brilliant researcher and role model

We would like to remember Angelika Amon, who died on the 29th of October 2020. Her pioneering work in the fields of cell cycle and cell size regulation was truly groundbreaking and she inspired countless individuals with her unwavering curiosity, perseverance, and passion for discovery. Angelika was also a devoted mentor and a fearless advocate for the rights of women and minorities in science. Her impact on our community and research will last a long time. We will remember her as a true pioneer and an inspiration to us all.

Author contributions

All authors listed have made a substantial, direct, and intellectual contribution to the work and approved it for publication.

Conflict of interest

The authors declare that the research was conducted in the absence of any commercial or financial relationships that could be construed as a potential conflict of interest.

Publisher's note

References

Cadart, C., Monnier, S., Grilli, J., Sáez, P. J., Srivastava, N., Attia, R., et al. (2018). Size control in mammalian cells involves modulation of both growth rate and cell cycle duration. *Nat. Commun.* 9, 3275. doi:10.1038/s41467-018-05393-0

Cadart, C., Venkova, L., Recho, P., Lagomarsino, M. C., and Piel, M. (2019). The physics of cell-size regulation across timescales. *Nat. Phys.* 15, 993–1004. doi:10.1038/s41567-019-0629-y

D'Ario, M., Tavares, R., Schiessl, K., Desvoyes, B., Gutierrez, C., Howard, M., et al. (2021). Cell size controlled in plants using DNA content as an internal scale. *Science* 372, 1176–1181. doi:10.1126/science.abb4348

Demidenko, Z. N., and Blagosklonny, M. V. (2008). Growth stimulation leads to cellular senescence when the cell cycle is blocked. *Cell. Cycle* 7, 3355–3361. doi:10.4161/cc.7.21.6919

Ginzberg, M. B., Chang, N., D'Souza, H., Patel, N., Kafri, R., and Kirschner, M. W. (2018). Cell size sensing in animal cells coordinates anabolic growth rates and cell cycle progression to maintain cell size uniformity. Elife*7* 7, e26957. doi:10.7554/eLife.26957

Giordano, E., Cirulli, V., Bosco, D., Rouiller, D., Halban, P., and Meda, P. (1993). B-cell size influences glucose-stimulated insulin secretion. *Am. J. Physiology-Cell Physiology* 265, C358–C364. doi:10.1152/ajpcell.1993.265.2.C358

Hernandez-Segura, A., Nehme, J., and Demaria, M. (2018). Hallmarks of cellular senescence. *Trends Cell. Biol.* 28, 436–453. doi:10.1016/j.tcb.2018.02.001

Lanz, M. C., Zatulovskiy, E., Swaffer, M. P., Zhang, L., Ilerten, I., Zhang, S., et al. (2022). Increasing cell size remodels the proteome and promotes senescence. *Mol. Cell.* 82, 3255–3269.e8. doi:10.1016/j.molcel.2022.07.017

Lengefeld, J., Cheng, C.-W., Maretich, P., Blair, M., Hagen, H., McReynolds, M. R., et al. (2021). Cell size is a determinant of stem cell potential during aging. *Sci. Adv.* 7, eabk0271. doi:10.1126/sciadv.abk0271

Liu, S., Ginzberg, M. B., Patel, N., Hild, M., Leung, B., Li, Z., et al. (2018). Size uniformity of animal cells is actively maintained by a p38 MAPK-dependent regulation of G1-length. *Elife* 7, e26947. doi:10.7554/eLife.26947

Neurohr, G. E., and Amon, A. (2020). Relevance and regulation of cell density. *Trends Cell Biol.* 30 (3), 213–225. doi:10.1016/j.tcb.2019.12.006

Neurohr, G. E., Terry, R. L., Lengefeld, J., Bonney, M., Brittingham, G. P., Moretto, F., et al. (2019). Excessive cell growth causes cytoplasm dilution and contributes to senescence. *Cell.* 176, 1083–1097. doi:10.1016/j.cell.2019.01.018

Oh, S., Lee, C., Yang, W., Li, A., Mukherjee, A., Basan, M., et al. (2022). Protein and lipid mass concentration measurement in tissues by stimulated Raman scattering microscopy. *Proc. Natl. Acad. Sci. U S A.* 119 (17), e2117938119. doi:10.1073/pnas.2117938119

Salans, L. B., Knittle, J. L., and Hirsch, J. (1968). The role of adipose cell size and adipose tissue insulin sensitivity in the carbohydrate intolerance of human obesity. *J. Clin. Investig.* 47, 153–165. doi:10.1172/JCI105705

Schmoller, K. M., Turner, J. J., Kõivomägi, M., and Skotheim, J. M. (2015). Dilution of the cell cycle inhibitor Whi5 controls budding-yeast cell size. *Nature* 526, 268–272. doi:10.1038/nature14908

Tan, C., Ginzberg, M. B., Webster, R., Iyengar, S., Liu, S., Papadopoli, D., et al. (2021). Cell size homeostasis is maintained by CDK4-dependent activation of p38 MAPK. *Dev. Cell.* 56, 1756–1769.e7. doi:10.1016/j.devcel.2021.04.030

Xie, S., and Skotheim, J. M. (2020). A G1 sizer coordinates growth and division in the mouse epidermis. *Curr. Biol.* 30 (5), 916–924.e2. doi:10.1016/j.cub.2019.12.062

Zatulovskiy, E., and Skotheim, J. M. (2020). On the molecular mechanisms regulating animal cell size homeostasis. *Trends Genet.* 36, 360–372. doi:10.1016/j.tig.2020.01.011

Zatulovskiy, E., Zhang, S., Berenson, D. F., Topacio, B. R., and Skotheim, J. M. (2020). Cell growth dilutes the cell cycle inhibitor Rb to trigger cell division. *Science* 369, 466–471. doi:10.1126/science.aaz6213

frontiers | Frontiers in Cell and Developmental Biology

TYPE Review
PUBLISHED 12 August 2022
DOI 10.3389/fcell.2022.949196

OPEN ACCESS

EDITED BY
Evgeny Zatulovskiy,
Stanford University, United States

REVIEWED BY
Shuyuan Zhang,
Stanford University, United States
Jianling Xie,
Flinders University, Australia

*CORRESPONDENCE
Stefano Fumagalli,
stefano.fumagalli@inserm.fr
Mario Pende,
Mario.pende@inserm.fr

SPECIALTY SECTION
This article was submitted to Cell Growth and Division, a section of the journal Frontiers in Cell and Developmental Biology

RECEIVED 20 May 2022
ACCEPTED 07 July 2022
PUBLISHED 12 August 2022

CITATION
Fumagalli S and Pende M (2022), S6 kinase 1 at the central node of cell size and ageing.
Front. Cell Dev. Biol. 10:949196.
doi: 10.3389/fcell.2022.949196

S6 kinase 1 at the central node of cell size and ageing

Stefano Fumagalli* and Mario Pende*

Université Paris Cité, INSERM UMR-S1151, CNRS UMR-S8253, Institut Necker Enfants Malades, Paris, France

Genetic evidence in living organisms from yeast to plants and animals, including humans, unquestionably identifies the Target Of Rapamycin kinase (TOR or mTOR for mammalian/mechanistic) signal transduction pathway as a master regulator of growth through the control of cell size and cell number. Among the mTOR targets, the activation of p70 S6 kinase 1 (S6K1) is exquisitely sensitive to nutrient availability and rapamycin inhibition. Of note, *in vivo* analysis of mutant flies and mice reveals that S6K1 predominantly regulates cell size versus cell proliferation. Here we review the putative mechanisms of S6K1 action on cell size by considering the main functional categories of S6K1 targets: substrates involved in nucleic acid and protein synthesis, fat mass accumulation, retrograde control of insulin action, senescence program and cytoskeleton organization. We discuss how S6K1 may be involved in the observed interconnection between cell size, regenerative and ageing responses.

KEYWORDS

mTOR, signal transduction, nutrition, growth, ageing, senescence

Genetic evidence of growth regulators and signal transduction mechanisms

At the turn of the second and third millennium, genetic screens for tissue overgrowth in *Drosophila* flies identify loss-of-function (LOF) mutants falling in two broad categories: hyperplastic with increased cell size, such as Gigas-Tuberous Sclerosis Complex 2 (*TSC2*), Tuberous Sclerosis Complex 1 (*TSC1*) and Phosphatase And Tensin Homolog (*PTEN*) (Huang et al., 1999; Ito and Rubin, 1999; Stocker and Hafen, 2000); and hyperplastic with constant cell size, such as Hippo, Salvador, Merlin, Warts (Pantalacci et al., 2003; Udan et al., 2003; Wu et al., 2003). At the same time, biochemical studies demonstrated that the gene products belong to two signal transduction pathways integrating environmental cues and regulating tissue growth: the mTOR and the Hippo kinase pathways (Ma et al., 2018; Liu and Sabatini, 2020). mTOR mainly senses nutrient availability, whereas the Hippo pathway mainly senses the physical environment. While TSC1, TSC2 and PTEN are negative regulators of the mTOR pathway, LOF mutants in positive regulators, such as Insulin Receptor Substrate (IRS), Phosphoinositide-3-Kinase (PI3K), Akt and mTOR itself, reduce both cell size and number (Leevers et al., 1996; Bohni et al., 1999; Verdu et al., 1999; Zhang et al., 2000; Gao et al., 2002; Zhang et al., 2003). Of note, adult flies lacking the *S6K* gene have the same cell number as wild type flies but their cell size is reduced, as measured in the eye and wing tissues (Montagne et al., 1999). The differential impact of

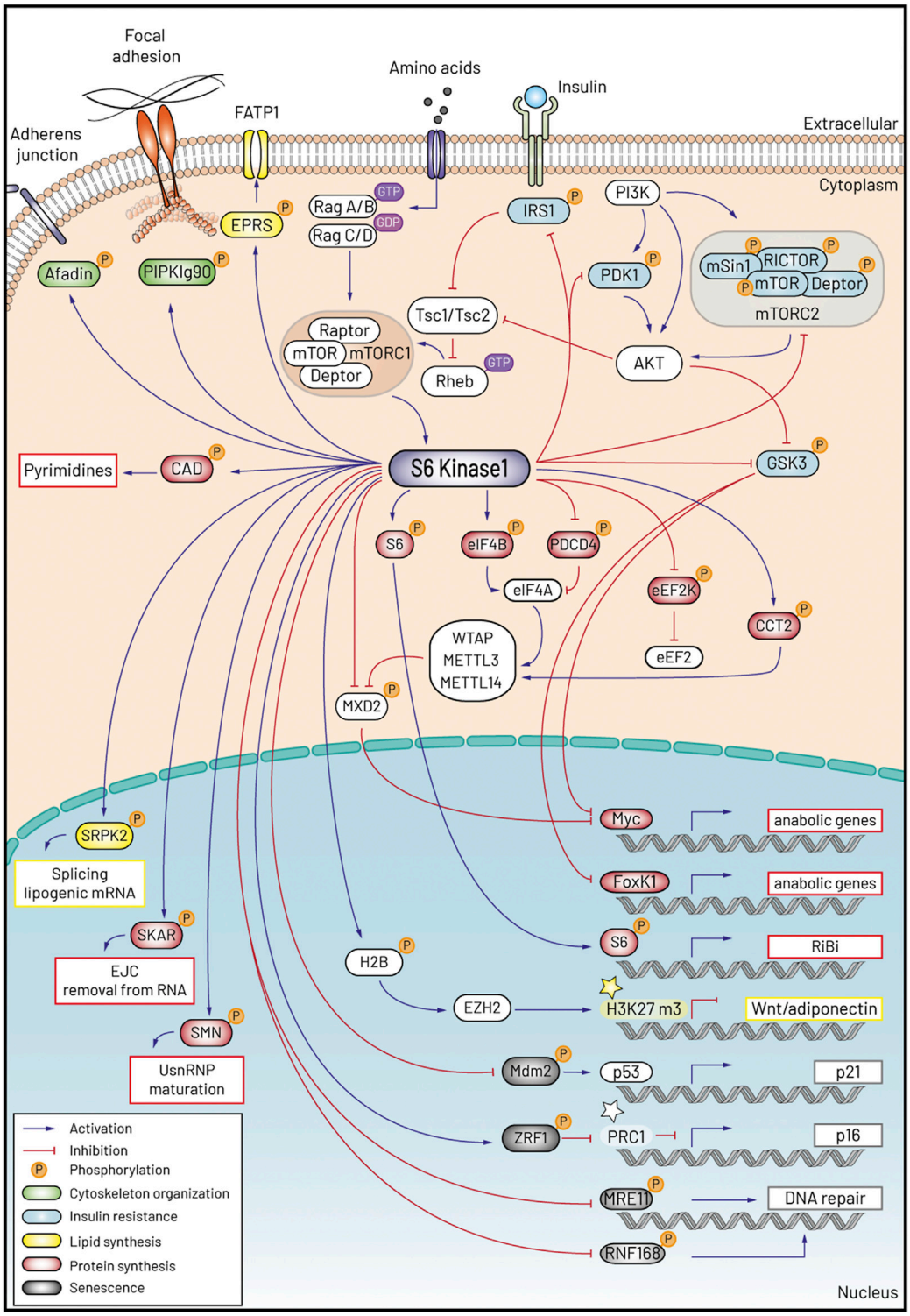

FIGURE 1
Schematic representation of S6K1 signaling and the five programs accounting for the control of cell size and ageing.

growth mutants on cell size and cell number points to a loose relationship between these parameters. While the *Drosophila* fly genome contains a single *S6K* gene, two orthologous *RPS6KB1* and *RPS6KB2* genes exist in mammals, encoding the S6K1 and S6K2 proteins, respectively (Banerjee et al., 1990; Kozma et al., 1990; Gout et al., 1998; Shima et al., 1998; Lee-Fruman et al., 1999). Here, we will review the studies detailing the effectors of S6 kinases and the physiological alterations concomitant with the cell size control by this molecular program.

S6K and Akt belong to the AGC family of serine and threonine protein kinases (Pearce et al., 2010). They are activated by phosphorylation on their hydrophobic motifs and T-loop motifs by mTOR and 3-Phosphoinositide Dependent Protein Kinase (PDK1), respectively (Alessi et al., 1997; Alessi et al., 1998; Pullen et al., 1998; Hara et al., 2002; Kim et al., 2002; Sarbassov et al., 2005). However, mTOR resides in different protein complexes when it catalyzes S6K or Akt phosphorylation. While S6K is phosphorylated by mTOR complex 1 (mTORC1), Akt is phosphorylated by mTOR complex 2 (mTORC2). mTORC1 and mTORC2 differ in their sensitivity to the two main anabolic signals from nutrition: small nutrients molecules, such as glucose, amino acids and lipids which enter in circulation after food digestion, and growth factor peptides, such as insulin, that are secreted after food intake and coordinate nutrient usage in peripheral organs. mTORC1 activity requires signals from both nutrients and growth factors, while mTORC2 activity is relatively insensitive to nutrient levels (Liu and Sabatini, 2020). In addition, mTORC2 promotes mTORC1 activity, while being negatively regulated by mTORC1 in a retrocontrol mechanism. This cross-talk and differential sensitivity of mTORC1 and mTORC2 to the anabolic signals explain many physiological adaptations to nutrition. For instance, protein synthesis and cell growth are mainly upregulated by mTORC1 when both insulin and nutrients are present (Pham et al., 2000). Conversely, the metabolic action of insulin on nutrient uptake and gluconeogenesis is mainly regulated by mTORC2, with an excess of nutrients causing insulin resistance through the negative feedback loop of mTORC1 on mTORC2 (Fingar et al., 1993; Tremblay and Marette, 2001).

The convergence of nutrients and insulin signals for mTORC1 activation takes place at the lysosomal membrane, through the regulation of two small GTPase family members Ras Related GTP Binding A/B/C/D (RagA/B/C/D) and Ras Homolog Enriched In Brain (Rheb) that are important for mTORC1 localization and activity, respectively (Liu and Sabatini, 2020). It is becoming increasingly clear that the phosphorylation of protein substrates by mTORC1 is differentially sensitive to upstream regulators. Since the relative activity of mTORC1 towards S6K1 is low, this phosphorylation event is very sensitive to rapamycin treatment and nutritional perturbations that change mTORC1 activity through Rheb and Rag GTP loading (Chung et al., 1992; Kang et al., 2013). Conversely, the phosphorylation of other mTORC1 substrates, such as 4EBPs, is more constitutive and less sensitive to nutritional fluctuations as well as pharmacological inhibition by rapamycin (Choo et al., 2008). Moreover, phosphorylation of certain substrates, such as TFEB, is insensitive to the Rheb-dependent regulation of mTORC1 and exquisitely depends on the regulation at the level of RagC/D (Napolitano et al., 2020). It appears therefore that mTORC1 is capable to integrate a large variety of information from the environment and adapt the output towards distinct classes of substrates depending on the conditions.

S6 kinases are also extensively phosphorylated in the proline rich C-terminus region, a pseudosubstrate domain possibly exerting autoinhibitory effects on kinase activity (Mukhopadhyay et al., 1992; Dennis et al., 1998). The phosphorylation of the C-terminus region has been proposed to relieve the autoinhibitory regulation and expose the kinase for phosphorylation on the hydrophobic motifs and T-loop motifs required for activation and substrate docking. Several proline directed kinases can phosphorylate the C-terminus region of S6K1 *in vitro*, including Cyclin dependent kinases (Cdk) Cdk5 and Cdk1, Mitogen Activated protein kinases (MAPK) and mTOR itself (Mukhopadhyay et al., 1992; Arif et al., 2019). It is still unclear whether these kinases can compensate each other or whether they directly phosphorylate specific sites *in vivo*. This model of S6K1 regulation is consistent with the genetic epistasis experiments and pharmacological treatments by rapamycin derivatives, indicating that mTOR-mediated phosphorylation on the hydrophobic motif is absolutely required for S6K1 action on downstream substrates. However, a recent study proposes that Cdk5-mediated S6K1 phosphorylation on the C-terminus region may trigger a conformational switch that directs S6K1 kinase activity towards a different class of substrates (Arif et al., 2019). This appealing and original control still requires further work, namely the *in vivo* analysis of Cdk5 knockout mice and the generation of phospho-specific antibodies against the Cdk5-directed substrates. Of note, additional Cdk, such as Cdk4 and Cdk6, impinge on mTOR/S6K activity by affecting upstream regulators, such as the lysosomal complexes and TSC, rather than directly on kinase phosphorylation (Martinez-Carreres et al., 2019; Romero-Pozuelo et al., 2020).

Given the peculiar sensitivity of S6K1 to mTORC1 activity, it is not surprising that S6K1 deficient mice mimic a caloric restriction phenotype. They have low insulin levels in their blood, are hypersensitive to action of insulin on glucose tolerance, do not become obese after high fat diet and live longer (Pende et al., 2000; Um et al., 2004;

Selman et al., 2009). Of note, all these physiological adaptations are accompanied by a reduction of cell size. The cell volume shrinkage is approximately 15%–35% depending on the cell type. This is less dramatic than the profound cell atrophy due to mTOR deletion, consistent with the idea that *S6K1* deletion does not induce autophagy. Similarly, *S6K* deletion in *Drosophila* flies rescues the overgrowth phenotype of the *Gigas-TSC2* mutation to the level of wild type tissues (Gao et al., 2002). The effect of S6K on cell size can be recapitulated *in vitro* after genome editing in cultured cells, pointing to a cell autonomous regulation of cell size by S6K1 (Bonucci et al., 2020). The decreased cell size is observed throughout different phases of cell cycle as well as in post-mitotic cells (Ohanna et al., 2005; Bonucci et al., 2020). *S6K1* deletion mimics the effect of rapamycin on cell size but not on cell proliferation (Ohanna et al., 2005; Dowling et al., 2010). Conversely, *4EBPs* deletion causes resistance to the anti-proliferative action of mTOR inhibitors without affecting cell size (Dowling et al., 2010).

Cell size fluctuations have been recently proposed to directly affect senescence or stem cell potential (Neurohr et al., 2019; Lengefeld et al., 2021). We will now discuss how the S6K dependent molecular program may contribute to these coordinated responses: protein and lipid mass accumulation, insulin resistance, cytoskeletal dynamics and senescence. The elucidation of the S6K substrates is rapidly progressing thanks to the deep coverage of the phosphoproteomics analysis after rapamycin treatment, mTORC1 or S6K1 genetic deletion (Moritz et al., 2010; Hsu et al., 2011; Yu et al., 2011; Robitaille et al., 2013; Bonucci et al., 2020). A comprehensive and updated list of S6K substrates can be found at the PhosphoSitePlus online tool: https://www.phosphosite.org/substrateSearchViewAction.action?id=1012&type=Protein: the phosphorylation sites and consensus sequences are also adequately indicated there and are therefore omitted in this review. Figure 1 is a graphic representation of the S6K1 signaling network.

Protein mass accumulation

Protein synthesis

Substrates belonging to the protein synthesis machinery represent the most important class of S6K targets for both historic reasons and their high number. S6 kinases were initially isolated due to their enzymatic activity phosphorylating the ribosomes. Phosphorylation of the 40S ribosomal protein S6 (eS6 according to the novel nomenclature (Ban et al., 2014)) occurs in mammals and *Xenopus* at the C-terminus of the protein (Krieg et al., 1988; Wettenhall et al., 1992). *In vivo*, S6K1 and S6K2 are the main kinases responsible for eS6 phosphorylation, although residual eS6 phosphorylation by compensating p90 Ribosomal Protein S6 Kinase RPS6KA1-3 (RSK 1-3) downstream of Mitogen Activated protein kinases (MAPK, ERK1 and ERK2) can occur in an S6K null background (Pende et al., 2004). The evidence of eS6 phosphorylation playing a stimulatory role on protein synthesis is correlative and its function in mRNA translation remains elusive. Some insights on a physiological function of eS6 phosphorylation have arisen from the analysis of the $S6^{-/-P}$ knock-in mice where all the five phosphorylatable serines of eS6 are mutated to alanines (Ruvinsky et al., 2005). Although the phenotype of $S6^{-/-P}$ knock-in mice is milder than S6K1−/− mice, they also display small cell size of pancreatic beta cells and muscle cells, suggesting that eS6 phosphorylation participates in cell size control (Pende et al., 2000; Ohanna et al., 2005; Ruvinsky et al., 2005; Ruvinsky et al., 2009). If the phenotype of $S6^{-/-P}$ mice would be consistent with a stimulatory role of eS6 phosphorylation on protein synthesis, it is puzzling that $S6^{-/-P}$ cells from different tissues display higher protein synthesis rates than their wild type (WT) controls, arguing that eS6 phosphorylation has an inhibitory function on mRNA translation (Ruvinsky et al., 2005; Hsieh et al., 2010). Consistently, S6K1 deficient mice do not display a reduction in global protein synthesis (Mieulet et al., 2007). The mechanistic aspects of these effects have not been thoroughly investigated and it cannot be excluded that they arise from the activation of compensatory mechanisms. Some clues come from a recent study that by comparing the translation efficiency of WT and $S6^{-/-P}$ cells provides evidence that eS6 phosphorylation has a mild stimulatory effect on the translation of short mRNAs (Bohlen et al., 2021). Among those, however, an exception is that of 5TOP mRNAs that mainly encode ribosomal proteins and are translated more efficiently in $S6^{-/-P}$ than WT cells. In agreement with this observation, ribosomal protein levels, a proxy of ribosome content, are higher in $S6^{-/-P}$ as compared to WT cell (Bohlen et al., 2021), which is consistent with the difference in the rates of protein synthesis (Ruvinsky et al., 2005). An *in vivo* study employing $S6^{P-/-}$ mice indicates that in liver of animals fed after fasting eS6 phosphorylation mediates in part the stimulatory effects of S6K on the transcription of genes encoding RiBi (ribosome biogenesis) factors, implicated in the assembly and maturation of ribosomal subunits, contributing therefore to the increase in ribosome synthesis that ensues in response to feeding (Chauvin et al., 2014). It is likely that these effects are due to an extra-ribosomal function of eS6, although it cannot be excluded that phosphorylated ribosomes regulate the synthesis of factors that impact on Ribi mRNA levels.

The major hub of protein synthesis control by the mTORC1 pathway is the eIF4F (eukaryotic initiation factor 4F) complex that mediates during the initiation phase the recruitment to the mRNA of the 43S pre-initiation complex, i.e., the 40S ribosomal subunit bound to the ternary complex (eIF2-GTP-Met-tRNA), and the initiation factors eIF1, eIF1A, eIF3, and eIF5 (Merrick and Pavitt, 2018). eIF4F is composed by a scaffold, eIF4G, that interacts with the two other components of

the complex, the cap binding protein eIF4E and the RNA helicase eIF4A. During initiation of protein synthesis, eIF4G interacts with the 43S preinitiation complex whereas the eIF4E moiety makes contact with the cap structure found at the 5′ end of mRNAs. This interaction is favoured by eIF4A that unwinds secondary structures proximal to the cap and facilitates therefore binding of the 43S complex to the mRNA. In this process the activity of eIF4A is greatly enhanced by the factor eIF4B (Merrick and Pavitt, 2018). Formation of the eIF4F complex is regulated in an mTORC1 dependent manner by growth factors and nutrients. Thus, under conditions of nutrient scarcity, members of the 4EBP (eIF4E binding protein) family efficiently compete with eIF4G for binding to eIF4E preventing therefore eIF4F complex formation and suppressing protein synthesis. Upon nutrient addition, phosphorylation of 4EBPs at several sites mainly by mTORC1, promotes their dissociation from eIF4E which becomes available for the formation of the eIF4F complex allowing an increase in the rates of protein synthesis (Merrick and Pavitt, 2018). A further layer of regulation on eIF4F formation is provided by S6K. This involves the phosphorylation and subsequent ubiquitin-dependent degradation of programmed cell death 4 (PDCD4), a protein that interferes with eIF4A activity and its binding to eIF4G (Dorrello et al., 2006). Furthermore, phosphorylation of eIF4B by S6K stimulates protein synthesis through a mechanism that may involve recruitment of eIF4B in proximity of eIF4F (Holz et al., 2005; Shahbazian et al., 2006).

Besides translation initiation, elongation is also subjected to regulation by the pathway. An inhibitory effect on protein synthesis occurs through phosphorylation and consequent inactivation of eukaryotic elongation factor 2 (eEF2) that, during elongation, catalyses the translocation of peptidyl-tRNA from the A to the P site of the translating ribosome (Dever and Green, 2012). The kinase responsible for eEF2 phosphorylation is the Ca2+/Calmodulin dependent kinase eEF2 kinase (eEF2K) (Kenney et al., 2014). This response is thought to promote cell survival under conditions of nutrient scarcity by limiting the highly energy-consuming process of protein synthesis (Leprivier et al., 2013; Faller et al., 2015). It has been shown that in response to mitogenic signals S6K phosphorylates and inactivates eEF2K, ensuring therefore high rates of protein synthesis (Wang et al., 2001; Kenney et al., 2014).

RNA metabolism

S6K might regulate specific mRNA translation through the regulation of their metabolism, including mRNA methylation and splicing. It has been recently shown that in *TSC2*−/− cells, S6K through the eIF4A-eIF4B axis promotes the translation of the mRNA encoding Wilms tumor 1-associated protein (WTAP), the scaffold component of the m^6A methyltransferase complex (MTC). This in turn results in formation of m^6A by the MTC components m^6A methyltransferase like proteins 3 and 14 (METTL3 and METTL14) on, among others, the mRNA encoding the c-myc suppressor MAX dimerization protein 2 (MXD2), triggering its degradation and leading to activation of c-myc transcriptional activity (Cho et al., 2021). MXD2 can also be directly phosphorylated by S6K1, an event promoting protein ubiquitination and degradation (Huang et al., 2018). A role of eIF4B phosphorylation by S6K in directly promoting translation of c-myc mRNA has also been documented in *TSC2*−/− cells (Csibi et al., 2014). Taken together, these findings converge on the Myc transcriptional program in mediating some of the growth-promoting actions of S6K.

Moreover, S6K intervenes in the final maturation steps of mRNAs. As introns are removed from pre-RNAs during splicing, a complex forms twenty four nucleotides upstream of exon-exon junctions known as EJC (Exon-Junction complex). mRNAs associate then to the nuclear CAP binding complex (CBP) and are exported from the nucleus into the cytosol. Here mRNAs, still bound to CBP, are inspected by the so-called pioneer round of translation, a quality control step during which EJC are removed unless an upstream premature translation stop codon is present. Successful removal of the EJC commits the mRNA toward productive protein synthesis (Woodward et al., 2017). It has been shown that S6K1 Aly/REF-like target (SKAR), an RNA binding protein phosphorylated by S6K1 (Richardson et al., 2004), is a component of the EJC (Ma et al., 2008). In response to Insulin, S6K1, by interacting with SKAR, is recruited to CBP-bound mRNPs and presumably stimulates the inspection of the associated mRNAs by the pioneer round of translation providing transcripts to support protein synthesis (Ma et al., 2008). It is interesting that knock down of SKAR results in a small cell size phenotype (Richardson et al., 2004). It will be important to analyse the role that SKAR phosphorylation by S6K plays on regulation of cell size as well as on SKAR function as a component of the EJC. Additional splicing factors controlled by S6K will be discussed in the next chapter.

Protein folding

Growth control by mTOR and S6K also relies on protein folding. In *Drosophila*, the overgrowth phenotype of TOR activation is suppressed by depletion of subunits of chaperonin containing tailless complex polypeptide 1 (CCT), a complex that assists the folding of about 10% of newly synthesized cytosolic proteins (Kim and Choi, 2019). TOR promotes transcription of CCT genes. Of note, CCT subunits are important to maintain the levels of METTL3 and METTL14 in MTC, which contribute to the inhibition of autophagy by catalysing formation of destabilising m6A on

mRNAs encoding autophagy effectors (Tang et al., 2021). Some aspects of this regulatory circuit are conserved in mammalian cells. A possible role of S6K in regulating both CCT and MTC functions is supported by the finding that the CCT2 subunit is phosphorylated by S6K (Abe et al., 2009). Interestingly a CCT2 phosphomutant fails to rescue the proliferation defect caused by depletion of CCT2 in human mammary epithelial cells. S6K also phosphorylates ZRF1, the HSP40 component of the ribosome-associated complex (RAC), a universally conserved broad specificity chaperone system that interacts with the 60S ribosomal subunit assist co-translational folding of nascent polypeptides as they emerge from the tunnel of the ribosome (Barilari et al., 2017). Furthermore, studies in yeast suggest that ZRF1 has a role in maintaining protein synthesis fidelity by interacting with the 40S subunit at a region that is involved in decoding (Lee et al., 2016). It will be important to determine the functional relevance of this phosphorylation event on protein synthesis fidelity.

Nucleotide biosynthesis

A major cellular function involved in cell growth is the synthesis of precursors employed in macromolecular synthesis. These include the pyrimidine and purine bases that are then employed for the synthesis of nucleosides, the components of DNA and RNA (Zhu and Thompson, 2019). Recent work from the Manning laboratory has shown that *de novo* synthesis of both pyrimidines and purines is driven by the mTOR pathway (Ben-Sahra et al., 2013; Ben-Sahra et al., 2016). Downstream of mTOR, S6K plays a crucial role on pyrimidines synthesis through the stimulatory phosphorylation of carbamoyl-phosphate synthetase 2, aspartate transcarbamoylase, dihydroorotase (CAD), the enzyme that catalyses the first three steps of *de novo* pyrimidine synthesis (Ben-Sahra et al., 2013; Robitaille et al., 2013).

Lipid mass accumulation

Interestingly, phosphorylation of splicing and translational machineries has been implicated in one of the most striking cellular responses to S6K1 activity, the fat accumulation. In *Drosophila*, a lipogenic program is sufficient to alter cell size (Porstmann et al., 2008). Although S6K1 has been proposed to directly phosphorylate and regulate the expression of the master regulator of lipid gene expression, the Sterol Regulatory Element-Binding Protein 1 (SREBP1), the experimental evidence is not conclusive (Lewis et al., 2011; Yecies et al., 2011). Two recent studies suggest alternative SREBP1- and transcription-independent mechanisms for the regulation of fat metabolism, involving the Serine-arginine rich protein kinase 2 (SRPK2) and the glutamyl prolyl tRNA synthetase EPRS. SRPK2 regulates serine arginine rich proteins (SR), whose function is to catalyze mRNA splicing by binding exons and recruiting small nuclear ribonucleoproteins (snRNPs) (Lee et al., 2017). S6K1 dependent phosphorylation of SRPK2 in cooperation with an additional Casein Kinase 1 (CK1)-dependent site upregulates nuclear localization of the protein. Nuclear SRPK2 promotes efficient intron splicing of acly, acss2, hmgcs1, mvd, fdft1, scd1, fasn mRNA, thus increasing the stability and the levels of these mRNA coding for proteins involved in lipid synthesis. Conversely, the S6K1-dependent phosphorylation of EPRS acts as a switch for the function of the protein, that becomes a partner of Long-Chain Fatty Acid Transport Protein (FATP1), promoting long chain FA uptake and TG synthesis (Arif et al., 2017). Similar to S6K1 deficient mice, EPRS phosphomutant mice also have reduced fat mass and increased longevity, indicating a participation of the post-translational modification in these phenotypes (Arif et al., 2017). Moreover, when S6K1 receives activating input by Cdk5, additional proteins involved in lipid synthesis can be phosphorylated, including cortactin, lipocalin 2 and coA synthase (Arif et al., 2019). Another original mechanism for the control of lipid synthesis is through epigenetic modifications triggered by S6K1-dependent Histone 2B (H2B) phosphorylation (Yi et al., 2016). In adipocytes, S6K1 can translocate to the nucleus upon treatment with the adipogenic factor Bone Morphogenetic Protein 4 (BMP4). The H2B phosphorylation recruits the Histone-Lysine N-Methyltransferase EZH2 and favours H3K27 trimethylation (H3K27m3), thus suppressing Wnt ligand expression which acts as a brake for adipogenic commitment. The expression of fat-regulating hormones in adipocytes and pancreas, such as adiponectin, insulin and glucagon, may also undergo a similar epigenetic regulation (Yi et al., 2018; Yi et al., 2022).

Insulin sensitivity

S6K1 is involved at multiple levels in the above-mentioned negative feedback mechanism by which an excess of nutrients through the mTORC1/S6K1 axis dowregulates insulin signaling and mTORC2 activity. First, S6K1 acts at the level of IRS proteins which initiate insulin signaling. IRS phosphorylation on Ser and Thr residues by S6K1 and additional kinases contributes to shut down the signal by promoting protein degradation or decreasing the interaction with the receptors (Harrington et al., 2004; Tremblay et al., 2007). Consistently, the increase in insulin sensitivity of S6K1-deficient mice correlates with a decrease in IRS1 Ser/Thr phosphorylation (Um et al., 2004). Second, S6K1 phosphorylates multiple proteins in mTORC1 and mTORC2. S6Ks phosphorylate mTOR itself, however the functional relevance of these phosphorylation sites is unclear (Holz and Blenis, 2005). S6Ks also phosphorylate two components of the mTOR

complex 2 (mTORC2), namely rapamycin-insensitive companion of mTOR (RICTOR) and stress-activated MAPK-interacting protein 1 (SIN1) (Dibble et al., 2009; Julien et al., 2010; Treins et al., 2010; Liu et al., 2013), and the Deptor protein present in both mTORC1 and mTORC2 (Gao et al., 2011; Zhao et al., 2011). Although there are some controversies on the function of each phosphorylation event, there is a general consensus that S6Ks act by inhibiting the mTORC2 substrate Akt. Phosphomimetic SIN1 mutants are unable to interact with RICTOR and mTOR, while phospho-ablative mutants increase Akt phosphorylation (Liu et al., 2013). Similarly, two studies have shown a mild inhibitory effect of RICTOR phosphorylation on AKT activity (Dibble et al., 2009; Julien et al., 2010). The reduced half life of Deptor upon its phosphorylation may also concur to decreased Akt activation (Gao et al., 2011; Zhao et al., 2011).

Another level by which S6K1 may suppress Akt activity is through the phosphorylation of PDK1 on the pleckstrin homology domain that impairs the interaction between PDK1 and Akt (Jiang et al., 2022). Interestingly, if S6K1 has clearly a negative role on the metabolic action of insulin and Akt, it can compensate the Akt action on some substrates that are important growth regulators, such as Glycogen Synthase Kinase 3 (GSK3). S6K1 can phosphorylate GSK3 in conditions of mTORC1 overactivation (Zhang et al., 2006), and thus relieve the GSK3-dependent inhibition of two transcription factors promoting growth, c-Myc and Forkhead Box Protein K1 (FoxK1) (He et al., 2018).

Senescence

Rapamycin treatment has a striking efficacy in delaying the senescence program in cultured cells and preserving their proliferative potential (Leontieva and Blagosklonny, 2013, 2014; Leontieva et al., 2013, 2014; Neurohr et al., 2019; Lengefeld et al., 2021). Primary cells undergoing senescent insults of DNA damage, replication stress, oncogenic mutations and constitutive mTOR activation are protected by rapamycin. Pharmacological inhibition of S6K1 or genetic knock-down/knock-out also rescues the senescent program (Leontieva et al., 2013; Barilari et al., 2017). In TSC1 deficient fibroblasts, S6K1 regulates the expression of the cell cycle inhibitor p16 (Barilari et al., 2017). This is accompanied by the S6K1-dependent phosphorylation of Zrf1, a protein containing a SANT domain for DNA and histone binding and interacting with inhibitor of differentiation 1 (Id1) (Shoji et al., 1995; Richly et al., 2010). Zrf1 has been shown to antagonize the action of polycomb repressive complex 1 (PRC1) that ubiquitinates H2A and silences the *Ink4a/ARF* locus encoding p16 (Richly et al., 2010). In addition, the Zrf1 partners Id proteins can also suppress the activity of ETS1 and ETS2 transcription factors, which are potent activators of p*16* transcription (Shoji et al., 1995). As outlined above, Zrf1 has also cytosolic functions as a co-chaperon forming the ribosome-associated complex (RAC). Although the phosphomutant of Zrf1 delays the senescence program (Barilari et al., 2017), how this post-translational modification affects the molecular function of Zrf1 has not been addressed yet.

S6K1 activity also modulates the DNA damage response, relevant to the induction of senescence. In cells exposed to DNA damaging agents and nutrient-rich conditions, S6K1 contributes to the phosphorylation and cytosolic retention of Mouse double minute homolog 2 (MDM2), the E3 ubiquitin ligase controlling the degradation of p53 (Lai et al., 2010). This potentiates the p53-dependent transcriptional response to DNA damaging agents, and in particular may explain how nutrients and growth factors can favour the pro-apoptotic and pro-senescent function of p53. Moreover, the S6K1-dependent phosphorylation of meiotic recombination 11 protein (MRE11) and Ring Finger Protein 168 (RNF168) triggers the degradation of these proteins crucial for DNA end resection and homologous recombination in the repair of double strand breaks (Piscitello et al., 2018; Xie et al., 2018). This impairs the DNA damage checkpoint and favours the entry of primary fibroblasts into senescence.

Cytoskeleton dynamics

The S6K1-dependent hypertrophy of *TSC1* mutant kidney epithelial cells correlates with misorientation of cell division leading to cyst deformation of renal tubules (Bonucci et al., 2020). However, micropattern experiments to measure the angle of cell division in single cells demonstrate that aberrant cell size is not sufficient to alter the mitotic angle. The defect of oriented cell division can be observed when cells are adjacent to each other in an epithelial layer. This suggests the importance of adhesion cues in the correct determination of planar polarity. Of note, a comprehensive phosphoproteomics analysis of the inner medullary collecting duct cell line mIMCD3 edited in the *TSC1* and *S6K1* genes revealed a broad list of putative S6K1 substrates involved in the regulation of the actin cortex and cell adhesion. These include slingshot protein phosphatase 1 (SSH1), phosphatase for the actin depolymerase cofilin; microtubule actin crosslinking factor 1 (Macf1), spectraplakin binding actin and microtubules; phosphatidylinositol 4-Kinase α (PI4K), regulating endocytic trafficking; myosin phosphatase-targeting subunit 1 and 2 (MyPT1 and MyPT2), myosin phosphatases regulating actomyosin contractility; missing in metastasis protein (Mtss1), cortactin-interacting protein. Among the phosphopeptides, Afadin, an actin binding and adapter protein regulating the nectin and cadherin adhesion systems, has been validated as a novel S6K1 substrate. Afadin phosphorylation alters Adherens

Junctions in kidney epithelial cells and favours cell migration of breast cancer cells (Elloul et al., 2014; Gao et al., 2017). Of note, it has been suggested that Afadin phosphorylation may also be involved in the negative feed-back regulation of insulin action in adipocytes (Lundh et al., 2019), and Afadin phospho-mutant mice display a mild amelioration of glucose homeostasis at the early stages of high fat diet (Tozzi et al., 2022). Consistent with an important role of the mTOR/S6K1 pathway on cell adhesion, S6K1 phosphorylation down-regulates PI 4 phosphate 5 kinase type I g (PIPKIg90), which mediates together with talin the assembly of focal adhesion (Jafari et al., 2016). As a result of S6K1 action on PIPKIg90, cells become more prone to matrix degradation and invasion.

Future perspectives on the spatial control of cell growth and ageing responses

It has been recently proposed that cell size alterations may influence important cell fate decisions, such as senescence or regenerative responses (Neurohr et al., 2019; Lengefeld et al., 2021). It is likely that mTOR and S6K affects physical properties of the cells and define spatially organized microdomains, therefore affecting molecular machineries involved in growth and ageing. Several evidences are consistent with this possibility, though the causal relationships will require further studies. It has been shown that inhibition of mTOR by rapamycin treatment is associated with a decrease of macromolecular crowding and viscosity of the cytosol due to loss of ribosomes, a result of suppression of ribosome biogenesis and increased ribophagy (Delarue et al., 2018). Although it is not defined whether the decrease in ribosome contents is responsible of the decrease in cell size caused by rapamycin, it is clear that the ensuing dilution of the cytosol increases the diffusion of macromolecules. This may favour signaling processes but also impair the assembly of biomolecular condensates. The disproportionate growth of senescent cells, which is associated with a gradual loss of biosynthetic capacity, may also lead eventually to the dilution of the cytosol (Neurohr et al., 2019). The implication of S6K in this phenomenon is suggested by the observation that S6K inactivation prevents senescence of *TSC1−/−* cells (Barilari et al., 2017). S6K might contribute to a level of cytoplasmic crowding appropriate to regulate the on-demand formation of biomolecular condensates that perform crucial cellular functions. This would require a correct balance between the synthesis of crowding agents and other S6K dependent and independent functions that contribute to cell growth. Loss of this coupling would be expected to lead then to variations in the concentration of crowder and consequent alterations in cellular homeostasis.

In recent years, S6K activity has been implicated in the formation of biomolecular condensates, defined as dynamic membraneless subcellular compartments with liquid like properties which perform specific functions and assemble through phase separation. These include among others, nucleoli, Cajal bodies, promyelocytic leukaemia bodies (PML) in the nucleus, and P bodies, stress granules, or synaptic densities in the cytosol (Banani et al., 2017). For instance, stress granules (SGs) formation in response to oxidative stress and heath shock is under the control of the mTOR pathway and sensitive to S6K inhibition (Sfakianos et al., 2018). Although the mechanism has not been elucidated, it probably implicates phosphorylation of SG components that modulate protein-protein interactions and favour the formation of the condensates. Another example is the phosphorylation of the Survival motor Neuron protein (SMN) by S6K. This promotes efficient condensation by liquid liquid phase separation of the SMN complex in Cajal bodies (CBs) (Schilling et al., 2021), thus favouring the final maturation of ribonucleoproteins containing small nuclear U RNAs (UsnRNPs) and assisting the different steps of pre-mRNA splicing (Raimer et al., 2017). Interestingly SMN has SMN-complex independent functions. It has been shown that in fibroblasts a population of SMN is found associated with caveolin at the plasma membrane (Gabanella et al., 2016). Under conditions of recovery from energy stress, SMN at newly-formed membrane protrusion mobilizes inactive membrane-bound ribosomes that are then engaged in local protein synthesis in order to provide proteins required for the stabilization and maintenance of these structures. It will be interesting to determine the dependency of this process on the mTOR/S6K pathway, as well as the elucidation of additional microdomains influenced by these kinases.

As outlined in the previous chapter, the control of cytoskeleton dynamics may present an underappreciated mechanism pervading the whole cell and coordinating biological responses in relationship with cell volume regulation by S6K. In addition, specific metabolite levels and pathway activities may underlie cell volume alterations. In skeletal muscle, it is well established that muscle fiber types relying on different energy sources have different sizes (van Wessel et al., 2010; Bourdeau Julien et al., 2018). Mitochondrial functionality has been associated with the establishment of an optimal cell size (Miettinen et al., 2014; Miettinen and Bjorklund, 2017). Of note, the small size of the *S6K1* mutant muscles correlate with alterations in the AMP/ATP ratios (Aguilar et al., 2007), and AMPK activity is a direct target of S6K (Dagon et al., 2012). In addition, the phosphorylation of Bcl-2-associated agonist of cell death (BAD) by Akt and S6K might be involved in reprogramming energy metabolism (Harada et al., 2001; Gimenez-Cassina et al., 2014). Future studies will address

the following outstanding questions: What physical properties of the cell, metabolic status and cystoskeleton modifications may contribute to the whole cell sensing of its size in relation with S6K activity? What S6K1 specific substrates, that cannot be compensated by S6K2 or Rsk activities, dictate the cell size adaptations? Can these mechanisms be targeted in age-related pathological conditions?

Author contributions

MP and SF conceptualized, researched, and wrote this review.

Funding

Research related to the subject of this review was supported by grants from European Research Council, Inserm Agemed, ANR and RHU-Cosy to MP.

Acknowledgments

We apologize to colleagues whose work we were unable to discuss due to space constraints. We thank Bertsy Goic for her expert iconography support.

Conflict of interest

The authors declare that the research was conducted in the absence of any commercial or financial relationships that could be construed as a potential conflict of interest.

Publisher's note

References

Abe, Y., Yoon, S. O., Kubota, K., Mendoza, M. C., Gygi, S. P., Blenis, J., et al. (2009). p90 ribosomal S6 kinase and p70 ribosomal S6 kinase link phosphorylation of the eukaryotic chaperonin containing TCP-1 to growth factor, insulin, and nutrient signaling. *J. Biol. Chem.* 284, 14939–14948. doi:10.1074/jbc.M900097200

Aguilar, V., Alliouachene, S., Sotiropoulos, A., Sobering, A., Athea, Y., Djouadi, F., et al. (2007). S6 kinase deletion suppresses muscle growth adaptations to nutrient availability by activating AMP kinase. *Cell Metab.* 5, 476–487. doi:10.1016/j.cmet.2007.05.006

Alessi, D. R., James, S. R., Downes, C. P., Holmes, A. B., Gaffney, P. R., Reese, C. B., et al. (1997). Characterization of a 3-phosphoinositide-dependent protein kinase which phosphorylates and activates protein kinase Balpha. *Curr. Biol.* 7, 261–269. doi:10.1016/s0960-9822(06)00122-9

Alessi, D. R., Kozlowski, M. T., Weng, Q. P., Morrice, N., and Avruch, J. (1998). 3-Phosphoinositide-dependent protein kinase 1 (PDK1) phosphorylates and activates the p70 S6 kinase *in vivo* and *in vitro*. *Curr. Biol.* 8, 69–81. doi:10.1016/s0960-9822(98)70037-5

Arif, A., Terenzi, F., Potdar, A. A., Jia, J., Sacks, J., China, A., et al. (2017). EPRS is a critical mTORC1-S6K1 effector that influences adiposity in mice. *Nature* 542, 357–361. doi:10.1038/nature21380

Arif, A., Jia, J., Willard, B., Li, X., and Fox, P. L. (2019). Multisite phosphorylation of S6K1 directs a kinase phospho-code that determines substrate selection. *Mol. Cell* 73, 446–457. doi:10.1016/j.molcel.2018.11.017

Ban, N., Beckmann, R., Cate, J. H., Dinman, J. D., Dragon, F., Ellis, S. R., et al. (2014). A new system for naming ribosomal proteins. *Curr. Opin. Struct. Biol.* 24, 165–169. doi:10.1016/j.sbi.2014.01.002

Banani, S. F., Lee, H. O., Hyman, A. A., and Rosen, M. K. (2017). Biomolecular condensates: organizers of cellular biochemistry. *Nat. Rev. Mol. Cell Biol.* 18, 285–298. doi:10.1038/nrm.2017.7

Banerjee, P., Ahmad, M. F., Grove, J. R., Kozlosky, C., Price, D. J., Avruch, J., et al. (1990). Molecular structure of a major insulin/mitogen-activated 70-kDa S6 protein kinase. *Proc. Natl. Acad. Sci. U. S. A.* 87, 8550–8554. doi:10.1073/pnas.87.21.8550

Barilari, M., Bonfils, G., Treins, C., Koka, V., De Villeneuve, D., Fabrega, S., et al. (2017). ZRF1 is a novel S6 kinase substrate that drives the senescence programme. *EMBO J.* 36, 736–750. doi:10.15252/embj.201694966

Ben-Sahra, I., Howell, J. J., Asara, J. M., and Manning, B. D. (2013). Stimulation of de novo pyrimidine synthesis by growth signaling through mTOR and S6K1. *Science* 339, 1323–1328. doi:10.1126/science.1228792

Ben-Sahra, I., Hoxhaj, G., Ricoult, S. J. H., Asara, J. M., and Manning, B. D. (2016). mTORC1 induces purine synthesis through control of the mitochondrial tetrahydrofolate cycle. *Science* 351, 728–733. doi:10.1126/science.aad0489

Bohlen, J., Roiuk, M., and Teleman, A. A. (2021). Phosphorylation of ribosomal protein S6 differentially affects mRNA translation based on ORF length. *Nucleic Acids Res.* 49, 13062–13074. doi:10.1093/nar/gkab1157

Bohni, R., Riesgo-Escovar, J., Oldham, S., Brogiolo, W., Stocker, H., Andruss, B. F., et al. (1999). Autonomous control of cell and organ size by CHICO, a Drosophila homolog of vertebrate IRS1-4. *Cell* 97, 865–875. doi:10.1016/s0092-8674(00)80799-0

Bonucci, M., Kuperwasser, N., Barbe, S., Koka, V., de Villeneuve, D., Zhang, C., et al. (2020). mTOR and S6K1 drive polycystic kidney by the control of Afadin-dependent oriented cell division. *Nat. Commun.* 11, 3200. doi:10.1038/s41467-020-16978-z

Bourdeau Julien, I., Sephton, C. F., and Dutchak, P. A. (2018). Metabolic networks influencing skeletal muscle fiber composition. *Front. Cell Dev. Biol.* 6, 125. doi:10.3389/fcell.2018.00125

Chauvin, C., Koka, V., Nouschi, A., Mieulet, V., Hoareau-Aveilla, C., Dreazen, A., et al. (2014). Ribosomal protein S6 kinase activity controls the ribosome biogenesis transcriptional program. *Oncogene* 33, 474–483. doi:10.1038/onc.2012.606

Cho, S., Lee, G., Pickering, B. F., Jang, C., Park, J. H., He, L., et al. (2021). mTORC1 promotes cell growth via m(6)A-dependent mRNA degradation. *Mol. Cell* 81, 2064–2075.e8. doi:10.1016/j.molcel.2021.03.010

Choo, A. Y., Yoon, S. O., Kim, S. G., Roux, P. P., and Blenis, J. (2008). Rapamycin differentially inhibits S6Ks and 4E-BP1 to mediate cell-type-specific repression of mRNA translation. *Proc. Natl. Acad. Sci. U. S. A.* 105, 17414–17419. doi:10.1073/pnas.0809136105

Chung, J., Kuo, C. J., Crabtree, G. R., and Blenis, J. (1992). Rapamycin-FKBP specifically blocks growth-dependent activation of and signaling by the 70 kd S6 protein kinases. *Cell* 69, 1227–1236. doi:10.1016/0092-8674(92)90643-q

Csibi, A., Lee, G., Yoon, S. O., Tong, H., Ilter, D., Elia, I., et al. (2014). The mTORC1/S6K1 pathway regulates glutamine metabolism through the eIF4B-dependent control of c-Myc translation. *Curr. Biol.* 24, 2274–2280. doi:10.1016/j.cub.2014.08.007

Dagon, Y., Hur, E., Zheng, B., Wellenstein, K., Cantley, L. C., Kahn, B. B., et al. (2012). p70S6 kinase phosphorylates AMPK on serine 491 to mediate leptin's effect on food intake. *Cell Metab.* 16, 104–112. doi:10.1016/j.cmet.2012.05.010

Delarue, M., Brittingham, G. P., Pfeffer, S., Surovtsev, I. V., Pinglay, S., Kennedy, K. J., et al. (2018). mTORC1 controls phase separation and the biophysical properties of the cytoplasm by tuning crowding. *Cell* 174, 338–349. doi:10.1016/j.cell.2018.05.042

Dennis, P. B., Pullen, N., Pearson, R. B., Kozma, S. C., and Thomas, G. (1998). Phosphorylation sites in the autoinhibitory domain participate in p70(s6k) activation loop phosphorylation. *J. Biol. Chem.* 273, 14845–14852. doi:10.1074/jbc.273.24.14845

Dever, T. E., and Green, R. (2012). The elongation, termination, and recycling phases of translation in eukaryotes. *Cold Spring Harb. Perspect. Biol.* 4, a013706. doi:10.1101/cshperspect.a013706

Dibble, C. C., Asara, J. M., and Manning, B. D. (2009). Characterization of Rictor phosphorylation sites reveals direct regulation of mTOR complex 2 by S6K1. *Mol. Cell. Biol.* 29, 5657–5670. doi:10.1128/MCB.00735-09

Dorrello, N. V., Peschiaroli, A., Guardavaccaro, D., Colburn, N. H., Sherman, N. E., Pagano, M., et al. (2006). S6K1- and betaTRCP-mediated degradation of PDCD4 promotes protein translation and cell growth. *Science* 314, 467–471. doi:10.1126/science.1130276

Dowling, R. J., Topisirovic, I., Alain, T., Bidinosti, M., Fonseca, B. D., Petroulakis, E., et al. (2010). mTORC1-mediated cell proliferation, but not cell growth, controlled by the 4E-BPs. *Science* 328, 1172–1176. doi:10.1126/science.1187532

Elloul, S., Kedrin, D., Knoblauch, N. W., Beck, A. H., and Toker, A. (2014). The adherens junction protein afadin is an AKT substrate that regulates breast cancer cell migration. *Mol. Cancer Res.* 12, 464–476. doi:10.1158/1541-7786.MCR-13-0398

Faller, W. J., Jackson, T. J., Knight, J. R., Ridgway, R. A., Jamieson, T., Karim, S. A., et al. (2015). mTORC1-mediated translational elongation limits intestinal tumour initiation and growth. *Nature* 517, 497–500. doi:10.1038/nature13896

Fingar, D. C., Hausdorff, S. F., Blenis, J., and Birnbaum, M. J. (1993). Dissociation of pp70 ribosomal protein S6 kinase from insulin-stimulated glucose transport in 3T3-L1 adipocytes. *J. Biol. Chem.* 268, 3005–3008. doi:10.1016/s0021-9258(18)53873-4

Gabanella, F., Pisani, C., Borreca, A., Farioli-Vecchioli, S., Ciotti, M. T., Ingegnere, T., et al. (2016). SMN affects membrane remodelling and anchoring of the protein synthesis machinery. *J. Cell Sci.* 129, 804–816. doi:10.1242/jcs.176750

Gao, X., Zhang, Y., Arrazola, P., Hino, O., Kobayashi, T., Yeung, R. S., et al. (2002). Tsc tumour suppressor proteins antagonize amino-acid-TOR signalling. *Nat. Cell Biol.* 4, 699–704. doi:10.1038/ncb847

Gao, D., Inuzuka, H., Tan, M. K., Fukushima, H., Locasale, J. W., Liu, P., et al. (2011). mTOR drives its own activation via SCF(βTrCP)-dependent degradation of the mTOR inhibitor DEPTOR. *Mol. Cell* 44, 290–303. doi:10.1016/j.molcel.2011.08.030

Gao, L., Yang, Z., Hiremath, C., Zimmerman, S. E., Long, B., Brakeman, P. R., et al. (2017). Afadin orients cell division to position the tubule lumen in developing renal tubules. *Development* 144, 3511–3520. doi:10.1242/dev.148908

Gimenez-Cassina, A., Garcia-Haro, L., Choi, C. S., Osundiji, M. A., Lane, E. A., Huang, H., et al. (2014). Regulation of hepatic energy metabolism and gluconeogenesis by BAD. *Cell Metab.* 19, 272–284. doi:10.1016/j.cmet.2013.12.001

Gout, I., Minami, T., Hara, K., Tsujishita, Y., Filonenko, V., Waterfield, M. D., et al. (1998). Molecular cloning and characterization of a novel p70 S6 kinase, p70 S6 kinase beta containing a proline-rich region. *J. Biol. Chem.* 273, 30061–30064. doi:10.1074/jbc.273.46.30061

Hara, K., Maruki, Y., Long, X., Yoshino, K., Oshiro, N., Hidayat, S., et al. (2002). Raptor, a binding partner of target of rapamycin (TOR), mediates TOR action. *Cell* 110, 177–189. doi:10.1016/s0092-8674(02)00833-4

Harada, H., Andersen, J. S., Mann, M., Terada, N., and Korsmeyer, S. J. (2001). p70S6 kinase signals cell survival as well as growth, inactivating the pro-apoptotic molecule BAD. *Proc. Natl. Acad. Sci. U. S. A.* 98, 9666–9670. doi:10.1073/pnas.171301998

Harrington, L. S., Findlay, G. M., Gray, A., Tolkacheva, T., Wigfield, S., Rebholz, H., et al. (2004). The TSC1-2 tumor suppressor controls insulin-PI3K signaling via regulation of IRS proteins. *J. Cell Biol.* 166, 213–223. doi:10.1083/jcb.200403069

He, L., Gomes, A. P., Wang, X., Yoon, S. O., Lee, G., Nagiec, M. J., et al. (2018). mTORC1 promotes metabolic reprogramming by the suppression of GSK3-dependent Foxk1 phosphorylation. *Mol. Cell* 70, 949–960. doi:10.1016/j.molcel.2018.04.024

Holz, M. K., and Blenis, J. (2005). Identification of S6 kinase 1 as a novel mammalian target of rapamycin (mTOR)-phosphorylating kinase. *J. Biol. Chem.* 280, 26089–26093. doi:10.1074/jbc.M504045200

Holz, M. K., Ballif, B. A., Gygi, S. P., and Blenis, J. (2005). mTOR and S6K1 mediate assembly of the translation preinitiation complex through dynamic protein interchange and ordered phosphorylation events. *Cell* 123, 569–580. doi:10.1016/j.cell.2005.10.024

Hsieh, A. C., Costa, M., Zollo, O., Davis, C., Feldman, M. E., Testa, J. R., et al. (2010). Genetic dissection of the oncogenic mTOR pathway reveals druggable addiction to translational control via 4EBP-eIF4E. *Cancer Cell* 17, 249–261. doi:10.1016/j.ccr.2010.01.021

Hsu, P. P., Kang, S. A., Rameseder, J., Zhang, Y., Ottina, K. A., Lim, D., et al. (2011). The mTOR-regulated phosphoproteome reveals a mechanism of mTORC1-mediated inhibition of growth factor signaling. *Science* 332, 1317–1322. doi:10.1126/science.1199498

Huang, H., Potter, C. J., Tao, W., Li, D. M., Brogiolo, W., Hafen, E., et al. (1999). PTEN affects cell size, cell proliferation and apoptosis during Drosophila eye development. *Development* 126, 5365–5372. doi:10.1242/dev.126.23.5365

Huang, Y., Hu, K., Zhang, S., Dong, X., Yin, Z., Meng, R., et al. (2018). S6K1 phosphorylation-dependent degradation of Mxi1 by beta-Trcp ubiquitin ligase promotes Myc activation and radioresistance in lung cancer. *Theranostics* 8, 1286–1300. doi:10.7150/thno.22552

Ito, N., and Rubin, G. M. (1999). gigas, a Drosophila homolog of tuberous sclerosis gene product-2, regulates the cell cycle. *Cell* 96, 529–539. doi:10.1016/s0092-8674(00)80657-1

Jafari, N., Zheng, Q., Li, L., Li, W., Qi, L., Xiao, J., et al. (2016). p70S6K1 (S6K1)-mediated phosphorylation regulates phosphatidylinositol 4-phosphate 5-kinase type I gamma degradation and cell invasion. *J. Biol. Chem.* 291, 25729–25741. doi:10.1074/jbc.M116.742742

Jiang, Q., Zhang, X., Dai, X., Han, S., Wu, X., Wang, L., et al. (2022). S6K1-mediated phosphorylation of PDK1 impairs AKT kinase activity and oncogenic functions. *Nat. Commun.* 13, 1548. doi:10.1038/s41467-022-28910-8

Julien, L. A., Carriere, A., Moreau, J., and Roux, P. P. (2010). mTORC1-activated S6K1 phosphorylates Rictor on threonine 1135 and regulates mTORC2 signaling. *Mol. Cell. Biol.* 30, 908–921. doi:10.1128/MCB.00601-09

Kang, S. A., Pacold, M. E., Cervantes, C. L., Lim, D., Lou, H. J., Ottina, K., et al. (2013). mTORC1 phosphorylation sites encode their sensitivity to starvation and rapamycin. *Science* 341, 1236566. doi:10.1126/science.1236566

Kenney, J. W., Moore, C. E., Wang, X., and Proud, C. G. (2014). Eukaryotic elongation factor 2 kinase, an unusual enzyme with multiple roles. *Adv. Biol. Regul.* 55, 15–27. doi:10.1016/j.jbior.2014.04.003

Kim, A. R., and Choi, K. W. (2019). TRiC/CCT chaperonins are essential for organ growth by interacting with insulin/TOR signaling in Drosophila. *Oncogene* 38, 4739–4754. doi:10.1038/s41388-019-0754-1

Kim, D. H., Sarbassov, D. D., Ali, S. M., King, J. E., Latek, R. R., Erdjument-Bromage, H., et al. (2002). mTOR interacts with raptor to form a nutrient-sensitive complex that signals to the cell growth machinery. *Cell* 110, 163–175. doi:10.1016/s0092-8674(02)00808-5

Kozma, S. C., Ferrari, S., Bassand, P., Siegmann, M., Totty, N., Thomas, G., et al. (1990). Cloning of the mitogen-activated S6 kinase from rat liver reveals an enzyme of the second messenger subfamily. *Proc. Natl. Acad. Sci. U. S. A.* 87, 7365–7369. doi:10.1073/pnas.87.19.7365

Krieg, J., Hofsteenge, J., and Thomas, G. (1988). Identification of the 40 S ribosomal protein S6 phosphorylation sites induced by cycloheximide. *J. Biol. Chem.* 263, 11473–11477. doi:10.1016/s0021-9258(18)37981-x

Lai, K. P., Leong, W. F., Chau, J. F., Jia, D., Zeng, L., Liu, H., et al. (2010). S6K1 is a multifaceted regulator of Mdm2 that connects nutrient status and DNA damage response. *EMBO J.* 29, 2994–3006. doi:10.1038/emboj.2010.166

Lee, K., Sharma, R., Shrestha, O. K., Bingman, C. A., and Craig, E. A. (2016). Dual interaction of the Hsp70 J-protein cochaperone Zuotin with the 40S and 60S ribosomal subunits. *Nat. Struct. Mol. Biol.* 23, 1003–1010. doi:10.1038/nsmb.3299

Lee, G., Zheng, Y., Cho, S., Jang, C., England, C., Dempsey, J. M., et al. (2017). Post-transcriptional regulation of de novo lipogenesis by mTORC1-S6K1-SRPK2 signaling. *Cell* 171, 1545–1558. doi:10.1016/j.cell.2017.10.037

Lee-Fruman, K. K., Kuo, C. J., Lippincott, J., Terada, N., and Blenis, J. (1999). Characterization of S6K2, a novel kinase homologous to S6K1. *Oncogene* 18, 5108–5114. doi:10.1038/sj.onc.1202894

Leevers, S. J., Weinkove, D., MacDougall, L. K., Hafen, E., and Waterfield, M. D. (1996). The drosophila phosphoinositide 3-kinase Dp110 promotes cell growth. *EMBO J.* 15, 6584–6594. doi:10.1002/j.1460-2075.1996.tb01049.x

Lengefeld, J., Cheng, C. W., Maretich, P., Blair, M., Hagen, H., McReynolds, M. R., et al. (2021). Cell size is a determinant of stem cell potential during aging. *Sci. Adv.* 7, eabk0271. doi:10.1126/sciadv.abk0271

Leontieva, O. V., and Blagosklonny, M. V. (2013). CDK4/6-inhibiting drug substitutes for p21 and p16 in senescence: duration of cell cycle arrest and MTOR activity determine geroconversion. *Cell cycle* 12, 3063–3069. doi:10.4161/cc.26130

Leontieva, O. V., and Blagosklonny, M. V. (2014). Gerosuppression in confluent cells. *Aging* 6, 1010–1018. doi:10.18632/aging.100714

Leontieva, O. V., Demidenko, Z. N., and Blagosklonny, M. V. (2013). S6K in geroconversion. *Cell cycle* 12, 3249–3252. doi:10.4161/cc.26248

Leontieva, O. V., Demidenko, Z. N., and Blagosklonny, M. V. (2014). Contact inhibition and high cell density deactivate the mammalian target of rapamycin pathway, thus suppressing the senescence program. *Proc. Natl. Acad. Sci. U. S. A.* 111, 8832–8837. doi:10.1073/pnas.1405723111

Leprivier, G., Remke, M., Rotblat, B., Dubuc, A., Mateo, A. R., Kool, M., et al. (2013). The eEF2 kinase confers resistance to nutrient deprivation by blocking translation elongation. *Cell* 153, 1064–1079. doi:10.1016/j.cell.2013.04.055

Lewis, C. A., Griffiths, B., Santos, C. R., Pende, M., and Schulze, A. (2011). Genetic ablation of S6-kinase does not prevent processing of SREBP1. *Adv. Enzyme Regul.* 51, 280–290. doi:10.1016/j.advenzreg.2010.09.001

Liu, G. Y., and Sabatini, D. M. (2020). mTOR at the nexus of nutrition, growth, ageing and disease. *Nat. Rev. Mol. Cell Biol.* 21, 183–203. doi:10.1038/s41580-019-0199-y

Liu, P., Gan, W., Inuzuka, H., Lazorchak, A. S., Gao, D., Arojo, O., et al. (2013). Sin1 phosphorylation impairs mTORC2 complex integrity and inhibits downstream Akt signalling to suppress tumorigenesis. *Nat. Cell Biol.* 15, 1340–1350. doi:10.1038/ncb2860

Lundh, M., Petersen, P. S., Isidor, M. S., Kazoka-Sorensen, D. N., Plucinska, K., Shamsi, F., et al. (2019). Afadin is a scaffold protein repressing insulin action via HDAC6 in adipose tissue. *EMBO Rep.* 20, e48216. doi:10.15252/embr.201948216

Ma, X. M., Yoon, S. O., Richardson, C. J., Julich, K., and Blenis, J. (2008). SKAR links pre-mRNA splicing to mTOR/S6K1-mediated enhanced translation efficiency of spliced mRNAs. *Cell* 133, 303–313. doi:10.1016/j.cell.2008.02.031

Ma, S., Meng, Z., Chen, R., and Guan, K. L. (2018). The hippo pathway: Biology and pathophysiology. *Annu. Rev. Biochem.* 88, 577–604. doi:10.1146/annurev-biochem-013118-111829

Martinez-Carreres, L., Puyal, J., Leal-Esteban, L. C., Orpinell, M., Castillo-Armengol, J., Giralt, A., et al. (2019). CDK4 regulates lysosomal function and mTORC1 activation to promote cancer cell survival. *Cancer Res.* 79, 5245–5259. doi:10.1158/0008-5472.CAN-19-0708

Merrick, W. C., and Pavitt, G. D. (2018). Protein synthesis initiation in eukaryotic cells. *Cold Spring Harb. Perspect. Biol.* 10, a033092. doi:10.1101/cshperspect.a033092

Miettinen, T. P., and Bjorklund, M. (2017). Mitochondrial function and cell size: An allometric relationship. *Trends Cell Biol.* 27, 393–402. doi:10.1016/j.tcb.2017.02.006

Miettinen, T. P., Pessa, H. K., Caldez, M. J., Fuhrer, T., Diril, M. K., Sauer, U., et al. (2014). Identification of transcriptional and metabolic programs related to mammalian cell size. *Curr. Biol.* 24, 598–608. doi:10.1016/j.cub.2014.01.071

Mieulet, V., Roceri, M., Espeillac, C., Sotiropoulos, A., Ohanna, M., Oorschot, V., et al. (2007). S6 kinase inactivation impairs growth and translational target phosphorylation in muscle cells maintaining proper regulation of protein turnover. *Am. J. Physiol. Cell Physiol.* 293, C712–C722. doi:10.1152/ajpcell.00499.2006

Montagne, J., Stewart, M. J., Stocker, H., Hafen, E., Kozma, S. C., Thomas, G., et al. (1999). Drosophila S6 kinase: a regulator of cell size. *Science* 285, 2126–2129. doi:10.1126/science.285.5436.2126

Moritz, A., Li, Y., Guo, A., Villen, J., Wang, Y., MacNeill, J., et al. (2010). Akt-RSK-S6 kinase signaling networks activated by oncogenic receptor tyrosine kinases. *Sci. Signal.* 3, ra64. doi:10.1126/scisignal.2000998

Mukhopadhyay, N. K., Price, D. J., Kyriakis, J. M., Pelech, S., Sanghera, J., Avruch, J., et al. (1992). An array of insulin-activated, proline-directed serine/threonine protein kinases phosphorylate the p70 S6 kinase. *J. Biol. Chem.* 267, 3325–3335. doi:10.1016/s0021-9258(19)50735-9

Napolitano, G., Di Malta, C., Esposito, A., de Araujo, M. E. G., Pece, S., Bertalot, G., et al. (2020). A substrate-specific mTORC1 pathway underlies Birt-Hogg-Dube syndrome. *Nature* 585, 597–602. doi:10.1038/s41586-020-2444-0

Neurohr, G. E., Terry, R. L., Lengefeld, J., Bonney, M., Brittingham, G. P., Moretto, F., et al. (2019). Excessive cell growth causes cytoplasm dilution and contributes to senescence. *Cell* 176, 1083–1097. doi:10.1016/j.cell.2019.01.018

Ohanna, M., Sobering, A. K., Lapointe, T., Lorenzo, L., Praud, C., Petroulakis, E., et al. (2005). Atrophy of S6K1(-/-) skeletal muscle cells reveals distinct mTOR effectors for cell cycle and size control. *Nat. Cell Biol.* 7, 286–294. doi:10.1038/ncb1231

Pantalacci, S., Tapon, N., and Leopold, P. (2003). The Salvador partner Hippo promotes apoptosis and cell-cycle exit in Drosophila. *Nat. Cell Biol.* 5, 921–927. doi:10.1038/ncb1051

Pearce, L. R., Komander, D., and Alessi, D. R. (2010). The nuts and bolts of AGC protein kinases. *Nat. Rev. Mol. Cell Biol.* 11, 9–22. doi:10.1038/nrm2822

Pende, M., Kozma, S. C., Jaquet, M., Oorschot, V., Burcelin, R., Le Marchand-Brustel, Y., et al. (2000). Hypoinsulinaemia, glucose intolerance and diminished beta-cell size in S6K1-deficient mice. *Nature* 408, 994–997. doi:10.1038/35050135

Pende, M., Um, S. H., Mieulet, V., Sticker, M., Goss, V. L., Mestan, J., et al. (2004). S6K1(-/-)/S6K2(-/-) mice exhibit perinatal lethality and rapamycin-sensitive 5'-terminal oligopyrimidine mRNA translation and reveal a mitogen-activated protein kinase-dependent S6 kinase pathway. *Mol. Cell. Biol.* 24, 3112–3124. doi:10.1128/mcb.24.8.3112-3124.2004

Pham, P. T., Heydrick, S. J., Fox, H. L., Kimball, S. R., Jefferson, L. S., Jr., Lynch, C. J., et al. (2000). Assessment of cell-signaling pathways in the regulation of mammalian target of rapamycin (mTOR) by amino acids in rat adipocytes. *J. Cell. Biochem.* 79, 427–441. doi:10.1002/1097-4644(20001201)79:3<427::aid-jcb80>3.0.co;2-0

Piscitello, D., Varshney, D., Lilla, S., Vizioli, M. G., Reid, C., Gorbunova, V., et al. (2018). AKT overactivation can suppress DNA repair via p70S6 kinase-dependent downregulation of MRE11. *Oncogene* 37, 427–438. doi:10.1038/onc.2017.340

Porstmann, T., Santos, C. R., Griffiths, B., Cully, M., Wu, M., Leevers, S., et al. (2008). SREBP activity is regulated by mTORC1 and contributes to Akt-dependent cell growth. *Cell Metab.* 8, 224–236. doi:10.1016/j.cmet.2008.07.007

Pullen, N., Dennis, P. B., Andjelkovic, M., Dufner, A., Kozma, S. C., Hemmings, B. A., et al. (1998). Phosphorylation and activation of p70s6k by PDK1. *Science* 279, 707–710. doi:10.1126/science.279.5351.707

Raimer, A. C., Gray, K. M., and Matera, A. G. (2017). SMN - a chaperone for nuclear RNP social occasions? *RNA Biol.* 14, 701–711. doi:10.1080/15476286.2016.1236168

Richardson, C. J., Broenstrup, M., Fingar, D. C., Julich, K., Ballif, B. A., Gygi, S., et al. (2004). SKAR is a specific target of S6 kinase 1 in cell growth control. *Curr. Biol.* 14, 1540–1549. doi:10.1016/j.cub.2004.08.061

Richly, H., Rocha-Viegas, L., Ribeiro, J. D., Demajo, S., Gundem, G., Lopez-Bigas, N., et al. (2010). Transcriptional activation of polycomb-repressed genes by ZRF1. *Nature* 468, 1124–1128. doi:10.1038/nature09574

Robitaille, A. M., Christen, S., Shimobayashi, M., Cornu, M., Fava, L. L., Moes, S., et al. (2013). Quantitative phosphoproteomics reveal mTORC1 activates de novo pyrimidine synthesis. *Science* 339, 1320–1323. doi:10.1126/science.1228771

Romero-Pozuelo, J., Figlia, G., Kaya, O., Martin-Villalba, A., and Teleman, A. A. (2020). Cdk4 and Cdk6 couple the cell-cycle machinery to cell growth via mTORC1. *Cell Rep.* 31, 107504. doi:10.1016/j.celrep.2020.03.068

Ruvinsky, I., Sharon, N., Lerer, T., Cohen, H., Stolovich-Rain, M., Nir, T., et al. (2005). Ribosomal protein S6 phosphorylation is a determinant of cell size and glucose homeostasis. *Genes Dev.* 19, 2199–2211. doi:10.1101/gad.351605

Ruvinsky, I., Katz, M., Dreazen, A., Gielchinsky, Y., Saada, A., Freedman, N., et al. (2009). Mice deficient in ribosomal protein S6 phosphorylation suffer from muscle weakness that reflects a growth defect and energy deficit. *PloS one* 4, e5618. doi:10.1371/journal.pone.0005618

Sarbassov, D. D., Guertin, D. A., Ali, S. M., and Sabatini, D. M. (2005). Phosphorylation and regulation of Akt/PKB by the rictor-mTOR complex. *Science* 307, 1098–1101. doi:10.1126/science.1106148

Schilling, M., Prusty, A. B., Boysen, B., Oppermann, F. S., Riedel, Y. L., Husedzinovic, A., et al. (2021). TOR signaling regulates liquid phase separation of the SMN complex governing snRNP biogenesis. *Cell Rep.* 35, 109277. doi:10.1016/j.celrep.2021.109277

Selman, C., Tullet, J. M., Wieser, D., Irvine, E., Lingard, S. J., Choudhury, A. I., et al. (2009). Ribosomal protein S6 kinase 1 signaling regulates mammalian life span. *Science* 326, 140–144. doi:10.1126/science.1177221

Sfakianos, A. P., Mellor, L. E., Pang, Y. F., Kritsiligkou, P., Needs, H., Abou-Hamdan, H., et al. (2018). The mTOR-S6 kinase pathway promotes stress granule assembly. *Cell Death Differ.* 25, 1766–1780. doi:10.1038/s41418-018-0076-9

Shahbazian, D., Roux, P. P., Mieulet, V., Cohen, M. S., Raught, B., Taunton, J., et al. (2006). The mTOR/PI3K and MAPK pathways converge on eIF4B to control its phosphorylation and activity. *EMBO J.* 25, 2781–2791. doi:10.1038/sj.emboj.7601166

Shima, H., Pende, M., Chen, Y., Fumagalli, S., Thomas, G., Kozma, S. C., et al. (1998). Disruption of the p70(s6k)/p85(s6k) gene reveals a small mouse phenotype and a new functional S6 kinase. *EMBO J.* 17, 6649–6659. doi:10.1093/emboj/17.22.6649

Shoji, W., Inoue, T., Yamamoto, T., and Obinata, M. (1995). MIDA1, a protein associated with Id, regulates cell growth. *J. Biol. Chem.* 270, 24818–24825. doi:10.1074/jbc.270.42.24818

Stocker, H., and Hafen, E. (2000). Genetic control of cell size. *Curr. Opin. Genet. Dev.* 10, 529–535. doi:10.1016/s0959-437x(00)00123-4

Tang, H. W., Weng, J. H., Lee, W. X., Hu, Y., Gu, L., Cho, S., et al. (2021). mTORC1-chaperonin CCT signaling regulates m(6)A RNA methylation to suppress autophagy. *Proc. Natl. Acad. Sci. U. S. A.* 118, e2021945118. doi:10.1073/pnas.2021945118

Tozzi, M., Brown, E. L., Petersen, P. S. S., Lundh, M., Isidor, M. S., Plucinska, K., et al. (2022). Dynamic interplay between Afadin(S1795) phosphorylation and diet regulates glucose homeostasis in obese mice. *J. Physiol.* 600, 885–902. doi:10.1113/JP281657

Treins, C., Warne, P. H., Magnuson, M. A., Pende, M., and Downward, J. (2010). Rictor is a novel target of p70 S6 kinase-1. *Oncogene* 29, 1003–1016. doi:10.1038/onc.2009.401

Tremblay, F., and Marette, A. (2001). Amino acid and insulin signaling via the mTOR/p70 S6 kinase pathway. A negative feedback mechanism leading to insulin resistance in skeletal muscle cells. *J. Biol. Chem.* 276, 38052–38060. doi:10.1074/jbc.M106703200

Tremblay, F., Brule, S., Hee Um, S., Li, Y., Masuda, K., Roden, M., et al. (2007). Identification of IRS-1 Ser-1101 as a target of S6K1 in nutrient- and obesity-induced insulin resistance. *Proc. Natl. Acad. Sci. U. S. A.* 104, 14056–14061. doi:10.1073/pnas.0706517104

Udan, R. S., Kango-Singh, M., Nolo, R., Tao, C., and Halder, G. (2003). Hippo promotes proliferation arrest and apoptosis in the Salvador/Warts pathway. *Nat. Cell Biol.* 5, 914–920. doi:10.1038/ncb1050

Um, S. H., Frigerio, F., Watanabe, M., Picard, F., Joaquin, M., Sticker, M., et al. (2004). Absence of S6K1 protects against age- and diet-induced obesity while enhancing insulin sensitivity. *Nature* 431, 200–205. doi:10.1038/nature02866

van Wessel, T., de Haan, A., van der Laarse, W. J., Jaspers, R. T., and de HAAn, A. (2010). The muscle fiber type-fiber size paradox: hypertrophy or oxidative metabolism? *Eur. J. Appl. Physiol.* 110, 665–694. doi:10.1007/s00421-010-1545-0

Verdu, J., Buratovich, M. A., Wilder, E. L., and Birnbaum, M. J. (1999). Cell-autonomous regulation of cell and organ growth in Drosophila by Akt/PKB. *Nat. Cell Biol.* 1, 500–506. doi:10.1038/70293

Wang, X., Li, W., Williams, M., Terada, N., Alessi, D. R., Proud, C. G., et al. (2001). Regulation of elongation factor 2 kinase by p90(RSK1) and p70 S6 kinase. *EMBO J.* 20, 4370–4379. doi:10.1093/emboj/20.16.4370

Wettenhall, R. E., Erikson, E., and Maller, J. L. (1992). Ordered multisite phosphorylation of Xenopus ribosomal protein S6 by S6 kinase II. *J. Biol. Chem.* 267, 9021–9027. doi:10.1016/s0021-9258(19)50382-9

Woodward, L. A., Mabin, J. W., Gangras, P., and Singh, G. (2017). The exon junction complex: a lifelong guardian of mRNA fate. *Wiley Interdiscip. Rev. RNA* 8. doi:10.1002/wrna.1411

Wu, S., Huang, J., Dong, J., and Pan, D. (2003). hippo encodes a Ste-20 family protein kinase that restricts cell proliferation and promotes apoptosis in conjunction with salvador and warts. *Cell* 114, 445–456. doi:10.1016/s0092-8674(03)00549-x

Xie, X., Hu, H., Tong, X., Li, L., Liu, X., Chen, M., et al. (2018). The mTOR-S6K pathway links growth signalling to DNA damage response by targeting RNF168. *Nat. Cell Biol.* 20, 320–331. doi:10.1038/s41556-017-0033-8

Yecies, J. L., Zhang, H. H., Menon, S., Liu, S., Yecies, D., Lipovsky, A. I., et al. (2011). Akt stimulates hepatic SREBP1c and lipogenesis through parallel mTORC1-dependent and independent pathways. *Cell Metab.* 14, 21–32. doi:10.1016/j.cmet.2011.06.002

Yi, S. A., Um, S. H., Lee, J., Yoo, J. H., Bang, S. Y., Park, E. K., et al. (2016). S6K1 phosphorylation of H2B mediates EZH2 trimethylation of H3: A determinant of early adipogenesis. *Mol. Cell* 62, 443–452. doi:10.1016/j.molcel.2016.03.011

Yi, S. A., Lee, J., Park, J. W., Han, J., Lee, M. G., Nam, K. H., et al. (2018). S6K1 controls epigenetic plasticity for the expression of pancreatic α/β cell marker genes. *J. Cell. Biochem.* 119, 6674–6683. doi:10.1002/jcb.26853

Yi, S. A., Jeon, Y. J., Lee, M. G., Nam, K. H., Ann, S., Lee, J., et al. (2022). S6K1 controls adiponectin expression by inducing a transcriptional switch: BMAL1-to-EZH2. *Exp. Mol. Med.* 54, 324–333. doi:10.1038/s12276-022-00747-7

Yu, Y., Yoon, S. O., Poulogiannis, G., Yang, Q., Ma, X. M., Villen, J., et al. (2011). Phosphoproteomic analysis identifies Grb10 as an mTORC1 substrate that negatively regulates insulin signaling. *Science* 332, 1322–1326. doi:10.1126/science.1199484

Zhang, H., Stallock, J. P., Ng, J. C., Reinhard, C., and Neufeld, T. P. (2000). Regulation of cellular growth by the Drosophila target of rapamycin dTOR. *Genes Dev.* 14, 2712–2724. doi:10.1101/gad.835000

Zhang, Y., Gao, X., Saucedo, L. J., Ru, B., Edgar, B. A., Pan, D., et al. (2003). Rheb is a direct target of the tuberous sclerosis tumour suppressor proteins. *Nat. Cell Biol.* 5, 578–581. doi:10.1038/ncb999

Zhang, H. H., Lipovsky, A. I., Dibble, C. C., Sahin, M., and Manning, B. D. (2006). S6K1 regulates GSK3 under conditions of mTOR-dependent feedback inhibition of Akt. *Mol. Cell* 24, 185–197. doi:10.1016/j.molcel.2006.09.019

Zhao, Y., Xiong, X., and Sun, Y. (2011). DEPTOR, an mTOR inhibitor, is a physiological substrate of SCF(βTrCP) E3 ubiquitin ligase and regulates survival and autophagy. *Mol. Cell* 44, 304–316. doi:10.1016/j.molcel.2011.08.029

Zhu, J., and Thompson, C. B. (2019). Metabolic regulation of cell growth and proliferation. *Nat. Rev. Mol. Cell Biol.* 20, 436–450. doi:10.1038/s41580-019-0123-5

frontiers | Frontiers in Cell and Developmental Biology

TYPE Brief Research Report
PUBLISHED 25 August 2022
DOI 10.3389/fcell.2022.965595

OPEN ACCESS

EDITED BY
Eiman Aleem,
University of Arizona, United States

REVIEWED BY
Ariz Mohammad,
Washington University in St. Louis, United States
Gabriel Neurohr,
ETH Zürich, Switzerland
Ran Kafri,
University of Toronto, Canada

*CORRESPONDENCE
Jan M. Skotheim,
skotheim@stanford.edu

SPECIALTY SECTION
This article was submitted to Cell Growth and Division, a section of the journal Frontiers in Cell and Developmental Biology

RECEIVED 09 June 2022
ACCEPTED 27 July 2022
PUBLISHED 25 August 2022

CITATION
Zhang S, Zatulovskiy E, Arand J, Sage J and Skotheim JM (2022), The cell cycle inhibitor RB is diluted in G1 and contributes to controlling cell size in the mouse liver.
Front. Cell Dev. Biol. 10:965595.
doi: 10.3389/fcell.2022.965595

The cell cycle inhibitor RB is diluted in G1 and contributes to controlling cell size in the mouse liver

Shuyuan Zhang[1], Evgeny Zatulovskiy[1], Julia Arand[2], Julien Sage[2] and Jan M. Skotheim[1,3]*

[1]Department of Biology, Stanford University, Stanford, CA, United States, [2]Departments of Pediatrics and Genetics, School of Medicine, Stanford University, Stanford, CA, United States, [3]Chan Zuckerberg Biohub, San Francisco, CA, United States

Every type of cell in an animal maintains a specific size, which likely contributes to its ability to perform its physiological functions. While some cell size control mechanisms are beginning to be elucidated through studies of cultured cells, it is unclear if and how such mechanisms control cell size in an animal. For example, it was recently shown that RB, the retinoblastoma protein, was diluted by cell growth in G1 to promote size-dependence of the G1/S transition. However, it remains unclear to what extent the RB-dilution mechanism controls cell size in an animal. We therefore examined the contribution of RB-dilution to cell size control in the mouse liver. Consistent with the RB-dilution model, genetic perturbations decreasing RB protein concentrations through inducible shRNA expression or through liver-specific *Rb1* knockout reduced hepatocyte size, while perturbations increasing RB protein concentrations in an $Fah^{-/-}$ mouse model increased hepatocyte size. Moreover, RB concentration reflects cell size in G1 as it is lower in larger G1 hepatocytes. In contrast, concentrations of the cell cycle activators Cyclin D1 and E2f1 were relatively constant. Lastly, loss of *Rb1* weakened cell size control, *i.e.*, reduced the inverse correlation between how much cells grew in G1 and how large they were at birth. Taken together, our results show that an RB-dilution mechanism contributes to cell size control in the mouse liver by linking cell growth to the G1/S transition.

KEYWORDS

retinablastoma protein, cell size, mouse liver, G1/S, inhibitor dilution

Introduction

Cell size is important for cell physiology because it determines the size of organelles including the nucleus, spindle, centrosome, mitochondrial network, and vacuole (Jorgensen et al., 2007; Neumann and Nurse, 2007; Decker et al., 2011; Rafelski et al., 2012; Good et al., 2013; Hazel et al., 2013; Chan and Marshall, 2014). Through this control of organelle size as well as ribosome number, cell size

impacts biosynthesis. In addition to biosynthesis, cell size is important for the function of diverse cell types. Erythrocytes are tiny because they must migrate through tight spaces, while macrophages must be large enough to engulf pathogens. The importance of cell size for diverse cell types is further reflected in the fact that the size of cells of a given type is remarkably uniform and deviations from the typical cell size are often associated with disease states. For example, the coefficient of variation of the size distribution of red blood cells is used as a common diagnostic parameter in comprehensive blood tests, and many cancers, such as small-cell lung cancer, are characterized by altered cell size (Bell and Waizbard, 1986; Evans and Jehle, 1991; Savage et al., 2007; Salvagno et al., 2015; Nguyen et al., 2016; Zatulovskiy and Skotheim, 2020; Sandlin, 2022).

To control their size to be within a target range, proliferating cells can either regulate their growth such that larger cells grow slower, or they can link cell growth to progression through the cell division cycle (Tzur et al., 2009; Kafri et al., 2013; Ginzberg et al., 2015; Ginzberg et al., 2018; Liu et al., 2022). Studies in cultured cells have now begun to elucidate some of the molecular mechanisms that are responsible. One model proposes that cell growth triggers the G1/S transition by diluting the cell cycle inhibitor RB, the retinoblastoma protein (Zatulovskiy et al., 2020). The amount of dilution required, and the target cell size, can then be modulated by the activity of the cyclin D-Cdk4 kinase complex (Tan et al., 2021). A second model proposes that small cell size activates the p38 stress kinase, which, in turn, inhibits cell division (Liu et al., 2018). Taken together, this recent work in the field is starting to uncover a series of molecular mechanisms through which cell growth triggers the G1/S transition to control cell size. However, these cell size control mechanisms are all based on *in vitro* cell culture studies, and their *in vivo* relevance remains unclear.

Here, we aimed to test the *in vivo* relevance of a cell size control model, namely, the RB-dilution model, in the liver of genetically engineered mice. Consistent with the RB-dilution model, increasing or decreasing RB protein concentrations in hepatocytes *in vivo* caused an increase or decrease in their cell size, respectively. In addition, we found that RB protein concentration decreased with cell size in G1 phase, consistent with RB concentration being a cell size sensor. Finally, we found that RB deletion reduced the ability of primary hepatocytes to control their size when grown in culture. More specifically, we found that deletion of *Rb1* reduced the inverse correlation between how large hepatocytes were at birth and how much they grew in G1. Taken together, our results suggest that the RB-dilution mechanism plays an important role in controlling hepatocyte cell size.

Results

Decreasing RB protein concentration in mouse liver reduces hepatocyte size

If the RB-dilution model applies to the mouse liver, reducing RB protein concentration would reduce hepatocyte size. To test this, we utilized two different mouse models to reduce RB protein concentration. The first model harbors a Doxycycline-inducible transgene broadly expressing an shRNA against *Rb1* (*Rosa-rtTA; TRE-shRb1* mouse (Doan et al., 2021)). We gave Doxycycline containing water (1 g/L) from birth to 4 weeks old to *Rosa-rtTA* (control) or *Rosa-rtTA; TRE-shRb1* mice from the same litter (Figure 1A). Then, the hepatocytes were isolated from these mice to check for knockdown efficiency (Figure 1B). To ensure that there was no difference in cell cycle status, we waited for another 3 weeks to measure their cell size distributions (Figure 1C, Supplementary Figures S1A,D). Since the liver is a highly polyploid organ (Zhang et al., 2019), and polyploid cells are bigger than diploid cells, we sorted the isolated hepatocytes based on viability and on ploidy before size measurements were made in order to eliminate the confounding effect of ploidy on size (Figure 1C, Supplementary Figure S1A). We found that within the same ploidy, the hepatocyte size in *Rb1* knockdown mice was smaller than that in the control mice, supporting the RB-dilution model.

To further test the RB-dilution model in the liver, we used a second mouse model that also reduced the RB protein concentration, but only in the liver. This mouse model contains an $Rb1^{flx/flx}$ allele and expresses the Cre recombinase only in the liver through an *Alb-CreERT2* allele. By injecting Tamoxifen into these mice, the *Rb1* gene can be knocked out in a liver-specific manner. We generated $Rb1^{-/-}$, $Rb1^{-/+}$, *and* $Rb1^{+/+}$ mice from the same litter by administering Tamoxifen to these mice when they were 15 days old (Figure 1D). At 6 weeks after Tamoxifen treatment, we harvested the livers and examined the hepatocyte size of these mice. We note that the $Rb1^{+/-}$ mice did not have significantly reduced RB protein concentrations compared to the $Rb1^{+/+}$ mice (Figure 1E). Consistent with this similar RB protein expression, we found that hepatocyte size in $Rb1^{+/-}$ mice was not significantly different from that in $Rb1^{+/+}$ mice (Figure 1F, Supplementary Figure S1B). In contrast, hepatocyte size was significantly smaller in $Rb1^{-/-}$ mice compared to $Rb1^{+/+}$ and $Rb1^{+/-}$ mice, which again supports a role for RB in controlling cell size in the mouse liver (Figure 1F, Supplementary Figure S1B).

Increasing RB concentration in mouse liver increases hepatocyte cell size

After finding that decreasing RB concentration decreases cell size, we sought to test if increasing RB protein concentration

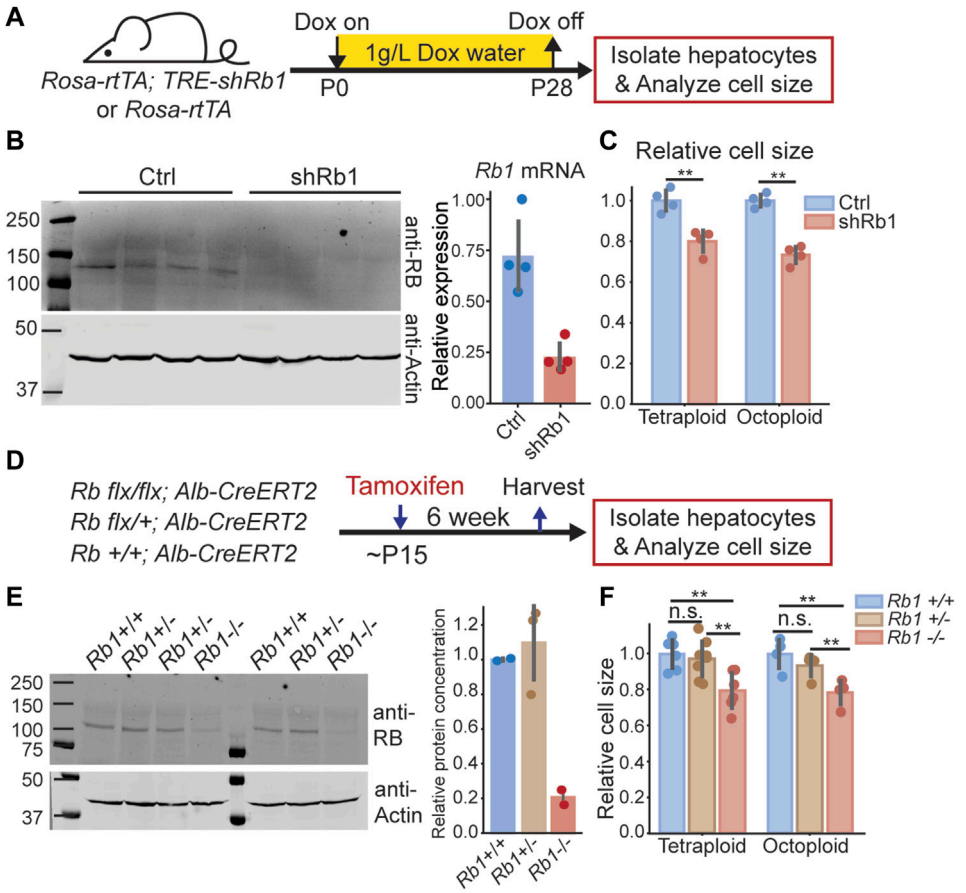

FIGURE 1
Decreasing RB protein concentration in mouse liver reduces hepatocyte size. **(A)**. Schematic of experimental timeline performed using *Rosa-rtTA; TRE-shRb1* mice. **(B)**. Immunoblot and qPCR analysis following shRb1 induction in mouse liver (n = 4). Mice were harvested after 4 weeks of Dox treatment (1 g/L) that started at birth. **(C)**. Coulter counter cell size measurement of the hepatocytes isolated from *Rosa-rtTA* (Ctrl, n = 4) and *Rosa-rtTA; TRE-shRb1* (shRb1, n = 4) mice at 3 weeks after Dox removal. **(D)** Schematic of experimental timeline performed using *Rb1* $^{flx/flx}$*; Alb-CreERT2* mice. **(E)** Immunoblot shows RB protein concentrations in the livers of *Rb1* $^{+/+}$, *Rb1* $^{+/-}$, and *Rb1* $^{-/-}$ mice. Mice were harvested at 6 weeks after Tamoxifen treatment. The right panel shows the quantification of protein concentration. RB protein concentration was normalized using actin. **(F)** Cell size measurements were made using a Coulter counter to examine hepatocytes isolated from *Rb1* $^{+/+}$ (n = 6 for tetraploid, n = 4 for octoploid), *Rb1* $^{+/-}$ (n = 8 for tetraploid, n = 4 for octoploid), and *Rb1* $^{-/-}$ (n = 6 for tetraploid, n = 4 for octoploid) mice at 6 weeks after Tamoxifen treatment. Each dot represents data from one mouse. The error bars indicate standard deviation. $^{**}p < 0.01$.

increases hepatocyte cell size. To overexpress RB, we utilized the *Fah*$^{-/-}$ mouse system (Azuma et al., 2007). Deletion of the *Fah* gene causes toxin accumulation in hepatocytes that will eventually lead to hepatocyte death. Toxin accumulation is prevented in *Fah*$^{-/-}$ mice by treating them with NTBC (2-(2-nitro-4-trifluoromethylbenzoyl)-1,3-cyclohexanedione) (Grompe, 2017). When NTBC is withdrawn, cells expressing exogenous *Fah*, introduced by injecting *Fah* + transposons, will clonally expand to repopulate the injured liver (Figure 2A) (Wuestefeld et al., 2013). Importantly, other genetic elements, such as transgenes, can be added to the *Fah* transposon so that they are co-integrated into some hepatocyte genomes. This system provides a versatile platform for genetic manipulations in the liver. To increase RB expression, we delivered an *Fah-P2A-Rb1* transposon and the SB100 transposase into *Fah*$^{-/-}$ mice via hydrodynamic transfection through the tail vein. As a control, we injected the transposon with *Fah-P2A-mCherry* (Figure 2B). 6 weeks after injection, the liver was almost fully repopulated by the cells containing *Fah* transposons, and there was an appreciable level of RB protein overexpression (Figures 2C,D, Supplementary Figure S2C). Consistent with the RB-dilution model, overexpression of RB resulted in bigger hepatocytes (Figure 2E, Supplementary Figure S1C).

In addition to RB dosage affecting cell size in cultured cells, it was also reported that the activity of the upstream kinase cyclin D-Cdk4/6 affected cell size (Tan et al., 2021). Lower Cdk4/6 activity resulted in larger cells, while higher activity reduced cell size. This can be integrated with the RB-dilution model since

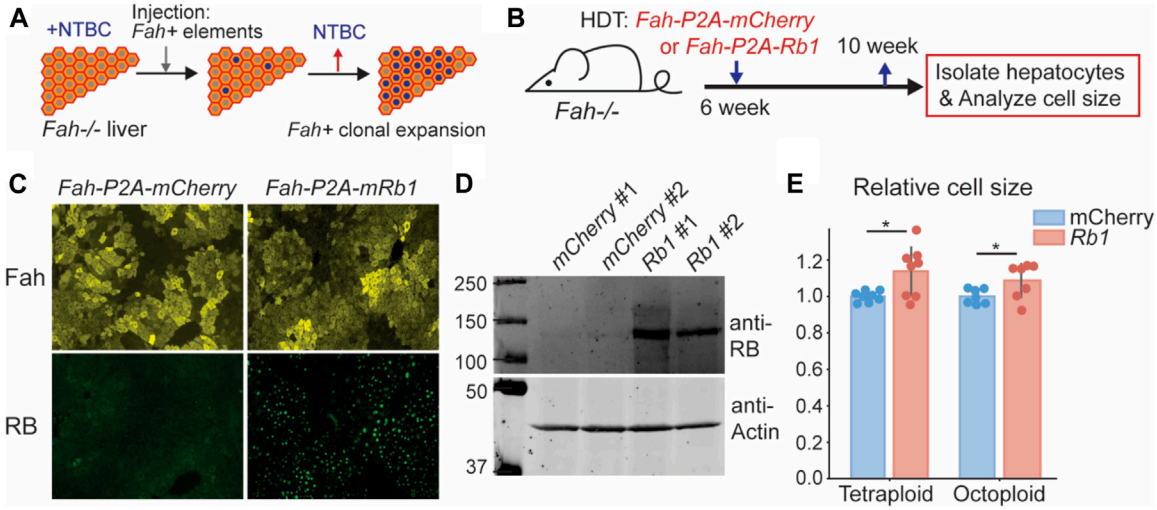

FIGURE 2
Increasing Rb1 concentration in mouse liver increases hepatocyte cell size. **(A)** Schematic of *Fah*−/− system as a platform for genetic manipulation of hepatocytes in the liver. **(B)** Schematic of experimental timeline. *Fah*$^{-/-}$ mice were injected with *Fah* transposons as indicated, and their livers were harvested 4 weeks after the injection. **(C,D)** Immunofluorescence staining **(C)** and immunoblots **(D)** were performed to measure Fah and RB expression. **(E)** Cell size measurement of the hepatocytes isolated from *Fah*$^{-/-}$ mice injected with *Fah* transposons were made with a Coulter counter. Each dot represents data from one mouse (n = 8 for tetraploid, n = 7 for octoploid). The error bars indicate standard deviation. *$p < 0.05$.

cyclin D-Cdk4/6-dependent RB phosphorylation contributes to RB inactivation. This means that the higher the Cdk4/6 activity, the more RB is phosphorylated and inactivated, and the less it needs to be diluted (Rubin et al., 2020). To test for the effect of Cdk4/6 activity on hepatocyte cell size, we used Palbociclib to inhibit Cdk4/6 activity during liver regeneration following a partial hepatectomy (Supplementary Figure S2A). In this experiment, the partial hepatectomy induces massive hepatocyte growth and proliferation during a short time window that can be monitored experimentally. More specifically, following partial hepatectomy, mice were treated with Palbociclib (80 mg/kg) for five consecutive days (Supplementary Figure S2A). We isolated hepatocytes from these mice at different time points and measured cell size. Consistent with the observations in cultured cells that the Cdk4/6-RB pathway controls cell size, Palbociclib treatment increased hepatocyte size following a partial hepatectomy (Supplementary Figure S2B).

RB protein is diluted in G1 in primary hepatocytes

So far, our data indicate that manipulations of RB protein concentrations *in vivo* changed hepatocyte size as the RB-dilution model predicted. However, these deletion and over-expression experiments cannot determine if RB protein concentration functions as a cell size sensor. For RB to be a cell size sensor responsible for cell size control, not only must its concentration affect cell size, but its concentration must also change with cell size. In other words, RB must be diluted in G1 for the model to work.

To test if RB is diluted in G1, we sought to measure the amounts of RB protein and cell size in single cells. However, detecting RB protein in single proliferating cells from the mouse liver tissue is challenging for several reasons. First, immunofluorescence measurements are challenging due to RB's low expression level and the high autofluorescence background of hepatocytes. Second, RB-dilution would control cell size by coordinating cell growth with the G1/S transition only in proliferating cells, who represent only a minority of adult hepatocytes (Magami et al., 2002; Wei et al., 2021). To circumvent these challenges, we sought to specifically measure RB protein concentrations in proliferating isolated primary hepatocytes. To do this, we used a 2D primary hepatocyte culture protocol (Peng et al., 2018; Jin et al., 2021) (Figure 3A). In these cultures, primary hepatocytes actively enter the cell cycle, and we can detect RB protein using immunfluorescence because the autofluorescence is significantly reduced in the isolated hepatocytes compared to those in the mouse liver.

To measure the RB protein concentrations in hepatocytes, we performed an immunofluorescence staining on 2D hepatocyte cultures isolated from *Fucci2* mice expressing G1 and S/G2 cell cycle phase reporters (Abe et al., 2013) (Figure 3A,B). Based on their DNA content, Cdt1-mCherry

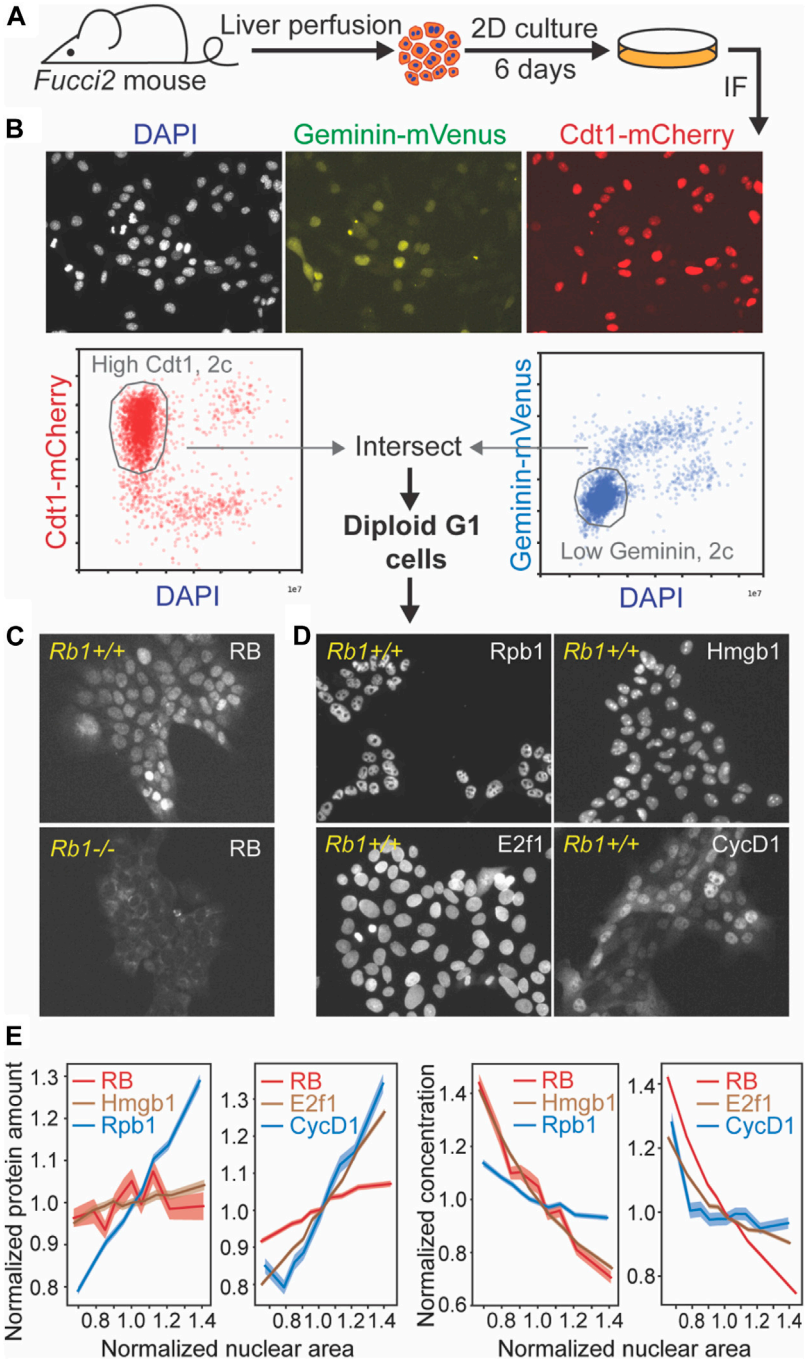

FIGURE 3
RB protein is diluted in G1 in primary hepatocytes. **(A)** Schematic of experiment examining RB protein concentrations in single primary hepatocytes in 2D cultures. **(B)** Representative immunofluorescence images of primary hepatocytes isolated from *Fucci2* mice and illustration of gating procedure used to isolate G1 cells. **(C)** Immunofluorescence staining of RB in *Fucci2* primary hepatocytes. The *Rb1*$^{-/-}$ hepatocytes were used as a negative control for RB antibody staining. **(D)** Immunofluorescence staining of Rpb1, Hmgb1, CycD1, and E2f1 in *Fucci2* primary hepatocytes grown in 2D culture. **(E)** Nuclear area of G1 hepatocytes plotted against the indicated protein amount (left panels) or concentration (right panels). The shaded area indicates 95% confidence interval.

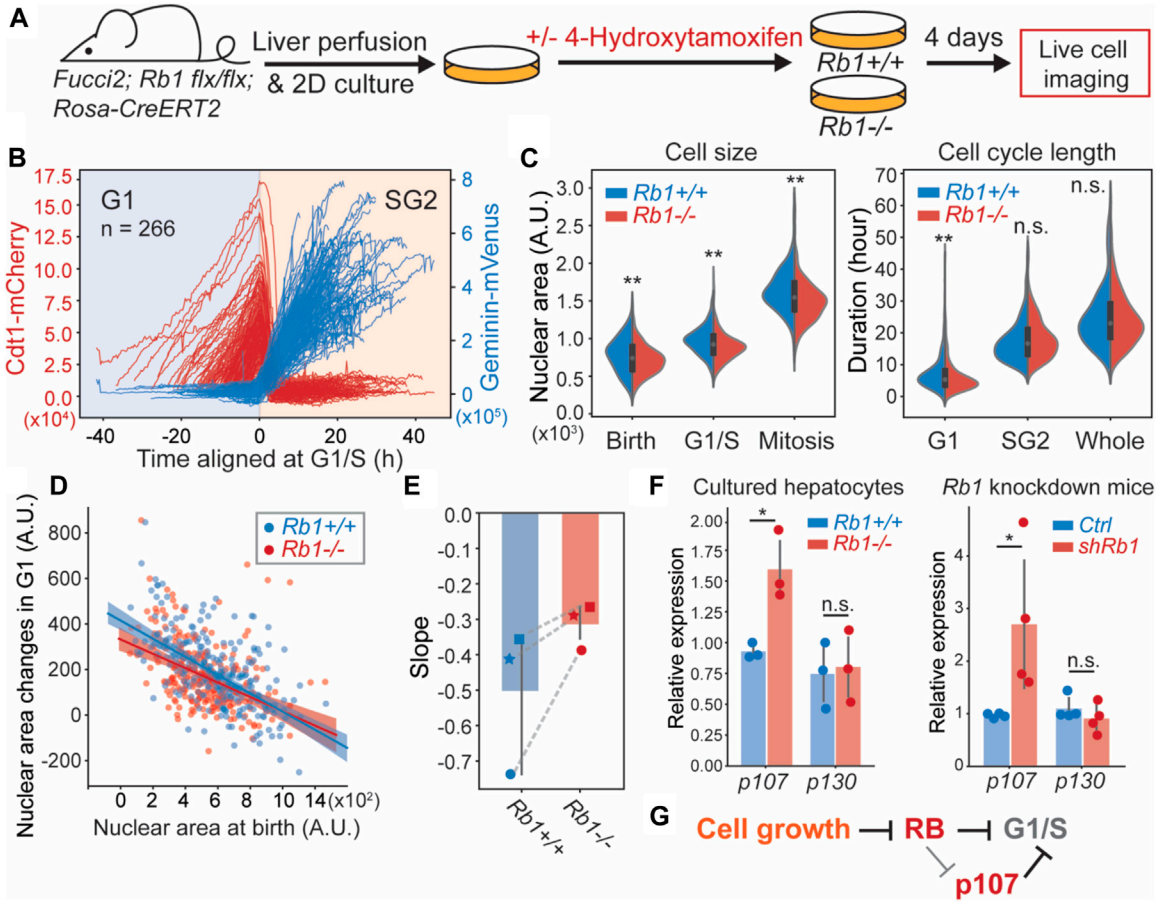

FIGURE 4
Deletion of *Rb1* weakens G1/S cell size control in primary hepatocytes. **(A)** Schematic of the experiment used to examine the role of *Rb1* in hepatocyte cell size control. **(B)** Live cell imaging traces of the Cdt1-mCherry and Geminin-Venus cell cycle reporters in *Fucci2* hepatocytes grown in 2D culture. The G1/S transition is determined using the inflection point of the Geminin-Venus signal and the point of maximum Cdt1-mCherry signal. **(C)** Cell size and cell cycle statistics of $Rb1^{+/+}$ and $Rb1^{-/-}$ hepatocytes. Cell size is approximated using nuclear area. **(D)** The correlations between nuclear area at birth and the nuclear area changes during G1 in $Rb1^{+/+}$ and $Rb1^{-/-}$ hepatocytes. The shaded area indicates the 95% confidence interval. **(E)** The slope values of the linear relationship in **(D)** are plotted from three independent biological replicates. Each experiment used hepatocytes from different mice, and $Rb1^{+/+}$ and $Rb1^{-/-}$ hepatocytes for each replicate experiment were derived from the same mouse. Dashed lines link experiments performed using hepatocytes derived from the same mouse. **(F)** *p107* mRNA measured by RT-qPCR from $Rb1^{+/+}$ and $Rb1^{-/-}$ 2D cultured primary hepatocytes (left panel) and *Rosa-rtTA; TRE-shRb1* mice (right panel). The error bars indicate standard deviation. $*p < 0.05$, $**p < 0.01$. **(G)** Model indicating multiple mechanisms through which RB regulates cell size at the G1/S transition.

signal, and Geminin-Venus signal, we determined which cells in the population were in G1 phase (Figure 3B). We then examined the relationship between target protein amount and cell size, which was estimated using nuclear area as a proxy for cell size (Figure 3C,D) (Berenson et al., 2019). We also measured the RNA Polymerase II subunit Rpb1, whose concentration was expected to stay constant, and Hmgb1, which has been found to be diluted by cell growth similarly to RB in other cell lines (Figure 3D) (Lanz et al., 2021). We found that unlike Rpb1, the total amount of RB protein did not increase in proportion to cell size, but behaved more similarly to the anticipated subscaling protein Hmgb1 (Figure 3E). We also examined amounts of two key activators of the G1/S transition, Cyclin D1 and E2f1 (Figure 3D). While RB protein amounts remained relatively unchanged as cells became larger in G1, Cyclin D1 and E2f1 protein amounts increased with cell size (Figure 3E), suggesting that the activator (Cyclin D1, E2f1) to inhibitor (RB) ratio is increasing as cells grow in G1. While immunofluorescence measurements to quantify protein amounts are not necessarily linear due to the particulars of specific antibody binding, our measurements of RB concentration as a function of nuclear area clearly demonstrate that RB is diluted as cells grow in G1. Taken together, our immunofluorescence measurements of RB concentration in proliferating hepatocytes are consistent with RB operating as a cell size sensor in G1.

Knocking out *Rb1* weakens G1/S cell size control in primary hepatocytes

At its most fundamental level, cell size control requires cells that are born smaller to grow more during the cell division cycle than cells that are born larger. Size control thus results in more similarly sized cells following a division cycle. The degree to which cells control their size can therefore be quantified by the inverse correlation between cell size at birth and the amount of cell growth. Therefore, the strength of cell size control can be evaluated by the slope of the linear fit between the cell size at birth and the amount of cell growth over the cell cycle (Cadart et al., 2018; Zatulovskiy and Skotheim, 2020). Perfect size control would yield a slope value of -1, and if the amount of growth was independent of the birth size, the slope would be 0. If RB contributed to cell size control, its deletion should reduce the degree of inverse correlation between cell size at birth and the amount of cell growth in the subsequent cell cycle (Zatulovskiy et al., 2020).

To test the extent to which RB was responsible for cell size control in G1, we sought to measure cell size and cell cycle phase durations in proliferating hepatocytes that we tracked through cell divisions. To do this, we performed live cell imaging on the 2D cultured hepatocytes isolated from *Rb1*$^{flx/flx}$*; Rosa26-CreERT2; Fucci2* mice. Four days before imaging, cells were treated with 4-Hydroxytamoxifen (4-OHT) to delete the *Rb1* gene (Figure 4A). We used the inflection point of the Geminin-Venus S/G2 reporter signal and the maximum point of the Cdt1-mCherry G1 reporter signal to determine the G1/S transition time at the midpoint between these two events (Figure 4B). We again used the nuclear area as a proxy for cell size. Consistent with RB contributing to cell size control, we found that the *Rb1*$^{-/-}$ hepatocytes exhibited smaller size and shorter G1 length (Figure 4C). Moreover, the correlation between birth nuclear area and the amount of growth in G1 was reduced in *Rb1*$^{-/-}$ hepatocytes compared to *Rb1*$^{+/+}$ hepatocytes (Figures 4D,E, Supplementary Figures S2D,E). We note that in each experiment, we used hepatocytes from different mice, but that experimental and control hepatocytes for each replicate were derived from the same mouse. Taken together, our data show that knocking out *Rb1* weakened G1/S cell size control in hepatocytes, consistent with the RB-dilution model.

While *Rb1* deletion weakened G1/S size control, it did not remove it completely as the slope between nuclear area at birth and G1 growth amount was not 0 (Figure 4D). It was previously shown that *Rb1* deletion resulted in the upregulation of the related protein p107, which can compensate for *Rb1* loss (Sage et al., 2000). Therefore, the partial loss of size control in *Rb1*$^{-/-}$ cells might be explained by p107 upregulation because p107 protein was previously found to be similarly diluted as RB (Zatulovskiy et al., 2020). Moreover, the combined deletion of *Rb1* and *p107* genes in mouse embryonic fibroblasts resulted in much smaller cells than either of the single deletions (Dannenberg et al., 2000; Sage et al., 2000). To test if *p107* was upregulated in *Rb1*$^{-/-}$ hepatocytes, we measured the mRNA levels of *p107* in *Rb1*$^{-/-}$ 2D cultured hepatocytes, as well as in the *Rosa-rtTA; TRE-shRb1* mouse livers. Indeed, *p107* mRNA was increased in *Rb1*$^{-/-}$ and *Rb1* knock down cells (Figure 4F), while another member of the pocket protein family, *p130*, remained same, supporting our hypothesis that *p107* is upregulated to compensate for *Rb1* loss and contributes to G1/S size control when *Rb1* was deleted (Figure 4G).

Discussion

Cell size is fundamental to cell physiology, yet we are only now beginning to understand the molecular mechanisms that control size through linking cell growth to division. Cell growth was found to trigger cell division by diluting a cell cycle inhibitor in budding yeast and *Arabidopsis* plant cells (Lanz et al., 2021; Schmoller et al., 2015; Xie et al., 2022; Swaffer et al., 2021; D'Ario et al., 2021). This general principle of inhibitor-dilution was also found in human cells grown in culture, who diluted the cell cycle inhibitor RB in G1 to trigger the G1/S transition (Zatulovskiy et al., 2020). This RB-dilution mechanism can be modulated by cyclin D-Cdk4/6 activity, which inactivates RB (Tan et al., 2021). However, it was not clear whether the RB-dilution mechanism was physiologically relevant to cells growing in tissues *in vivo*. This is because of the large differences between the conditions cells experience when growing in a 2D *in vitro* culture compared to a 3D tissue environment. In tissues, cells send and receive many more paracrine and endocrine signals, have multiple cell-cell contacts, experience dynamic forces and pressures, and experience an environment with very different nutrients and growth factors. In addition to these differences in culture and tissue environments, size control models developed in culture are cell autonomous and do not take into account the possibility that tissue level processes could be used to sense and control the size of neighboring cells.

Due to the significant differences of *in vitro* and *in vivo* growth conditions, it is crucial to test molecular models developed using cell culture in animal contexts. We therefore sought to test the RB-dilution model *in vivo* in the mouse liver. The RB-dilution model has two main requirements. First, that changing the concentration of RB should have an effect on the average cell size, and second, that the concentration of endogenous RB should reflect cell size. Both of these requirements were satisfied in mouse hepatocytes. By using genetically engineered mouse models to manipulate RB concentrations, we found hepatocyte size was correlated with RB protein concentrations in mouse liver. Moreover, the endogenous RB protein was diluted in larger G1 cells. Finally, we examined cell size control in proliferating isolated primary hepatocytes transferred into culture. Loss of *Rb1* weakened G1/S cell size control, *i.e.,* reduced the correlation between how much

cells grew in G1 and how large they were at birth. Taken together, these results support a role for the RB-dilution model in regulating hepatocyte cell size. As previous work showed similar mechanisms operate in yeast and plants, it is now clear that examples of the inhibitor-dilution class of mechanisms can be found across the tree of life.

In addition to being broadly applicable, inhibitor dilution models can easily be modified to link cell size to cell cycle progression in polyploid cells, which are common in mouse liver. Indeed, polyploidy is a common feature of mammalian livers, where ploidy is generally proportional to cell size (Mu et al., 2020). The RB-dilution model is compatible with hepatocyte polyploidization, which is predominantly mediated by cytokinesis failure (Celton-Morizur and Desdouets, 2010; Gentric et al., 2012). This is because the link between cell growth and cell cycle progression through the dilution of a cell cycle inhibitor does not actually require division. RB may be diluted in G1 so that S phase is triggered. The, RB accumulates through S/G2 and cells can return to a subsequent stable tetraploid G1 phase without division. Crucially, the RB-dilution model is based on protein concentrations, which will be the same in two diploid G1 cells (if division was successful) as in one tetraploid G1 cell (if division was unsuccessful). Inhibitor dilution thus potentially provides an elegant mechanism to explain the repeated growth requirements for DNA synthesis and the large size of polyploid eukaryotic cells.

While our data here support a role for RB-dilution in controlling cell size in the mouse liver, they also indicate that this is unlikely to be the only size control mechanism working in this context. The presence of compensatory mechanisms can be inferred from the fact that *Rb1* deletion and over-expression produce modest changes in cell size (Figures 1, 2). Moreover, *Rb1* deletion in primary hepatocytes grown in culture only partially eliminated the correlation between growth and progression through G1 (Figure 4). One possible explanation for these results is that other cell size control mechanisms inhibit the division of small cells in the absence of RB. One possibility is that signaling through the stress activated kinase p38 inhibits cell division in small cells to prevent their division and allow them more time to grow in G1[21,22]. A second possibility is that RB loss is compensated for by the upregulation of another cell cycle inhibitor. Indeed, RB regulates the expression of the related cell cycle inhibitor p107 (Dannenberg et al., 2000; Sage et al., 2000; Burkhart et al., 2010; Wirt and Sage, 2010). Consistent with prior work, we found that deletion of *Rb1* In hepatocytes strongly increased p107 expression. This regulation of *p107* by RB could buffer cell size against changes in RB protein concentrations (Figure 4G). Further investigation into this mechanism is needed, which can be achieved by incorporating *p107* knockout in the *Rb1* knockout background.

In addition to p107 regulation buffering the effect of *Rb1* deletion, there could be additional size-control mechanisms. In yeast, Whi5-dilution is one of several mechanisms that operate based on size-dependent gene expression (Keifenheim et al., 2017; Chen et al., 2020). In this model, a series of cell cycle activators generally increase in concentration as cells grow, while cell cycle inhibitors decrease in concentration. The balance of activators and inhibitors then sets cell size. Removal of any one component would serve to shift the mean cell size, but not remove the ability of the cell to control size around the new setpoint. Supporting the applicability of this multiple size-scaling mechanism model to mammalian cells, recent proteomics analyses found that cell size-dependent concentration changes were widespread across the proteome of human cells grown in culture (Cheng et al., 2021; Lanz et al., 2021). Moreover, beyond such size-scaling concentration-based mechanisms, there may be additional mechanisms operating by other mechanistic principles yet to be discovered. Much more work remains to be done to identify the mechanistic links between cell growth and division. As a first step, we anticipate such work will need to be done in yeast and cultured cells. While this work will need to be validated *in vivo*, our results here, indicating that the RB-dilution model contributes to controlling cell size in hepatocytes, should serve as encouragement for future studies *in vitro* and their application *in vivo*.

Materials and methods

Mice

All mice were handled in accordance with the guidelines of the Institutional Animal Care and Use Committee at Stanford University. The *Rosa-rtTA; TRE-shRb1* mice were described before (Doan et al., 2021). *Rosa-rtTA* or *Rosa-rtTA; TRE-shRb1* mice were given Doxycyclin water (RPI, 1 g/L) from birth to when they were 4 weeks old. At 6 weeks old, the mice were sacrificed to isolate primary hepatocytes. *Alb-CreERT2* mice were a kind gift of Dr. Pierre Chambon [51], and $Rb1^{flx/flx}$; $p107^{-/-}$; $p130^{flx/flx}$; *Alb-CreERT2* were described before [52]. We bred $Rb1^{flx/flx}$; $p107^{-/-}$; $p130^{flx/flx}$; *Alb-CreERT2* mice to $Rb1^{flx/flx}$ mice to generate $Rb1^{flx/flx}$; *Alb-CreERT2*, $Rb1^{flx/+}$; *Alb-CreERT2, and* $Rb1^{+/+}$; *Alb-CreERT2* mice from the same cohort. Then, tamoxifen (Sigma, 50 mg/kg, five consecutive doses) was given to these mice when they were ~15 days old through i. p. Injection. At 6 weeks old, the mice were sacrificed to isolate primary hepatocytes. The $Fah^{-/-}$ mice were kindly shared by Dr. Markus Grompe's group at Oregon Health and Science University. At 6 weeks old, the $Fah^{-/-}$ mice were subjected to hydrodynamical transfection through their tail vein. The DNA plasmids we injected contain a transposon and transposase. The plasmid backbone was kindly provided by Dr. Hao Zhu's lab at UT Southwestern Medical Center. We modified the transposons to express the *Fah* gene and mCherry or Rb1. The transposase was SB100.6 weeks after the injection, the mice were sacrificed to isolate primary hepatocytes. The *Fucci2* mice (Abe et al., 2013)

were kindly shared by Dr. Valentina Greco's lab at Yale University. The *Fucci2* mice contained the transgene expressing Cdt1-mCherry and Geminin-Venus from the *ROSA26* locus.

Partial hepatectomy and palbociclib treatment

2/3rd partial hepatectomies were performed on 8-week-old male CD1 mice (JAX). The procedure followed an established protocol [53]. At day 0 to day 5 after the surgery, mice were injected with either vehicle or Palbociclib HCl (80 mg/kg). Palbociclib HCl was dissolved in 50 mmol/L sodium lactate (pH 4) at a concentration of 10 μg/ml under a fume hood. Then, the drug was given to mice at a dosage of 80 mg/kg via oral gavage for five consecutive days. On day 0, 1, 2, 3, 4, 5 after surgery, one mouse from each treatment was sacrificed to isolate primary hepatocytes.

Primary hepatocyte isolation and size measurement

Primary hepatocytes were isolated by two-step collagenase perfusion [54]. Liver perfusion medium (Thermo Fisher Scientific, 17701038), liver digest medium (Thermo Fisher Scientific, 17703034) and hepatocyte wash medium (Thermo Fisher Scientific, 17704024) were used. After isolation, cells were washed with PBS once and stained with Zombie Green (Biolegend, 423,111) at room temperature for 15 min to mark dead cells. After washing with cold PBS twice, cells were fixed in 4% PFA (Thermo Fisher Scientific, 28,906) at 37°C for 15 min. Then, cells were washed with PBS 3 times, subjected to DNA staining using Hoechst (Thermo Fisher Scientific, 62,249), and sorted on a Flow Cytometer (BD FACSAria II) based on their live/dead staining and their DNA staining. Only live (without Zombie Green signal) hepatocytes with same ploidy were sorted. 10,000–20000 cells were sorted for each population. After sorting, the cell size distributions for each population were measured using a Z2 Coulter counter (Beckman).

Since male and female mice have different hepatocyte size, they were analyzed separately, normalized, and then combined. Therefore, only when there were all genotypes within one gender, the mice of that gender in that litter would be used for the experiment. The mice genotypes in each litter used for this study can be found in Supplementary Figure S1.

Primary hepatocyte 2D culture

The protocol for 2D culture of primary hepatocytes was kindly shared by Yinhua Jin from Dr. Roeland Nusse's lab at Stanford University (Peng et al., 2018; Jin et al., 2021). Briefly, primary hepatocytes from *Rb1*$^{flx/flx}$*; Rosa26-CreER2; Fucci2* mice were isolated by two-step collagenase perfusion. After isolation, cells were washed 3 times with hepatocyte wash medium (Thermo Fisher Scientific, 17704024). Cells were then plated in a 6-well plate precoated with collagen I (50 μg/ml) at a density of 200,000 per well. The culture medium contained 3 μM CHIR99021 (Peprotech), 25 ng/ml EGF (Peprotech), 50 ng/ml HGF (Peprotech), and 100 ng/ml TNFa (Peprotech) in Basal medium. The Basal medium contained William's E medium (GIBCO), 1% Glutamax (GIBCO), 1% Non-Essential Amino Acids (GIBCO), 1% Penicillin/streptomycin (GIBCO), 0.2% normocin (Invitrogen), 2% B27 (GIBCO), 1% N2 supplement (GIBCO), 2% FBS (Corning), 10 mM nicotinamide (Sigma), 1.25 mM N-acetylcysteine (Sigma), 10 μM Y27632 (Peprotech) and 1 μM A83-01 (Tocris). The culture medium was refreshed every other day. Cells were passaged via trypsinization using TrypLE (Thermo-Fisher).

Live cell imaging and analysis

The cultured Fucci2 hepatocytes were seeded on collagen coated 35-mm glass-bottom dishes (MatTek) 1 day before imaging. Then, the cells were transferred to a Zeiss Axio Observer Z1 microscope equipped with an incubation chamber and imaged for 48 h at 37°C and 5% CO_2. Brightfield and fluorescence images were collected from *Rb1*$^{+/+}$ and *Rb1*$^{-/-}$ *Fucci2* hepatocytes at multiple positions every 20 min using an automated stage controlled by the Micro-Manager software. We used a Zyla 5.5 sCMOS camera and an A-plan 10x/0.25NA Ph1 objective. For each cell, the transition from G1 to S phase was taken as the midpoint between when the inflection point of the Geminin-Venus signal and the point of maximum Cdt1-mCherry signal occurred. Cell size was approximated using the area of the nucleus (Berenson et al., 2019).

Immunoblots

Mouse liver tissues or isolated primary hepatocyte pellets were homogenized and lysed in RIPA buffer (Thermo Scientific) supplemented with protease inhibitors and phosphatase inhibitors. Lysates were separated on 8% SDS-PAGE gels and transferred to nitrocellulose membranes. Membranes were then blocked with SuperBlock™ (TBS) Blocking Buffer (Thermo Fisher Scientific) and incubated overnight at 4°C with primary antibodies in 3% BSA solution in PBS. The primary antibodies were detected using the fluorescently labeled secondary antibodies IRDye® 680LT Goat anti-Mouse IgG (LI-COR 926–68020) and IRDye®

800CW Goat anti-Rabbit IgG (LI-COR 926–32211). Membranes were imaged on a LI-COR Odyssey CLx and analyzed with LI-COR Image Studio software. The following antibodies were used: anti-β-Actin (Sigma, A2103, 1:2000), Anti-Rb (Santa cruz, sc-74570, 1:500).

Immunofluorescence staining

Fucci2 hepatocytes were seeded on a 35-mm collagen-coated glass-bottom dish (MatTek) 1 day before immunofluorescence staining and analysis. For the staining, cells were fixed with 4% paraformaldehyde for 20 min at room temperature, permeabilized with 0.5% Triton™ X-100 (Sigma-Aldrich) for 15 min at room temperature, and then blocked with 3% BSA in PBS. Then, the cells were incubated with primary antibodies overnight at 4°C. After three washes with PBS, the cells were incubated with Alexa Fluor 647 conjugated goat anti-mouse secondary antibodies (Invitrogen, A32728) at 1:1,000 for 1 h at room temperature. After three washes with PBS, cells were incubated with 500 nM DAPI for 30 min at room temperature before imaging. The primary antibodies used for immunofluorescence were Anti-Rb (Santa cruz, sc-74570, 1:100), Anti-Rpb1-CTD (Abcam, ab252854, 1:250), Anti-HMGB1 (Abcam, ab79823, 1:250), Anti-E2F1 (Santa cruz, sc-251, 1:100), and Anti-Ccnd1 (Abcam, ab16663, 1:250). The cells were imaged using a Zeiss Axio Observer Z1 microscope with an A-plan 10x/0.25NA objective.

Image analysis

For microscopy data quantification, cell nuclei were segmented using either the mCherry channel for cells in G1 that express Cdt1-mCherry or the GFP channel for cells in S/G2 that express Geminin-Venus. Segmentation was performed using the Fiji plugin StarDist, which is a deep-learning tool for segmenting nuclei in images that are difficult to segment using thresholding-based methods. The total pixel intensities within the segmented masks in each channel were recorded, and each object's background was subtracted based on the median intensity of the image. G1 cells were selected based on their Cdt1-mCherry and Geminin-Venus signals. The cells that had high Cdt1-mCherry and low Geminin-Venus were selected as G1 cells. When analyzing the scaling behavior of immunostained proteins, nuclear area was used as a proxy for cell size 7.

RNA extraction and qRT-PCR

Total RNA was isolated using Direct-zol RNA Miniprep kit (Zymo Research). For qRT-PCR, cDNA synthesis was performed with 1 μg of total RNA using an iScript Reverse Transcription Kit (Biorad). qPCR reactions were made with the 2x SYBR Green Master Mix (Biorad). Gene expression levels were measured using the ΔΔCt method.

Statistical analysis

The data in most figure panels reflect multiple experiments performed on different days using mice derived from different litters. For comparison between groups, we conducted the hypothesis test using the two-tailed student's t-test. Statistical significance is displayed as $p < 0.05$ (*) or $p < 0.01$ (**) unless specified otherwise.

Data availability statement

The raw data supporting the conclusion of this article will be made available by the authors, without undue reservation.

Ethics statement

The animal study was reviewed and approved by the Administrative panel on laboratory animal care of Stanford University.

Author contributions

SZ and JMS designed the project, performed the experiments, and wrote the manuscript. JS and JA shared the genetically engineered mouse models, and assisted with manuscript preparation. EZ assisted with project design and manuscript preparation.

Funding

This work was supported by the National Institutes of Health (R01 DK128578, P01 CA254867).

Acknowledgments

We thank Roel Nusse and Jinghua Li for assistance in establishing the protocol to culture primary hepatocytes in 2D, Thuyen Nguyen for maintaining the mouse colonies in the Sage lab, Dr. Marcus Grompe for sharing the *Fah*$^{-/-}$ mice, and the members of the Skotheim laboratory for discussions and feedback on the work.

Conflict of interest

The authors declare that the research was conducted in the absence of any commercial or financial relationships that could be construed as a potential conflict of interest.

Publisher's note

All claims expressed in this article are solely those of the authors and do not necessarily represent those of their affiliated organizations, or those of the publisher, the editors and the reviewers. Any product that may be evaluated in this article, or claim that may be made by its manufacturer, is not guaranteed or endorsed by the publisher.

Supplementary material

The Supplementary Material for this article can be found online at: https://www.frontiersin.org/articles/10.3389/fcell.2022.965595/full#supplementary-material

References

Abe, T., Sakaue-Sawano, A., Kiyonari, H., Shioi, G., Inoue, K. i., Horiuchi, T., et al. (2013). Visualization of cell cycle in mouse embryos with Fucci2 reporter directed by Rosa26 promoter. *Development* 140, 237–246. doi:10.1242/dev.084111

Azuma, H., Paulk, N., Ranade, A., Dorrell, C., Al-Dhalimy, M., Ellis, E., et al. (2007). Robust expansion of human hepatocytes in Fah-/-/Rag2-/-/Il2rg-/- mice.-/-/Il2rg-/- mice. *Nat. Biotechnol.* 25, 903–910. doi:10.1038/nbt1326

Bell, C. D., and Waizbard, E. (1986). Variability of cell size in primary and metastatic human breast carcinoma. *Invasion Metastasis* 6, 11–20.

Berenson, D. F., Zatulovskiy, E., Xie, S., and Skotheim, J. M. (2019). Constitutive expression of a fluorescent protein reports the size of live human cells. *Mol. Biol. Cell* 30, 2985–2995. doi:10.1091/mbc.E19-03-0171

Burkhart, D. L., Wirt, S. E., Zmoos, A.-F., Kareta, M. S., and Sage, J. (2010). Tandem E2F binding sites in the promoter of the p107 cell cycle regulator control p107 expression and its cellular functions. *PLoS Genet.* 6, e1001003. doi:10.1371/journal.pgen.1001003

Cadart, C., Monnier, S., Grilli, J., Saez, P. J., Srivastava, N., Attia, R., et al. (2018). Size control in mammalian cells involves modulation of both growth rate and cell cycle duration. *Nat. Commun.* 9, 3275. doi:10.1038/s41467-018-05393-0

Celton-Morizur, S., and Desdouets, C. (2010). Polyploidization of liver cells. *Adv. Exp. Med. Biol.* 676, 123–135. doi:10.1007/978-1-4419-6199-0_8

Chan, Y.-H. M., and Marshall, W. F. (2014). Organelle size scaling of the budding yeast vacuole is tuned by membrane trafficking rates. *Biophys. J.* 106, 1986–1996. doi:10.1016/j.bpj.2014.03.014

Chen, Y., Zhao, G., Zahumensky, J., Honey, S., and Futcher, B. (2020). Differential scaling of gene expression with cell size may explain size control in budding yeast. *Mol. Cell* 78, 359.e6–370.e6. doi:10.1016/j.molcel.2020.03.012

Cheng, L., Chen, J., Kong, Y., Tan, C., Kafri, R., and Björklund, M. (2021). *Size-scaling promotes senescence-like changes in proteome and organelle content*. 2021.08.05.455193. doi:10.1101/2021.08.05.455193

Dannenberg, J. H., van Rossum, A., Schuijff, L., and te Riele, H. (2000). Ablation of the retinoblastoma gene family deregulates G(1) control causing immortalization and increased cell turnover under growth-restricting conditions. *Genes Dev.* 14, 3051–3064. doi:10.1101/gad.847700

D'Ario, M., Tavares, R., Schiessl, K., Desvoyes, B., Gutierrez, C., Howard, M., et al. (2021). Cell size controlled in plants using DNA content as an internal scale. *Science* 372, 1176–1181. doi:10.1126/science.abb4348

Decker, M., Jaensch, S., Pozniakovsky, A., Zinke, A., O'Connell, K. F., Zachariae, W., et al. (2011). Limiting amounts of centrosome material set centrosome size in *C. elegans* embryos. *Curr. Biol.* 21, 1259–1267. doi:10.1016/j.cub.2011.06.002

Doan, A., Arand, J., Gong, D., Drainas, A. P., Shue, Y. T., Lee, M. C., et al. (2021). RB depletion is required for the continuous growth of tumors initiated by loss of RB. *PLoS Genet.* 17, e1009941. doi:10.1371/journal.pgen.1009941

Evans, T. C., and Jehle, D. (1991). The red blood cell distribution width. *J. Emerg. Med.* 9 (1), 71–74. doi:10.1016/0736-4679(91)90592-4

Gentric, G., Desdouets, C., and Celton-Morizur, S. (2012). Hepatocytes polyploidization and cell cycle control in liver physiopathology. *Int. J. Hepatol.* 2012, 282430. doi:10.1155/2012/282430

Ginzberg, M. B., Chang, N., D'Souza, H., Patel, N., Kafri, R., and Kirschner, M. W. (2018). Cell size sensing in animal cells coordinates anabolic growth rates and cell cycle progression to maintain cell size uniformity. *eLife* 7, e26957. doi:10.7554/eLife.26957

Ginzberg, M. B., Kafri, R., and Kirschner, M. (2015). Cell biology. On being the right (cell) size. *Science* 348, 1245075. doi:10.1126/science.1245075

Good, M. C., Vahey, M. D., Skandarajah, A., Fletcher, D. A., and Heald, R. (2013). Cytoplasmic volume modulates spindle size during embryogenesis. *Science* 342, 856–860. doi:10.1126/science.1243147

Grompe, M. (2017). Fah knockout animals as models for therapeutic liver repopulation. *Adv. Exp. Med. Biol.* 959, 215–230. doi:10.1007/978-3-319-55780-9_20

Hazel, J., Krutkramelis, K., Mooney, P., Tomschik, M., Gerow, K., Oakey, J., et al. (2013). Changes in cytoplasmic volume are sufficient to drive spindle scaling. *Science* 342, 853–856. doi:10.1126/science.1243110

Jin, Y., Anbarchian, T., Wu, P., Sarkar, A., Fish, M., and Nusse, R. (2021). Hepatocyte cell cycle progression depends on a transcriptional repressor cascade downstream of wnt signaling. *bioRxiv*

Jorgensen, P., Edgington, N. P., Schneider, B. L., Rupes, I., Tyers, M., and Futcher, B. (2007). The size of the nucleus increases as yeast cells grow. *Mol. Biol. Cell* 18, 3523–3532. doi:10.1091/mbc.e06-10-0973

Kafri, R., Levy, J., Ginzberg, M. B., Oh, S., Lahav, G., and Kirschner, M. W. (2013). Dynamics extracted from fixed cells reveal feedback linking cell growth to cell cycle. *Nature* 494, 480–483. doi:10.1038/nature11897

Keifenheim, D., Sun, X. M., D'Souza, E., Ohira, M. J., Magner, M., Mayhew, M. B., et al. (2017). Size-dependent expression of the mitotic activator Cdc25 suggests a mechanism of size control in fission yeast. *Curr. Biol.* 27, 1491e4–1497.e4. doi:10.1016/j.cub.2017.04.016

Lanz, M. C., Zatulovskiy, E., Swaffer, M. P., Zhang, L., Ilerten, I., Zhang, S., et al. (2021). *Increasing cell size remodels the proteome and promotes senescence*. 2021.07.29.454227. doi:10.1101/2021.07.29.454227

Liu, S., Ginzberg, M. B., Patel, N., Hild, M., Leung, B., Li, Z., et al. (2018). Size uniformity of animal cells is actively maintained by a p38 MAPK-dependent regulation of G1-length. *eLife* 7, e26947. doi:10.7554/eLife.26947

Liu, X., Yan, J., and Kirschner, M. W. (2022). *Beyond G1/S regulation: How cell size homeostasis is tightly controlled throughout the cell cycle?* 2022.02.03.478996. doi:10.1101/2022.02.03.478996

Magami, Y., Azuma, T., Inokuchi, H., Kokuno, S., Moriyasu, F., Kawai, K., et al. (2002). Cell proliferation and renewal of normal hepatocytes and bile duct cells in adult mouse liver. *Liver* 22, 419–425. doi:10.1034/j.1600-0676.2002.01702.x

Mu, L., Kang, J. H., Olcum, S., Payer, K. R., Calistri, N. L., Kimmerling, R. J., et al. (2020). Mass measurements during lymphocytic leukemia cell polyploidization decouple cell cycle- and cell size-dependent growth. *Proc. Natl. Acad. Sci. U. S. A.* 117, 15659–15665. doi:10.1073/pnas.1922197117

Neumann, F. R., and Nurse, P. (2007). Nuclear size control in fission yeast. *J. Cell Biol.* 179, 593–600. doi:10.1083/jcb.200708054

Nguyen, A., Yoshida, M., Goodarzi, H., and Tavazoie, S. F. (2016). Highly variable cancer subpopulations that exhibit enhanced transcriptome variability and metastatic fitness. *Nat. Commun.* 7, 11246. doi:10.1038/ncomms11246

Peng, W. C., Logan, C. Y., Fish, M., Anbarchian, T., Aguisanda, F., Alvarez-Varela, A., et al. (2018). Inflammatory cytokine TNFα promotes the long-term expansion of primary hepatocytes in 3D culture. *Cell* 175, 1607–1619.e15. doi:10.1016/j.cell.2018.11.012

Rafelski, S. M., Viana, M. P., Zhang, Y., Chan, Y. H. M., Thorn, K. S., Yam, P., et al. (2012). Mitochondrial network size scaling in budding yeast. *Science* 338, 822–824. doi:10.1126/science.1225720

Rubin, S. M., Sage, J., and Skotheim, J. M. (2020). Integrating old and new paradigms of G1/S control. *Mol. Cell* 80, 183–192. doi:10.1016/j.molcel.2020.08.020

Sage, J., Mulligan, G. J., Attardi, L. D., Miller, A., Chen, S., Williams, B., et al. (2000). Targeted disruption of the three Rb-related genes leads to loss of G1 control and immortalization. *Genes Dev.* 14, 3037–3050. doi:10.1101/gad.843200

Salvagno, G. L., Sanchis-Gomar, F., Picanza, A., and Lippi, G. (2015). Red blood cell distribution width: A simple parameter with multiple clinical applications. *Crit. Rev. Clin. Lab. Sci.* 52, 86–105. doi:10.3109/10408363.2014.992064

Sandlin, C. (2022). *3D characterization of cell size dysregulation in human lung adenocarcinoma reveals a network of fine processes connecting alveolar type 2 cells*.

Savage, V. M., Allen, A. P., Brown, J. H., Gillooly, J. F., Herman, A. B., Woodruff, W. H., et al. (2007). Scaling of number, size, and metabolic rate of cells with body size in mammals. *Proc. Natl. Acad. Sci. U. S. A.* 104, 4718–4723. doi:10.1073/pnas.0611235104

Schmoller, K. M., Turner, J. J., Kõivomägi, M., and Skotheim, J. M. (2015). Dilution of the cell cycle inhibitor Whi5 controls budding-yeast cell size. *Nature* 526, 268–272. doi:10.1038/nature14908

Swaffer, M. P., Kim, J., Chandler-Brown, D., Langhinrichs, M., Marinov, G. K., Greenleaf, W. J., et al. (2021). Transcriptional and chromatin-based partitioning mechanisms uncouple protein scaling from cell size. *Mol. Cell* 81, 4861e7–4875.e7. doi:10.1016/j.molcel.2021.10.007

Tan, C., Ginzberg, M. B., Webster, R., Iyengar, S., Liu, S., Papadopoli, D., et al. (2021). Cell size homeostasis is maintained by CDK4-dependent activation of p38 MAPK. *Dev. Cell* 56, 1756e7–1769.e7. doi:10.1016/j.devcel.2021.04.030

Tzur, A., Kafri, R., LeBleu, V. S., Lahav, G., and Kirschner, M. W. (2009). Cell growth and size homeostasis in proliferating animal cells. *Science* 325, 167–171. doi:10.1126/science.1174294

Wei, Y., Wang, Y. G., Jia, Y., Li, L., Yoon, J., Zhang, S., et al. (2021). Liver homeostasis is maintained by midlobular zone 2 hepatocytes. *Science* 371, eabb1625. doi:10.1126/science.abb1625

Wirt, S. E., and Sage, J. (2010). p107 in the public eye: an Rb understudy and more. *Cell Div.* 5, 9. doi:10.1186/1747-1028-5-9

Wuestefeld, T., Pesic, M., Rudalska, R., Dauch, D., Longerich, T., Kang, T. W., et al. (2013). A Direct *in vivo* RNAi screen identifies MKK4 as a key regulator of liver regeneration. *Cell* 153, 389–401. doi:10.1016/j.cell.2013.03.026

Xie, S., Swaffer, M., and Skotheim, J. M. (2022). Eukaryotic cell size control and its relation to biosynthesis and senescence. *Annu. Rev. Cell Dev. Biol.* 38. doi:10.1146/annurev-cellbio-120219-040142

Zatulovskiy, E., and Skotheim, J. M. (2020). On the molecular mechanisms regulating animal cell size homeostasis. *Trends Genet.* 36, 360–372. doi:10.1016/j.tig.2020.01.011

Zatulovskiy, E., Zhang, S., Berenson, D. F., Topacio, B. R., and Skotheim, J. M. (2020). Cell growth dilutes the cell cycle inhibitor Rb to trigger cell division. *Science* 369, 466–471. doi:10.1126/science.aaz6213

Zhang, S., Lin, Y.-H., Tarlow, B., and Zhu, H. (2019). The origins and functions of hepatic polyploidy. *Cell Cycle* 18, 1302–1315. doi:10.1080/15384101.2019.1618123

frontiers | Frontiers in Cell and Developmental Biology

TYPE Original Research
PUBLISHED 05 September 2022
DOI 10.3389/fcell.2022.980721

OPEN ACCESS

EDITED BY
Marti Aldea,
Institute of Molecular Biology of Barcelona (CSIC), Spain

REVIEWED BY
Akshay Narkar,
United States Food and Drug Administration, United States
David Moreno,
Independent researcher, Lleida, Spain

*CORRESPONDENCE
Jan M. Skotheim,
skotheim@stanford.edu

†These authors have contributed equally to this work

SPECIALTY SECTION
This article was submitted to Cell Growth and Division, a section of the journal Frontiers in Cell and Developmental Biology

RECEIVED 28 June 2022
ACCEPTED 09 August 2022
PUBLISHED 05 September 2022

CITATION
Zatulovskiy E, Lanz MC, Zhang S, McCarthy F, Elias JE and Skotheim JM (2022), Delineation of proteome changes driven by cell size and growth rate.
Front. Cell Dev. Biol. 10:980721.
doi: 10.3389/fcell.2022.980721

Delineation of proteome changes driven by cell size and growth rate

Evgeny Zatulovskiy[1†], Michael C. Lanz[1,2†], Shuyuan Zhang[1], Frank McCarthy[2], Joshua E. Elias[2] and Jan M. Skotheim[1,2*]

[1]Department of Biology, Stanford University, Stanford, CA, United States, [2]Chan Zuckerberg Biohub, Stanford, CA, United States

Increasing cell size drives changes to the proteome, which affects cell physiology. As cell size increases, some proteins become more concentrated while others are diluted. As a result, the state of the cell changes continuously with increasing size. In addition to these proteomic changes, large cells have a lower growth rate (protein synthesis rate per unit volume). That both the cell's proteome and growth rate change with cell size suggests they may be interdependent. To test this, we used quantitative mass spectrometry to measure how the proteome changes in response to the mTOR inhibitor rapamycin, which decreases the cellular growth rate and has only a minimal effect on cell size. We found that large cell size and mTOR inhibition, both of which lower the growth rate of a cell, remodel the proteome in similar ways. This suggests that many of the effects of cell size are mediated by the size-dependent slowdown of the cellular growth rate. For example, the previously reported size-dependent expression of some senescence markers could reflect a cell's declining growth rate rather than its size *per se*. In contrast, histones and other chromatin components are diluted in large cells independently of the growth rate, likely so that they remain in proportion with the genome. Finally, size-dependent changes to the cell's growth rate and proteome composition are still apparent in cells continually exposed to a saturating dose of rapamycin, which indicates that cell size can affect the proteome independently of mTORC1 signaling. Taken together, our results clarify the dependencies between cell size, growth, mTOR activity, and the proteome remodeling that ultimately controls many aspects of cell physiology.

KEYWORDS

cell size, growth rate, quantitative proteomics, mTOR, rapamycin, protein synthesis rate, senescence

Introduction

The importance of cell size is reflected in its uniformity within any given cell type. Deviations from a typical size are often associated with disease states, such cancer and aging (Ginzberg et al., 2015; Li et al., 2015; Nguyen et al., 2016; Neurohr et al., 2019; Zatulovskiy and Skotheim, 2020; Cheng et al., 2021; Lengefeld et al., 2021; Lanz et al.,

2022; Sandlin, 2022). To avoid such problematic disease states, eukaryotic cells rely on dedicated mechanisms that correct for deviations from their target cell size (Ginzberg et al., 2015; Cadart et al., 2018; Ginzberg et al., 2018; Liu et al., 2018; Zatulovskiy et al., 2020; Zatulovskiy and Skotheim, 2020).

The relationship between cell size and cell physiology is apparent from size-dependent changes to the proteome. While most protein concentrations remain fairly constant as cells grow larger (protein amounts scale in proportion to cell size), many others increase (superscaling proteins) or decrease (subscaling proteins) in concentration (Chen et al., 2020; Cheng et al., 2021; Claude et al., 2021; Lanz et al., 2022) (Figure 1A). Although a small change in a single protein's concentration may not substantially affect cell physiology, the cumulative effect of thousands of such changes could account for profound changes in cell physiology. For example, recent work shows that excessively large cell size promotes senescence (Demidenko and Blagosklonny, 2008; Neurohr et al., 2019; Lengefeld et al., 2021; Wilson et al., 2021; Crozier et al., 2022; Lanz et al., 2022). Thus, while differential size scaling of protein concentrations likely has important implications for cell physiology, the mechanistic origins of such size scaling remain unknown. In other words, how do increases in cell size result in size-dependent changes of protein concentrations?

One possibility for how cell size drives changes in protein concentrations would be that this is an indirect effect through the cell's protein synthesis rate per unit volume (hereby referred to as growth rate), which decreases in larger cells (Cadart et al., 2018; Neurohr et al., 2019; Liu et al., 2022) (Figure 1B). There seems to be a limit to the size range of effective biosynthesis, with larger cells exhibiting a loss of mitochondrial membrane potential (Miettinen and Björklund, 2016) and reduced proliferative capacity (Demidenko and Blagosklonny, 2008; Cheng et al., 2021; Lengefeld et al., 2021; Wilson et al., 2021; Lanz et al., 2022). As cells get larger, their growth becomes less efficient, and this may affect the concentrations of diverse sets of proteins. Another possibility is that cell size directly affects protein concentrations independent of the cell's growth rate. Because the size-scaling behavior of each individual protein is in part predicted by its synthesis efficiency and degradation rate (Lanz et al., 2022), we hypothesized that the effects of cell size on the proteome may be mediated by the decrease in growth rate observed in larger cells.

Here, we investigate how cell size and growth rate account for measurable differences in protein concentrations. We found that a decrease in global protein synthesis rates induced with the mTOR inhibitor rapamycin remodels the proteome to resemble that found in large cells. However, among rapamycin-treated cells we still observe size-dependent changes to the proteome similar to those found in untreated cells. This indicates that many size-dependent changes to protein concentrations are mediated by growth slowdown in large cells, which can occur independently of mTORC1 signaling. Moreover, we identify specific proteome changes that occur only in large cells or only upon rapamycin treatment. Thus, our work identifies both growth-dependent and size-dependent contributions to the proteome's size-dependence.

Materials and methods

Cell culture

Telomerase-immortalized retinal pigment epithelium cells (*hTERT RPE-1*, here also referred to as RPE-1 for brevity) were obtained from the Cyert laboratory at Stanford. All cells were cultured at 37°C with 5% CO_2 in Dulbecco's modification of Eagle's medium (DMEM) with L-glutamine, 4.5 g/L glucose and sodium pyruvate (Corning), supplemented with 10% heat-inactivated fetal bovine serum (FBS, Corning) and 1% penicillin/streptomycin.

Fluorescence-activated cell sorting

Fluorescence-activated cell sorting (FACS) was used to sort rapamycin-treated RPE-1 cells by their size and cell cycle phase. To do this, the cells were cultured for 48 h in the presence of 20 nM rapamycin, then harvested from dishes by trypsinization, stained with 20 μM Hoechst 33342 DNA dye in PBS for 15 min at 37°C, and then sorted on a BD FACSAria Fusion flow cytometer. Consecutive SSC-A over FSC-A, and FSC-H over FSC-A gates were used to isolate single cells. Then, G1 cells were gated by DNA content (Hoechst 33342 staining). Finally, we collected the 10% smallest and 10% largest cells, as well as another 10% of the cells near the average size, using the gating based on SSC-A signal, as in (Lanz et al., 2022). During sorting, all cell samples and collection tubes were kept at 4°C. To determine the cell size distributions of the collected samples, aliquots were taken from each sorted size bin and measured on a Z2 Coulter counter (Beckman). Sorted cells were then spun down, lysed in RIPA buffer on ice and used for subsequent proteomics analysis.

Protein synthesis rate measurement

To calculate the rate of protein synthesis, RPE-1 cells were pulse-labeled with a puromycin analog O-Propargyl-puromycin (OP-puromycin), which incorporates into nascent polypeptide chains and terminates their translation (OP-puromycin was purchased from ClickChemistryTools, Cat 1407). RPE-1 cells were plated 1 day before labeling and reached ~70% confluence by the time of labeling. Cells were labeled with 20 μM OP-puromycin (final concentration) for 30 min. Then cells were trypsinized, fixed with 3% paraformaldehyde, and permeabilized with 90% ice-cold methanol. Click reaction was performed using

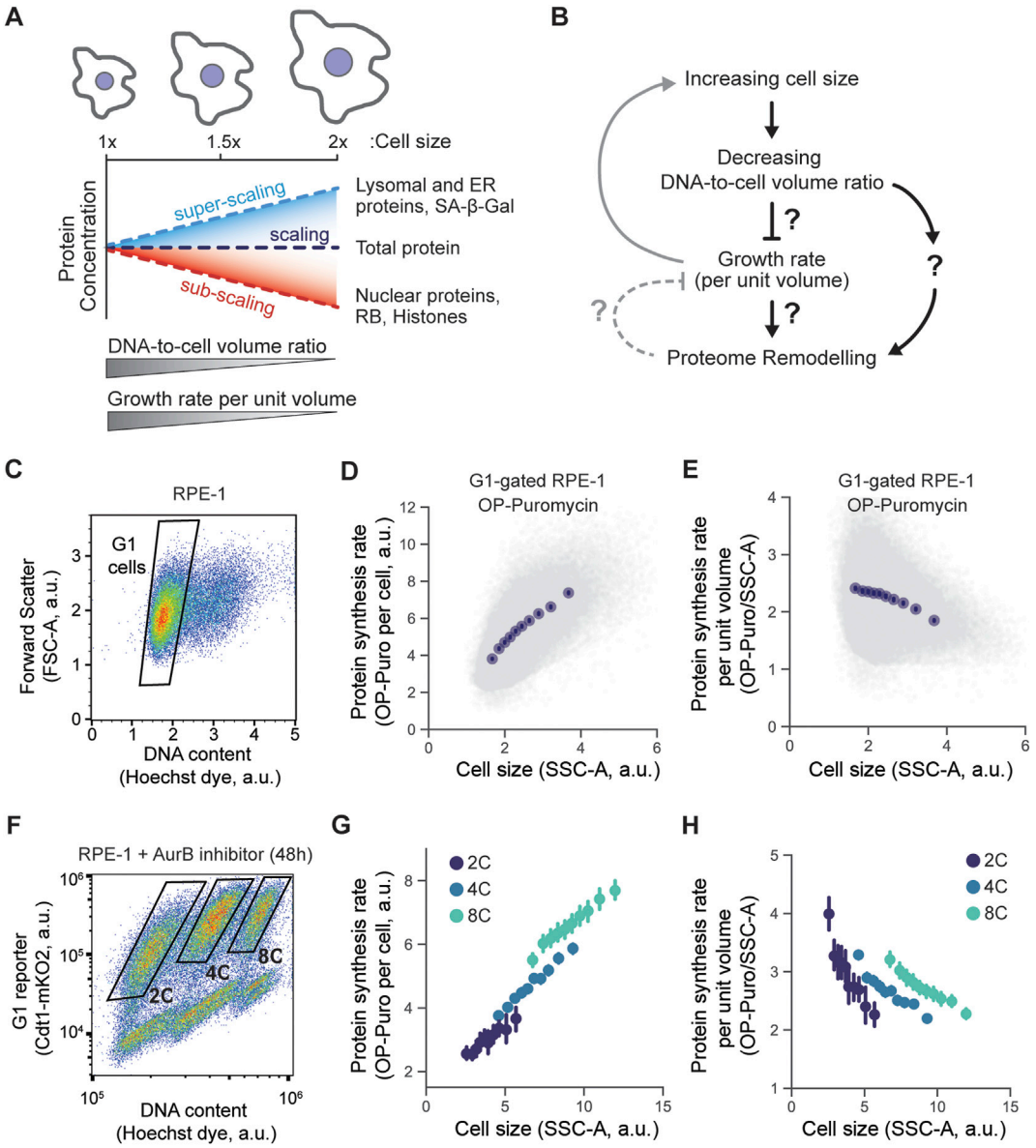

FIGURE 1
The relationship between cell size and growth rate. **(A,B)** Schematics depicting the phenotypes associated with increasing cell size. Increase in cell size leads to the decrease in DNA to cell volume ratio and reduction of cell growth rate per unit volume. Changes in cell size are also accompanied by global proteome remodeling, i.e., some proteins are concentrated while others are diluted as cells grow larger. **(C-E)** Protein synthesis rate measured using OP-puromycin incorporation. After 30 min labeling, OP-puromycin was click-conjugated to a fluorescent azide and measured using flow cytometry. RPE-1 cells were gated for G1 DNA content **(C)**, and the incorporated OP-puromycin amount, which reflects the nascent protein synthesis rate, was plotted against the Side Scatter (SSC-A), a proxy for cell size **(D)**. To represent the synthesis rate per unit volume, the conjugated OP-puromycin fluorescence intensity was divided by the cell volume proxy SSC-A and plotted against the SSC-A **(E)**. **(F-H)** Same experiment performed in **(C–E)** but measuring the protein synthesis rates in populations of RPE-1 cells with different ploidies. To generate tetraploid and octoploid cells, the cytokinesis was partially inhibited in RPE-1 cells using the Aurora kinase B inhibitor barasertib (100 nM, 48 h) (Mu et al., 2020; Lanz et al., 2022), then 2C, 4C, and 8C were then gated using flow cytometry **(F)**. The overall protein synthesis rate **(G)** and the protein synthesis rate per unit volume **(H)** were plotted against the SSC-A, a proxy for cell volume. Each experiment was performed in $n = 3$ biological replicates, and a representative example for each experiment is shown in this Figure. Data in plots **(D)**, **(E)**, **(G)**, and **(H)** were binned by cell size (SSC-A), and means ±95% confidence intervals were plotted for each bin.

the Click-&-Go Cell Reaction Buffer kit (ClickChemistryTools, 1263) with AZDye-488 azide (ClickChemistryTools, 1275). Following the Click-reaction and PBS washes, cells were then stained with DAPI and analyzed using Flow Cytometry. In polyploidy experiments, RPE-1 cells expressing a FUCCI cell cycle reporter (Sakaue-Sawano et al., 2008) were used, which

allowed us to gate out 2C, 4C, and 8C G1-phase cells based on the Cdt1-mKO2 marker fluorescence and the DNA content.

LC-MS/MS sample preparation

RPE-1 cells were lysed in RIPA buffer on ice, and cell lysates were cleared by centrifugation at 15000xg for 30 min at 4°C. Lysates were then denatured in 1% SDS and reduced with 5 mM DTT (10 min at 65°C), then alkylated with 7.5 mM iodoacetamide (15 min at room temperature), and precipitated with three volumes of a solution containing 50% acetone and 50% ethanol (with 0.1% Acetic acid). Proteins were re-solubilized in the buffer containing 2 M urea, 50 mM Tris-HCl, and 150 mM NaCl. Re-solubilized proteins were then digested with TPCK-treated trypsin (50:1) overnight at 37°C. Peptides were desalted using 50 mg Sep-Pak columns. 20 µg of dried peptides were resuspended in 20 µl of 100 mM TEAB for TMT labeling reaction. Our method for TMT labeling was adapted from Zecha et al. (2018) and the Thermo TMT10plex™ Isobaric Label Reagent Set Protocol. 20µg of peptide was labeled using 100 µg of Thermo TMT10plex™ in a reaction volume of 25 µl for 1 h. The labeling reaction was quenched with 8 µL of 0.5% hydroxylamine for 15 min. Labeled peptides were pooled, acidified to a pH of ~2 using drops of 10% TFA, and desalted again with a Sep-Pak 50 mg C18 column as described previously (Lanz et al., 2022).

High-pH reverse phase fractionation

TMT-labeled peptides were fractionated using a Pierce™ High pH Reversed-Phase Peptide Fractionation Kit. Peptides collected from eight fractions were dried and reconstituted in 0.1% formic acid.

LC-MS/MS data acquisition

Fractionated TMT-labeled peptides were analyzed on a Fusion Lumos mass spectrometer (Thermo Fisher Scientific, San Jose, CA) equipped with a Thermo EASY-nLC 1200 LC system (Thermo Fisher Scientific, San Jose, CA). Peptides were separated by capillary reverse phase chromatography on a 25 cm column (75 µm inner diameter, packed with 1.6 µm C18 resin, AUR2-25075C18A, Ionopticks, Victoria Australia). Electrospray Ionization voltage was set to 1550 V. Peptides were resuspended in 10 µl of 0.1% formic acid. 2 µl was introduced into the Fusion Lumos mass spectrometer using a two-step linear gradient with 6–33% buffer B (0.1% (v/v) formic acid in 80% acetonitrile) for 145 min followed by 33–45% buffer B for 15 min at a flow rate of 300 nL/min. Column temperature was maintained at 40°C throughout the procedure. Xcalibur software (Thermo Fisher Scientific) was used for the data acquisition and the instrument was operated in data-dependent mode. Survey scans were acquired in the Orbitrap mass analyzer over the range of 380–1800 m/z with a mass resolution of 70,000 (at m/z 200). Ions were selected for fragmentation from the 10 most abundant ions with a charge state of either 2, 3 or 4 and within an isolation window of 2.0 m/z. Selected ions were fragmented by Higher-energy Collision-induced dissociation (CID) with normalized collision energies of 35%, and the tandem mass spectra were acquired in the Ion trap mass analyzer with a "Rapid" scan rate. Repeated sequencing of peptides was kept to a minimum by dynamic exclusion of the sequenced peptides for 60 seconds. For MS/MS, the AGC target was set to "Standard" and max injection time was set to 35 ms. Relative changes in peptide concentration were determined at the MS3-level by isolating and fragmenting the 5 most dominant MS2 ion peaks using HCD. TMT reporter ions were resolved in the orbitrap at a resolution of 50,000.

Spectral searches

All raw files were searched using the Andromeda engine (Cox et al., 2011) embedded in MaxQuant (v1.6.7.0) (Cox and Mann, 2008). Reporter ion MS3 search was conducted using 10plex TMT isobaric labels. Variable modifications included oxidation (M) and protein N-terminal acetylation. Carbamidomethyl (C) was a fixed modification. The number of modifications per peptide was capped at five. Digestion was set to tryptic (proline-blocked). Database search was conducted using the UniProt proteome - Human_UP000005640_9606. Minimum peptide length was seven amino acids. FDR was determined using a reverse decoy proteome (Elias and Gygi, 2007).

Peptide quantitation

Our TMT analysis pipeline uses the peptide feature information in MaxQuant's "evidence.txt" output file. Each row of the "evidence.txt" file represents an independent MS3-level TMT measurement. Contaminant and decoy peptide identifications were discarded. Peptides without signal in any of the TMT channels were also excluded. TMT peptide measurements were assigned to proteins based on MaxQuant's "Leading razor protein" designation. For each peptide, the fraction of ion intensity in each TMT channel was calculated by dividing the "Reporter ion intensity" column by the sum of all reporter ion intensities. TMT channels were normalized by adjusting the fraction of ion intensity in each channel by the median for all measured peptides. Changes in the concentration of a protein were determined by the median concentration change for all its peptides. Protein Slope values were calculated as described previously (Lanz et al., 2022).

2D annotation enrichment analysis

Annotation enrichment analysis in Figure 6 was performed as described previously (Cox and Mann, 2012). The protein annotation groups were deemed significantly enriched and plotted in Figure 6 if the Benjamini-Hochberg FDR was smaller than 0.02. The position of each annotation group on the plot is determined by the enrichment score (S). The enrichment score is calculated from the rank ordered distribution of Protein Slope and Rapamycin ratio values:

$$S = 2\left(R_{group} - R_{remaing\ proteins}\right)/n$$

Where R_{group} and $R_{remaing\ proteins}$ are the average ranks for the proteins within an annotation group and all remaining proteins in the experiment, respectively, and n is the total number of proteins. Groups of annotations colored in Figure 6 were manually curated (see Table S2).

Principle component analysis

PCA analysis was performed in Python using the sklearn package. A data frame was created that contained individual proteins as rows with columns corresponding to the relative protein concentration in each TMT channel (obtained from the median of all peptide measurements for a given protein). For principal component analyses in Supplementary Table S3, S4, the cell size and rapamycin treatment datasets were both filtered for proteins with at least eight independent peptide measurements to increase quantitative accuracy for individual proteins.

Protein annotations

Protein annotations in Figures 3D,E were based on UniProt columns named "Subcellular location [CC]" or "Protein names". Protein localization was strictly parsed so that each annotated protein belongs to only one of the designated groups. Proteins with 2 or more of the depicted annotations were ignored (except for the "Cytoplasm/Nucleus" category, which required a nuclear and cytoplasmic annotation).

Results

Protein synthesis rate per unit volule decreases with decreasing DNA-to-cell volume ratio

Increasing cell size results in large-scale remodeling of the proteome (Lanz et al., 2022). Larger cells also have a lower protein synthesis rate per unit volume (hereby referred to as growth rate) (Tzur et al., 2009; Cadart et al., 2018; Neurohr et al., 2019; Liu et al., 2022), so that it is unclear if the size-dependent remodeling of the proteome that we have recently reported (Lanz et al., 2022) was due to changing growth rates or due to cell size *per se*. We therefore sought to determine if and how the cell's growth rate contributes to proteome remodeling (Figure 1B).

To assess the effect of a cell's growth rate on its proteome, we first sought to quantitatively examine the size-dependence of the protein synthesis rate in *hTERT*-immortalized RPE-1 cells. We chose to examine RPE-1 cells because they are commonly used in studies of cell growth and division. To measure protein synthesis rates, we pulse-labeled cells with a puromycin analog O-Propargyl-puromycin (OP-puromycin), which incorporates into nascent polypeptide chains and can be subsequently click-conjugated to fluorescent azides. The incorporation of OP-puromycin into a cell, which is a readout for the cell's overall protein synthesis rate, was then measured by flow cytometry. We used the Side Scatter (SSC-A) parameter as a metric of cell size as it has been previously proven to be a good proxy for the cell volume (Tzur et al., 2011; Lanz et al., 2022). We found that the absolute protein synthesis rates were higher in larger G1 cells, consistent with the general increase in cellular biosynthesis in larger cells (Figures 1C,D). However, this increase in protein synthesis rate is outpaced by the increase in cell size so that the growth rate (protein synthesis per unit volume) is lower in larger cells, as observed previously (Cadart et al., 2018; Neurohr et al., 2019; Liu et al., 2022) (Figure 1E).

While we observe a decrease in cell growth rate with increasing cell size among diploid G1 cells, it has been shown recently that even very large cells can maintain efficient growth if the increase in cell size coincides with a proportional increase in ploidy (Mu et al., 2020). Moreover, our own work has demonstrated that size-dependent changes to the proteome are attenuated if cell ploidy is also increased in proportion to the cell volume (Lanz et al., 2022). We therefore hypothesized that the size-dependent decrease in protein synthesis rate per unit volume is determined by the DNA-to-cell volume ratio, rather than by cell size itself. To test this, we induced polyploidization in RPE-1 cells by treating them with Aurora kinase B inhibitor barasertib (as in Mu et al., 2020). We then measured OP-puromycin incorporation rates in diploid (2C), tetraploid (4C), and octoploid (8C) cells (Figures 1F–H). Like before, the protein synthesis rate per unit volume decreased with cell size within each of the 2C, 4C, and 8C populations of cells. However, when we compared similar-sized cells with different ploidies we found that increases in ploidy counteracted the decline in protein synthesis per unit volume in large cells. We therefore conclude that growth rate in cells decreases in proportion to the DNA-to-cell volume ratio.

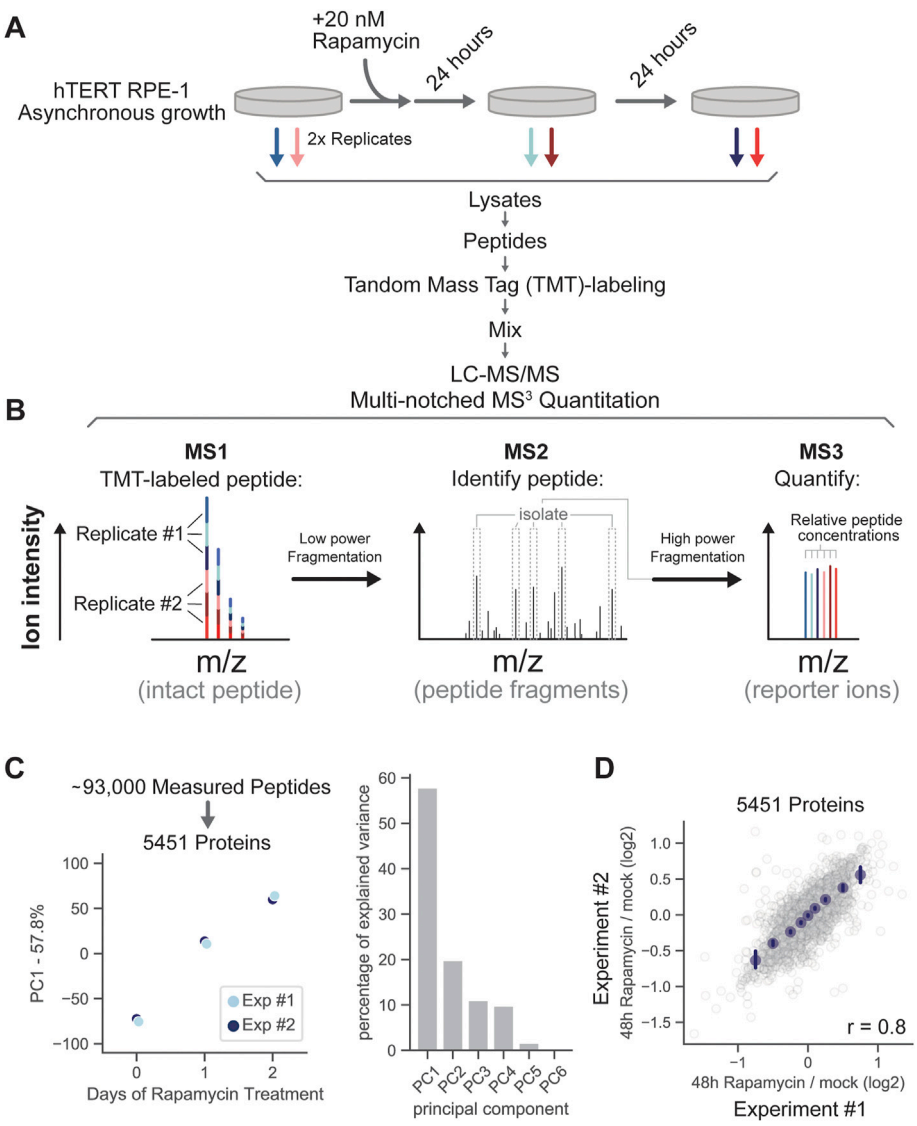

FIGURE 2
Proteome remodeling in response to mTOR inhibition. **(A)** Asynchronously growing RPE-1 cells were treated with 20 nM rapamycin for 24 and 48 h and subjected to multiplexed proteomic analysis. **(B)** Diagram outlining TMT-labeled peptide quantitation *via* multi-notched MS3 mass spectrometry. Peptides labeled with tandem mass tags (TMT) are fragmented with low collisional energy between MS-level 1 and 2 to break peptide bonds. The fragmentation steps are depicted by the two horizontal arrows. Prominent fragment ions in the MS2 spectra are then collected and fragmented with high energy to release the TMT reporter ions (MS3), which are then used to quantify changes in peptide concentration. **(C)** Principal component analysis of the relative changes in protein concentration after 0, 24, and 48 h of rapamycin treatment. **(D)** Correlation of relative protein concentration changes in replicate experiments (48 h of rapamycin treatment/0 h of rapamycin treatment). Binned average values are shown in navy blue dots and the error bars represent 99% confidence intervals. Pearson's r value is displayed on the bottom right of the figure panel. Measurements for each individual protein can be found in Supplementary Table S1.

Partial cell growth inhibition with rapamycin leads to global proteome remodeling

To disentangle the effects of cell size and cell growth rate on the proteome, we treated RPE-1 cells with a saturating dose of the mTOR inhibitor rapamycin for 24 or 48 h (20 nM, see Supplementary Figure S1) and used Tandem Mass Tag (TMT) proteomics to directly compare the relative concentrations of thousands of proteins across these time points (Figure 2A; Supplementary Table S1). Although mTOR inhibition reduces cell growth rate (Fingar et al., 2002; Wang and Proud, 2006; Tee, 2018), it had only a minimal effect on cell size in our experiments (Supplementary Figure S2) because the cells compensated for the

decreased growth rate by reducing the cell division rate (Liu et al., 2018; Tan et al., 2021). We collected and lysed rapamycin-treated and untreated cells for simultaneous proteomic analysis. All proteins from the lysates were then digested into peptides using trypsin. Peptides originating from each of the six cell cultures (three experimental conditions, two biological replicate experiments) were labeled with TMT reagents, mixed together, and quantified together using a tribrid mass spectrometer (Figure 2B). The relative changes in protein concentrations were then inferred from the measurement of their peptides (Lanz et al., 2022).

We measured the relative concentrations of 5,451 proteins in response to rapamycin treatment (Figures 2C,D). Changes to the proteome between untreated cells and 24 h treatment were similar in magnitude to those between 24 and 48 h (Figure 2C), and very few proteins either increased or decreased in concentration by more than 2-fold throughout the time course (Figure 2D). While rapamycin treatment increased the fraction of G1 cells, this increase was slight and therefore unlikely to be responsible for the proteomic changes throughout the time course (Supplementary Figure S3). Replicate experiments were highly correlated (Pearson's r = 0.8) (Figure 2D; Supplementary Table S1).

mTOR inhibition causes proteomic changes similar to those observed in larger cells

To investigate how the cellular growth rate contributes to the proteome changes previously associated with cell size, we compared our new proteome dataset for rapamycin treated cells with our recently published proteomic dataset for G1 cells of different sizes (Lanz et al., 2022). To describe how the concentrations of individual proteins change with cell size, we use the "Protein Slope" value (as described in Lanz et al., 2022) (Figure 3A). In brief, the Protein Slope is calculated from a linear regression between the $\log_2$ of an individual protein's concentration and the $\log_2$ of the cell volume. A Protein Slope value of 0 describes proteins for which concentration does not change with cell volume (scaling); a Protein Slope value of 1 describes proteins for which concentrations increase proportionally to cell volume (superscaling); and protein slope of −1 describes proteins that are perfectly diluted by cell growth so that their concentration is inversely proportional to cell volume (subscaling).

The changes to the proteome in response to increasing cell size were very similar to those measured for rapamycin treatment. The slopes describing concentration size-dependence and the concentration fold-changes induced by mTOR inhibition were highly correlated (Pearson's r = 0.46, $p < 10^{-3}$) (Figure 3B), which is consistent with both large cell size and rapamycin treatment similarly reducing the cell growth rate by about 1.7-fold (Figure 3C). We note that both experiments examining the proteomes of rapamycin-treated and cell-size-sorted cells were performed using RPE-1 cells. The correlation between the datasets increases with a requirement for more peptide measurements per protein (Supplementary Figure S4A). These similarities between size-dependent and rapamycin-induced proteome changes are particularly apparent when proteins are grouped by subcellular localization as was done in Lanz et al. (2022) (Figures 3D,E). Moreover, we have previously shown that cell size-dependent changes to the proteome observed in RPE-1 cells are similar to those taking place in primary human lung fibroblasts (HLFs), which suggests that most of the scaling relationships we are describing are not cell type-dependent (Lanz et al., 2022).

Size-dependent changes to the proteome persist in rapamycin-treated cells

That mTOR inhibition led to protein concentration changes similar to those that took place in larger cells suggested that declining mTOR activity in large cells may be responsible for the size-dependent changes to the proteome that we previously reported (Lanz et al., 2022). To test this, we treated cells with a saturating dose (20 nM) of rapamycin for 48 h, then sorted G1 cells by size into small, medium, and large cell size populations using fluorescence-activated cell sorting (FACS) (Figures 4A,B). We then measured protein concentration changes across the proteome as a function of G1 cell size and calculated Protein Slopes for each protein as described above (Lanz et al., 2022) (Figure 3A). The slopes describing size-dependence of protein concentrations were similar in both untreated and rapamycin-treated cells (Pearson's r = 0.85, $p < 10^{-3}$) (Figure 4C). This experiment suggests that while mTOR is generally an important contributor to proteome remodeling, much of the proteome's size-dependence is independent of mTOR.

To test whether the size-dependent decrease in protein synthesis rate per unit volume is dependent on the mTOR signaling, we performed an OP-puromycin incorporation assay in rapamycin-treated RPE-1 cells. We found that larger rapamycin-treated cells still had a lower protein synthesis rate per unit volume compared to their smaller counterparts (Figure 4D). This indicates that cell size reduces the growth rate per unit volume independently of mTOR signaling (Figure 4E). Alternatively, this could be partially explained by the fact that rapamycin efficiently inhibits only the mTOR complex 1 (mTORC1), while the mTOR complex 2 retains some its activities (Saxton and Sabatini, 2017; Yang et al., 2021).

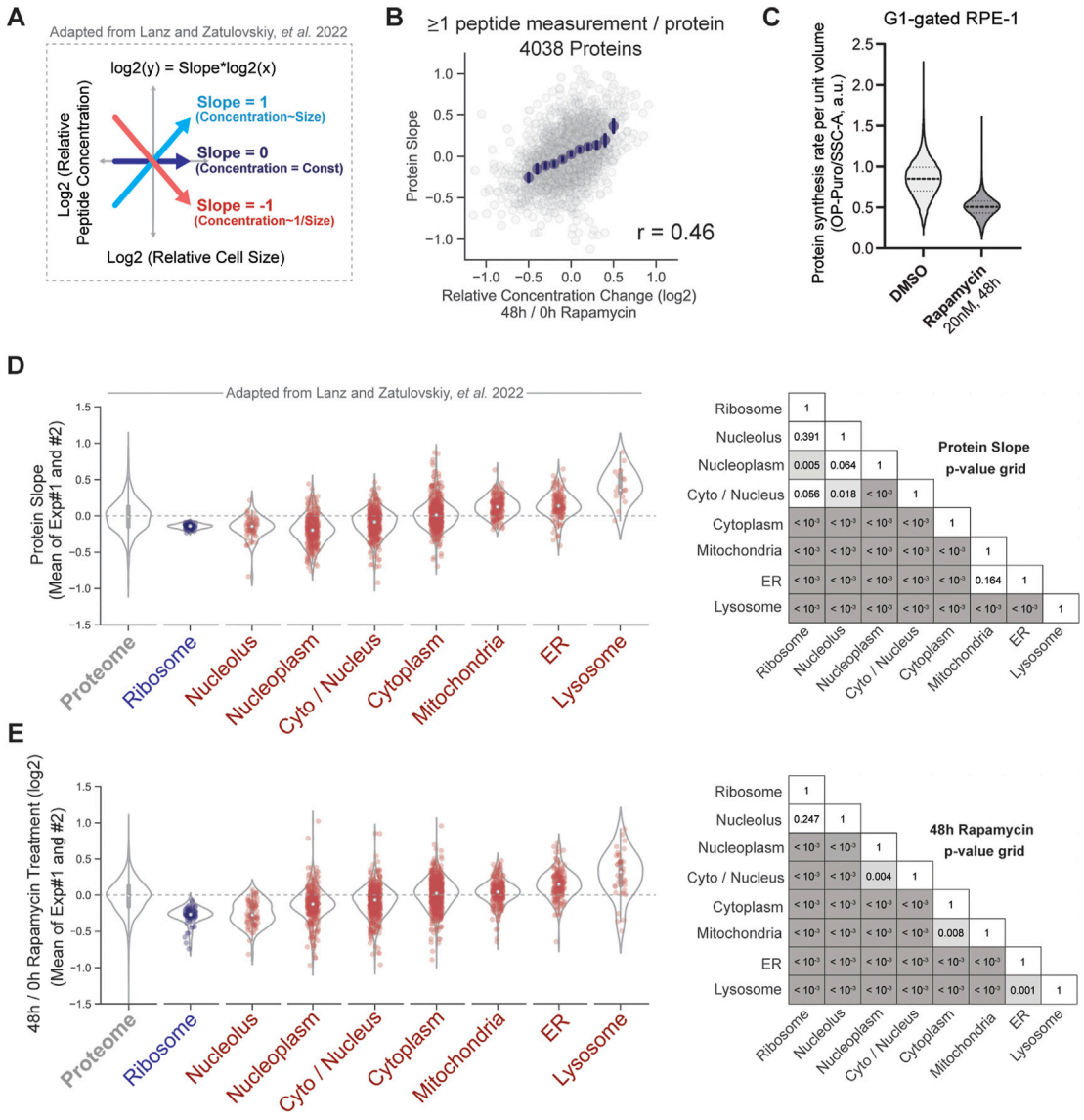

FIGURE 3
Similarities in how the proteome changes with cell size and with mTOR inhibition. **(A)** Protein slope value describes how the concentrations of individual proteins scale with the volume of the cell, as in Lanz et al., 2022. Proteins with a slope of 0 maintain a constant cellular concentration regardless of cell volume. A slope value of 1 corresponds to an increase in protein concentration that is proportional to the increase in volume, and a slope of −1 corresponds to dilution (1/volume). **(B)** Cell size-dependent changes to the proteome strongly correlate with proteome changes induced by 48 h of rapamycin treatment. Binned average values are shown in navy blue dots, and the error bars represent 99% confidence intervals. **(C)** Protein synthesis rate per unit volume measured in rapamycin-treated and untreated G1 RPE-1 cells. OP-puromycin incorporation was used as readout for protein synthesis rate, and Side Scatter as a proxy for cell volume, as in Figure 1. Violin plots show the distribution of OP-puromycin/SSC-A ratios, with dashed lines showing the medians and 25th and 75th percentiles. **(D,E)** Increase in cell size **(D)** and mTOR inhibition **(E)** elicit similar changes in organelle protein content. Violin plots depict the distribution of slope **(D)** or concentration ratio **(E)** values for each group of proteins. Individual proteins in each annotation group are plotted as dots. The *p*-values comparing the slopes **(D)** or ratios **(E)** for every pair of protein groups within the same experiment are visualized in a grid format. Proteins are non-redundantly parsed by subcellular localization using UniProt annotations (see Methods).

Senescence markers differentially respond to mTOR inhibition and increasing cell size

While cellular senescence has long been associated with large cell size, it was thought that this was a consequence of continued growth during the irreversible cell cycle arrest that defines the senescent state (Sharpless and Sherr, 2015; Hernandez-Segura et al., 2018). However, recent work has questioned the direction of causality and established that large cell size is not just a consequence of senescence but also contributes to cell cycle arrest (Demidenko and Blagosklonny, 2008; Neurohr et al., 2019; Lengefeld et al., 2021; Lanz et al., 2022). This

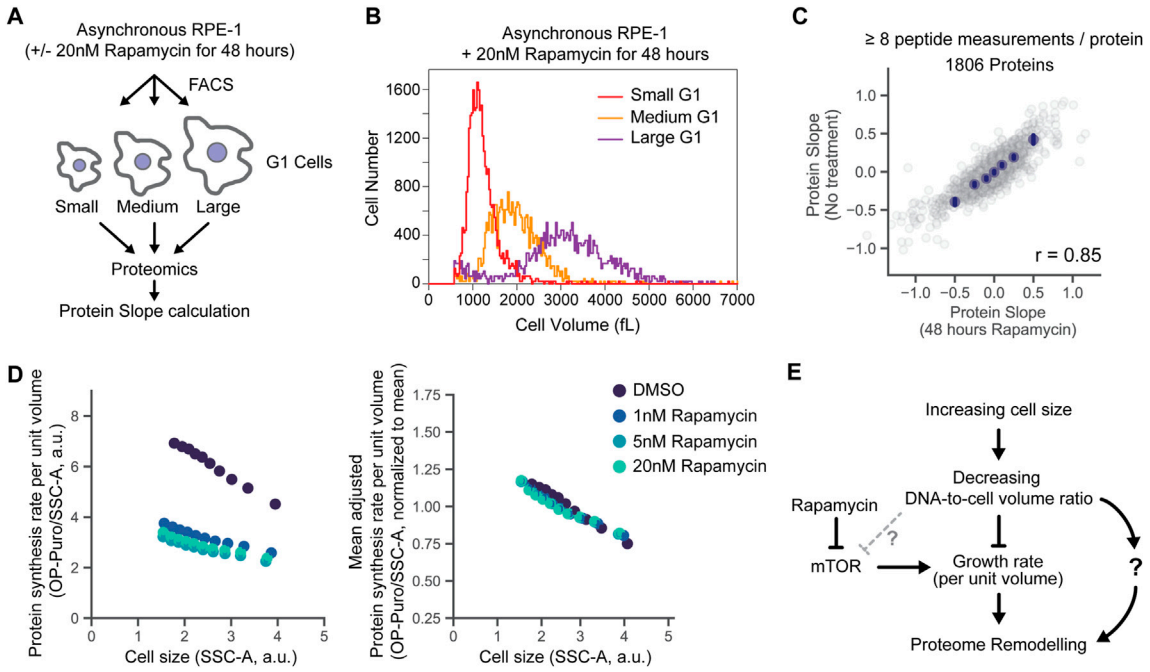

FIGURE 4
Size-dependent changes to the proteome persist in mTOR inhibited cells. **(A)** Measurement of size-dependent changes to the proteome in cells pre-incubated with rapamycin. Protein Slope calculations were determined as described previously, see Figure 3A (Lanz et al., 2022). **(B)** A representative example of cell size distributions for rapamycin-treated (20nM, 48 h) G1-phase RPE-1 cells sorted into three size bins by FACS and measured on a Coulter counter. **(C)** Correspondence of proteome scaling in the presence and absence of a saturating dose of the mTOR inhibitor rapamycin. Binned average values are shown in navy blue dots and the error bars represent 99% confidence intervals. Pearson's correlation coefficient r is shown in the bottom right. **(D)** Size-dependent changes in protein synthesis rate per unit volume in untreated and rapamycin-treated RPE-1 cells measured by OP-puromycin incorporation, as in Figure 1E. Right hand panel shows protein synthesis rates per unit volume normalized to the mean values for each condition for easier side by side comparison. **(E)** Updated schematic depicting the possible relationships between cell size, cell growth, and mTOR and their effect on the proteome.

relationship between cell size and senescence can also be seen in the proteome. In fact, hallmarks of senescence are increasingly pronounced in larger proliferating cells (Lanz et al., 2022), suggesting that cells continually approach a senescent state as they grow larger. Consistent with this view that large size promotes senescence, the inhibition of growth by rapamycin protects cells from becoming excessively large and senescent (Demidenko et al., 2009; Lengefeld et al., 2021; Lanz et al., 2022).

While large cell size is increasingly accepted as promoting senescence, the effect of rapamycin on preventing senescence is questioned by our proteomic analysis. We found that rapamycin treatment remodeled the proteome, making it *more similar* to larger cells approaching the senescent state. Yet, rapamycin treatment clearly promotes the ability of cells to reenter the cell cycle following a long cell cycle arrest (Demidenko and Blagosklonny, 2008; Demidenko et al., 2009; Leontieva and Blagosklonny, 2014; Wilson et al., 2021; Lanz et al., 2022). This paradox raises the question as to how the specific markers of senescence are changing following rapamycin exposure. To address this question, we examined how a set of commonly used markers of senescence responded to increasing cell size and to rapamycin treatment (Hernandez-Segura et al., 2018) (Figure 5). The results were mixed. Markers of senescence whose concentrations increase with cell size (superscaling), including lysosomal proteins, also increased in concentration during rapamycin exposure. The subscaling proliferative marker, Ki67, decreased in response to rapamycin treatment too (Figure 5). However, some subscaling markers, such as HMGB1 and HMGB2, whose concentrations decrease in senescent cells and in large proliferating cells, remained at constant concentration during rapamycin treatment. Thus, some markers of senescence respond to rapamycin while others do not.

Some senescence markers whose changes were specific to increasing cell size, including HMBG1 and HMGB2, were chromatin associated. That these concentrations were diluted in larger cells but not by rapamycin treatment suggests that the expression of these proteins is tied to the DNA-to-cell volume ratio, as has been recently described for histone proteins (Claude et al., 2021; Swaffer et al., 2021). We therefore examined if other chromatin components behaved similarly. Indeed, the concentrations of chromatin proteins, such as histone H4 and HMGB3, which is not linked to senescence, did not change upon rapamycin exposure (Figure 5).

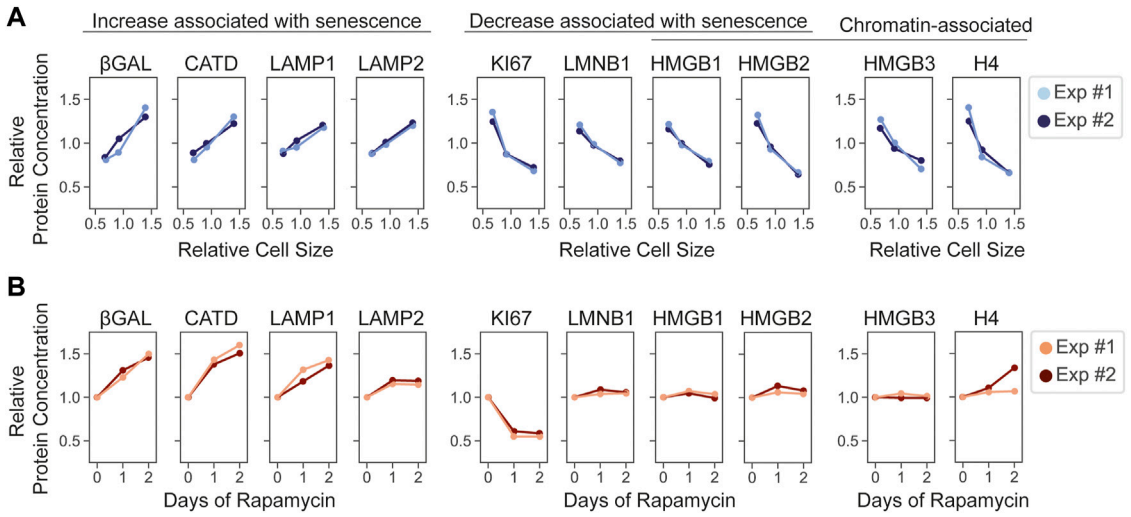

FIGURE 5
The effects of cell size and mTOR inhibition on reporters of cellular senescence. Cell-size-dependent **(A)** and rapamycin-induced **(B)** changes in the relative concentration of the indicated proteins. Two replicate experiments are depicted. For **(B)**, protein concentration is plotted relative to the Day 0 of the rapamycin time course described in Figure 2.

It remains unclear how individual markers of senescence impact the irreversible exit from the cell cycle, which is the determining feature of senescence in proliferating cells (Sharpless and Sherr, 2015). Our analysis suggests that these markers may reflect different aspects of cell physiology such as the growth rate (e.g., β-galactosidase) or the DNA-to-cell volume ratio (e.g., HMGB proteins), both of which correlate with the onset of senescence.

Global analysis of how the proteome changes with cell size and mTOR inhibition

After observing the differential response of senescence markers to cell size and rapamycin, we next investigated the corresponding proteome response. To do so, we used 2D annotation enrichment analysis (Cox and Mann, 2012) to identify groups of significantly changing proteins and to visualize the degree of their change in both experiments (Figure 6A; Supplementary Table S2) (See Methods for a description of Enrichment Score).

As expected, rapamycin treatment resulted in the significant downregulation of proteins involved in translation, including the ribosome itself. While the translation-associated proteins also become less concentrated in large cells, the degree of change is not as great when compared to the direct inhibition of mTOR (Figure 6A, red dots). Conversely, the decrease in the concentration of DNA- and chromatin-associated proteins was more profound in large cells when compared to rapamycin-treated cells (Figure 6A, blue dots), which is consistent with the concentration of chromatin-associated proteins being more dependent on the concentration of DNA than on the relative growth rate (Claude et al., 2021; Swaffer et al., 2021). Unexpectedly, proteins involved in the actin cytoskeletal regulation were specifically upregulated in rapamycin-treated cells (Figure 6A, light blue dots), whereas proteins that regulate ion homeostasis increased with cell size but were largely unaffected by mTOR inhibition (Figure 6A, light green dots).

As a final way to further explore the similarities and differences in the way rapamycin and increasing cell size remodel the proteome, we performed a combined principal component analysis for the relative protein concentration changes in both experiments (Figure 6B and Supplementary Figure S4B). The first principal component (PC1) explained 49% of the variance and correlated directly with both the increasing cell size and the duration (0, 24, 48 h) of rapamycin exposure (Figures 6B,C (left panel); see Supplementary Table S3 for the detailed list of PC1 components). Interestingly, the two experiments were anti-correlated with one another in the second principal component (PC2), which explained ~20% of the variance (Figure 6B). The second principal component is therefore enriched for proteins whose concentrations change in opposite directions in larger cells and in rapamycin-treated cells (Figure 6C (right panel); see Supplementary Table S4 for the detailed list of PC2 components). A gene ontology analysis highlighted mitochondrial components, transmembrane ion transporters, translation machinery, and non-coding RNA-

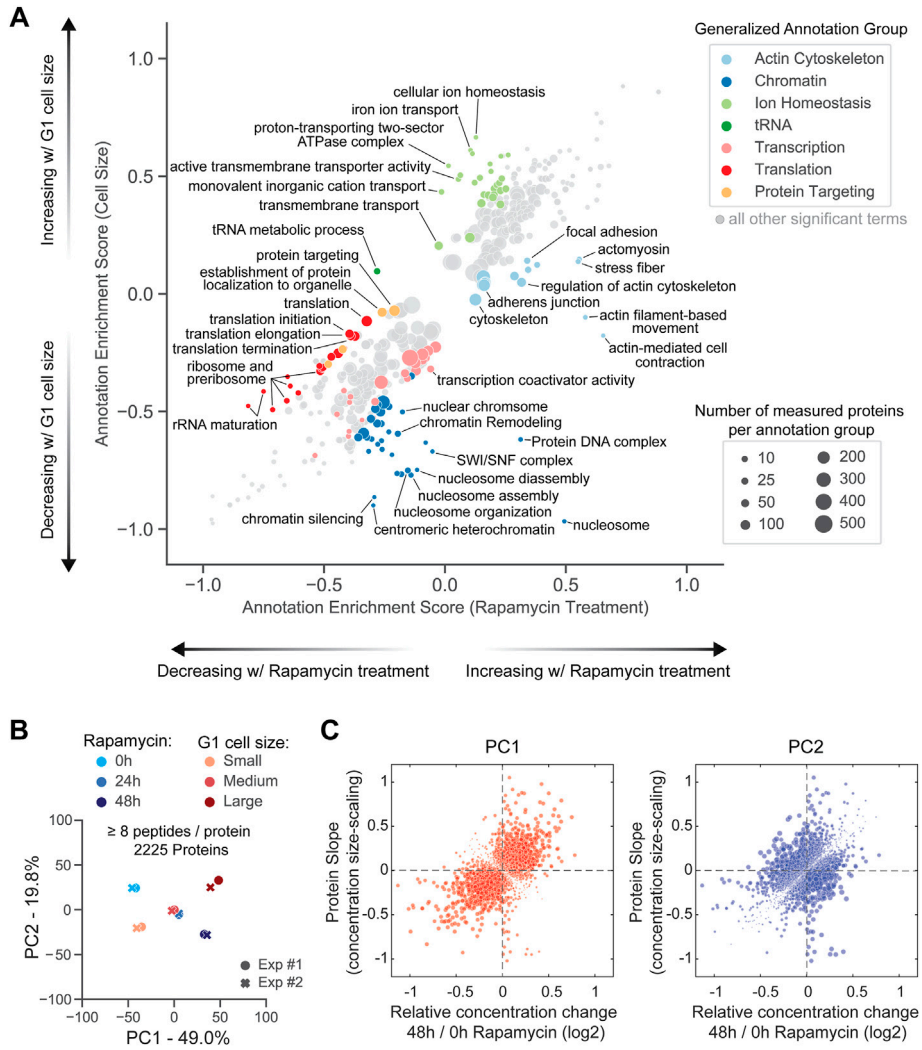

FIGURE 6
Differences in how the proteome changes with cell size and with mTOR inhibition. **(A)** 2D annotation enrichment analysis of cell-size- and rapamycin-induced proteome changes (see Methods and Supplementary Table S2). The protein annotation groups were deemed significantly enriched and displayed on the plot if the Benjamini-Hochberg FDR was smaller than 0.02. Each dot represents a group of annotated proteins. The size of the dot corresponds to the number of proteins within that annotation group, and the dot's position along the axes represents the degree to which those proteins' concentrations are changing in both datasets (based on rank ordering). Protein groups occupying the 4 sectors that deviate most from the x = y diagonal were manually curated into a larger "generalized" annotation group and colored. **(B)** Principal component analysis comparing the relative changes in protein concentrations in G1 cells of different sizes and asynchronously proliferating cells treated with a saturating dose of rapamycin for 48 h. Exp #1 and Exp #2 are two biological replicates for each experiment. **(C)** Comparison of rapamycin-induced protein concentration changes and size-scaling slopes for the components of the first (PC1, left plot) and second (PC2, right plot) principal components, determined in **(B)**. The size of each dot, corresponding to an individual protein, is proportional to the weight coefficient of this protein within the principal component (see Supplementary Tables S3, S4) for annotated lists of PC1 and PC2 components, respectively).

related processes as enriched among these differentially modulated proteins.

Discussion

As cells grow larger, the total protein amount increases in proportion to cell volume so that total protein concentration remains nearly constant (Berenson et al., 2019) (Figure 1A). While it had long been thought that the concentrations of individual gene products also remain constant as cells grow larger (Zhurinsky et al., 2010; Padovan-Merhar et al., 2015), we recently identified size-dependent changes in the concentrations of thousands of individual proteins (Lanz et al., 2022). Because even small changes in the concentration of so many proteins will likely impact cell physiology, this finding

led to the new expectation that cell size should affect many aspects of cell physiology.

While the importance of cell size for cell physiology is becoming increasingly appreciated (Demidenko and Blagosklonny, 2008; Miettinen and Björklund, 2016; Neurohr et al., 2019; Cheng et al., 2021; Lengefeld et al., 2021; Wilson et al., 2021; Lanz et al., 2022), the mechanisms through which cell size affects different processes in the cell are largely unknown. Here, we sought to understand more about the origins of size-dependent changes to protein concentrations across the proteome. Since large cells are characterized by a diminished capacity for biosynthesis per unit volume, i.e., growth rate (Cadart et al., 2018; Neurohr et al., 2019; Liu et al., 2022), it was not clear from our earlier study if size-dependent gene expression simply reflected a cell's declining growth rate or its increasing cell size *per se*. To explore the potentially interdependent effects of cell size and cell growth rate on protein size-scaling, we isolated the effects of decreased cell growth rate by inhibiting mTOR in asynchronously dividing cells. We found that rapamycin-mediated mTOR inhibition, despite modestly reducing the cell size (Supplementary Figure S2), remodeled the proteome in a manner similar to increasing cell size (Lanz et al., 2022) (Figure 3). The striking similarity of these measurements suggests that changes to the proteome in larger cells are associated with the fact that larger cells are unable to scale protein synthesis proportionally with cell volume. It is also possible that cell size drives other changes to the morphology and biomechanical properties of the cell that can also modulate gene expression (Battich et al., 2015).

Since the proteomic changes caused by increasing cell size and by rapamycin treatment were similar, one possibility was that the proteomic effects of cell size were due to its effect on mTOR activity. To test this, we exposed cultured cells to rapamycin for 2 days to inhibit mTOR signaling, and then measured their protein synthesis rates and the proteomes. Although the overall protein synthesis rate decreased about two-fold upon rapamycin treatment, the larger rapamycin-treated cells still had a lower protein synthesis rate per unit volume than their smaller counterparts, and the size-scaling of the proteome was largely unaffected by rapamycin treatment (Figures 4C,D). This result indicates that while we can experimentally decrease the cellular growth rates by treating the cells with rapamycin, it seems unlikely that the naturally occurring size-dependent decrease in cell growth rate and the resulting proteome rearrangements are mediated by the mTORC1 signaling. Instead, they are likely to be mediated by the changes in the DNA-to-cell volume ratio, with DNA becoming a limiting factor in large cells (Figure 4E). However, it remains unclear how changes in the DNA-to-cell volume ratio drive changes to the proteome.

That increasing cell size and rapamycin treatment drive similar changes to the proteome is surprising since large cell size promotes cellular senescence while rapamycin protects against senescence (Demidenko and Blagosklonny, 2008; Demidenko et al., 2009; Leontieva and Blagosklonny, 2014; Lengefeld et al., 2021; Wilson et al., 2021; Crozier et al., 2022; Lanz et al., 2022). Rapamycin treatment results in the upregulation of certain proteins commonly used as senescence markers, including β-galactosidase. This raises the question as to how rapamycin inhibits cell senescence when it drives senescence-like changes to the proteome. One possibility is that the effects of rapamycin in damaged or cell cycle-arrested cells are different from those observed when normally proliferating cells were treated with this drug. In the case of damaged cells, slowing down pathological cell enlargement may have a protective effect that outweighs the senescence-like gene expression changes caused by the slowdown in biosynthesis. A second possibility is that it is the minority of proteins that are expressed differently in large cells and rapamycin treated cells that are the key drivers of cellular senescence (Figure 6 and Supplementary Figure S4B, Supplementary Table S3). Certainly, further investigation of the relationship between the onset of senescence, cell size and growth rate is required for understanding the mechanistic origins of both cellular senescence and differential size scaling across the proteome.

Data availability statement

The datasets presented in this study can be found in online repositories. The mass spectrometry proteomics data have been deposited to the ProteomeXchange Consortium *via* the PRIDE partner repository with the dataset identifier PXD035769.

Author contributions

EZ, ML, and JS conceived and designed this project. EZ, ML, SZ, and FM performed experiments and collected the data. EZ, ML, and SZ analyzed the data. EZ, ML, and JS wrote the manuscript. JE and JS supervised the project.

Funding

This work was supported by the National Institutes of Health (R35 GM134858) and the Chan Zuckerberg Biohub (Investigator Award to JMS and Postdoctoral Fellow Award to ML).

Acknowledgments

We thank Matthew Swaffer for comments on the manuscript and the members of the Skotheim laboratory for discussions and feedback on the work.

Conflict of interest

The authors declare that the research was conducted in the absence of any commercial or financial relationships that could be construed as a potential conflict of interest.

Publisher's note

Supplementary material

The Supplementary Material for this article can be found online at: https://www.frontiersin.org/articles/10.3389/fcell.2022.980721/full#supplementary-material

SUPPLEMENTARY FIGURE S1
The effect of different doses of rapamycin on the proteome after 48 h of treatment. Comparison of PC1 vs. the dose of rapamycin indicates that the mTOR inhibition is saturated at 1 nM. Dashed line corresponds to where the 1 nM dose lies in the first principal component.

SUPPLEMENTARY FIGURE S2
The effect of rapamycin on cell size. **(A)** Cumulative cell volume distributions of asynchronously proliferating RPE-1 cells exposed to 20 nM rapamycin for 0, 24, or 48 h. **(B)** Cumulative cell volume distributions of asynchronously proliferating RPE-1 cells exposed to 0, 1, 5, 20, or 100 nM rapamycin for 48 h. Cell volume distributions were measured using a Coulter counter. The distribution plots show that rapamycin treatment for 48 h at a saturating dose has a minimal effect on cell size.

SUPPLEMENTARY FIGURE S3
Cell cycle phase distributions of RPE-1 cells treated with rapamycin. RPE-1 cells were treated with DMSO (48 h) or rapamycin (24, 48 h), then stained with DNA dye Hoechst 33342 and measured by flow cytometry. 50,000 cells were analyzed and plotted for each condition.

SUPPLEMENTARY FIGURE S4
Comparison of size-dependent and growth-rate-dependent changes to the cell proteome. **(A)** Left plot: Increasing measurement confidence (peptide measurements per protein for both experiments) increases the correlation between the measured size-dependent and rapamycin-dependent changes in protein concentrations (Figure 3B). Right plot: Increasing requirement for measurement confidence decreases the number of proteins considered in the correlation. **(B)** Principal component analysis comparing the relative changes in protein concentrations in G1 cells of different sizes and asynchronously proliferating cells treated with a saturating dose of rapamycin for 48 h. Tables S3 and S4, containing annotated lists of PC1 and PC2 components, respectively, were generated from the principal component analysis with a measurement requirement of at least 8 peptides per protein.

References

Battich, N., Stoeger, T., and Pelkmans, L. (2015). Control of transcript variability in single mammalian cells. *Cell* 163, 1596–1610. doi:10.1016/j.cell.2015.11.018

Berenson, D. F., Zatulovskiy, E., Xie, S., and Skotheim, J. M. (2019). Constitutive expression of a fluorescent protein reports the size of live human cells. *Mol. Biol. Cell* 30, 2985–2995. doi:10.1091/mbc.E19-03-0171

Cadart, C., Monnier, S., Grilli, J., Sáez, P. J., Srivastava, N., Attia, R., et al. (2018). Size control in mammalian cells involves modulation of both growth rate and cell cycle duration. *Nat. Commun.* 9, 3275. doi:10.1038/s41467-018-05393-0

Chen, Y., Zhao, G., Zahumensky, J., Honey, S., and Futcher, B. (2020). Differential scaling of gene expression with cell size may explain size control in budding yeast. *Mol. Cell* 78, 359–370.e6. doi:10.1016/j.molcel.2020.03.012

Cheng, L., Chen, J., Kong, Y., Tan, C., Kafri, R., and Björklund, M. (2021). *Size-scaling promotes senescence-like changes in proteome and organelle content*. BioRxiv. doi:10.1101/2021.08.05.455193

Claude, K.-L., Bureik, D., Chatzitheodoridou, D., Adarska, P., Singh, A., and Schmoller, K. M. (2021). Transcription coordinates histone amounts and genome content. *Nat. Commun.* 12, 4202. doi:10.1038/s41467-021-24451-8

Cox, J., and Mann, M. (2012). 1D and 2D annotation enrichment: A statistical method integrating quantitative proteomics with complementary high-throughput data. *BMC Bioinforma.* 13, S12. doi:10.1186/1471-2105-13-S16-S12

Cox, J., and Mann, M. (2008). MaxQuant enables high peptide identification rates, individualized p.p.b.-range mass accuracies and proteome-wide protein quantification. *Nat. Biotechnol.* 26, 1367–1372. doi:10.1038/nbt.1511

Cox, J., Neuhauser, N., Michalski, A., Scheltema, R. A., Olsen, J. V., and Mann, M. (2011). Andromeda: A peptide search engine integrated into the MaxQuant environment. *J. Proteome Res.* 10, 1794–1805. doi:10.1021/pr101065j

Crozier, L., Foy, R., Mouery, B. L., Whitaker, R. H., Corno, A., Spanos, C., et al. (2022). CDK4/6 inhibitors induce replication stress to cause long-term cell cycle withdrawal. *EMBO J.* 41, e108599. doi:10.15252/embj.2021108599

Demidenko, Z. N., and Blagosklonny, M. V. (2008). Growth stimulation leads to cellular senescence when the cell cycle is blocked. *Cell Cycle* 7, 3355–3361. doi:10.4161/cc.7.21.6919

Demidenko, Z. N., Zubova, S. G., Bukreeva, E. I., Pospelov, V. A., Pospelova, T. V., and Blagosklonny, M. V. (2009). Rapamycin decelerates cellular senescence. *Cell Cycle* 8, 1888–1895. doi:10.4161/cc.8.12.8606

Elias, J. E., and Gygi, S. P. (2007). Target-decoy search strategy for increased confidence in large-scale protein identifications by mass spectrometry. *Nat. Methods* 4, 207–214. doi:10.1038/nmeth1019

Fingar, D. C., Salama, S., Tsou, C., Harlow, E., and Blenis, J. (2002). Mammalian cell size is controlled by mTOR and its downstream targets S6K1 and 4EBP1/eIF4E. *Genes Dev.* 16, 1472–1487. doi:10.1101/gad.995802

Ginzberg, M. B., Chang, N., D'Souza, H., Patel, N., Kafri, R., and Kirschner, M. W. (2018). Cell size sensing in animal cells coordinates anabolic growth rates and cell cycle progression to maintain cell size uniformity. *Elife* 7, e26957. doi:10.7554/eLife.26957

Ginzberg, M. B., Kafri, R., and Kirschner, M. (2015). Cell biology. On being the right (cell) size. *Science* 348, 1245075. doi:10.1126/science.1245075

Hernandez-Segura, A., Nehme, J., and Demaria, M. (2018). Hallmarks of cellular senescence. *Trends Cell Biol.* 28, 436–453. doi:10.1016/j.tcb.2018.02.001

Lanz, M. C., Zatulovskiy, E., Swaffer, M. P., Zhang, L., Ilerten, I., Zhang, S., et al. (2022). Increasing cell size remodels the proteome and promotes senescence. *Mol. Cell.* doi:10.1016/j.molcel.2022.07.017

Lengefeld, J., Cheng, C.-W., Maretich, P., Blair, M., Hagen, H., McReynolds, M. R., et al. (2021). Cell size is a determinant of stem cell potential during aging. *Sci. Adv.* 7, eabk0271. doi:10.1126/sciadv.abk0271

Leontieva, O. V., and Blagosklonny, M. V. (2014). Tumor promoter-induced cellular senescence: Cell cycle arrest followed by geroconversion. *Oncotarget* 5, 12715–12727. doi:10.18632/oncotarget.3011

Li, Q., Rycaj, K., Chen, X., and Tang, D. G. (2015). Cancer stem cells and cell size: A causal link? *Semin. Cancer Biol.* 35, 191–199. doi:10.1016/j.semcancer.2015.07.002

Liu, S., Ginzberg, M. B., Patel, N., Hild, M., Leung, B., Li, Z., et al. (2018). Size uniformity of animal cells is actively maintained by a p38 MAPK-dependent regulation of G1-length. *Elife* 7, e26947. doi:10.7554/eLife.26947

Liu, X., Yan, J., and Kirschner, M. W. (2022). *Beyond G1/S regulation: How cell size homeostasis is tightly controlled throughout the cell cycle?* 2022.02.03.478996. doi:10.1101/2022.02.03.478996

Miettinen, T. P., and Björklund, M. (2016). Cellular allometry of mitochondrial functionality establishes the optimal cell size. *Dev. Cell* 39, 370–382. doi:10.1016/j.devcel.2016.09.004

Mu, L., Kang, J. H., Olcum, S., Payer, K. R., Calistri, N. L., Kimmerling, R. J., et al. (2020). Mass measurements during lymphocytic leukemia cell polyploidization decouple cell cycle- and cell size-dependent growth. *Proc. Natl. Acad. Sci. U. S. A.* 117, 15659–15665. doi:10.1073/pnas.1922197117

Neurohr, G. E., Terry, R. L., Lengefeld, J., Bonney, M., Brittingham, G. P., Moretto, F., et al. (2019). Excessive cell growth causes cytoplasm dilution and contributes to senescence. *Cell* 176, 1083–1097.e18. doi:10.1016/j.cell.2019.01.018

Nguyen, A., Yoshida, M., Goodarzi, H., and Tavazoie, S. F. (2016). Highly variable cancer subpopulations that exhibit enhanced transcriptome variability and metastatic fitness. *Nat. Commun.* 7, 11246. doi:10.1038/ncomms11246

Padovan-Merhar, O., Nair, G. P., Biaesch, A. G., Mayer, A., Scarfone, S., Foley, S. W., et al. (2015). Single mammalian cells compensate for differences in cellular volume and DNA copy number through independent global transcriptional mechanisms. *Mol. Cell* 58, 339–352. doi:10.1016/j.molcel.2015.03.005

Sakaue-Sawano, A., Kurokawa, H., Morimura, T., Hanyu, A., Hama, H., Osawa, H., et al. (2008). Visualizing spatiotemporal dynamics of multicellular cell-cycle progression. *Cell* 132, 487–498. doi:10.1016/j.cell.2007.12.033

Sandlin, C. (2022). *3D characterization of cell size dysregulation in human lung adenocarcinoma reveals a network of fine processes connecting alveolar type 2 cells*.

Saxton, R. A., and Sabatini, D. M. (2017). mTOR signaling in growth, metabolism, and disease. *Cell* 168, 960–976. doi:10.1016/j.cell.2017.02.004

Sharpless, N. E., and Sherr, C. J. (2015). Forging a signature of *in vivo* senescence. *Nat. Rev. Cancer* 15, 397–408. doi:10.1038/nrc3960

Swaffer, M. P., Kim, J., Chandler-Brown, D., Langhinrichs, M., Marinov, G. K., Greenleaf, W. J., et al. (2021). Transcriptional and chromatin-based partitioning mechanisms uncouple protein scaling from cell size. *Mol. Cell* 81, 4861–4875.e7. doi:10.1016/j.molcel.2021.10.007

Tan, C., Ginzberg, M. B., Webster, R., Iyengar, S., Liu, S., Papadopoli, D., et al. (2021). Cell size homeostasis is maintained by CDK4-dependent activation of p38 MAPK. *Dev. Cell* 56, 1756–1769.e7. doi:10.1016/j.devcel.2021.04.030

Tee, A. R. (2018). The target of rapamycin and mechanisms of cell growth. *Int. J. Mol. Sci.* 19, 880. doi:10.3390/ijms19030880

Tzur, A., Kafri, R., LeBleu, V. S., Lahav, G., and Kirschner, M., W. (2009). Cell growth and size homeostasis in proliferating animal cells. *Science* 325, 167–171. doi:10.1126/science.1174294

Tzur, A., Moore, J. K., Jorgensen, P., Shapiro, H. M., and Kirschner, M. W. (2011). Optimizing optical flow cytometry for cell volume-based sorting and analysis. *PLOS ONE* 6, e16053. doi:10.1371/journal.pone.0016053

Wang, X., and Proud, C. G. (2006). The mTOR pathway in the control of protein synthesis. *Physiology* 21, 362–369. doi:10.1152/physiol.00024.2006

Wilson, G. A., Sava, G., Vuina, K., Huard, C., Meneguello, L., Coulombe-Huntington, J., et al. (2021). *Active growth signalling promotes cancer cell sensitivity to the CDK7 inhibitor ICEC0942*. 2021.09.10.459733. doi:10.1101/2021.09.10.459733

Yang, G., Francis, D., Krycer, J. R., Larance, M., Zhang, Z., Novotny, C. J., et al. (2021). Dissecting the biology of mTORC1 beyond rapamycin. *Sci. Signal.* 14, eabe0161. doi:10.1126/scisignal.abe0161

Zatulovskiy, E., and Skotheim, J. M. (2020). On the molecular mechanisms regulating animal cell size homeostasis. *Trends Genet.* 36, 360–372. doi:10.1016/j.tig.2020.01.011

Zatulovskiy, E., Zhang, S., Berenson, D. F., Topacio, B. R., and Skotheim, J. M. (2020). Cell growth dilutes the cell cycle inhibitor Rb to trigger cell division. *Science* 369, 466–471. doi:10.1126/science.aaz6213

Zecha, J., Meng, C., Zolg, D. P., Samaras, P., Wilhelm, M., and Kuster, B. (2018). Peptide level turnover measurements enable the study of proteoform dynamics. *Mol. Cell. Proteomics.* 17, 974–992. doi:10.1074/mcp.RA118.000583

Zhurinsky, J., Leonhard, K., Watt, S., Marguerat, S., Bähler, J., and Nurse, P. (2010). A coordinated global control over cellular transcription. *Curr. Biol.* 20, 2010–2015. doi:10.1016/j.cub.2010.10.002

frontiers | Frontiers in Cell and Developmental Biology

ORIGINAL RESEARCH
published: 07 September 2022
doi: 10.3389/fcell.2022.942374

Expansion of the Inguinal Adipose Tissue Depot Correlates With Systemic Insulin Resistance in C57BL/6J Mice

Claes Fryklund[1]†, Mathis Neuhaus[1†], Björn Morén[1,2], Andrea Borreguero-Muñoz[1], Richard Lundmark[2] and Karin G. Stenkula[1]*

[1]Department of Experimental Medical Science, Lund University, Lund, Sweden, [2]Integrative Medical Biology, Umeå University, Umeå, Sweden

OPEN ACCESS

Edited by:
Evgeny Zatulovskiy,
Stanford University, United States

Reviewed by:
Elma Zaganjor,
Vanderbilt University, United States
Henver Simionato Brunetta,
State University of Campinas, Brazil

***Correspondence:**
Claes Fryklund
claes.fryklund@med.lu.se

†These authors have contributed equally to this work and share first authorship

Specialty section:
This article was submitted to Cell Growth and Division, a section of the journal Frontiers in Cell and Developmental Biology

Received: 12 May 2022
Accepted: 21 June 2022
Published: 07 September 2022

Citation:
Fryklund C, Neuhaus M, Morén B, Borreguero-Muñoz A, Lundmark R and Stenkula KG (2022) Expansion of the Inguinal Adipose Tissue Depot Correlates With Systemic Insulin Resistance in C57BL/6J Mice. Front. Cell Dev. Biol. 10:942374. doi: 10.3389/fcell.2022.942374

To accommodate surplus energy, the adipose tissue expands by increasing adipocyte size (hypertrophy) and number (hyperplasia). The presence of hypertrophic adipocytes is a key characteristic of adipose tissue dysfunction. High-fat diet (HFD) fed C57BL/6J mice are a commonly used model to study obesity and obesity-related complications. In the present study, we have characterized adipose plasticity, at both the cellular and tissue level, by examining the temporal development of systemic insulin resistance and adiposity in response to HFD-feeding for 4, 8, and 12 weeks (4w, 8w, and 12w). Within the same time frame, we examined systemic metabolic flexibility and adipose plasticity when switching from HFD- to chow-diet during the last 2 weeks of diet intervention (referred to as the reverse (REV) group: 4wREV (2w HFD+2w chow), 8wREV (6w HFD+2w chow), 12wREV (10w HFD+2w chow)). In response to HFD-feeding over time, the 12w group had impaired systemic insulin sensitivity compared to both the 4w and 8w groups, accompanied by an increase in hypertrophic inguinal adipocytes and liver triglycerides. After reversing from HFD- to chow-feeding, most parameters were completely restored to chow control levels for 4wREV and 8wREV groups. In contrast, the 12wREV group had a significantly increased number of hypertrophic adipocytes, liver triglycerides accumulation, and impaired systemic insulin sensitivity compared to chow-fed mice. Further, image analysis at the single-cell level revealed a cell-size dependent organization of actin filaments for all feeding conditions. Indeed, the impaired adipocyte size plasticity in the 12wREV group was accompanied by increased actin filamentation and reduced insulin-stimulated glucose uptake compared with chow-fed mice. In summary, these results demonstrate that the C57BL/6J HFD-feeding model has a large capacity to restore adipocyte cell size and systemic insulin sensitivity, and that a metabolic tipping point occurs between 8 and 12w of HFD-feeding where this plasticity deteriorates. We believe these findings provide substantial understanding of C57BL/6J mice as an obesity model, and that an increased pool of hypertrophic ING adipocytes could contribute to aggravated insulin resistance.

Keywords: adipocytes, cell size, obesity, glucose transport, insulin, cytoskeleton

1 INTRODUCTION

Adipose tissue constitutes the main storage site of excess energy in the body and plays an important role in meeting the energy demand of other tissues. Diet-induced obesity mouse models, such as high-fat diet (HFD) feeding in C57BL/6J mice, are a well-established approach to study obesity and obesity-related complications, including systemic and peripheral insulin resistance (Surwit et al., 1998; Winzell and Ahren, 2004; Hansson et al., 2018). Several studies have shown that glucose tolerance in mice is impaired already after a few days of HFD-feeding and further deteriorates over time (Winzell and Ahren, 2004; Williams et al., 2014; Fisher-Wellman et al., 2016; Hansson et al., 2018). The immediate onset of systemic insulin resistance in response to HFD-feeding is linked to impaired hepatic insulin action, which is followed by peripheral insulin resistance in adipose and muscle tissue (Turner et al., 2013). The length of intervention, mouse strain used, and fat content of HFD vary greatly between studies (de Moura e Dias et al., 2021). Nevertheless, an increase in fat mass commonly correlates with impaired systemic glucose tolerance. Both fat mass and insulin resistance are adjustable, and are restored once mice are switched from HFD- to chow-feeding (Hansson et al., 2019). This also applies for long-term HFD-feeding if the period of chow-feeding is prolonged (Parekh et al., 1998). Interestingly, recovery from systemic glucose intolerance occurs before body weight and adiposity are fully reverted, suggesting that excess adipose tissue mass *per se* cannot account for HFD-induced systemic glucose intolerance (Shi et al., 2009; Kowalski et al., 2016). Still, obesity is one of the main risk factors for insulin resistance, type 2 diabetes, and cardiovascular disease, underscoring the importance of adipose tissue in maintaining normal glucose homeostasis.

Adipose tissue expands by increasing the total adipocyte number (hyperplasia) and adipocyte size (hypertrophy). The ability of adipose tissue to expand and reduce its mass in response to energy intake has been exemplified by mathematical modelling, illustrating a cell size-dependent growth/shrinkage rate of adipocytes (Jo et al., 2010). The impact of adipocyte size on cellular function and whole-body glucose homeostasis has been addressed in many studies, where large adipocytes are described as less insulin responsive (Franck et al., 2007; Laurencikiene et al., 2011; Acosta et al., 2016), and as contributing to impaired whole-body glucose homeostasis (Weyer et al., 2000). Indeed, increased adipocyte size has been shown to positively correlate with impaired systemic insulin sensitivity and impaired glucose tolerance in humans, independently of the degree of obesity (Acosta et al., 2016). Interestingly, both expansion and shrinkage of adipocyte size have been shown to correlate with changes in insulin signaling, intracellular actin organization and glucose transport (Hansson et al., 2019), emphasizing that not only cell size but also cellular function is restorable during reduced energy intake.

The aim of the present study was to characterize adipose plasticity in response to energy intake, at both cellular and tissue level, and further address its time dependency.

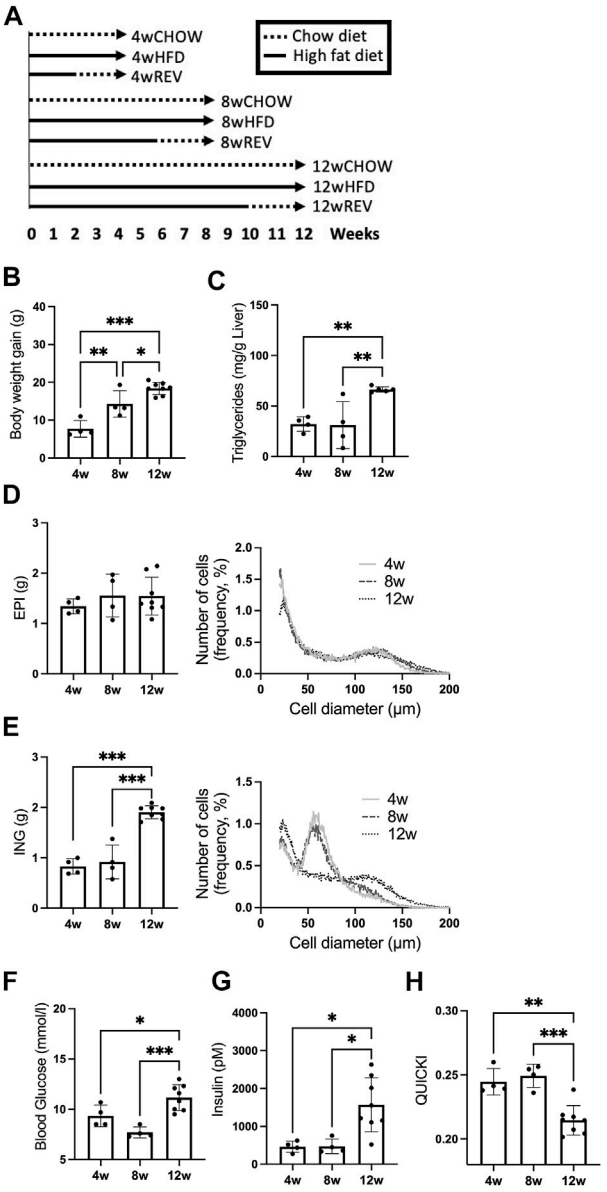

FIGURE 1 | Study outline and time-resolved effect of HFD-feeding on systemic metabolism and adipocyte expansion. **(A)** Study outline for time-resolved analysis of HFD-feeding and reversal from HFD to chow. C57BL/6J mice, 9 weeks old, were subjected to time-resolved analysis for 4, 8, and 12 weeks of diet intervention, each time point including the following three groups: CHOW, chow-feeding throughout the diet intervention, $n = 7$ (4w), $n = 10$ (8w), $n = 9$ (12w). HFD, high-fat diet feeding throughout the diet intervention, $n = 4$ (4w), $n = 4$ (8w), $n = 8$ (12w). REV, high-fat diet feeding, switched to chow-feeding during the final 2 weeks of diet intervention, $n = 11$ (4w), $n = 5$ (8w), $n = 10$ (12w). **(B–H)** Mice subjected to HFD-feeding for 4, 8, or 12 weeks. Final **(B)** body-weight gain and **(C)** liver triglycerides (mg/g liver). Final fat depot weight and adipose cell-size distribution of **(D)** EPI and **(E)** ING. Cell-size distribution graphs display the percentage of cells (y-axis) and cell diameter (µm) (x-axis), 4w and 8w $n = 4$/time point, 12w $n = 5$. **(F)** Blood glucose (mM), **(G)** serum insulin (pM), and corresponding **(H)** QUICKI. Data are displayed as mean ± SD and one-way ANOVA, Tukey's post-hoc test, was used as statistical analysis. Significance was determined according to $^{*}p \leq 0.05$, $^{**}p \leq 0.01$ and $^{***}p \leq 0.001$.

Therefore, we examined the temporal development of systemic insulin resistance and adiposity in response to HFD-feeding (4, 8 and 12 weeks) in C57BL/6J mice. Within the same time frame, we assessed systemic metabolic flexibility (measured as insulin sensitivity and liver triglycerides) and adipose plasticity when switching from HFD- to chow-diet (the last 2 weeks). Additionally, cell-size distribution, actin organization and cellular insulin response were monitored in both subcutaneous (inguinal) and visceral (epididymal) adipocytes to examine depot-specific alterations.

2 MATERIALS AND METHODS

2.1 Antibodies

Antibodies raised against insulin receptor substrate 1 (IRS-1) and acetyl-CoA carboxylase (ACC) were from Cell Signaling Technologies (Danvers, United States). Heat shock protein (HSP) 90 antibody was from BD Transduction Laboratories (Franklin Lakes, United States). Phosphorylated (S3) Cofilin-1 antibody was from Santa Cruz Biotechnology (Dallas, United States). GLUT4 antibody was kindly provided by Sam Cushman (NIH, United States). Phospho-specific antibodies raised against Akt substrate of 160 kDa (AS160) pT642, IRS-1 pY612, and Akt pS473 were from Cell Signaling Technologies (Danvers, United States).

2.2 Animals and Diet Intervention

Male C57BL/6J mice (Taconic, Ry, Denmark) were 9 weeks of age at the start of the diet-intervention. Mice were on a 12-hour light cycle with non-restricted food and water supply and were acclimatized 1 week before start. Mice (n = 4–11/group) were fed either chow (4, 8 or 12 weeks), high-fat diet (HFD) (#D12492, 60E% fat, Research Diets, New Brunswick, United States), or HFD (2, 6, or 10 weeks) followed by 2 weeks of chow [defined as reverse (REV)]. The study outline and feeding groups are shown in **Figure 1A**. Body weight of individual mice was measured weekly. Mice were fasted 2 h prior to termination, where after liver and adipose tissue (epididymal (EPI), inguinal (ING), and retroperitoneal (RETRO) adipose tissue) were excised, weighed, and used for adipose cell size distribution analyses, adipocyte isolation, or directly placed in liquid nitrogen for mRNA extraction. Blood samples were collected from the *vena saphena* to measure blood glucose and serum insulin levels. All animal procedures were approved by the Malmö/Lund Committee for Animal Experiment Ethics, Lund, Sweden.

2.3 Serum Analysis

Fasting (2 h) blood glucose levels were measured (OnetouchUltra2 (Lifescan, Milpitas, CA, United States), and fasting (2 h) insulin levels were assayed in terminal serum samples using ELISA (Mercodia, Uppsala, Sweden). Quantitative insulin sensitivity check index (QUICKI) was calculated as described previously: QUICKI = 1/[log(fasting insulin (μU/ml))+log(fasting glucose (mg/dl))], using the conversion factor 1 μU/mL = 6.00 p.m. for insulin (Katz et al., 2000).

2.4 Liver Triglyceride Content

Liver triglyceride concentration was determined according to Abcam protocol (Ab65336). In short, ~100 mg frozen liver sample was homogenized using a Dounce homogenizer in buffer containing 5% (w/v) NP-40. The homogenized samples were heated at 90°C for 3 min, cooled down for 15 min at room temperature, reheated at 90°C for 3 min, and then centrifuged at 10000xg for 2 min at 20°C. The supernatant was collected and placed in a 96-well plate with triglyceride reagent (Thermo Scientific, #TR22421) for triglyceride concentration determination.

2.5 Isolation of Primary Adipocytes

Primary adipocytes were isolated from adipose tissue depots as described previously (Rodbell, 1964). The cells were suspended in Krebs Ringer Bicarbonate HEPES (KRBH) buffer, pH 7.4, containing 200 nM adenosine and 3% (w/v) Bovine serum albumin (BSA).

2.6 Glucose Uptake

Glucose uptake was determined as previously described (Gliemann et al., 1984). Cells (7.5 % (v/v) suspension) were incubated with or without 10 nM insulin in KRBH buffer in triplicates for 30 min, followed by the addition of D-^{14}C(U)-glucose (2.5 μL/ml, NEC042, Perkin Elmer, Waltham, United States), and an additional 30 min of incubation. The uptake was terminated by centrifugation of 300 μL of each cell suspension in microtubes containing 80 μL dinonylphtalate oil. The cell fraction was collected, dissolved in scintillation fluid (Ultima Gold, Perkin Elmer), and subjected to scintillation counting.

2.7 Western Blot Analysis

For western blot analysis of primary adipocytes, cells were washed twice with KRBH medium without BSA and subsequently lysed in lysis buffer containing 50 mM Tris/HCl pH 7.5, 1 mM EGTA, 1 mM EDTA, 0.27 M sucrose, 1% NP-40, and complete protease- and phosphatase inhibitor cocktail (Roche, Basel, Switzerland). Lysates were centrifuged for 10 min at 13000xg, and protein concentrations were determined using the Bradford method. Samples were subjected to polyacrylamide gel electrophoresis and electro-transfer to nitrocellulose membranes. Membranes were blocked with non-fat dry milk [5% (w/v)] and probed (overnight, 4°C) with the indicated antibodies. Detection was performed using horseradish peroxidase-conjugated secondary antibodies and enhanced chemiluminescence reagent. The signal was visualized using a BioRad Image camera (Biorad, Hercules, United States). All data were normalized using HSP90 as a loading control.

2.8 Adipose Cell-Size Distribution

At termination, adipose tissue samples (8 × 4 mg/sample) were obtained from the inguinal and epididymal depots and fixed

with osmium for adipose cell-size distribution analysis using a Multisizer 4e Coulter Counter (Beckman-Coulter, Brea, United States) as described previously (McLaughlin et al., 2007). For each sample, the size of 6,000 particles was counted and run in technical duplicates. Data were analyzed using linear bins (400 bins, bin-size 0.55 μm) Multisizer3 version 3.53. Large adipocytes in **Figure 4C** and **Supplementary Figure S1** were defined as cells larger than cell diameter corresponding to the 95th percentile from 4wCHOW [>95 (EPI) and >70 (ING) μm diameter]. The total number of adipocytes per fat depot was calculated from the results obtained from the Coulter counter. The average volume (ml) of 6,000 cells and the fat depot weight (g) was converted to total cells per fat depot by using the density $\rho = 0.915$ g/ml as a conversion factor for adipose tissue mass. The total number of large adipocytes was calculated by multiplying the total number of adipocytes by the fraction of cells larger than >95 (EPI) and >70 (ING) μm diameter.

2.9 RT-qPCR Analysis

Adipose tissue samples were obtained from the inguinal and epididymal adipose tissue depots (n = 3–5). Total RNA was extracted from frozen adipose tissue using a guanidinium thiocyanate-phenol-chloroform extraction method (miRNeasy mini kit (Qiagen #74104)). RNA integrity was assessed using NanoDrop. RT-qPCR was performed using the Quantifast SYBR Green RT-PCR kit (Qiagen #204156), and Quantitect primer assays for *18S* (QT02448075), CD44 antigen (*Cd44*; QT00173404), collagen type VI alpha 3 (*Col6a3*; QT00251671) and CD68 (*Cd68*; QT00254051). Primer sequences are considered proprietary information by Qiagen. mRNA expression levels were measured using a StepOnePlus real-time thermal cycler (Applied Biosystems Waltham, United States) and quantitated using the ΔΔCT method as described by Livak and Schmittgen (Livak and Schmittgen, 2001). 18S rRNA was used for normalization throughout. Statistical analysis was carried out on ΔCT values.

2.10 Total Internal Reflection Fluorescence Microscopy

For total internal reflection fluorescence (TIRF) imaging we used a commercial TIRF system based on a Nikon Ti-E eclipse microscope equipped with a 100× Apo TIRF DIC oil immersion objective NA of 1.49 (Nikon Instruments Inc.), an iXon Ultra DU-897 EMCCD camera (Andor Technology Ltd.), and four main laser lines, 405 (Cube, Coherent Inc), 488 (Melles-Griot), 561 (Sapphire, Coherent Inc), and 640 (Cube, Coherent Inc) with corresponding filter sets. Isolated cells were fixed using 4% PFA and labelled with phalloidin using a buffer containing 0.05% saponin for 1 h.

For quantification of the grade of actin polymerization, an ImageJ plugin ridge detection was used to trace actin filaments, detected with phalloidin stain, in TIRF microscopy images. Standard values were used, and the threshold adjusted until most of the visible actin was traced. Images were exported using the "make binary" command. A region of interest (ROI) of roughly ¼ of the cell was chosen and used to obtain consistent data on the grade of polymerization. This ROI was used on all cells to obtain the area of binary cell traces within the threshold.

2.11 Statistical Analysis

Statistical analyses were performed by one-way ANOVA, Tukey's post-hoc test, or Student's t-test, using GraphPad Prism (GraphPad Software Inc.) software. Significance was determined according to $^{*}p \leq 0.05$, $^{**}p \leq 0.01$, $^{***}p \leq 0.001$. All data are displayed as mean ± SD. Linear correlation analysis was performed by calculating Pearson's correlation coefficient (r).

3 RESULTS

3.1 Time-dependent Progression of Systemic Insulin Resistance and Adipose Tissue Expansion During High-Fat Diet-Feeding

To characterize the time-dependent influence of HFD-feeding on insulin sensitivity and adiposity, we examined systemic parameters and adipose tissue expansion using three different feeding periods: 4, 8 and 12 weeks (4w, 8w and 12w) of HFD. We found body-weight gain to be the only parameter that increased significantly between 4w and 8w (**Figure 1B**). Liver triglycerides were significantly increased between 8w and 12w (**Figure 1C**). The epididymal (EPI) fat weight was similar at all time points, while the inguinal (ING) fat expanded and doubled in weight comparing 8w with 12w group (**Figures 1D,E**). Using the Coulter counter, we assessed EPI and ING tissue expansion at a cellular level. The EPI cell-size distribution did not differ over time with HFD-feeding and showed an accumulation of large (>95 μm diameter) adipocytes already after 4w (**Figure 1D**, right panel). The ING depot displayed primarily medium-sized adipocytes (50–70 μm diameter) after 4w and 8w, then accumulated a substantial fraction of large (>70 μm diameter) adipocytes after 12w (**Figure 1E**, right panel). Taking the total adipose tissue depot weight into account, the number of large, hypertrophic adipocytes increased significantly in the ING, but not EPI depot after 12w (**Supplementary Figure S1**). Further, both fasting blood glucose and serum insulin, and thus insulin sensitivity (determined as QUICKI) were impaired in the 12w group compared to 4w and 8w groups (**Figures 1F–H**). Thus, in our cohort of mice, we observed a markedly impaired systemic insulin sensitivity between 8w to 12w of HFD-feeding which coincided with an accumulation of hypertrophic ING adipocytes and increased ING fat mass.

3.2 Time-dependent Changes in Systemic Insulin Sensitivity and Adipose Plasticity When Switching From High-Fat Diet- to Chow-Feeding

Next, we wanted to address the capacity of systemic insulin sensitivity and adiposity to recuperate after HFD-feeding. Therefore, groups of mice were switched from HFD to chow-

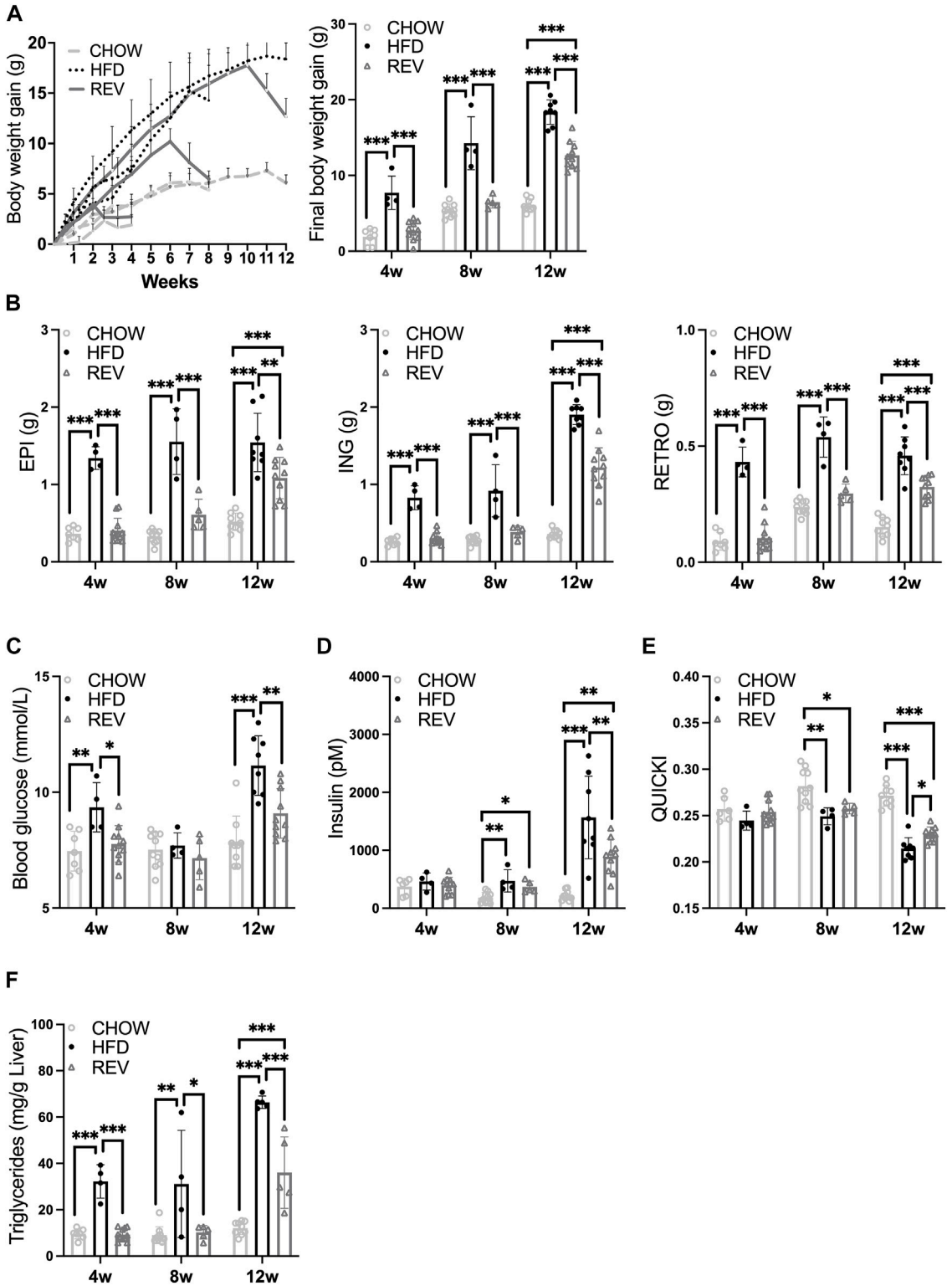

FIGURE 2 | Time-resolved analysis of systemic metabolic response and adipose tissue plasticity after switching from HFD to chow. Mice were subjected to diet intervention for 4, 8 or 12 weeks, each timepoint containing the following three groups: CHOW, HFD and REV (see **Figure 1** for study outline). Note, the same data from HFD are displayed in **Figure 1**. **(A)** Body-weight gain was monitored weekly (left panel) and at termination (right panel). **(B)** Final fat depot weight (EPI, ING, and RETRO). **(C)** Blood glucose (mM), **(D)** serum insulin (pM) and corresponding **(E)** QUICKI. **(F)** Liver triglycerides (mg/g liver). Data are displayed as mean±SD and one-way ANOVA, Tukey's post-hoc test, was used as statistical analysis of differences between CHOW, HFD and REV for each time point (4, 8, and 12w). Significance was determined according to $*p \leq 0.05$, $**p \leq 0.01$ and $***p \leq 0.001$.

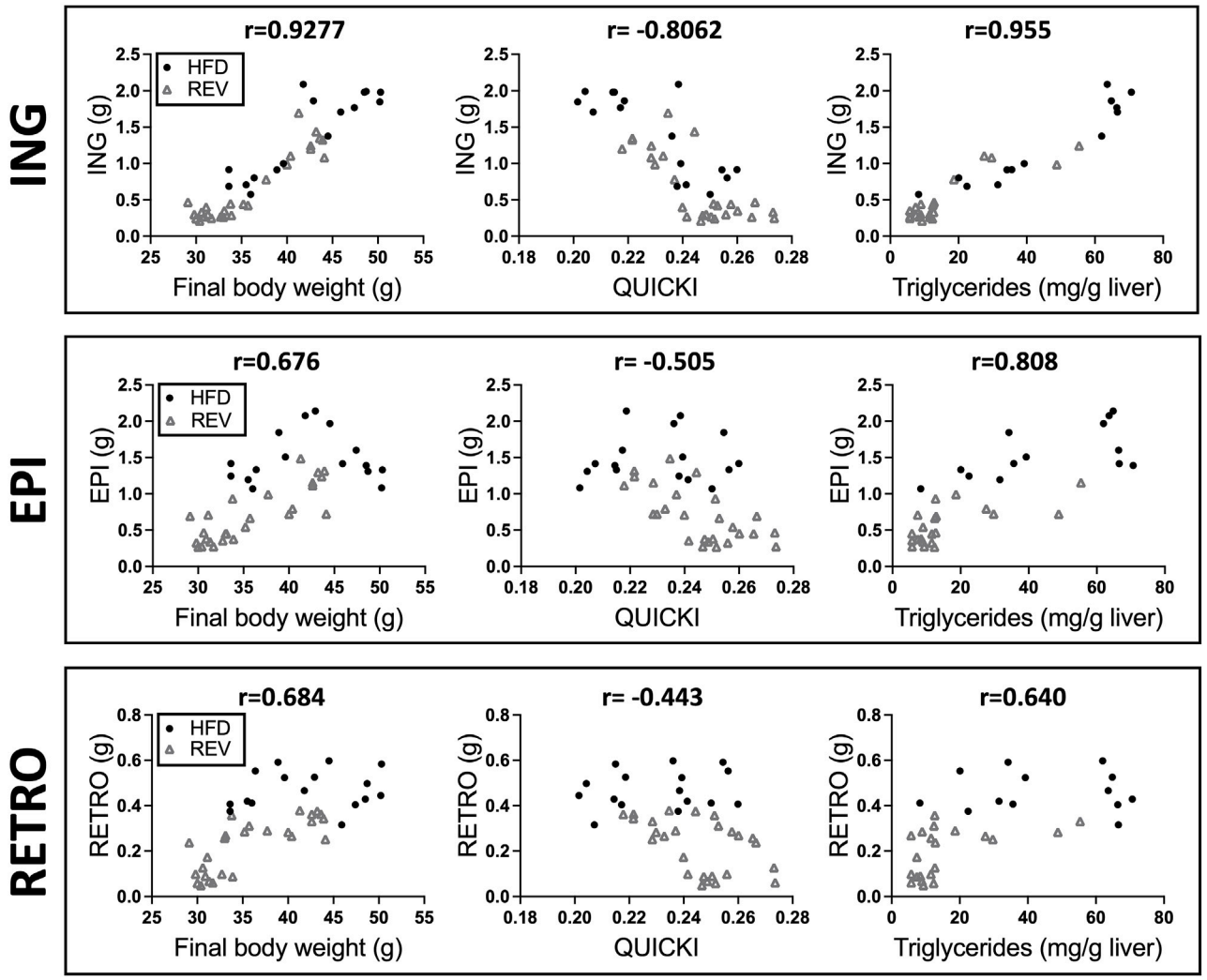

FIGURE 3 | Correlation analysis between different fat depots and body weight, QUICKI or liver triglycerides. Scatter plot displaying correlation between fat depot mass (g) and final body weight, QUICKI or liver triglycerides, (ING, top panel), (EPI, middle panel), and (RETRO, bottom panel). Pearson correlation with corresponding r value is displayed in each graph. The data are obtained from HFD (black dot) and REV (gray square) groups from 4, 8 and 12w of intervention (see study outline **Figure 1**).

feeding for the last 2 weeks of intervention, referred to as reverse (REV): 4wREV (2w HFD+2w chow), 8wREV (6w HFD+2w chow), 12wREV (10w HFD+2w chow). Mice fed chow only (CHOW) for 4/8/12 weeks were included as a control (see study outline in **Figure 1A**).

Body-weight gain and fat depot weights were fully reverted to CHOW levels for 4wREV and 8wREV, while the 12wREV had significantly increased body-weight gain and fat depot weights compared to CHOW (**Figures 2A,B**). Fasting blood glucose levels were not significantly different at any time point comparing REV to CHOW, while serum insulin was increased for both 8wREV and 12wREV compared to CHOW (**Figures 2C,D**). The 8wREV and 12wREV also displayed impaired insulin sensitivity, measured as QUICKI, compared to CHOW (**Figure 2E**). Still, insulin sensitivity was significantly lower for both the 12wHFD and 12wREV in comparison to 8wHFD, indicating that insulin sensitivity progressively worsened during this feeding period (from 8 to 10 weeks of HFD) and that reversing the diet at this time point only partially improved insulin sensitivity (QUICKI: 0.215 for 12wHFD, 0.23 for 12wREV and 0.25 for 8wHFD) (**Figure 2E**). Liver triglycerides were reverted to CHOW for 4wREV and 8wREV but not for the 12wREV group, which had levels comparable to the 4wHFD and 8wHFD (**Figure 2F**). Interestingly, ING adipose tissue mass correlated with body weight, liver triglycerides and QUICKI to a higher degree than both EPI and retroperitoneal (RETRO) adipose tissue mass (**Figure 3**).

Changes in adipose tissue mass involve remodeling of the extracellular matrix (Sun et al., 2013) and an increased infiltration of immune cells, which is considered to contribute to systemic insulin resistance (Kodama et al., 2012). Therefore, we examined the mRNA expression of collagen, type VI, alpha 3 (*Col6a3)*, encoding one of the most abundant collagens in the adipose tissue matrix, as well as cell-surface glycoprotein CD44, known to

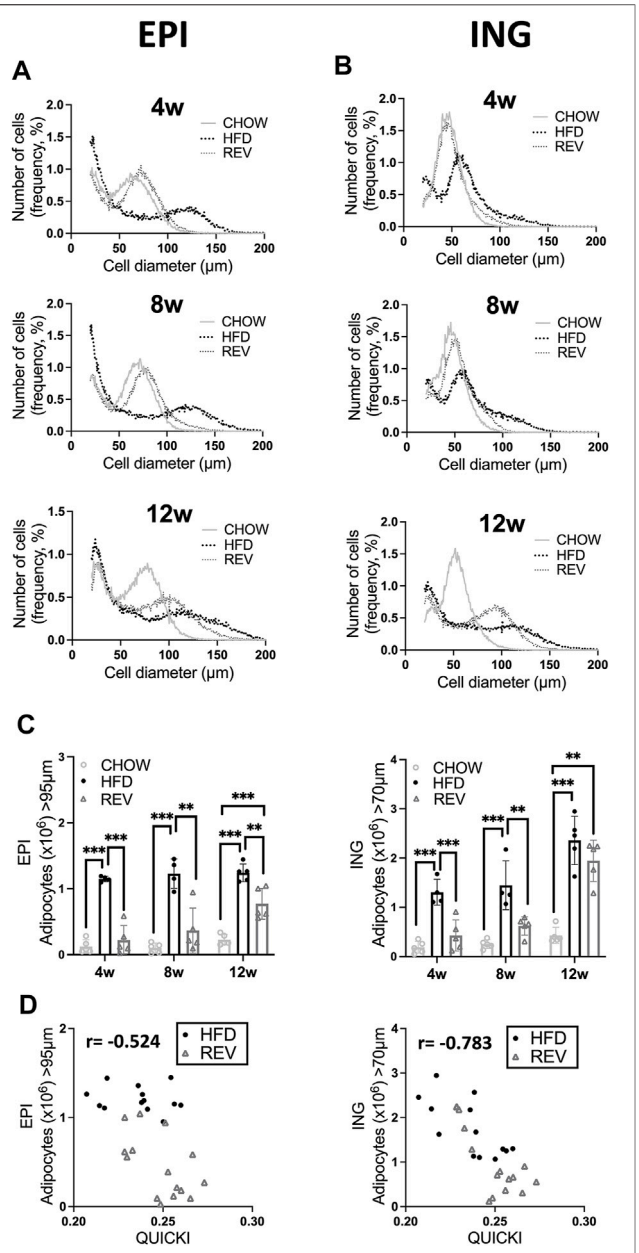

FIGURE 4 | Time resolved analysis of cell-size distribution from epididymal and inguinal adipose tissue. Mice were subjected to diet intervention for 4, 8 or 12 weeks, each timepoint containing the following three groups: CHOW, HFD and REV (see **Figure 1** for study outline). Adipocyte cell-size distribution of **(A)** EPI and **(B)** ING fat depot, obtained from Coulter counter analysis, displaying CHOW, HFD and REV groups from 4 weeks (top panel), 8 weeks (middle panel) and 12 weeks (bottom panel). Cell-size distribution graphs display the percentage of cells (y-axis) and cell diameter (μm) (x-axis), n = 4–5/condition and time point. **(C)** Total number of hypertrophic adipocytes (EPI > 95 μm, ING > 70 μm, definition and calculation see method **Section 2.8**) in EPI (left) and ING (right) adipose tissue. **(D)** Scatter plot displaying correlation between number of hypertrophic adipocytes (defined as above) and insulin sensitivity (QUICKI) in EPI (left panel) and ING (right panel) fat depot, with corresponding r value from Pearson correlation. Data are displayed as mean ± SD. One-way ANOVA, Tukey's post-hoc test, was used as statistical analysis of differences between CHOW, HFD and REV for each time point (4, 8, and 12w). Significance was determined according to $^{*}p \leq 0.05$, $^{**}p \leq 0.01$ and $^{***}p \leq 0.001$.

induce immune cell infiltration and to correlate with insulin resistance (Kodama et al., 2012), and also *CD68*, a macrophage marker. In the EPI adipose tissue depot, we found increased mRNA levels of *Col6a3, CD44* and *CD68* in the 12wHFD group compared to CHOW, which stayed elevated also in the 12wREV group (**Supplementary Figure S2A**). In contrast, no changes in these targets were observed in the ING adipose tissue depot (**Supplementary Figure S2A**). Notably, in chow-fed mice, the expression levels of *Col6a3, CD44* and *CD68* were relatively higher in ING compared with EPI (**Supplementary Figure S2A**). We also examined the temporal (4w, 8w and 12w) expression of *CD44* in the RETRO fat depot. There was an increase in *CD44* expression in response to HFD, which was reverted to chow level for the 4w and 8w REV group, but not for the 12w REV group (**Supplementary Figure S2B**).

Together, while the metabolic flexibility in the 8wREV group was similar to the 4wREV group, a much more blunted recovery of adiposity and insulin sensitivity was observed in the 12wREV group. The data also suggest that the mass of the ING depot is more strongly correlated with systemic insulin sensitivity than the EPI and RETRO depots during prolonged HFD-feeding.

3.3 Cell-Size Distribution and Cellular Actin Density When Switching From High-Fat Diet- to Chow-Feeding

To examine how changes in fat depot mass affected adipocyte size, we assessed cell-size distribution in the EPI and ING fat depots. The accumulation of large, hypertrophic adipocytes [>95 (EPI) and >70 (ING) μm diameter] observed after 4w and 8w of HFD-feeding was reduced to similar levels as observed in CHOW in the REV groups for both fat depots (**Figures 4A–C**). In contrast, the 12wREV group had a cell-size distribution resembling that observed with 12wHFD rather than CHOW (**Figures 4A,B** bottom panel). Quantification of the total number of hypertrophic adipocytes at the tissue level in the EPI depot (**Figure 4C**) revealed a significant decrease in the number of hypertrophic adipocytes when reversing the diet, independent of the duration of HFD-feeding. However, the ING depot had similar number of hypertrophic adipocytes even after reversing the diet at the 12 weeks' time point (**Figure 4C**). Further, the number of hypertrophic ING adipocytes displayed a strong correlation with systemic insulin sensitivity (measured as QUICKI), which was not observed in hypertrophic EPI adipocytes (**Figure 4D**). These results suggest that the hypertrophic inguinal adipocytes that develop after prolonged HFD-feeding might negatively influence systemic metabolism.

Further, we have previously shown that adipose cell size correlates positively with the density of filamentous actin and that both cell size and density of filamentous actin are reversible when switching from HFD- to chow-feeding during short feeding intervention (corresponding to the 4 weeks feeding used herein) (Hansson et al., 2019). To investigate if adipose plasticity was also sustained after prolonged HFD-feeding, we used TIRF microscopy and phalloidin labelling to detect filamentous actin in single adipocytes isolated from CHOW, HFD, and REV

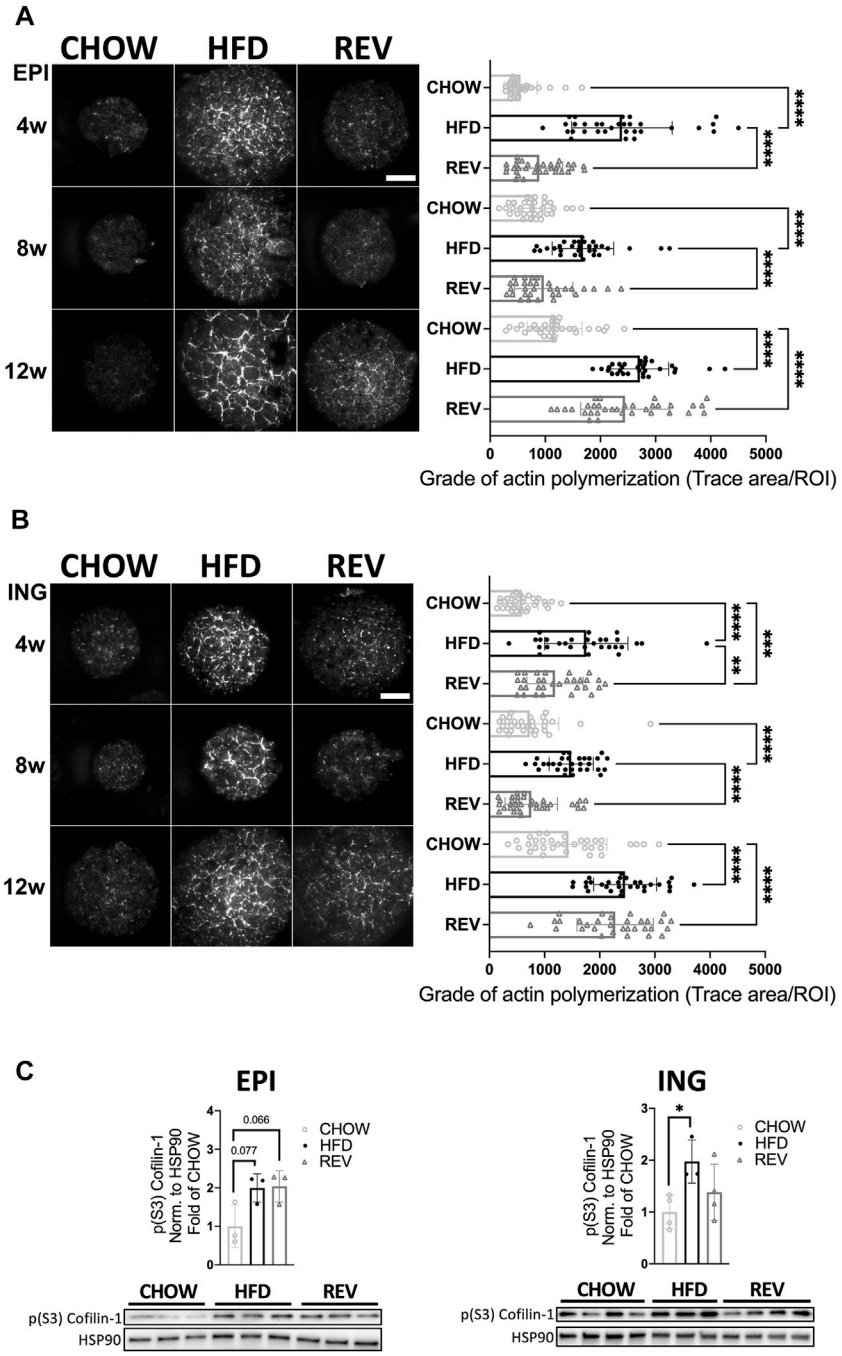

FIGURE 5 | Time resolved analysis of actin polymerization in primary adipocytes following diet intervention. TIRF microscopy of primary adipocytes isolated from EPI **(A)** and ING **(B)** fat depot stained with phalloidin to detect filamentous actin. Representative images (left panel) from CHOW, HFD and REV during 4w, 8w, or 12w of diet intervention, and corresponding quantification (right panel) for each time point, $n = 29–35$ cells/condition. **(C)** Western blot analysis and corresponding quantification of phosphorylated (S3) Cofilin-1 in lysates from EPI (left panel) and ING (right panel) adipocytes after 12w of diet. Values are expressed as fold of CHOW and HSP90 was used as a loading control. Data are displayed as mean±SD. One-way ANOVA, Tukey's post-hoc test, was used as statistical analysis of differences between CHOW, HFD and REV for each time point (4, 8, and 12w). Significance was determined according to $^{*}p \leq 0.05$, $^{**}p \leq 0.01$ and $^{***}p \leq 0.001$.

groups. Indeed, the density of polymerized actin was significantly increased in HFD compared to CHOW at all time points tested, in both EPI and ING adipocytes (**Figures 5A,B**). At the 4w and 8w time points, the level of filamentous actin was significantly increased in HFD compared to REV, while they displayed similar levels comparing 12wREV to 12wHFD. By western blot analysis,

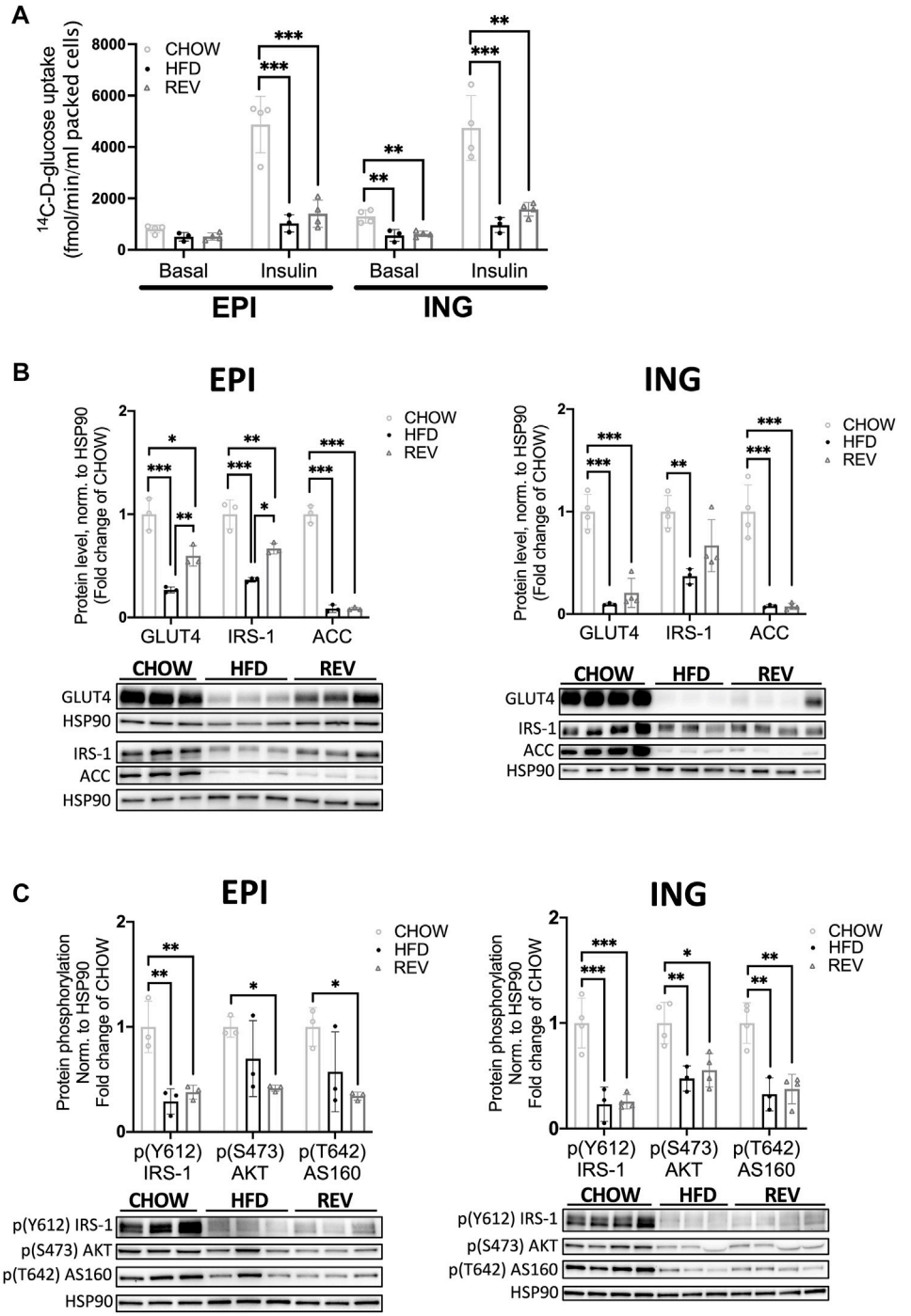

FIGURE 6 | Insulin-stimulated glucose uptake in primary adipocytes following 12 weeks of diet intervention. **(A)** Non (basal) and insulin stimulated glucose uptake in primary adipocytes isolated from EPI or ING fat depot following 12-week diet-intervention of CHOW, HFD and REV. In short, adipocytes were isolated and then non-stimulated (basal) or stimulated with insulin (10 nM) for 30 min before adding a glucose-tracer for additional 30 min incubation. Glucose uptake is expressed as femtomole glucose uptake per min per ml packed cells. n = 3–4/condition. **(B)** Western blot analysis from 12-week diet-intervention and corresponding quantification of GLUT4, IRS-1 and ACC from isolated EPI (left panel) and ING (right panel) adipocytes. **(C)** Western blot analysis from 12-week diet-intervention and corresponding quantification of phosphorylation of IRS-1 (Y612), AKT (S473) and AS160 (T642) from non-stimulated (basal) EPI (left panel) and ING (right panel) adipocytes. Values are expressed as fold of CHOW and HSP90 was used as a loading control. Data are displayed as mean±SD and one-way ANOVA, Tukey's post-hoc test, was used as statistical analysis. Significance was determined according to $^{*}p \leq 0.05$, $^{**}p \leq 0.01$ and $^{***}p \leq 0.001$.

we found a trend ($p = 0.07$) towards increased levels (~2-fold) of phosphorylated Cofilin-1 (pS3), known to regulate the severing of polymeric actin, in the EPI 12wHFD and 12wREV groups compared with CHOW, which supports the increased actin density observed by microscopy (**Figure 5C**).

Together, these data illustrate that the plasticity in adipocyte size mirrors adaptations in adipose tissue mass, and that actin is structured in a cell-size dependent fashion independent of the feeding regime.

3.4 Cellular Insulin Response After Diet Reversal From High-Fat Diet- to Chow-Feeding

Next, we set out to examine whether the impaired systemic insulin sensitivity after 12w of HFD and the blunted recovery in the 12wREV group were also seen at the cellular level, by using a glucose tracer assay in isolated adipocytes. Both EPI and ING adipocytes from HFD-fed mice displayed a sharp drop (~80%) in insulin-stimulated glucose uptake compared to CHOW (**Figure 6A**). Adipocytes obtained from the REV group had significantly lower insulin-stimulated uptake compared to CHOW, even though ING adipocytes showed a trend towards improved insulin sensitivity comparing HFD to REV ($p = 0.089$) (**Figure 6A**). Notably, ING adipocytes from both HFD and REV had significantly lowered non-stimulated (Basal) uptake compared with CHOW (**Figure 6A**).

Further, the protein levels of insulin receptor substrate 1 (IRS-1), the intermediate downstream target of the insulin receptor, and the insulin-regulated glucose transporter (GLUT)4 protein were clearly decreased in response to HFD in both EPI and ING adipocytes (**Figure 6B**). Both IRS-1 and GLUT4 were modestly but significantly increased in the REV group in EPI but not ING adipocytes (**Figure 6B**). Further, the expression of Acetyl Co-A carboxylase (ACC), a protein that catalyzes *de novo* lipid synthesis, was suppressed by ~90% with HFD. ACC levels remained low also in the REV group in both fat depots (**Figure 6B**). Further, the temporal expression of IRS-1, GLUT4 and ACC in EPI adipocytes revealed that 12wREV, but not 4wREV or 8wREV, had significant reduced protein levels compared to CHOW (**Supplementary Figure 5**). Thus, the poor cellular recovery of insulin responsiveness after reversing the diet in the 12 week group could reflect the presence of a high fraction of hypertrophic adipocytes (shown in **Figures 4A,B**). We also examined the insulin signaling pathway and found that the phosphorylation of IRS-1 (Y612), AKT (S473) and AS160 (T642) were significantly reduced in the 12w REV group compared to chow in non-stimulated (basal) EPI and ING adipocytes (**Figure 6C**), consistent with the reduced basal glucose uptake that we observed.

4 DISCUSSION

In the current study, we report several novel observations that illustrate the capacity of C57BL/6J mice to adjust adiposity and insulin sensitivity in response to diet, and how this capacity changes over time. After 12 weeks of HFD-feeding, we observed a significant increase in liver triglyceride levels, reduced insulin sensitivity, a substantial expansion of the ING fat depot and an accumulation of hypertrophic ING adipocytes. The negative correlation between ING fat mass and insulin sensitivity was somewhat unexpected as the ability to expand subcutaneous fat in humans has been suggested to be protective against metabolic diseases (Tchernof and Despres, 2013). Fat depot transplantation and fat removal studies in mice also support that the ING fat depot is protective against metabolic diseases while the opposite is true for the EPI fat depot (Hocking et al., 2008; Foster et al., 2013; Franczyk et al., 2021). Most transplantation studies are conducted using ING fat that, based on length of HFD-feeding, does not exhibit very large ING hypertrophic adipocytes at the time of transplant. Therefore, there is a possibility that contrary results would be found if these studies were to be repeated using ING fat that contained very large hypertrophic adipocytes. Further, the increased lipid deposits in liver and ING depot reported herein may be related to a restricted capacity of the EPI depot to expand further. Such an impairment has previously been linked to adipose tissue inflammation, adipocyte apoptosis, hepatic steatosis and deteriorating systemic insulin sensitivity (Strissel et al., 2007). We found an increased mRNA expression of *CD68* and *CD44* in the EPI, but not ING fat depot, following 12 weeks of HFD-feeding, which supports that inflammation primarily occurs in the EPI depot. Notably, both *CD44* and *CD68* maintained upregulated also in the REV group suggesting that inflammation is not reversible at this timepoint. Our finding that the EPI depot reached a maximal expansion at body weights around 40–45 g and thereafter declined despite further increase in body weight, is consistent with findings in previous studies (see **Supplementary Figure S3**) (Strissel et al., 2007; van Beek et al., 2015). The decrease in EPI fat mass is likely related to increased apoptosis (Strissel et al., 2007; Jo et al., 2010; van Beek et al., 2015). In contrast, the ING fat depot and cell sizes expanded significantly after prolonged HFD-feeding. The large population of hypertrophic adipocytes could account for the negative correlation between ING fat mass and insulin sensitivity shown in **Figure 4**. Thus, the role ascribed to the ING depot as a metabolic sink, protecting against metabolic disease (Tchernof and Despres, 2013) may be diminished at this point.

We also examined the capacity for adiposity and insulin sensitivity to recuperate after reversing from HFD to chow diet. At the 12 weeks' time point, mice had an impaired capacity to recuperate systemic metabolism and adiposity when switching from HFD- to chow-feeding, compared with the shorter times tested. Interestingly, the 8wREV group had smaller adipocyte sizes than observed in 4wHFD in both EPI and ING adipocytes (see **Supplementary Figure S4**, left panel). This was only found in EPI, not ING, adipocytes when comparing the 12wREV group with the 8wHFD group (see **Supplementary Figure S4**, right panel), which pinpoints fat depot-specific differences in the capacity to adjust to energy intake. Further, we have previously reported changes in actin organization mirror adipocyte size during shorter feeding interventions (Hansson et al., 2019). Herein, we could confirm that this is also true

during more extended feeding periods. After 12 weeks of HFD-feeding we observed an impairment in insulin-stimulated glucose uptake in isolated adipocytes, which was not recovered by reversing the diet. This is most likely related to the abundance of large adipocytes (relatively to chow) and the increased density of actin filaments. Indeed, numerous studies have highlighted that actin turnover plays a vital role in promoting insulin-mediated GLUT4 exocytosis (Lopez et al., 2009; Yang et al., 2014). Possibly, decreased GLUT4 exocytosis is caused by a shift towards increased filamentous actin, required to maintain cellular integrity of the expanding adipocyte (Rivero et al., 1996). Interestingly, the partial restoration of IRS-1 and GLUT4 protein levels in EPI adipocytes after reversing the diet was not sufficient to improve insulin-stimulated glucose uptake. Thus, factors other than GLUT4 expression must contribute to the lowered insulin response, again emphasizing that actin dynamics could provide a mechanistic explanation for hypertrophic adipocyte dysfunction.

Numerous studies have addressed changes in adiposity and glucose homeostasis in response to diet-induced obesity in mice. However, there are several varying parameters, for example, mice strains, diet composition, length of feeding (de Moura e Dias et al., 2021). A study using an experimental design comparable to the 12 weeks' group used herein, described a resistance to fat loss after reversing the diet, which was suggested to arise from leptin insufficiency (Shi et al., 2009). Despite having increased adiposity compared with chow, the reversal of HFD to chow-diet resulted in restored glucose tolerance (Shi et al., 2009). We found similar changes with respect to adiposity and reduced adipocyte sizes but observed significantly higher insulin levels. This discrepancy could be related to the difference in dietary fat content (45% versus 60% in our study).

The time of diet-intervention is an important factor for the outcome and herein we only evaluated the plasticity during a short reversing period. The outcome may have been different if we had prolonged the reversed feeding period, in line with a previous report where mice fed HFD for 4 months, followed by 4 months of low-fat, completely recovered (Parekh et al., 1998). Still, our study gives insight into the cell-size distribution and characteristics of subcutaneous and visceral adipose tissue, when metabolic flexibility and adipose tissue plasticity start to decline during HFD-feeding. In support of our protocol, it was mentioned in the study by Shi et al. (2009) that 2 weeks of diet reversal had been evaluated as a time point where body weight was confirmed to be stabilized. A limitation of our study design was the assessment of systemic insulin sensitivity. In order to correlate insulin sensitivity and adipose tissue parameters from the same individual, we used fasting insulin and glucose levels to calculate QUICKI as a measurement of insulin sensitivity, which serves as a valid measurement but does not fully dissect glucose tolerance (Bowe et al., 2014).

In summary, our results demonstrate that the C57BL/6J HFD-feeding model has a large capacity to restore adipocyte cell size and systemic insulin sensitivity, but also emphasize that a metabolic tipping point occurs between 8 and 12w of HFD-feeding, where these parameters are not restored at the same rate. Furthermore, at this time point we observed that the expansion of the ING depot, both in total mass and adipocyte size, coincides with deterioration of systemic insulin sensitivity. In conclusion, we believe these findings provide substantial understanding of C57BL/6J mice as an obesity model, and that an increased pool of hypertrophic ING adipocytes could contribute to aggravated insulin resistance.

DATA AVAILABILITY STATEMENT

The raw data supporting the conclusions of this article will be made available by the authors, without undue reservation.

ETHICS STATEMENT

The animal study was reviewed and approved by Malmö/Lund Committee for Animal Experiment Ethics, Lund, Sweden.

AUTHOR CONTRIBUTIONS

KS, CF, BM, MN, RL, and AB-M conceived and designed the experiments. KS, CF, BM, MN, and AB-M collected, analyzed, and interpreted data. KS, CF, and MN drafted the article and/or revised it critically for important intellectual content. All authors made comments on the manuscript and approved the final version submitted for publication. All persons designated as authors qualify for authorship, and all those who qualify for authorship are listed.

FUNDING

This work was financially supported by the Swedish Research Council (2019-00978) and Strategic Research Area Exodiab (2009-1039), the Swedish Foundation for Strategic Research (IRC15-0067), Novo Nordisk (NNF20OC0063659), Swedish Diabetes Foundation, The Crafoord Foundation, and Albert Påhlsson Foundation.

ACKNOWLEDGMENTS

We would like to thank Maria Lindahl and Tina Ovlund for excellent technical support.

SUPPLEMENTARY MATERIAL

The Supplementary Material for this article can be found online at: https://www.frontiersin.org/articles/10.3389/fcell.2022.942374/full#supplementary-material

REFERENCES

Acosta, J. R., Douagi, I., Andersson, D. P., Bäckdahl, J., Rydén, M., Arner, P., et al. (2016). Increased Fat Cell Size: a Major Phenotype of Subcutaneous White Adipose Tissue in Non-obese Individuals with Type 2 Diabetes. *Diabetologia* 59, 560–570. doi:10.1007/s00125-015-3810-6

Bowe, J. E., Franklin, Z. J., Hauge-Evans, A. C., King, A. J., Persaud, S. J., and Jones, P. M. (2014). Metabolic Phenotyping Guidelines: Assessing Glucose Homeostasis in Rodent Models. *J. Endocrinol.* 222, G13–G25. doi:10.1530/JOE-14-0182

de Moura e Dias, M., Dos Reis, S. A., da Conceição, L. L., Sediyama, C. M. N. d. O., Pereira, S. S., de Oliveira, L. L., et al. (2021). Diet-induced Obesity in Animal Models: Points to Consider and Influence on Metabolic Markers. *Diabetol. Metab. Syndr.* 13, 32. doi:10.1186/s13098-021-00647-2

Fisher-Wellman, K. H., Ryan, T. E., Smith, C. D., Gilliam, L. A. A., Lin, C.-T., Reese, L. R., et al. (2016). A Direct Comparison of Metabolic Responses to High-Fat Diet in C57BL/6J and C57BL/6NJ Mice. *Diabetes* 65, 3249–3261. doi:10.2337/db16-0291

Foster, M. T., Softic, S., Caldwell, J., Kohli, R., deKloet, A. D., and Seeley, R. J. (2013). Subcutaneous Adipose Tissue Transplantation in Diet-Induced Obese Mice Attenuates Metabolic Dysregulation while Removal Exacerbates it. *Physiol. Rep.* 1, e00015. doi:10.1002/phy2.15

Franck, N., Stenkula, K. G., Öst, A., Lindström, T., Strålfors, P., and Nystrom, F. H. (2007). Insulin-induced GLUT4 Translocation to the Plasma Membrane Is Blunted in Large Compared with Small Primary Fat Cells Isolated from the Same Individual. *Diabetologia* 50, 1716–1722. doi:10.1007/s00125-007-0713-1

Franczyk, M. P., He, M., and Yoshino, J. (2021). Removal of Epididymal Visceral Adipose Tissue Prevents Obesity-Induced Multi-Organ Insulin Resistance in Male Mice. *J. Endocr. Soc.* 5, bvab024. doi:10.1210/jendso/bvab024

Gliemann, J., Rees, W. D., and Foley, J. A. (1984). The Fate of Labelled Glucose Molecules in the Rat Adipocyte. *Biochim Biophys Acta.* 804, 68–76. doi:10.1016/0167-4889(84)90100-9

Hansson, B., Morén, B., Fryklund, C., Vliex, L., Wasserstrom, S., Albinsson, S., et al. (2019). Adipose Cell Size Changes Are Associated with a Drastic Actin Remodeling. *Sci. Rep.* 9, 12941. doi:10.1038/s41598-019-49418-0

Hansson, B., Wasserstrom, S., Morén, B., Periwal, V., Vikman, P., Cushman, S. W., et al. (2018). Intact Glucose Uptake Despite Deteriorating Signaling in Adipocytes with High-Fat Feeding. *J. Mol. Endocrinol.* 60, 199–211. doi:10.1530/JME-17-0195

Hocking, S. L., Chisholm, D. J., and James, D. E. (2008). Studies of Regional Adipose Transplantation Reveal a Unique and Beneficial Interaction between Subcutaneous Adipose Tissue and the Intra-abdominal Compartment. *Diabetologia* 51, 900–902. doi:10.1007/s00125-008-0969-0

Jo, J., Guo, J., Liu, T., Mullen, S., Hall, K. D., Cushman, S. W., et al. (2010). Hypertrophy-driven Adipocyte Death Overwhelms Recruitment under Prolonged Weight Gain. *Biophysical J.* 99, 3535–3544. doi:10.1016/j.bpj.2010.10.009

Katz, A., Nambi, S. S., Mather, K., Baron, A. D., Follmann, D. A., Sullivan, G., et al. (2000). Quantitative Insulin Sensitivity Check Index: a Simple, Accurate Method for Assessing Insulin Sensitivity in Humans. *J. Clin. Endocrinol. Metab.* 85, 2402–2410. doi:10.1210/jcem.85.7.6661

Kodama, K., Horikoshi, M., Toda, K., Yamada, S., Hara, K., Irie, J., et al. (2012). Expression-based Genome-wide Association Study Links the Receptor CD44 in Adipose Tissue with Type 2 Diabetes. *Proc. Natl. Acad. Sci. U.S.A.* 109, 7049–7054. doi:10.1073/pnas.1114513109

Kowalski, G. M., Hamley, S., Selathurai, A., Kloehn, J., De Souza, D. P., O'Callaghan, S., et al. (2016). Reversing Diet-Induced Metabolic Dysregulation by Diet Switching Leads to Altered Hepatic De Novo Lipogenesis and Glycerolipid Synthesis. *Sci. Rep.* 6, 27541. doi:10.1038/srep27541

Laurencikiene, J., Skurk, T., Kulyté, A., Hedén, P., Åström, G., Sjölin, E., et al. (2011). Regulation of Lipolysis in Small and Large Fat Cells of the Same Subject. *J. Clin. Endocrinol. Metab.* 96, E2045–E2049. doi:10.1210/jc.2011-1702

Livak, K. J., and Schmittgen, T. D. (2001). Analysis of Relative Gene Expression Data Using Real-Time Quantitative PCR and the 2−ΔΔCT Method. *Methods* 25, 402–408. doi:10.1006/meth.2001.1262

Lopez, J. A., Burchfield, J. G., Blair, D. H., Mele, K., Ng, Y., Vallotton, P., et al. (2009). Identification of a Distal GLUT4 Trafficking Event Controlled by Actin Polymerization. *Mol. Biol. Cell.* 20, 3918–3929. doi:10.1091/mbc.E09-03-0187

McLaughlin, T., Sherman, A., Tsao, P., Gonzalez, O., Yee, G., Lamendola, C., et al. (2007). Enhanced Proportion of Small Adipose Cells in Insulin-Resistant vs Insulin-Sensitive Obese Individuals Implicates Impaired Adipogenesis. *Diabetologia* 50, 1707–1715. doi:10.1007/s00125-007-0708-y

Parekh, P. I., Petro, A. E., Tiller, J. M., Feinglos, M. N., and Surwit, R. S. (1998). Reversal of Diet-Induced Obesity and Diabetes in C57BL/6J Mice. *Metabolism* 47, 1089–1096. doi:10.1016/s0026-0495(98)90283-9

Rivero, F., Koppel, B., Peracino, B., Bozzaro, S., Siegert, F., Weijer, C. J., et al. (1996). The Role of the Cortical Cytoskeleton: F-Actin Crosslinking Proteins Protect against Osmotic Stress, Ensure Cell Size, Cell Shape and Motility, and Contribute to Phagocytosis and Development. *J. Cell Sci.* 109 (Pt 11), 2679–2691. doi:10.1242/jcs.109.11.2679

Rodbell, M. (1964). Metabolism of Isolated Fat Cells. *J. Biol. Chem.* 239, 375–380. doi:10.1016/s0021-9258(18)51687-2

Shi, H., Akunuru, S., Bierman, J. C., Hodge, K. M., Mitchell, M. C., Foster, M. T., et al. (2009). Diet-induced Obese Mice Are Leptin Insufficient after Weight Reduction. *Obes. (Silver Spring)* 17, 1702–1709. doi:10.1038/oby.2009.106

Strissel, K. J., Stancheva, Z., Miyoshi, H., Perfield, J. W., 2nd, DeFuria, J., Jick, Z., et al. (2007). Adipocyte Death, Adipose Tissue Remodeling, and Obesity Complications. *Diabetes* 56, 2910–2918. doi:10.2337/db07-0767

Sun, K., Tordjman, J., Clément, K., and Scherer, P. E. (2013). Fibrosis and Adipose Tissue Dysfunction. *Cell Metab.* 18, 470–477. doi:10.1016/j.cmet.2013.06.016

Surwit, R. S., Wang, S., Petro, A. E., Sanchis, D., Raimbault, S., Ricquier, D., et al. (1998). Diet-induced Changes in Uncoupling Proteins in Obesity-Prone and Obesity-Resistant Strains of Mice. *Proc. Natl. Acad. Sci. U.S.A.* 95, 4061–4065. doi:10.1073/pnas.95.7.4061

Tchernof, A., and Després, J.-P. (2013). Pathophysiology of Human Visceral Obesity: an Update. *Physiol. Rev.* 93, 359–404. doi:10.1152/physrev.00033.2011

Turner, N., Kowalski, G. M., Leslie, S. J., Risis, S., Yang, C., Lee-Young, R. S., et al. (2013). Distinct Patterns of Tissue-specific Lipid Accumulation during the Induction of Insulin Resistance in Mice by High-Fat Feeding. *Diabetologia* 56, 1638–1648. doi:10.1007/s00125-013-2913-1

van Beek, L., van Klinken, J. B., Pronk, A. C. M., van Dam, A. D., Dirven, E., Rensen, P. C. N., et al. (2015). The Limited Storage Capacity of Gonadal Adipose Tissue Directs the Development of Metabolic Disorders in Male C57Bl/6J Mice. *Diabetologia* 58, 1601–1609. doi:10.1007/s00125-015-3594-8

Weyer, C., Foley, J. E., Bogardus, C., Tataranni, P. A., and Pratley, R. E. (2000). Enlarged Subcutaneous Abdominal Adipocyte Size, but Not Obesity Itself, Predicts Type II Diabetes Independent of Insulin Resistance. *Diabetologia* 43, 1498–1506. doi:10.1007/s001250051560

Williams, L. M., Campbell, F. M., Drew, J. E., Koch, C., Hoggard, N., Rees, W. D., et al. (2014). The Development of Diet-Induced Obesity and Glucose Intolerance in C57BL/6 Mice on a High-Fat Diet Consists of Distinct Phases. *PLoS One* 9, e106159. doi:10.1371/journal.pone.0106159

Winzell, M. S., and Ahrén, B. (2004). The High-Fat Diet-Fed Mouse. *Diabetes* 53 (Suppl. 3), S215–S219. doi:10.2337/diabetes.53.suppl_3.s215

Yang, W., Thein, S., Lim, C.-Y., Ericksen, R. E., Sugii, S., Xu, F., et al. (2014). Arp2/3 Complex Regulates Adipogenesis by Controlling Cortical Actin Remodelling. *Biochem. J.* 464, 179–192. doi:10.1042/BJ20140805

Conflict of Interest: The authors declare that the research was conducted in the absence of any commercial or financial relationships that could be construed as a potential conflict of interest.

Publisher's Note: All claims expressed in this article are solely those of the authors and do not necessarily represent those of their affiliated organizations, or those of the publisher, the editors and the reviewers. Any product that may be evaluated in this article, or claim that may be made by its manufacturer, is not guaranteed or endorsed by the publisher.

frontiers | Frontiers in Cell and Developmental Biology

TYPE Original Research
PUBLISHED 12 October 2022
DOI 10.3389/fcell.2022.1017499

OPEN ACCESS

EDITED BY
Jette Lengefeld,
University of Helsinki, Finland

REVIEWED BY
Scott Manalis,
Massachusetts Institute of Technology, United States
Teemu Miettinen,
Massachusetts Institute of Technology, United States
Gabriel Neurohr,
ETH Zürich, Switzerland

*CORRESPONDENCE
Marc W. Kirschner,
marc@hms.harvard.edu

†These authors have contributed equally to this work

SPECIALTY SECTION
This article was submitted to Cell Growth and Division, a section of the journal Frontiers in Cell and Developmental Biology

RECEIVED 12 August 2022
ACCEPTED 23 September 2022
PUBLISHED 12 October 2022

CITATION
Liu X, Oh S and Kirschner MW (2022), The uniformity and stability of cellular mass density in mammalian cell culture. *Front. Cell Dev. Biol.* 10:1017499. doi: 10.3389/fcell.2022.1017499

The uniformity and stability of cellular mass density in mammalian cell culture

Xili Liu†, Seungeun Oh† and Marc W. Kirschner*

Department of Systems Biology, Harvard Medical School, Boston, MA, United States

Cell dry mass is principally determined by the sum of biosynthesis and degradation. Measurable change in dry mass occurs on a time scale of hours. By contrast, cell volume can change in minutes by altering the osmotic conditions. How changes in dry mass and volume are coupled is a fundamental question in cell size control. If cell volume were proportional to cell dry mass during growth, the cell would always maintain the same cellular mass density, defined as cell dry mass dividing by cell volume. The accuracy and stability against perturbation of this proportionality has never been stringently tested. Normalized Raman Imaging (NoRI), can measure both protein and lipid dry mass density directly. Using this new technique, we have been able to investigate the stability of mass density in response to pharmaceutical and physiological perturbations in three cultured mammalian cell lines. We find a remarkably narrow mass density distribution within cells, that is, significantly tighter than the variability of mass or volume distribution. The measured mass density is independent of the cell cycle. We find that mass density can be modulated directly by extracellular osmolytes or by disruptions of the cytoskeleton. Yet, mass density is surprisingly resistant to pharmacological perturbations of protein synthesis or protein degradation, suggesting there must be some form of feedback control to maintain the homeostasis of mass density when mass is altered. By contrast, physiological perturbations such as starvation or senescence induce significant shifts in mass density. We have begun to shed light on how and why cell mass density remains fixed against some perturbations and yet is sensitive during transitions in physiological state.

KEYWORDS

cellular mass density, cell volume regulation, mass density homeostasis, cell size control, normalized Raman imaging

Introduction

The process of cell size control has recently attracted considerable interest (Ginzberg, Kafri and Kirschner, 2015; Amodeo and Skotheim, 2016; Xie, Swaffer and Skotheim, 2022). Cell size is the outcome of active control of cell growth, coupled to changes in the cell cycle, and reflects changes in metabolism and physiological adaptations to the environment. Studies of cell size in mammalian cells have recently focused on the regulation of cell mass or cell volume (Cadart et al., 2019). Cell volume is generally

measured by the Coulter principle or by 3D microscopy, while single cell mass quantification utilizes physical techniques to directly register buoyant or dry mass, rather than wet mass. Cell size and volume have long been known to vary dramatically with cell type. The mass and volume of cells in the human body can vary more than 1000-fold (Ginzberg, Kafri and Kirschner, 2015). By contrast, cellular mass density, which is simply computed by dividing the cell dry mass by the cell volume, has a much narrower distribution than the distributions of either cell mass or cell volume for cells grown *in vitro* and cells in tissues (Bryan et al., 2014; Neurohr and Amon, 2020). In this paper, we use Normalized Raman Imaging (NoRI) to measure single cell's protein and lipid mass density accurately and directly. We show that cellular mass density for a population of cells is maintained within a remarkably tight distribution when examined for 3 cell lines of different cell types. By perturbing cells mechanically and pharmacologically, we demonstrate the extraordinary stability of cellular mass density, which cannot simply be explained as a passive resultant of mass or volume regulation. Rather it suggests the existence of a homeostatic process of mass density control through active feedback.

The simplest physical model of cell size envisages a bag of impermeable macromolecules bound by a flexible semipermeable membrane. The volume of the bag at steady state would be controlled by osmotic pressure generated by the concentration of impermeable molecules and by the transport of sodium and potassium ions. In this picture, the doubling of the number of impermeant molecules during the cell cycle causes the cell to double both in mass and in volume, hence, maintaining the same mass density. The biophysical picture has been described by a set of flux and constraint equations of the so-called pump leak model (Kay and Blaustein, 2019). The pump leak mechanism predicts that, even without a feedback mechanism, the ratio of cell dry mass to cell volume would be stable, and hence cellular mass density would be constant, provided that the pump rate of ions and the macromolecular and osmolyte composition remain stable during the process of growth. Indeed, cell volume and cell dry mass are thought to be regulated in such a manner in proliferating cells (Cadart et al., 2018; Liu, Yan and Kirschner, 2022). In this process of growth, it is assumed that the cellular molecular composition is unchanging though the total mass changes, thus maintaining the mass density. However, the volume stabilizing behavior of this model is limited to maintaining a steady state mass density independent of size. It may not be able to explain the large variability of cell mass density observed in different cell types, nor does it necessarily explain dynamic cell mass density regulation seen in changing physiological states. Indeed, when cells differentiate or senesce, the composition of the cell changes. The strict parallel of protein content with volume may be abrogated, leading not only to changes in mass but also changes in mass density at steady state. This has been seen in chondrocyte differentiation (Cooper et al., 2013) and in cell senescence (Neurohr et al., 2019; Oh et al., 2022).

It would be ideal if we could accurately measure mass density directly, rather than calculate it by dividing dry mass by volume from independent measurements (Zangle and Teitell, 2014; Cadart et al., 2017; Liu et al., 2020). For very rapid volume changes, it can be assumed that the dry mass does not change appreciably, and mass density could then be calculated from volume change alone (Guo et al., 2017; Roffay et al., 2021; Venkova et al., 2022). But during many physiological changes like differentiation, mass density changes slowly. Under these conditions, it would be unreasonable to assume that there is no change in dry mass (Cooper et al., 2013). Only a few methods can measure mass density directly. The Suspended Microchannel Resonator (SMR) can derive mass density by measuring cell buoyant mass in two different media of different densities, providing sensitivity of 1–6 mg/ml (Grover et al., 2011; Bryan et al., 2014; Miettinen et al., 2022). However, this method is limited to cells grown in suspension and requires medium replacement. Similarly, Quantitative Phase Microscopy (QPM) measures the three variables by measuring the optical path difference of the same cell twice in media of different refractive indices (Cooper et al., 2013). This method also requires medium replacement, and the errors in volume and density measurements are much larger than that of direct dry mass measurement. Refractive index tomography measures local dry mass density in optical cross sections and provides information on the volumetric distribution of subcellular dry mass density (Choi et al., 2007; Kim et al., 2018; Kim and Guck, 2020). However, due to the subtle difference in the refractive index increments of macromolecules, this method has a larger bias in lipid-rich regions and cannot distinguish the contributions of protein and lipid. In part to circumvent these limitations, our laboratory developed Normalized Raman Imaging (NoRI), which has unique advantages for mass density measurements (Oh et al., 2022). It directly and quantitatively measures *mass density* with 15 mg/ml sensitivity in optical z-cross sections (lateral and axial resolutions 0.57 and 1.58 μm) using the stimulated Raman scattering of macromolecules. This principle enables NoRI to separately measure protein and lipid densities of living cells and provides their subcellular localization. The method can also be performed with confluent cultures or in 3-dimensional tissue samples.

In this study, we employed NoRI microscopy on living cultured mammalian cells as a means to measure the protein and lipid mass density directly. We use three mammalian cell lines representing different cell types. We investigate how the mass density responds to perturbations such as extracellular osmotic stress, inhibition of protein synthesis, inhibition of protein degradation, disruption of the cytoskeleton, and other physiological state changes. Though these perturbations have previously been studied extensively for changes in physical and biochemical properties, they had not been compared in terms of changes in cellular mass density. Nor have previous studies distinguished protein from lipid density. We find strong evidence that cellular mass density is under stringent control

and is maintained in a remarkably tight range in proliferating cells. It is resistant to some perturbations but can respond to others. These differential responses can help us understand the nature of cell size and mass density regulation during physiological and pathological conditions.

Materials and Methods

Cell culture and chemical treatment

HeLa (CCL-2), NIH3T3 (CRL-1658), and RPE-1 (CRL-4000) cells were purchased directly from the ATCC. MDCK II cells were obtained from Jeffrey J. Fredberg laboratory, Harvard T. H. Chan School of Public Health. All cell lines were cultured at 37°C with 5% CO_2 in Dulbecco's modified Eagle's medium (DMEM) (11965; Thermo Fisher Scientific) with 10% fetal bovine serum (FBS) (16000044; Thermo Fisher Scientific), 1% penicillin/streptomycin (15140122; Thermo Fisher Scientific), 25 mM HEPES (15630080; Thermo Fisher Scientific), and 10 mM sodium pyruvate (11360070; Thermo Fisher Scientific), unless indicated otherwise. The starvation medium had the same constitution as the normal medium except 0.1% FBS replaced the standard 10% FBS. The osmolarity of the media was judged to be 350 mOsm using a vapor pressure osmometer (Vapro); all other media were evaluated in the same fashion. The +200 mOsm hyper-osmotic medium was made from normal medium with added 100 mM sodium chloride (S5886, Millipore Sigma), and the +400 mOsm medium was made with added 200 mM sodium chloride; their respective osmolarities were 542 and 742 mOsm. The composition of the hypo-osmotic medium was normal medium diluted with an equal volume of deionized water; it had an osmolarity of 158 mOsm. Rapamycin was purchased from LC Laboratories (R-5000); Cycloheximide, Nocodazole, and Ouabain octahydrate were purchased from Millipore Sigma (C4859, SML1665, and O3125); MG132 and Doxorubicin were purchased from Selleckchem (S2619 and S1208); Cytochalasin D was purchase from Cayman (11330). The NoRI samples were seeded on 55 mm glass bottom dishes with 30 mm micro-well #1.5 cover glass (D60-30-1.5-N, Cellvis), other microscopic samples were seeded on 12 Well or 24 Well glass bottom plates with high performance #1.5 cover glass (P12-1.5H-N and P24-1.5H-N, Cellvis). For trypsinization we used 0.05% trypsin-EDTA (25300054, Thermo-Fisher Scientific) or 0.25% trypsin-EDTA solutions (25200056, Thermo-Fisher Scientific). HeLa and NIH3T3 cells were incubated in 0.05% trypsin-EDTA solution for 10 min and MDCK cells were incubated in 0.25% trypsin-EDTA for 15 min. Trypsinized cells were centrifuged, the supernatant aspirated, and cell pellets were resuspended in a volume of culture medium to achieve the desired seeding density.

Measurement of the rates of protein synthesis

Protein synthesis rates were assayed by the Click-iT™ Plus OPP Alexa Fluor™ 647 Protein Synthesis Assay Kit (C10458, Thermo Fisher Scientific). Cells were pulse labelled with 10 μM O-propargyl-puromycin (OPP) for 1 h. The Click-iT™ chemistry was carried out according to manufacturer's instructions. After OPP conjugation with Alexa Fluor™ 647, the cells were stained with 10 μM Hoechst 33342 (62249, Thermo Fisher Scientific) and 500 ng/ml Alexa Fluor™ 568 NHS Ester (SE) (A20003, Thermo Fisher Scientific) for 30 min, followed by two washings with PBS. Cells were then imaged by an Eclipse Ti microscope with the Perfect Focus System (PFS), Plan Fluor 10×/0.3 N.A. PFS dry objective lens (Nikon, Japan), and an ORCA-ER camera (Hamamatsu, Japan). Images were acquired by the NIS-Elements AR ver. 4.13.0.1 software with the WellPlate plugin.

Assays for cell proliferation

Proliferating cells were detected by the Click-iT™ Plus EdU Cell Proliferation Kit for Imaging, Alexa Fluor™ 647 dye (C10640, Thermo Fisher Scientific). Cells were pulse labeled with 10 μM EdU (5-ethynyl-2′-deoxyuridine) for 1 h. The Click-iT™ chemistry was carried out according to manufacturer's instructions. After Click-iT™ conjugation, the cells were stained with 10 μM Hoechst 33342 for 30 min and then imaged by fluorescence microscope at 10x magnification.

Assays for SA-beta-galactosidase activity

SA-beta-galactosidase activity was detected by CellEvent™ Senescence Green Detection Kit (C10850, Thermo Fisher Scientific). Cells were fixed in 2% paraformaldehyde in PBS (diluted from 8% paraformaldehyde, RT 157–8, Electron Microscopy Sciences) for 10 min. The assay was carried out according to manufacturer's instructions. Cells were stained with 10 μM Hoechst 33342 and 500 ng/ml Alexa Fluor™ 568 NHS Ester for 30 min, followed by two washings with PBS, then imaged by fluorescence microscopy at 10X magnification.

Measurement of cell size

Cell dry mass was estimated by the SE staining of fixed cells by the following method: cells were fixed with 4% paraformaldehyde for 20 min, permeabilized with 0.5% Triton X-100 in PBS for 20 min, stained with 10 μM Hoechst and 500 ng/ml Alexa Fluor™ 568 NHS Ester (the SE protein dye) for 30 min, and then imaged by fluorescence microscopy. Cell

volume was measured by Moxi GO II (Orflo, United States) using the Coulter principle by the following method: live cells were trypsinized by 0.05% or 0.25% trypsin-EDTA, resuspended in DMEM with corresponding drugs or osmotic pressure, and then measured by Moxi GO II using the Cell Count (Size Only) Assay according to manufacturer's instructions. Debris or dead cells were gated out based on their small diameter.

Immunofluorescence procedures

Antibodies used in this study are: Anti-S6 Ribosomal Protein (5G10) Rabbit mAb (2217, Cell Signaling), Anti-YAP1 Antibody (63.7) (sc-101199, Santa Cruz), Anti-rabbit IgG (H + L), F (ab') 2 Fragment (Alexa Fluor® 488 Conjugate) (4412, Cell Signaling), Anti-mouse IgG (H + L), F (ab')2 Fragment (Alexa Fluor® 488 Conjugate) (4408, Cell Signaling), and Goat anti-Mouse IgG (H + L) Cross-Adsorbed Secondary Antibody, Alexa Fluor™ 647 (A-21235, Thermo Fisher Scientific). During immunofluorescence, cells were fixed with 4% paraformaldehyde for 20 min, then permeabilized and blocked with the blocking buffer (2% BSA, 0.3 M glycine, and 0.1% Tween-20 in PBS) for 1 h. Cells were next incubated with the primary antibody at 1:100 dilution overnight at 4°C, followed by incubation with the secondary antibody at 1:500 dilution for 1 h. Finally, cells were stained with 2 μM DAPI (4, 6- diamidino-2-phenylindole) (D8417; Sigma-Aldrich) and 500 ng/ml Alexa Fluor™ 568 NHS Ester for 30 min, washed three times, and then imaged by fluorescence microscopy at 10x magnification.

To compare cellular mass density and YAP immunofluorescence at the single-cell level, we added a silicon insert confining cells in a small area (81176, ibid) at plating to help locate the imaging area. After NoRI scanning, the cells were immediately fixed and immunostained as described above. The same area imaged by NoRI was found under fluorescence microscopy and imaged at 10X magnification. The fluorescence images of the SE channel were registered to the NoRI images of the protein channel by the Normalized Cross-Correlation (NCC) algorithm (Haralick and Shapiro, 1993).

Protein and lipid mass density measurements using NoRI microscopy

Protein and lipid concentrations were calculated from stimulated Raman scattering images following the procedure described in our previous report (Oh et al., 2022). Briefly, Stimulated Raman Spectroscopy (SRS) images at 2853 cm^{-1}, 2935 cm^{-1}, and 3420 cm^{-1} bands (corresponding to the methylene- and methyl-groups, and water characteristic vibrational bands, respectively) were acquired from live or fixed cells using a custom-built spectral-focusing femtosecond SRS microscope. This microscope was constructed using synchronized femtosecond pulse lasers for the Pump and Stokes beams. (Figure 1A). A pair of dense flint (DF) glass rods chirped the pulses. Electro-optical modulator (EOM) modulated the amplitude of the Stokes beam at 20 MHz. A retro-reflector prism mounted on a motorized delay (Delay) was adjusted to control the overlap of the Pump and Stokes beams. The pump and Stokes beams, combined by a dichroic mirror (DM), were focused on the sample by the objective lens. Images were acquired by point-scanning by a pair of galvanized mirrors (scan mirror). After passage through the stimulated Raman scattering at the sample plane, the Pump beam was collected by a high numerical aperture condenser lens, selected by a short pass filter (SF), and its intensity was measured by a high-speed photodetector. Cells were maintained at 37°C in 5% CO_2 during imaging using TomoChamber stage-top incubator (Tomocube, South Korea) with a custom-fitting adapter for the immersion condenser. (Figure 1B). The three SRS images were spectrally unmixed into protein, lipid, and water components using reference spectra measured from bovine serum albumin solution in water, dioleoyl-phosphocholine solution in per-deuterated methanol, water, and per-deuterated methanol. Unmixed images of protein, lipid, and water components were converted to the absolute concentration by using the sum of the three components as the normalization reference at each pixel. Dry mass density was calculated from the sum of protein mass density and lipid mass density.

Cell cycle determination with NoRI

To determine cell cycle position of single cells along with their NoRI mass density measurement, we stained live cells with 2 μM Hoechst 33342 and acquired fluorescence images using the confocal microscope embedded in the NoRI microscope (Olympus FV3000, excitation at 405 nm) at 10x magnification with a fully opened confocal pinhole. The field illumination was corrected by a fluorescence reference slide (2273, Ted Pella). The large field Hoechst fluorescence image at 10x magnification was registered to the NoRI image mediated by a Hoescht image taken at the same magnification (60x) as the NoRI image.

Data analysis

All images were processed by customized codes in Matlab (Mathworks) or ImageJ (National Institute of Health). Single cells, nuclei, and nucleoli in NoRI images were automatically segmented by thresholding using protein densities greater 0.0666 g/ml to define the cell body and lipid densities of less than 0.0099 g/ml for the nucleus. Nucleoli were segmented by applying Otsu's method (Otsu, 1979) on protein density within the nucleus. Morphological operation were used to select the

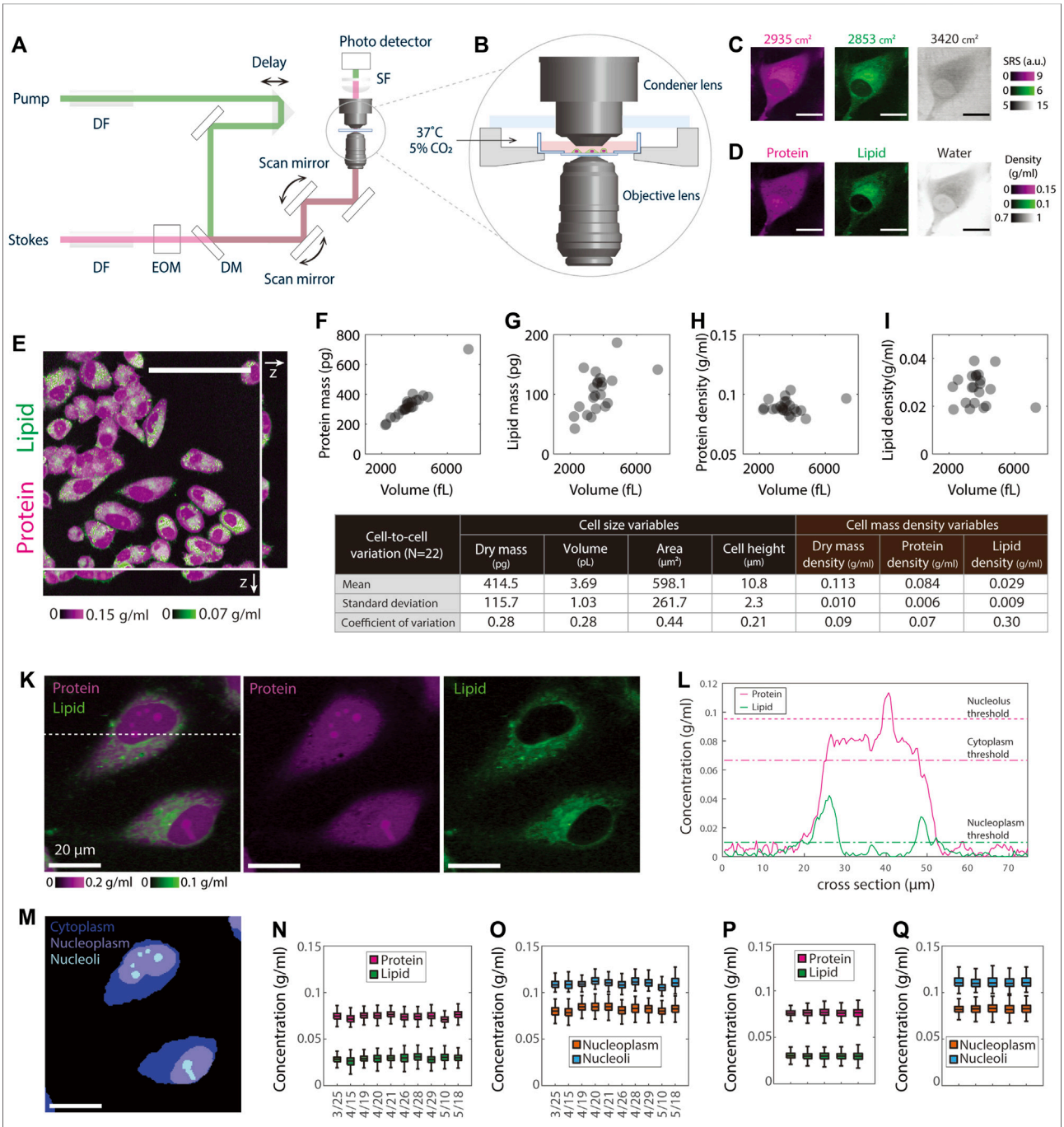

Cell-to-cell variation (N=22)	Cell size variables				Cell mass density variables		
	Dry mass (pg)	Volume (pL)	Area (μm^2)	Cell height (μm)	Dry mass density (g/ml)	Protein density (g/ml)	Lipid density (g/ml)
Mean	414.5	3.69	598.1	10.8	0.113	0.084	0.029
Standard deviation	115.7	1.03	261.7	2.3	0.010	0.006	0.009
Coefficient of variation	0.28	0.28	0.44	0.21	0.09	0.07	0.30

FIGURE 1
NoRI measurement of single cell mass density demonstrating the stability of protein and lipid mass densities. **(A)** Schematic of the stimulated Raman scattering microscope. DF, dense flint; EOM electro-optical modulator; DM, dichroic mirror; SF, short-pass filter. **(B)** A close-up view of the environmental chamber for live cell NoRI imaging. **(C)** Raw SRS images acquired using the SRS microscope at the Raman bands of 2853, 2935, and 3420 cm^{-1}, corresponding to the vibrational modes of CH_2, CH_3, and water, respectively. Scale bar, 20 μm. Image intensities are derived directly from the photocurrent at the photodetector. **(D)** The local concentrations of protein, lipid, and water are computed from the raw SRS images by the NoRI algorithm following Oh et al., 2022. **(E)** z-stack NoRI image of fixed A7 cells displaying protein and lipid concentrations. Scale bar, 100 μm. **(F–I)** Correlation plots of protein mass **(F)**, lipid mass **(G)**, protein density **(H)**, and lipid density **(I)** with cell volume measured from single cells (n = 22) in **(E)**. The correlation coefficient R is 0.97 (p < 1e-13) for protein mass, 0.56 (p = 0.007) for lipid mass, 0.06 (p = 0.78) for protein density, and −0.18, (p = 0.42) for lipid density, respectively. **(J)** Table summarizing the mean, standard deviation, and CV of the cell size and cell density variables in **(F–I)**. **(K)** Representative NoRI images of live HeLa cells with protein density displayed in magenta and lipid density displayed in green. Scale bar, 20 μm. **(L)** Protein and lipid density profiles along the dashed cross line in **(K)**. The dashed lines indicate the protein (magenta) and lipid (green) thresholds used in the segmentation. **(M)** Segmentation of **(K)** indicating cell bodies, nuclei, and nucleoli. Cytoplasm represents the area inside the cell body outside of the nucleus. Nucleoplasm refers to the area inside the nucleus excluding the nucleoli. **(N–O)** Day-to-day variability of HeLa cell mass density
(*Continued*)

FIGURE 1 (Continued)
measurements. The average number of cells in each data set is 596 per day. **(P–Q)** Mass densities from five independent cultures of HeLa cells measured on the same day. Mean and standard deviation (cell-to-cell variability) are 76.3 ± 4.8 mg/ml for the cytoplasmic protein, 29.7 ± 5.1 mg/ml for the cytoplasmic lipid, 82.1 ± 5.6 mg/ml for the nucleoplasmic protein and 111.6 ± 10.2 mg/ml for the nucleolar protein. The standard deviation of the mean (sample-to-sample variability) is 0.3, 0.3, 0.4, and 0.8 mg/ml for cytoplasm protein, cytoplasm lipid, nucleoplasm protein, and nucleoli protein, respectively. The average number of cells in each sample is 430.

relevant features by size thresholds. The watershed algorithm was used to draw the boundary of adjacent cells in confluent culture. See accompanying online materials for the Matlab codes. Statistical analyses were performed by customized codes in Matlab. Samples were compared by the one-way ANOVA test, and N.S., $p > 0.05$; *, $p < 0.05$; **, $p < 0.01$; ***, $p < 0.001$; ****, $p < 0.0001$ were used to denote the statistical significance. All measurements reported in this manuscript were repeated more than once to confirm reproducibility. However, in the figures we chose to display the data from single experiments rather than pooling multiple datasets to avoid noise introduced by day-to-day variability. This improves the visibility of data trends.

Results

Protein and lipid densities measured by NoRI are strikingly consistent within cells of each cell type

To measure the density of protein and lipid in subcellular compartments of live cells in absolute terms, we turned to Normalized Raman Imaging (NoRI), which we recently described (Oh et al., 2022). NoRI enables a label-free direct measurement of protein, lipid, and water density in optical sections of live or fixed cells; total mass can be calculated from a z-stack image by integrating the mass density over cell volume. In brief, this method works as follows: Near-infrared pulse lasers at the pump and Stokes wavelengths were combined and scanned through the sample using a point scanning microscope (Figure 1A); The intensity of the Stokes beam was modulated using an electro-optical modulator (EOM), and the stimulated Raman loss (SRL) of the transmitted pump beam was measured by a photo detector; Live cell samples were maintained at 37°C under 5% CO_2 atmosphere (Figure 1B); The SRL signal was demodulated by a lock-in amplifier at the EOM modulation frequency to obtain the SRS images at whichever Raman band is selected by the energy difference between the pump photons and Stokes photons (Figure 1C); A "NoRI algorithm" computes the absolute concentrations of protein, lipid, and water from the SRS intensities at 2935, 2853, and 3420 cm^{-1} Raman bands, which correspond to the vibrational modes of CH_3 groups, CH_2 groups, and water molecules, respectively (Figure 1D). In this scheme, the mass of nucleic acids is not separately measured but is added to protein mass after significant fractional reduction, since the nucleotide absorption only slightly overlaps the protein peak (Oh et al., 2022; details in Discussion). This is only a small correction since the mass concentration of nuclei acids is much smaller than that of protein in mammalian cells (Oh et al., 2022); therefore the protein mass measured in this manuscript is predominantly from proteins, not nucleic acids. In other circumstances where this is important, for example, in mitotic chromosomes, we can separately measure nucleic acids, protein, lipid, and water by the 4-band NoRI (Oh et al., 2022).

In the following assay, we ask what the most stringently regulated parameters of cell size are by comparing the coefficients of variations of cell volume, cell dry mass, and cellular mass density. Furthermore, we ask this question by separately considering the mass and density of protein and lipid. We initially assessed the relationship between cell dry mass and cell volume in A7 cells, a human cell line that was originally derived from a malignant melanoma (Figure 1E), by integrating the z-stack of NoRI images. To avoid any issues of phototoxicity in living cells, we used fixed cells in this experiment. To identify the contours of the cell, we thresholded the z-stack images of protein density of roughly 1 μm optical sections, from which we obtained the cell volume segmentation. The integration of protein or lipid density over the cell volume constituted the total protein or lipid mass; the ratio of mass to cell volume represented the averaged protein or lipid density of the cell. Not surprisingly, we found that both total protein and lipid mass linearly scaled with cell volume (R = 0.97 and 0.56, respectively) (Figures 1F,G). Notably, protein and lipid densities were nearly completely independent of cell volume (R = 0.06 and R = 0.01, respectively) (Figures 1H,I). The variability of cells in the population, as quantified in terms of the coefficient of variation (CV), was 28% for both cell volume and cell dry mass (the sum of protein and lipid mass). If cell volume and cell dry mass were independent variables, the CV of mass density should be equal to or greater than the combined CVs of the two. However, the observed CV of cellular mass density (the sum of protein and lipid density) was only 9%, and the CV of protein mass density was only 7%, much smaller than either the CV of cell dry mass or the CV of cell volume. We conclude that there must be tight coordination of cell dry mass and cell volume in individual cells (Figure 1J). The CV (30%) of lipid mass density was much higher than that of protein mass density. The much weaker correlation between lipid *content* and cell volume may reflect very different regulatory circuits for lipid and protein mass regulation (Alberts et al., 2002).

To carry out measurements in live cells, we took the NoRI image of the cells only at the midsection. We did this for two purposes: to avoid phototoxicity from extensive 3D scanning and as a strategy to greatly increase the number of cells we practically could measure. We verified that the protein and lipid density measured from a single z-plane showed excellent agreement with those averaged over the whole cell volume (Supplementary Figures S1A,B). We estimated the measurement error of protein density in a single cell cross-section as the following: The measurement sensitivity of the protein channel is 15 mg/ml (Oh et al., 2022), and the cell area at the mid-section is about several hundred pixels at 60x magnification; As the error decreases with the squared root of the number of pixels measured, the error of protein density averaged in one section is less than 1.5 mg/ml; As the cell protein density is about 80 mg/ml in cultured cells, the measurement error for protein density is less than 2%. Similarly, we estimated the lipid measurement error, which is less than 5%. Both the measurement errors of protein and lipid densities were much less than the cell-to-cell variation we observed in total, protein, and lipid mass densities (Figure 1J). For this reason, we felt confident quantifying cell protein and lipid densities from single NoRI cross sections in live cells, an approach we used for the rest of this manuscript.

To process the large number of images required to generate statistically significant results, we developed automated segmentation algorithms for single cells and organelles (Figures 1K–M, Supplementary Figures S1I–K). Benefiting from the remarkable homogeneity in cytoplasmic protein density and its sharp drop at the cell edge (Figure 1L, Supplementary Figure S1J), we were able to apply a universal protein density threshold to detect the boundary of the cell bodies. Since nuclei have much lower lipid density than cytoplasm, they can be easily segmented as the area inside the cell body that has the lipid density smaller than a lipid threshold. Nucleoli were segmented as denser areas within nucleus by the Otsu's thresholding method (details see Material and Methods: Data Analysis). Such segmentation algorithms allowed us to process efficiently the NoRI images of different cell lines under all the different perturbations using a common objective approach without the use of additional segmentation markers or the need for subjective adjustment of the detection thresholds. Throughout the rest of this manuscript, we characterized protein and lipid densities in three subcellular compartments: the cytoplasm, nucleoplasm, and nucleolus (Figure 1M). Since the lipid density is very low in the nucleus (an average of 5 mg/ml), we analyzed the lipid density only in the cytoplasm.

To assess the reproducibility of the density measurements by NoRI, we measured the protein and lipid density in live HeLa cell cultures over a period of 7 weeks. This day-to-day variability should encompass all the instrumental variation, the variability introduced in the instrument calibration process, any biological variation introduced by using different aliquots of culture media and serum, and variation caused by cell passage number, plating density, and fluctuations in the environment. We found all the cytoplasmic, nucleoplasmic, and nucleolar protein and cytoplasmic lipid densities were maintained within tight ranges (Figures 1N,O). Consistent with the fixed cell measurements (Figure 1J), the cytoplasmic protein density was 74.5 ± 5.2 mg/ml (CV = 0.07), the cytoplasmic lipid density was 29.1 ± 5.3 mg/ml (CV = 0.18). In addition, the nucleoplasmic protein density was 81.9 ± 5.4 mg/ml (CV = 0.07), and the nucleolar protein density was 110.0 ± 5.9 mg/ml (CV = 0.05). Day-to-day variability of daily mean values showed standard deviations of 1.7 mg/ml (CV = 0.02) for the cytoplasmic protein, 1.5 mg/ml (CV = 0.05) for the cytoplasmic lipid, 2.2 g/ml (CV = 0.03) for the nucleoplasmic protein, and 2.1 mg/ml (CV = 0.02) for the nucleolar protein, which was less than half of the corresponding cell-to-cell variability. Biological replicates measured on a single day (Figures 1P,Q) showed even less variability (CV = 0.004–0.009), demonstrating both the excellent repeatability of our NoRI measurements and the remarkable stability of protein and lipid densities in HeLa cells.

Protein densities are maintained in tight ranges in each of the cell lines investigated

To test the pump leak model's prediction of that mass density is independent of cell dry mass, we quantified protein and lipid density in three different mammalian cultured cell lines: HeLa, as a representative cancer cell line from human, MDCK II as a representative epithelial cell line from dog, and NIH3T3 as a representative fibroblast cell line from mouse (Figures 2A–C). We chose these different cell types with their divergent genetic backgrounds so that any consistent behavior of mass density observed among the three would suggest that it could be a universal, conserved property of cultured, proliferating mammalian cells.

Since protein constitutes more than 70% of cell dry mass (Alberts et al., 2002), we estimated the total dry mass in these cell lines by the SE protein dye (Kafri et al., 2013) and quantified the protein and lipid densities by NoRI. The SE staining is specific for lysine groups which are nearly all on the surface of proteins and should not respond to conformational changes or denaturation. Thus, the SE modification of proteins should be stoichiometric or nearly stoichiometric (Kafri et al., 2013). However, we are aware that there could be some potential limitation of SE staining when comparing different cell lines or the same cell line under different conditions, which might express proteins with different lysine content. Nevertheless, in our measurements of different cell lines, we found that the difference in mass density was much smaller than the difference in cell dry mass. Among the 3 cell lines, HeLa is the most massive, and MDCK is the least. Their mean dry mass difference is 1.9 fold (Figure 2D). By contrast, the densest cell line, MDCK, is only 1.2 fold more dense than the most diluted

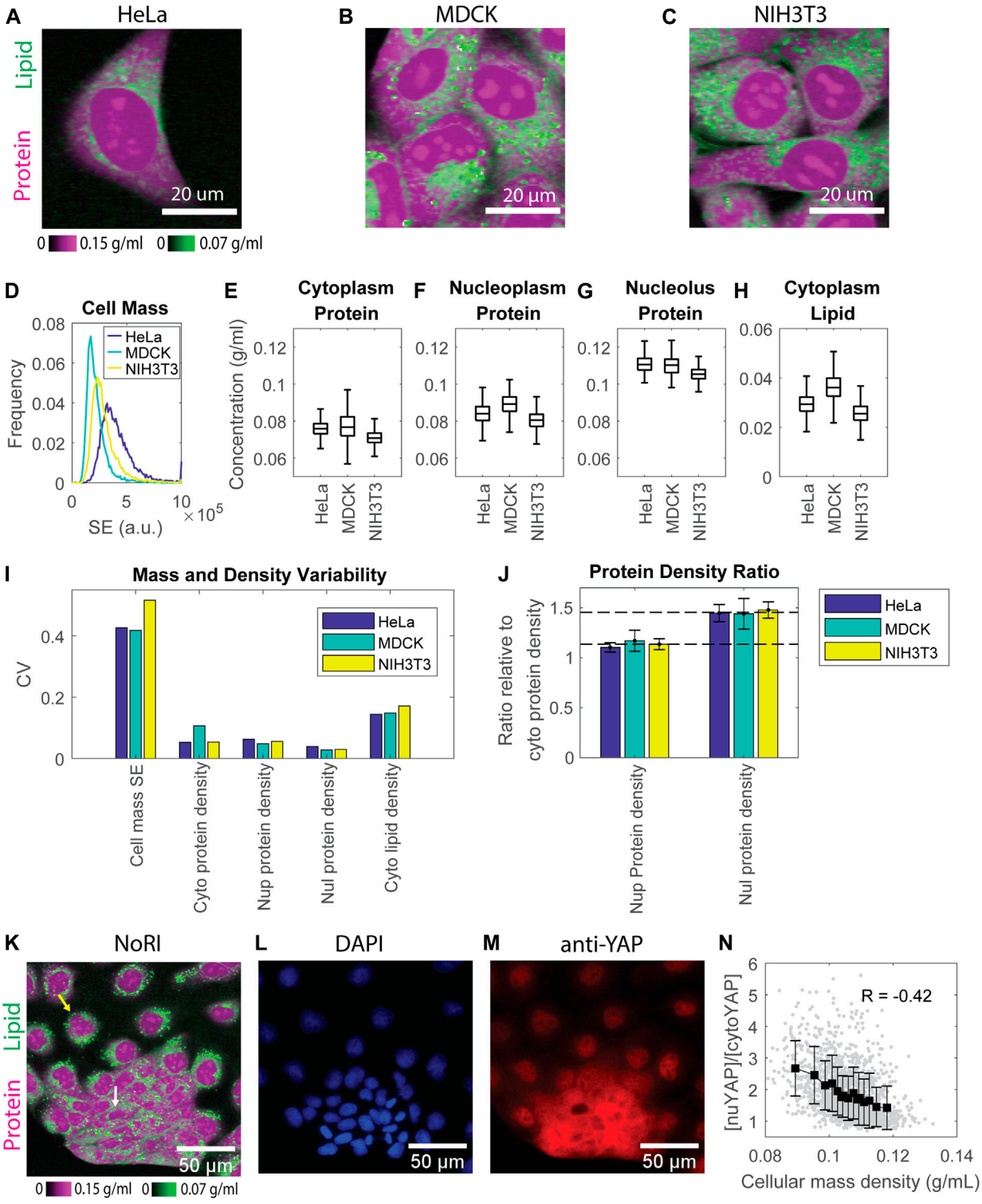

FIGURE 2
Protein densities are maintained within tight ranges in all 3 cell lines investigated. **(A–C)** NoRI images of HeLa **(A)**, MDCK **(B)**, and NIH3T3 **(C)** cells. **(D)** Dry mass distribution of the 3 cell lines estimated by the SE protein stain. *n* = 9019 for HeLa, 14478 for MDCK, and 12892 for NIH3T3, respectively. **(E–H)** Protein concentration in the cytoplasm **(B)**, nucleoplasm **(C)**, nucleolus **(D)**, and lipid concentration in the cytoplasm **(E)** measured by NoRI. *n* = 1570 (HeLa), *n* = 3056 (MDCK), *n* = 2330 (NIH3T3). **(I)** CVs of dry mass and mass densities in **(D–H)**; Nup, nucleoplasm; Nul, nucleolus; Cyto, cytoplasm. **(J)** The ratio of nucleoplasm (Nup) or nucleolus (Nul) protein density to cytoplasm (Cyto) protein density. The long dashed line indicates the averaged nucleoplasm to cytoplasm protein density ratio of the 3 cell lines at 1.1. The short dashed line indicates the
(*Continued*)

FIGURE 2 (Continued)
averaged nucleolus to cytoplasm protein density ratio of the 3 cell lines at 1.45. **(K)** NoRI image of MDCK cells showing the heterogeneous morphology: the yellow arrow indicates a representative spread-out cell, and the white arrow indicates a representative compact cell **(L,M)** Fluorescence images of DAPI stained nuclei **(L)** and immunostained YAP **(M)** in the same FOV as **(K)**. **(N)** YAP localization, quantified as nuclear YAP mean intensity divided by cytoplasmic YAP mean intensity, versus cellular mass density. Each grey dot represents a cell; black squares are the mean of each bin; error bars indicate the standard deviation of the bin; R is Pearson's correlation.

cell line, NIH3T3. The difference in protein density in all three compartments is no larger than 1.1 fold (Figures 2E–G). Cytoplasmic lipid density is more variable, with the difference between the densest and most dilute cell lines being 1.4 fold (Figure 2H). These results suggest that cultured mammalian cells maintain mass density in a much narrower range than they maintain their dry mass. Furthermore, in each cell line, the protein densities in all three compartments were maintained in tight ranges. The cell-to-cell variability (CV) was 5%–11% for cytoplasm, 5%–6% for nucleoplasm, and 3%–4% for nucleolus protein density, respectively. The variability of cytoplasm lipid density was higher, with 14%–17% CV (Figure 2I).

Consistently among all 3 cell lines, protein density in the nucleolus was higher than that in the nucleoplasm, which was higher than that in the cytoplasm (Figures 2E–G). The ratio of protein density in the three compartments is very close among the 3 cell lines, with 1.5:1.1:1 in HeLa, 1.4:1.2:1 in MDCK, and 1.5:1.1:1 in NIH3T3 cells (Figure 2J). The much denser nucleolus than other cell compartments is consistent with published measurements of cellular mass density by refractive index (Kim and Guck, 2020). The cellular mass density (the sum of protein and lipid density) ratio of these three compartments was around 1:0.85:1.05 (Supplementary Figure S2), close to the 1:0.8: 1.2 ratio found in chick nerve cells originally measured by interference microscopy (Merriam and Koch, 1960). Merriam et al. found that the ratio was constant during chick embryo development. We now find that it is also constant in three different cell lines of different cell types and genetic backgrounds, raising the question of whether the ratio might be a universal biophysical property of mammalian cells and under which conditions it might be perturbed. Note that in the 3-component NoRI method, nucleic acid mass was attributed to protein mass due to its partial overlap with the Raman band of proteins at 2935 cm^{-1}. In fixed HeLa cells, it caused 8 ± 2 mg/ml (12 ± 3%) and 11 ± 3 mg/ml (19 ± 5%) increment in protein density in the interphase nucleus and condensed chromatins in mitotic cells, respectively (Oh et al., 2022). Taking this into consideration, the protein densities in the nucleoplasm and cytoplasm are very close, consistent with the indistinguishable nuclear and cytoplasmic densities in fission yeast (Odermatt et al., 2021).

Although protein densities are maintained in a tight range for each of the 3 cell lines, we noted that MDCK cells had a nearly 2-fold higher variation in cytoplasmic protein density than HeLa and NIH3T3 cells (CV 10.6% in MDCK vs. CV 5.3% in HeLa and NIH3T3). A closer look at MDCK NoRI images revealed obvious heterogeneity in the cell morphology within the culture. There were two distinct groups of cells: one group was more spread-out and dilute, whereas the other group appeared more compact and dense (Figure 2K). Their cellular mass density was only weakly correlated with their cell dry mass (Pearson's correlatio4 0.08, p = 0.002) (Supplementary Figure S3A), suggesting that the major difference between the groups was in their volumes. Since YAP (the key transcriptional cofactor in the Hippo pathway) has been linked to cell volume regulation (Gonzalez et al., 2018; Perez-Gonzalez et al., 2019), we investigated the distribution of YAP protein by immunofluorescence in the MDCK cells. YAP is stable and can act as a transcription factor when it is in the nucleus, but it is subjected to degradation when it is translocated to the cytoplasm, where it is phosphorylated (Pocaterra, Romani and Dupont, 2020; Kwon, Kim and Jho, 2021). We found that YAP was primarily localized to the nucleus in the cells with a spread morphology, whereas in cells with a compact morphology YAP was primarily present in the cytoplasm (Figures 2K–M). To express this observation more quantitatively, we denoted the YAP localization by the ratio between the mean intensities of nuclear and cytoplasmic YAP. We found a strong correlation between that ratio and the cellular mass density (Pearson's correlation = −0.42, $p < 1e^{-66}$) (Figure 2N). However, the total YAP intensity was only weakly correlated to the cellular mass density (Pearson's correlation = −0.05, $p = 0.03$) (Supplementary Figure S3B). Therefore, the mass density depends more on YAP localization than the level of YAP expression. These results suggest a functional connection between cellular mass density and YAP localization. However, at this point, we cannot conclude that YAP activity is actually higher in dilute cells. Since dense cells have the same mass as dilute cells (Supplementary Figure S3A), they also must have a smaller volume, and the observed density increase could mean that the concentrations of all proteins are higher. We cannot assume this as different proteins could be differently affected. However, this may be the reason that the YAP concentration is higher in both the nucleus and cytoplasm of denser cells. (Supplementary Figures S3C,D). The N/C ratio was also higher in dense cells, resulting in more YAP molecules in the nucleus (Supplementary Figures S3E,F). Thus, YAP's partition between nucleus and cytoplasm and its absolute concentration in these two compartments point to different directions of YAP regulation: the partition suggests it is downregulated in denser cells, but the concentrations suggest the opposite. A firm mechanistic understanding of the

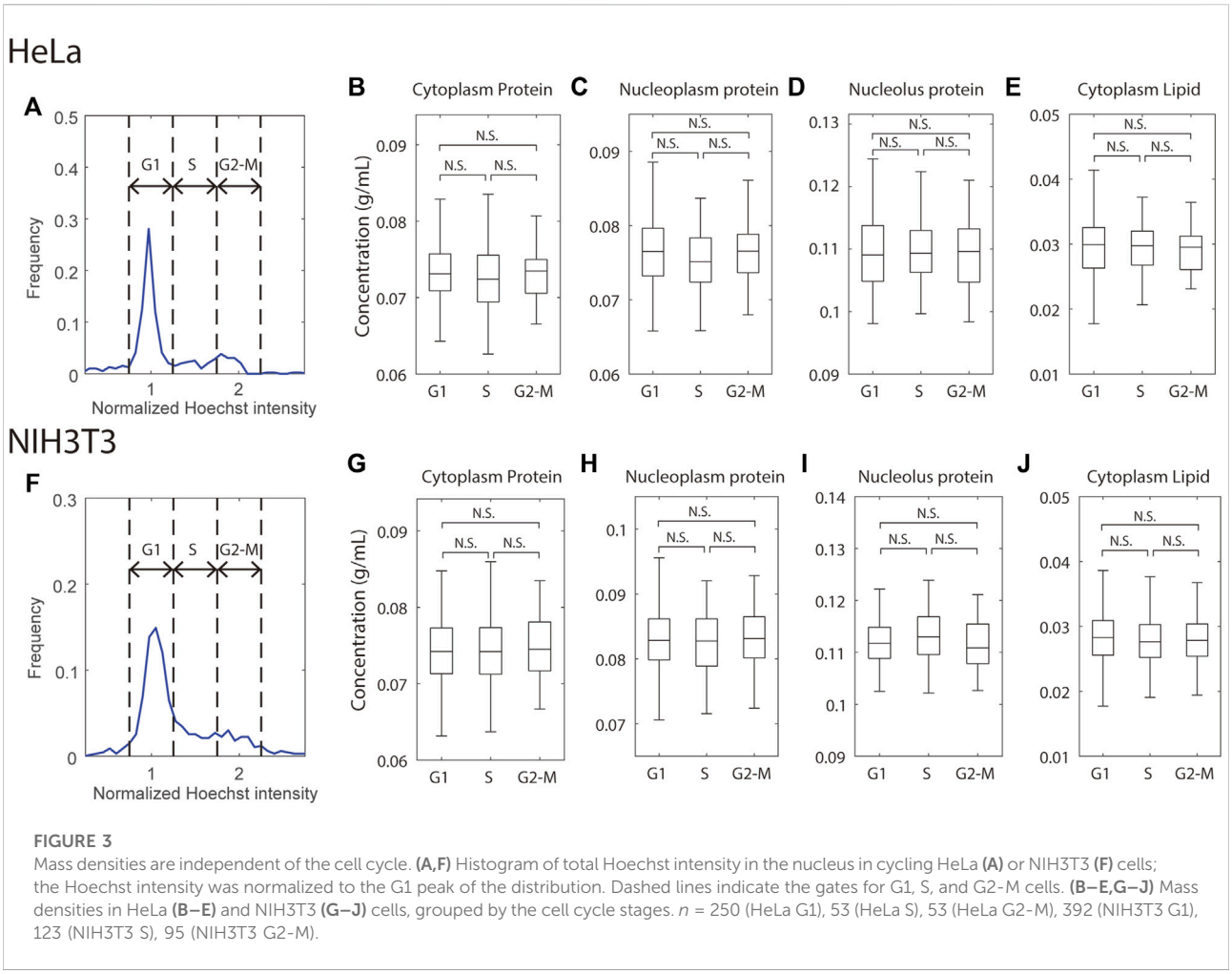

FIGURE 3
Mass densities are independent of the cell cycle. **(A,F)** Histogram of total Hoechst intensity in the nucleus in cycling HeLa **(A)** or NIH3T3 **(F)** cells; the Hoechst intensity was normalized to the G1 peak of the distribution. Dashed lines indicate the gates for G1, S, and G2-M cells. **(B–E,G–J)** Mass densities in HeLa **(B–E)** and NIH3T3 **(G–J)** cells, grouped by the cell cycle stages. *n* = 250 (HeLa G1), 53 (HeLa S), 53 (HeLa G2-M), 392 (NIH3T3 G1), 123 (NIH3T3 S), 95 (NIH3T3 G2-M).

relationship of YAP transcriptional activity and YAP localization to mass density will require further experiments.

Mass density does not vary appreciably in the cell cycle

To ask whether mass densities change during the cell cycle, we used Hoechst staining to monitor DNA content and from that, infer cell cycle stage in live cells. The cells were imaged on the confocal optics embedded in the NoRI microscope to quantify Hoechst intensity; we acquired images of protein and lipid mass densities with NoRI (see Material and Methods for more details). In this manner, we were able to identify the cell cycle stage and mass density in the same cell. The confocal pinhole was fully open to capture the Hoechst signal from the entire height of the nucleus. Due to the fact that MDCK cells are very tall, as measured from the dish to their apex, we were only able to quantify DNA content in HeLa and NIH3T3 cells (Figures 3A,F).

There was a small complication in NoRI imaging with Hoechst-stained cells. Hoechst staining is accompanied by a decrease in protein signal and an increase in lipid signal (Supplementary Figure S4). The effect is especially pronounced in the nucleoplasm protein density, where it caused a 3.7 mg/ml (4.5%) decrease in HeLa and a 4.2 mg/ml (4.8%) decrease in MDCK cells, respectively. Hoechst dye might affect mass density quantification in two ways. First, two-photon absorption (TPA) of Hoechst would add non-specific background to the SRS signals, which, after spectral decomposition and normalization, could artificially increase the lipid density and decrease the protein density. Second, most Hoechst molecules carry a positive charge at the intracellular pH (Swain et al., 2020). When Hoechst localizes to the nucleoplasm, their counter ions can increase the osmotic pressure inside the nuclear envelope and thus decrease nuclear mass density. At saturation, Hoechst can cause a 1–2 mg/ml artificial decrease in nucleoplasmic protein density quantified by NoRI and add somewhat less than 5 mOsm osmotic pressure to the nucleus. The two effects combined most likely generated the

observed small density changes seen with Hoechst stain. Nevertheless, because the nuclear volume increases with the cell volume during cell cycle, the DNA (or Hoechst) concentration (not content!) is independent of the cell cycle except for mitotic cells. Therefore, we assume that Hoechst stain does not appreciably change the relative differences in protein and lipid mass densities at different cell cycle stages.

With these considerations in mind, we binned cells at the G1, S, and G2-M stages by their total Hoechst intensity in the nucleus and found no significant difference in protein or lipid density in any of the compartments between any 2 cell cycle stages in either HeLa or NIH3T3 cells (Figures 3B–E,G–J). This result is consistent with the previous density measurement by refractive index (Kim and Guck, 2020) but contrasts with measurements of the cell cycle-dependent molecular crowding (Lecinski et al., 2021; Yamamoto et al., 2021) and diffusion rate (Pradeep and Zangle, 2022). Although mass density, molecular crowding, and diffusion rate are related, they are evaluated by molecules of very different size, which may result in distinct behaviors. For example, the cytoskeleton will perturb movement/diffusion of large macromolecular diffusion probes while being invisible to smaller ones. It is known that mitotic cells swell and dilute their mass density in prophase and prometaphase (Son et al., 2015; Zlotek-Zlotkiewicz et al., 2015), which we have confirmed with NoRI (Oh et al., 2022). However, we did not observe noticeable decreases in the G2-M densities. This may be because swollen mitotic cells only constitute a small fraction of the G2-M cells, and our automatic segmentation code has difficulty segmenting the mitotic cells as they do not have a recognizable nucleus. To conclude, the NoRI measurements are consistent with the expectations of the pump leak model, where mass density is conserved when applied to proliferating cells. In the pump leak model, mass density is maintained at a constant value because dry mass itself is the principal regulator of cell volume. Therefore, this relationship between dry mass and volume maintains mass density through the cell cycle, even though DNA content, cell dry mass, and cell volume double.

How external osmotic stress affects cytoplasmic density

According to both the simple van't Hoff equation (Atkins and De Paula, 2006) and the more sophisticated pump leak model of Essig (Essig, 1968), external osmotic stress has a direct effect on cell volume. Since a cell's response to such an external osmotic force is nearly instantaneous, it has usually been assumed that cell dry mass does not change and that any change in mass density can be directly attributed to the change in cell volume. To evaluate whether this assumption holds, we measured both the effect of external osmotic stress on intracellular density, cell mass, and cell volume. Specifically, we measured the mass densities in MDCK and HeLa cells at 1 and 3 h after switching to hypo-osmotic or hyper-osmotic media. The hypo-osmotic medium used in this study was made by diluting the complete medium with de-ionized water, and the hyper-osmotic media was by adding additional sodium chloride. As expected, cytoplasmic protein and lipid densities decreased in hypo-osmotic medium and increased in hyper-osmotic media (Figures 4A–E,H, Supplementary Figures S5A–E,H). The magnitude of the density shift decreased from 1 h to 3 h, perhaps because the cells may have changed their composition in response to the osmotic shock and/or because the initial osmotic volume change was counteracted by regulatory responses in the direction of restoring the initial volume. However, the density changes could not be solely attributed to changes in cell volume. Even a 1 hour exposure to hypo-osmotic medium caused a sizable dry mass increase (21%) in MDCK cells. The surprisingly large dry mass increase may be partially due to the compositional change of cell proteome, resulting in a disproportional change in the SE stain. Despite the dry mass increase, the volume increase was more dramatic (35%) (Supplementary Figure S6). Together, they accounted for the observed but nevertheless muted mass density decrease.

Nucleoplasmic protein density changes matched the changes in cytoplasmic protein density; the ratio of the two remained constant (Figure 4I, Supplementary Figure S7A). This behavior suggests that cells rapidly adjust their nuclear volume, perhaps in response to pressure exerted on the nuclear envelope during the osmotic response. This explanation is consistent with the previous findings that nuclear size is controlled by osmotic force within the cell (Finan and Guilak, 2009; Deviri and Safran, 2022; Lemière et al., 2022). Though nucleolar protein density changed in the same direction as nucleoplasmic protein density, the amplitude was smaller (Figure 4I, Supplementary Figure S7A). Therefore, in the hypo-osmotic medium the protein density in nucleoli became even more distinct from that of nucleoplasm, whereas in hyper-osmotic media, the protein densities in the two compartments were similar. Particularly in the +400 mOsm medium, the protein densities in the two compartments were so close that the nucleoli became indistinguishable from nucleoplasm. As a consequence, we were no longer able to segment nucleoli using protein mass density differences (Figure 4D, Supplementary Figure S5D). The protein densities of nucleolus and nucleoplasm were 0.12–0.14 g/ml in the +400 mOsm hyper-osmotic medium, a density, that is, still far below the upper limit of protein compaction (the cytoplasmic protein density of bacteria or red blood cells are over 0.3 g/ml). This suggests that the slow increase of nucleus protein density in hyper-osmotic media was not limited by protein compaction. The behaviors of nucleolus protein density in hypo- and hyper-osmotic media are consistent with the theory that nucleoli are formed by liquid-liquid phase separation generating a biomolecular condensate (Feric et al., 2016; Lafontaine et al., 2021); such a condensate would not be expected to respond to osmotic forces in the same way as the nucleoplasm, which behaves more as a classical solution.

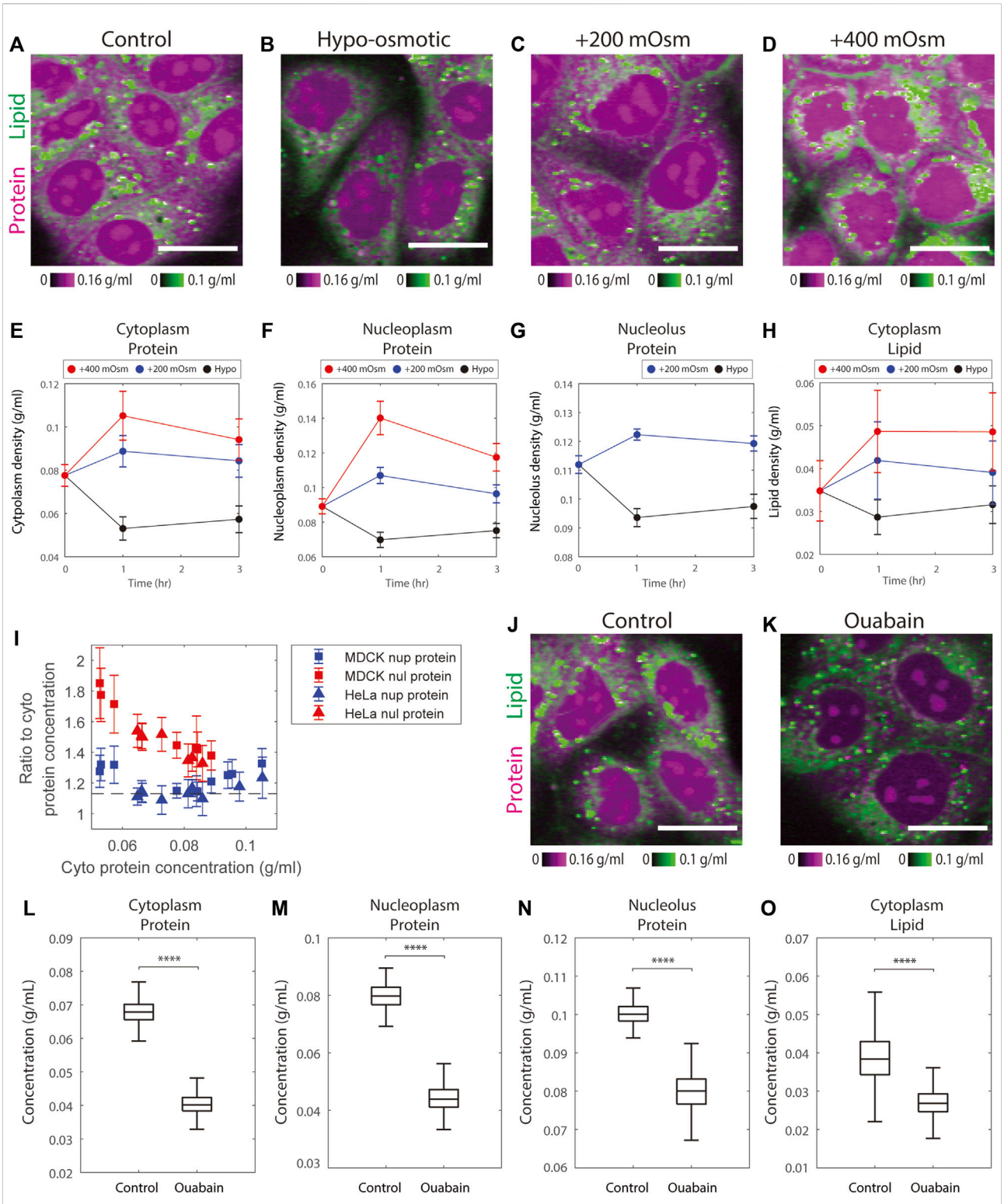

FIGURE 4
Osmotic stress alters protein and lipid densities. **(A–D)** Representative NoRI images of control MDCK cells in complete medium and MDCK cells after 3 h in hypo-osmotic or hyper-osmotic media. Scale bar, 20 μm. **(E–H)** Time course of protein and lipid density change by hyper-osmotic and hypo-osmotic treatment. Time 0 shows the control sample. Data points and error bars are the mean and standard deviation. The number of cells in each data point is between 452 and 1204 cells, with a mean of 790 cells. **(I)** The ratio of nucleoplasm (nup) or nucleolus (nul) protein density to cytoplasm protein density versus cytoplasm protein density measured in the control, hypo-, and hyper-osmotic media. The dashed line indicates the mean ratio between nucleoplasm and cytoplasm protein density from Figure 2J. **(J–K)** Representative NoRI images of control MDCK cells and MDCK cells treated with 3 μM ouabain for 5 h. Scale bar, 20 μm. **(L–O)** Change of protein and lipid density in cytoplasm, nucleoplasm, and nucleolus in MDCK cells treated with 3 μM ouabain for 5 h. *n* = 548 (Control).*n* = 665 (Ouabain).

In iso-osmotic conditions, cell volume is thought to be maintained by ion channels and transporters at the plasma membrane through the pump-leak mechanism (Essig, 1968). As the model predicts, when we inhibited the sodium-potassium pumps by ouabain for 5 h, there was a dramatic decrease in the protein densities of the cytoplasm, nucleoplasm, and nucleoli to 0.6, 0.6, and 0.8 times their original densities, respectively, as compared to control cells (Figures 4J–N). Cytoplasmic lipid density also decreased by 0.7 fold times its original density (Figure 4O). These changes were consistent with the previously observed 35% volume increase in MDCK cells treated with ouabain for 5 h (Platonova et al., 2011). In short, the results of cells treated with hypo- or hyper-osmotic media or ion pump inhibitors demonstrate the expected direct effect of osmoregulation on mass density.

Cytoskeleton disruption leads to slight increases in protein density

The pump leak model assumes that the plasma membrane maintains little tension and that it is very compliant in expansion and contraction (Kay, 2017). If the plasma membrane cannot exert much tension, perhaps the cytoskeleton can absorb some of the osmotic forces (Sitarska and Diz-Muñoz, 2020). How much the contractile and/or tensile forces of the cytoskeleton contribute to cell volume regulation has not been fully resolved (Tao and Sun, 2015; Guo et al., 2017; Kim and Guck, 2020; Venkova et al., 2022). The uncertainty that exists in the literature may be because membrane tension is specific to cell type, cell shape, and interactions with the extracellular matrix (Le Roux et al., 2019). To account for contributions of the cytoskeleton (Venkova et al., 2022). further extended the classic pump leak model by adding the mechano-sensing factor, which would act to change of membrane tension by modulating the activity of ion pumps thus changing mass density (Venkova et al., 2022). We investigated the effect of cytoskeleton on mass density by treating HeLa and MDCK cells with cytoskeleton depolymerizing drugs and with trypsin, which would act to release cells from the extracellular matrix.

Cytochalasin D is an actin depolymerizer that acts at the level of the actin subunit (Schliwa, 1982). Nocodazole is widely studied as directly acting on the tubulin dimer and blocks polymerization. Its limited toxicity and rapid reversibility have led to its wide use as an easily reversible cell cycle blocker (Downing, 2000). The effects of both drugs on cells are very rapid. Therefore, we needed to treat cells with these drugs for 1 h to massively depolymerize the cellular actin and tubulin. Neither drug caused a significant change in DNA replication (Figures 5F,L). We expected if there were any changes in mass density caused by these drugs, it should be due to a change in cell volume, not in cell dry mass. However, we found small yet significant mass *increases* in Hela treated with Cytochalasin D and MDCK treated with Nocodazole (5 and 9%, respectively) (Figures 5C,I). Cytochalasin D also caused a 10%–14% volume decrease in HeLa and MDCK cells (Figure 5D). Nocodazole caused a 7% volume decrease in HeLa but no significant change in MDCK cells (Figure 5J). The increase of cell dry mass and decrease of cell volume together caused mass density elevation in cells treated with either of the drugs. Cytochalasin D caused a 6%–9% increase in cytoplasmic protein density, a 6%–7% increase in nucleoplasmic protein density, and a 5% increase in nucleolar protein density (Figure 5G). The effect of Nocodazole was less pronounced (Figure 5M). It caused a 0%–3% increase in cytoplasmic protein density, a 4% increase in nucleoplasmic protein density, and a 2% increase in nucleolar protein density. The effects of the drugs on cytoplasmic lipid density were inconsistent among cell lines (Figures 5H,N), with a 10% increase in HeLa treated with Cytochalasin D or Nocodazole and a 6% decrease in MDCK treated with Nocodazole. The change in MDCK cells treated with Cytochalasin D was insignificant. Overall, we observed a slight protein density increase (no greater than 9% in Cytochalasin D and no greater than 4% in Nocodazole).

We observed blebs formed on 5 μM Cytochalasin D treated HeLa and MDCK cells, consistent with previous findings (Meek and Davis, 1986). Nocodazole is known to be a highly reversible drug (Zieve et al., 1980), whereas high concentrations of Cytochalasin D trigger cell death in some cell lines but not in others (White et al., 2001; Kulms et al., 2002; Ailenberg and Silverman, 2003). The morphological changes, including blebbing, in cells treated with 5 μM Cytochalasin D might be interpreted as early signs of apoptosis. To rule out the possibility that the protein density increase in cells treated with Cytochalasin D was caused by apoptosis, we measured mass densities in cells treated with a low concentration of Cytochalasin D at 1 μM. The cells were barely distinguishable from control cells in their morphology, and their trends of mass density changes were consistent with the cells treated with 5 μM Cytochalasin D (Supplementary Figures S8Q–T). Thus, we concluded that the protein density increase in Cytochalasin D was the effect of actin perturbation. Bleb formation indicates a detachment of plasm membrane from cortex and a positive hydrostatic pressure difference (outward pressure) across the plasma membrane (Dai and Sheetz, 1999; Peukes and Betz, 2014). Such outward hydrostatic pressure seems contradictory to the observed cell volume decrease (Supplementary Figures S8B,J). Furthermore, blebbing of Cytochalasin D treated cells seems paradoxical as well. Cortical tension generates the hydrostatic pressure and drives bleb expansion (Tinevez et al., 2009). However, with Cytochalasin D treatment, cortical tension drops dramatically, and blebbing would expect to cease (Tinevez et al., 2009; Peukes and Betz, 2014). What causes the bleb formation and the volume decrease in Cytochalasin D treatment require further investigation.

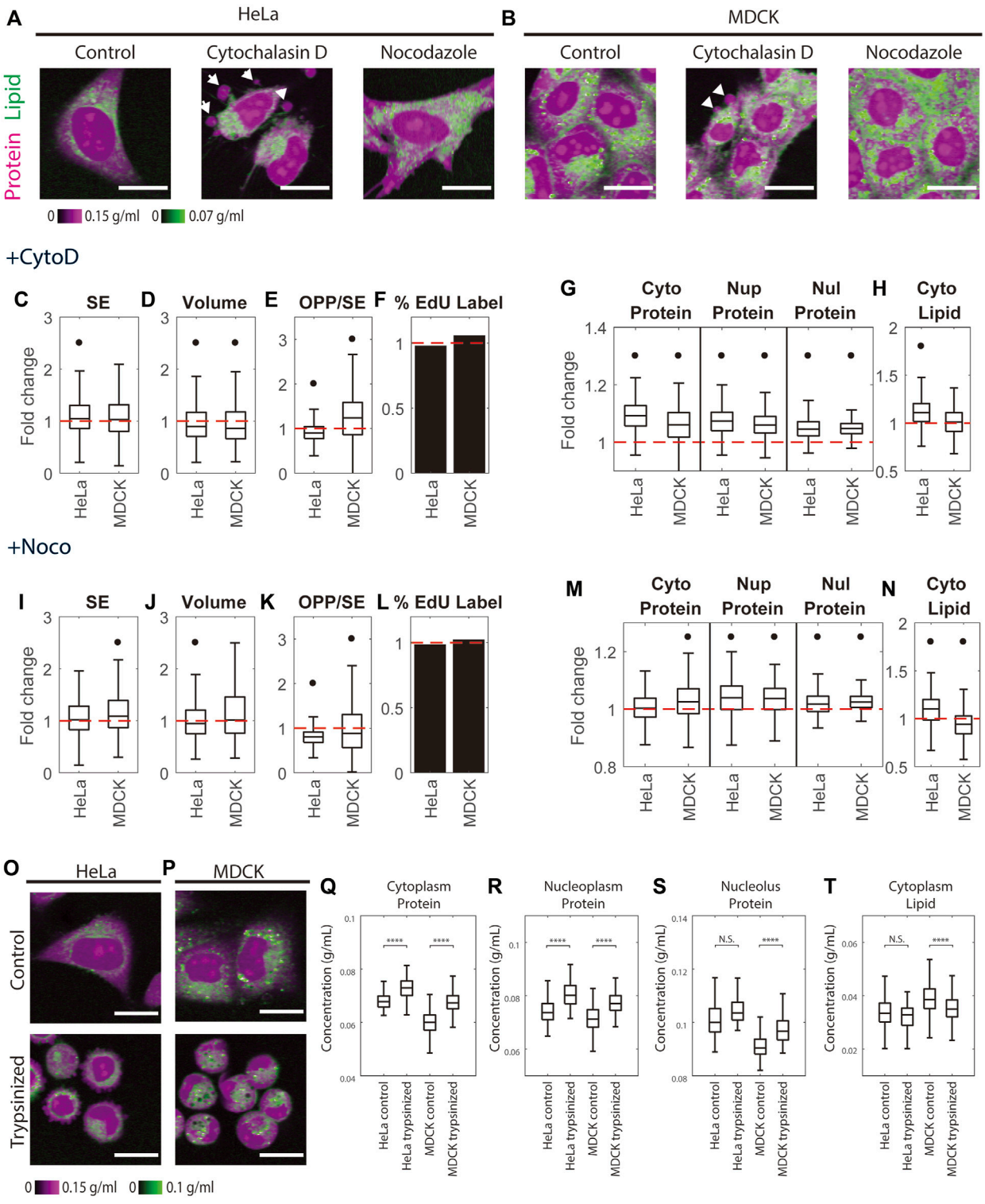

FIGURE 5
Cytoskeleton perturbation increases protein density. **(A–B)** Representative NoRI images of untreated HeLa and MDCK cells and cells treated with 5 μM Cytochalasin D or 5 μM Nocodazole for 1 h. White arrows indicate blebs. Scale bar, 20 μm. **(C–F, I–L)** Fold change of cell dry mass (SE) **(C,I)**, cell volume **(D,J)**, protein synthesis rate quantified by the pulse labeled OPP to SE protein stain ratio (OPP/SE) **(E,K)**, and DNA replication (percentage of EdU labeled cells) **(F,L)** in Cytochalasin D treated (+CytoD) or Nocodazole treated (+Noco) cells normalized to the median of untreated cells. **(G–H, M–N)** Fold change of protein densities and cytoplasmic lipid density in Cytochalasin D treated **(G–H)** or Nocodazole treated

(*Continued*)

FIGURE 5 (Continued)
(M–N) cells normalized to the median of untreated cells. Red dashed lines in **(C–N)** indicate fold change = 1 (no change). Black dots in **(C–N)** denote significant changes compared to control. The absolute changes in **(C–N)** are summarized in Supplementary Figures S8. **(O,P)** Representative NoRI images of HeLa **(O)** and MDCK **(P)** cells before and 1 h after trypsinization. **(Q–T)** Cytoplasmic protein density **(Q)**, nucleoplasm protein density **(R)**, nucleolus protein density **(S)**, and cytoplasm lipid density **(T)** in pre-trypsinized (n = 213) and post-trypsinized (n = 108) HeLa cells and pre-trypsinized (n = 578) and post-trypsinized (n = 313) MDCK cells.

We further investigated mass density change upon trypsinization which alters cytoskeleton organization in a manner different from the cytoskeletal drugs. Trypsin is a digestive protease normally secreted into the small intestine, that breaks down proteins generally. But in the context used here, it digests the extracellular matrix and extracellular domains of integral plasma membrane proteins, resulting in cell detachment from its proteinaceous substrate. The detachment of the cell from the substrate disrupts actin filament and cortical microtubule organization but does not depolymerize them as does Cytochalasin D or Nocodazole (Furcht and Wendelschafer-Crabb, 1978). After resuspending the trypsin-dissociated cells in the complete medium and plating them in a glass-bottom dish, we monitored their spreading under the NoRI microscope. We found that cells spread slowly on uncoated glass and that the protein density in all three compartments did not change significantly in the first 30 min to 2 h after plating (Supplementary Figures S9). When we compared trypsinized cells 1-h after replating with the untreated cells, we found that trypsinization caused a 7%–12.5% increase in cytoplasmic protein density, an 8%–9% increase in nucleoplasmic protein density, a 1%–8% increase in nucleolar protein density, and a 4%–10% decrease in cytoplasmic lipid density (Figures 5Q–T). Although the effect of trypsinization on cytoskeleton is less dramatic than Cytochalasin D or Nocodazole, we found that it caused more pronounced changes in mass densities. The density changes we observed in trypsinized cells might be a combined effect of cytoskeleton disruption and mechano-osmotic feedback during cell spreading (Venkova et al., 2022). It was surprising to us that lipid changed in the opposite direction from proteins, which would argue that the effects we observed were not just due to changes in volume. Although quantitative regulation of cellular lipid of non-adipocyte cells is not well understood, a recent publication reported a rapid loss of lipid during mitosis (Miettinen et al., 2022), suggesting that exocytosis can have a sizable effect on the lipid mass. An understanding of the nature of lipid mass changes during perturbation of cell shape and cell volume will require future studies.

Paradoxically protein mass density is resistant to changes in the rates of protein synthesis and protein degradation

Mass density of protein and lipid in various compartments changes very little with cell size in proliferating cells (Figures 2, 3), suggesting that total metabolites are generally proportional to cell dry mass during cell growth (Rollin, Joanny and Sens, 2022). However, this proportionality may not hold when protein synthesis, protein degradation, or global regulators of growth and degradation like mTOR activity are administered. We might, for example, expect that blocking protein synthesis or blocking protein degradation would perturb cell proteostasis in opposite ways. Such perturbations might change cell protein mass and its composition and also affect the state of free amino acid pools (Ennis and Lubin, 1964; Han et al., 2009; Nofal et al., 2017; Santos et al., 2019). A similar expectation would apply to inhibition of mTOR activity, which suppresses protein synthesis and promotes protein degradation (Zhao et al., 2015). mTOR is known to decrease cell dry mass, modulate the production of metabolites, and alter the expression of amino acid transporters (Inoki et al., 2005; Roos et al., 2009; Tucci et al., 2013). We therefore expected dramatic effects of direct pharmacological inhibition of protein synthesis, protein degradation, and mTOR activity on the concentration and composition of impermeant molecules, including protein and small metabolites, and greatly affect mass density. To test these expectations, we quantified mass densities in HeLa, MDCK, and NIH3T3 cells treated with the protein synthesis inhibitor, Cycloheximide, the protein degradation inhibitor, MG132, and the mTOR inhibitor, Rapamycin. As the change of cell dry mass and gene expression profile takes hours to reach the new steady state, we measured the cells after 24 h of treatment with these very well-characterized inhibitors.

Different cell lines are known to have different drug sensitivities and different physiological responses; therefore, we examined the effects of these inhibitors on 3 cell lines. We monitored the effects of these treatments on protein synthesis rates by the ratio of pulse-labeled OPP (O-propargyl-puromycin) to the SE protein stain, which would monitor the rate of protein synthesis per unit protein mass (Figures 6A,B). As expected, Cycloheximide and Rapamycin inhibited protein synthesis in different cell lines by 0.09–0.61 and 0.54–0.87 fold, respectively, when delivered at the same dose (Figures 6F,R). The effect of the proteasome inhibitor MG132 was more variable. It caused a 0.51-fold decrease in protein synthesis rate in MDCK cells, a 1.21-fold increase in NIH3T3 cells, and no change in HeLa cells (Figure 6L). These inhibitors also had clear effects on cell dry mass (Figures 6H,N,T). The most pronounced changes were a 1.37 fold increase in dry mass in HeLa and NIH3T3 cells treated with MG132, a 0.56 fold decrease in dry mass in NIH3T3 cells treated with Cycloheximide, and a 0.72 fold decrease in dry mass in HeLa cells treated with Rapamycin. The effect on the cell cycle

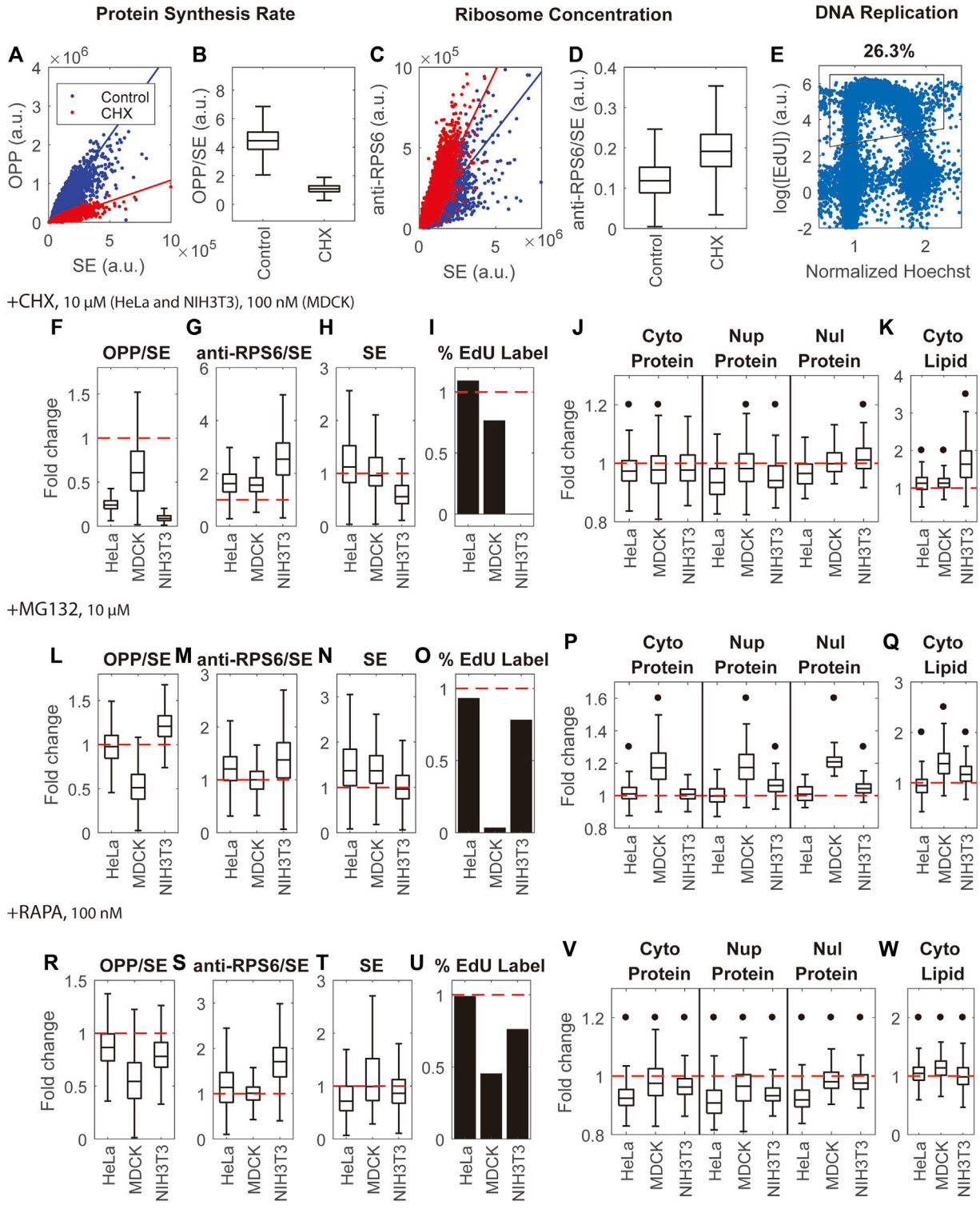

FIGURE 6
Inhibition of protein synthesis, protein degradation, and mTOR activity have little effect on mass density. **(A,B)** Quantification of protein synthesis rate by the ratio of OPP pulse label to SE protein stain (OPP/SE) demonstrated by untreated HeLa cells and HeLa cells treated by Cycloheximide (CHX). Solid lines in **(A)** are y = kx, where k is the median of the OPP to SE ratio. **(C,D)** Quantification of ribosome concentration by the anti-RPS6 immunostain to SE protein stain ratio (anti-RPS6/SE) demonstrated by untreated HeLa cells and HeLa cells treated by CHX. Solid lines in **(C)** are y = kx, where k is the median of the anti-RPS6 to SE ratio. **(E)** Quantification of DNA replication by EdU labeling in untreated HeLa cells. The

(*Continued*)

FIGURE 6 (Continued)
X-axis is the nuclear Hoechst intensity normalized by the highest peak of Hoechst distribution. The Y-axis is the logarithm of mean intensity of EdU in the nucleus. Each blue dot is a cell. The black outline is the gate for EdU label cells. **(F–I)** Fold change of protein synthesis rate (OPP/SE) **(F)**, ribosome concentration (anti-RPS6/SE) **(G)**, cell dry mass (SE) **(H)**, and DNA replication (percentage of EdU labeled cells) **(I)** in CHX treated cells **(J,K)** Fold change of protein densities **(J)** and cytoplasmic lipid density **(K)** in CHX treated cells. **(L–O)** Fold change of protein synthesis rate (OPP/SE) **(L)**, ribosome concentration (anti-RPS6/SE) **(M)**, cell dry mass (SE) **(N)**, and DNA replication (percentage of EdU labeled cells) **(O)** in MG132 treated cells. **(P,Q)** Fold change of protein densities **(P)** and cytoplasmic lipid density **(Q)** in MG132 treated cells. **(R–U)** Fold change of protein synthesis rate (OPP/SE) **(R)**, ribosome concentration (anti-RPS6/SE) **(S)**, cell dry mass (SE) **(T)**, and DNA replication (percentage of EdU labeled cells) **(U)** in Rapamycin (RAPA) treated cells. **(V,W)** Fold change of protein density **(V)** and cytoplasmic lipid density **(W)** in Rapamycin treated cells. **(F–W)** are normalized to the median of untreated cells. Red dashed lines in **(F–W)** indicate fold change = 1 (no change). Black dots in **(J–K,P–Q,V–W)** denote significant changes over controls. The absolute changes and representative NoRI images are in Supplementary Figures S10–12. Drug concentrations used in this assay are 100 nM cycloheximide for MDCK cells, 10 μM cycloheximide for HeLa and NIH3T3 cells, and 10 μM MG132 and 100 nM Rapamycin for all 3 cell lines.

of these protein synthesis and degradation inhibitors also varied. By quantifying the percentage of EdU-labeled cells (Figure 6E), we could track replication of DNA. We found that most of the drugs and cell line combinations had little effect or simply slowed down the cell cycle (Figure 6I,O,U). The two exceptions were NIH3T3 cells treated with Cycloheximide and MDCK cells treated with MG132, where the cell cycle was arrested almost completely. Since the ribosome comprises a sizable fraction (around 6%) of the protein content in mammalian cells (An et al., 2020), we investigated whether the ribosome concentration (quantified by the ratio of anti-RPS6 immunostain to the SE protein stain) correlated with mass density. Although ribosome subunit proteins are commonly used to quantify ribosome content, this has limitations because certain conditions may generate more unassembled ribosome proteins and break the proportionality between ribosome proteins and assembled ribosomes (Zhang et al., 2016; An and Harper, 2020). Thus the anti-RPS6/SE measurements should be interpreted with caution. Nevertheless, we found that the three inhibitors either had negligible effects on or increased ribosome concentration (Figures 6G,M,S). The pronounced changes in anti-RPS6 to SE ratio were a 2.6-fold increase in NIH3T3 cells in Cycloheximide, a 1.7-fold increase in NIH3T3 cells in Rapamycin, and a 1.6-fold increase in HeLa and MDCK cells in Cycloheximide.

The general conclusion from all the pharmacological treatments on multiple cell lines is that most drug treatments on the various cell lines had unexpectedly small effects on *mass density*, despite their dramatic effects on protein synthesis and degradation. There were two exceptions: NIH3T3 cells in Cycloheximide and MDCK cells in MG132, where in both cases the cell cycle was arrested. Several measurements of pharmacologic effects on mass density, though small, were statistically significant since they involved a very large number of cells (150–1000). To compare the effects of the drugs on different cell lines, we plotted the inhibitors' effects on mass density as relative changes. We found that Rapamycin decreased protein density in all measured compartments of all cell lines by 2%–9% and altered lipid density by 1%–14% (Figures 6V,W). The effect of Cycloheximide was smaller. It decreased protein density by 0%–7% and increased lipid density by 13% in HeLa and MDCK cells (Figures 6J,K). MG132 increased protein density by 1–7% and altered lipid density by 7%–16% in HeLa and NIH3T3 cells (Figure 6). The relative changes were either smaller than or comparable to the spontaneous cell-to-cell variability of these cell lines. The outlier cases, which suffered arrest of the cell cycle, showed larger effects on mass density: NIH3T3 cells in Cycloheximide showed a 2%–6% change in protein densities and a 63% increase in lipid density; MDCK cells in MG132 showed a 17%–21% increase in protein densities and a 38% increase in lipid density.

Cell senescence and starvation dramatically change cell mass density

We demonstrated that cellular protein mass density for a given cell type is stable over multiple passages, stable throughout the cell cycle, and robust to perturbation by drugs that dramatically affect cell protein mass, such as inhibitors of protein synthesis and degradation. The resistance of mass density to perturbation suggests that there is some kind of feedback that effectively maintains the protein mass density against diverse perturbations. To begin to define this feedback mechanism, we looked for perturbations that significantly affect mass density either by overwhelming the purported feedback or acting through some other regulatory pathways. The two we considered are senescence, caused by DNA damage, and quiescence, induced by serum starvation.

A common way to induce cellular senescence is by inhibiting the cell cycle through DNA damage. We treated MDCK cells with the genotoxic drug, Doxorubicin, for 5 days. As expected, cell dry mass had increased massively at the endpoint of the treatment. Measurement with the SE protein dye revealed an average 12.6-fold increase in cell dry mass (Figure 7A). Furthermore, most cells had exited the cell cycle either before or after DNA replication, as indicated by the negligible level of EdU incorporation (0.1%) (Figure 7B). We further confirmed the senescence phenotype by the high level of senescence-associated β-galactosidase (SA-β-galactosidase) activity (Dimri

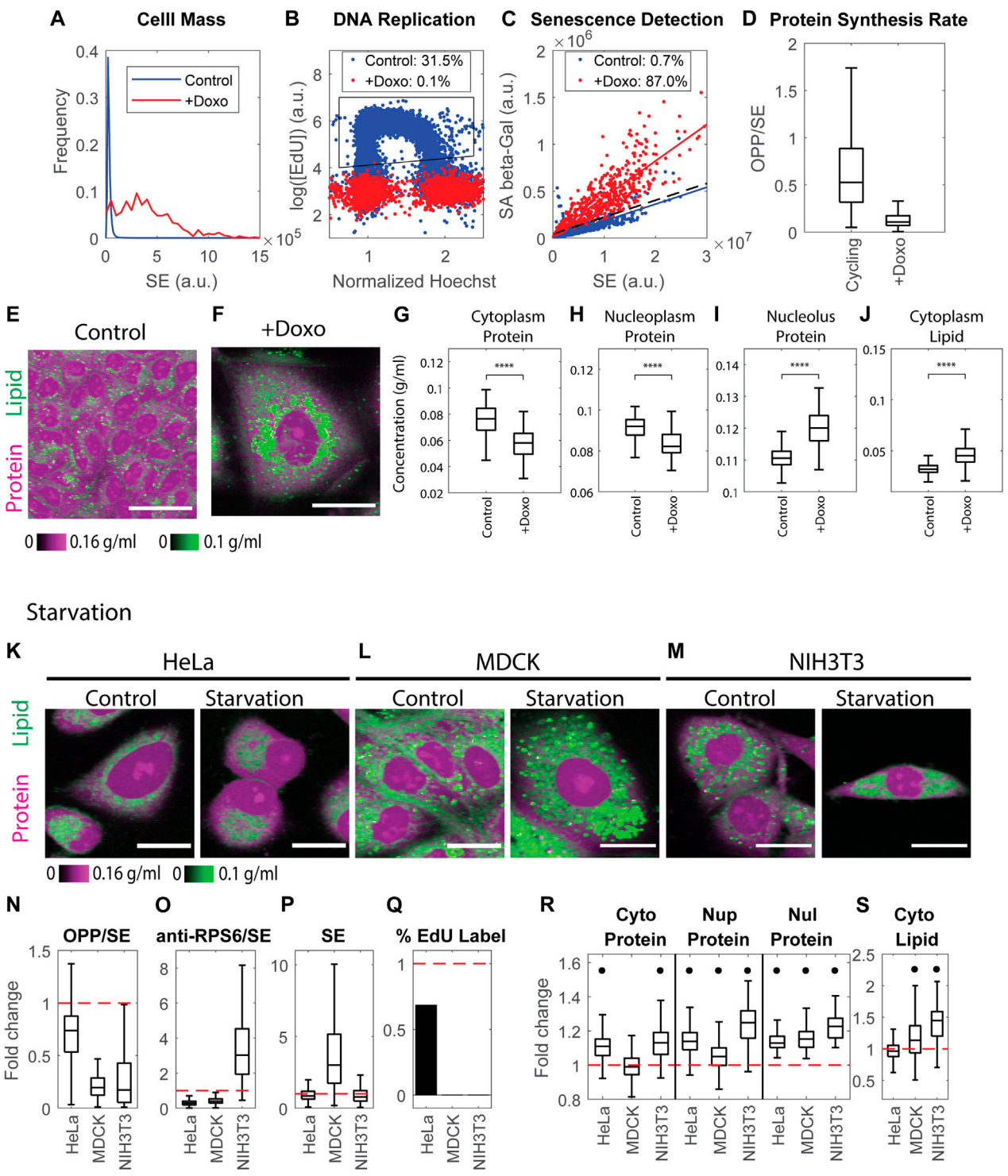

FIGURE 7
Cell senescence and quiescence change mass densities dramatically. **(A)** Cell mass distributions quantified by the SE protein stain in untreated MDCK cells and MDCK cells treated with 100 ng/ml Doxorubicin for 5 days. *n* = 26391(Control), *n* = 523 (+Doxo). **(B)** DNA replication detected by EdU incorporation in untreated MDCK cells and MDCK cells treated with 100 ng/ml Doxorubicin for 5 days. *n* = 17816 (Control), *n* = 1939 (+Doxo). Legends indicate the percentage of cells in the gated region (black polygon) of EdU incorporation. **(C)** Senescent cells detected by SA-β-galactosidase activity vs. SE protein stain. Each dot is an individual cell. Solid colored lines are the linear fit of the correlation. The dashed black line y = (*Continued*)

FIGURE 7 (Continued)
ax + 3b is the threshold used to detect senescent cells, where a is the slope of the linear fit of the control correlation, and b is the Root Mean Square Error (RMSE) of the fit. Legends indicate the percentage of senescent cells detected by this threshold. **(D)** Protein synthesis rate quantified by the OPP/SE ratio in cycling cells (Control n = 20481), and senescent cells (+Doxo n = 1134). **(E,F)** Protein and lipid concentration image of cycling **(E)** and senescent **(F)** MDCK cells. Scale bar is 40 μm. **(G–J)** Cytoplasmic protein density **(G)**, nucleoplasm protein density **(H)**, nucleolus protein density **(I)**, and cytoplasm lipid density **(J)** in senescent MDCK cells (+Doxo n = 112), compared to cycling cells (Control n = 1169). **(K–M)** Representative NoRI images of control and 0.1% serum-starved HeLa **(K)**, MDCK **(L)**, and NIH3T3 **(M)** cells. Scale bar, 20 μm. **(N–Q)** Fold change of protein synthesis rate quantified by the ratio of pulse-labeled OPP to SE protein stain (OPP/SE) **(N)**, ribosome concentration quantified by the ratio of anti-RPS6 immunostain to SE protein stain (anti-RPS6/SE) **(O)**, cell dry mass (SE) **(P)**, and DNA replication (percentage of EdU labeled cells) **(Q)** in serum starved cells normalized to the median of control cells. Red dashed line indicates change fold = 1 (no change). **(R,S)** Fold change of protein densities and cytoplasmic lipid density in serum starved cells normalized to the median of control cells. Red dashed lines indicate change fold = 1 (no change). Black dots denote significant changes. The absolute changes in **(N–S)** are summarized in Supplementary Figures S13.

et al., 1995) in the treated cells, correcting for the increase expected from the increased cell mass (Lee et al., 2006) (Figure 7C). Using this criterion, we found that 87% of treated cells were senescent. The protein synthesis rate in the senescent cells was drastically reduced, as the OPP to SE ratio was only one-fifth of that of control cells (Figure 7D). Thus, we concluded the vast majority of treated cells had reached a state of senescence.

In the starvation experiments, we confirmed the quiescent phenotype by the documented reduced protein synthesis and cell cycle arrest. MDCK and NIH3T3 cells starved in 0.1% serum for 5 days were completely arrested in the cell cycle; in addition, the rate of protein synthesis decreased by more than 80% (Figures 7N,Q). However, HeLa cells (perhaps reflecting their origin as an aggressive tumor) were more resistant to serum starvation. After being cultured in 0.1% serum for 5 days, the cell cycle was only partially inhibited, and protein synthesis decreased by only 25% (Figures 7N,Q). We concluded that most of the serum-starved MDCK and NIH3T3 cells had reached some form of quiescent state, but HeLa cells might not have achieved what is considered the typical quiescent state. Due to the reduced rates of protein synthesis, we might have expected that starvation-induced quiescence would be accompanied by lower expression in RPS6 and have resulted in reduced cell mass (Alessio et al., 2021). However, we found the phenotypes were inconsistent among cell lines. HeLa and MDCK cells had a lower RPS6 concentration (0.29 or 0.4 fold of the control cells, respectively), whereas NIH3T3 cells increased RPS6 concentration by three fold (Figure 7O). The dry mass of HeLa and NIH3T3 was 0.85 or 0.78 fold of the control cells, whereas serum-starved MDCK cells increased their dry mass by three fold (Figure 7P).

Senescence and quiescence share similarities in cell cycle repression, elevated SA-β-galactosidase activity, increase in lysosome content, and the changes in their transcriptomic profiles (Cho and Hwang, 2012; Fujimaki et al., 2019; Alessio et al., 2021). Cells in quiescence that have been starved for many days can gradually shift into a senescence-like state by increasing lysosome biogenesis and decreasing autophagy (Fujimaki et al., 2019). In stark contrast to the results of protein synthesis inhibition presented in the previous section, both senescent and quiescent states were dramatically altered in their protein and lipid *mass densities*. Furthermore, despite some similarities between senescence and quiescence, the resultant mass densities were altered in different directions. Consistent with previous findings (Okumura et al., 2015; Flor et al., 2017; Neurohr et al., 2019; Oh et al., 2022), we found that senescent cells had a significantly diluted cytoplasmic protein density (0.87 fold compared to control cells) (Figure 7G). The nucleoplasm protein density was diluted to a similar extent (0.9 fold) (Figure 7H). Surprisingly, nucleolus protein density increased by 1.08 fold (Figure 7I), and cytoplasmic lipid density also increased greatly by 1.66 fold (Figure 7J), which was consistent with previous findings (Flor et al., 2017; Oh et al., 2022).

In contrast to senescent cells, quiescent cells *increased* cytoplasm and nucleoplasm protein density (Figure 7R). Starved HeLa and NIH3T3 cells increased cytoplasmic protein density by 1.11–1.13 fold. By contrast, the change in cytoplasmic protein density in MDCK cells was negligible (Figure 7R). Nucleoplasm protein density increased by 13%, 5%, and 25% in HeLa, MDCK, and NIH3T3 cells, respectively (Figure 7R). The nucleolus protein density also increased by 13%–23% in all 3 cell lines (Figure 7R). Cytoplasm lipid density increased in MDCK cells by 1.13 fold and in NIH3T3 cells by 1.45 fold, yet the change in HeLa cells was negligible (Figure 7S). The effects of starvation on mass densities were generally more pronounced than the effects of Rapamycin. Although starvation causes mTOR inhibition, its impact on cell physiology must encompass a wider range of targets.

Discussion

Cell size is itself an ambiguous term. In various contexts it might refer to a cell's longest dimension, its area, volume, total mass, dry or buoyant mass, protein, lipid, or carbohydrate content and other macromolecular parameters. When the structure and composition of the cell over time remains uniform, these parameters should vary in parallel, meaning that each can equally serve as a measure of growth. But when they do not vary in parallel, then we have to ask what we mean by growth and ask how each might be independently regulated.

Until recently it has been very difficult to characterize growth accurately enough to answer such a question. Now with improved methods, we can gain insight into the regulation of volume, mass, and mass density and can characterize their interdependencies. Although there have been efforts to measure protein mass, lipid mass has seldom been evaluated. Previous measurements have shown that total cell dry mass is mostly regulated through protein synthesis and degradation and is very tightly controlled throughout the cell cycle to maintain cell mass homeostasis (Liu, Yan and Kirschner, 2022). By contrast, cell volume is known to vary with changes in the external milieu, responding rapidly to mechanical and osmotic stress (Hoffmann, Lambert and Pedersen, 2009; Xie, Yang and Jiang, 2018; Wang et al., 2021). Furthermore, even in the absence of such stress, cell volume swells during the prophase and prometaphase (Son et al., 2015; Zlotek-Zlotkiewicz et al., 2015) by more than 10% and fluctuates with cell shape changes, such as cell spreading (causing several percent loss in cell volume) (Venkova et al., 2022). These studies give the impression that cell dry mass and volume are independently regulated or only loosely coupled (Neurohr and Amon, 2020). However, if mass and volume were independently varying, we would expect to also see mass density (mass/volume) reflect this. Mass density changes should be consequential, since volume changes would affect all reactions, whose rate would be determined by the concentration of reactants. The effect of concentration change might be especially pronounced in highly cooperative transitions that operate near the switching threshold, such as those occurring in protein complexes (Neurohr and Amon, 2020). Reactions of high degrees of cooperativity or order could show higher sensitivity to reactant concentration, where even a small change would result in substantial changes in reaction rates or equilibrium state and perturb certain pathways (Ferrell and Ha, 2014). For this reason, we would anticipate that the cell might need to sensitively control mass density. The development of a new quantitative imaging modality for proteins and lipids, called Normalized Raman Imaging (NoRI), now allows us to address these questions through precise and direct measures of protein and lipid mass density.

Is a given mass density simply a resultant of all the reactions, synthetic and degradatory, in the cell? How fragile is that balance? We tested the resilience of cell mass density by treating cells pharmacologically with protein synthesis inhibitors, inhibitors of the proteasome, or broad inhibitors of protein metabolism by the mTOR inhibitor, Rapamycin. Such inhibitors would be expected to change the proteome and the metabolic networks significantly. As expected, these drugs strongly affect protein synthesis and degradation rates, ribosome concentration, and total cell dry mass (Figure 6), but to our surprise, they leave protein mass density essentially unchanged. This resilience suggests some form of homeostatic regulation of the mass density steady state.

Though protein mass density is remarkably stable in proliferating cells, it is not unalterable. We observed apparently spontaneous variation in mass density in unperturbed MDCK cells. Notably, this variation was strongly correlated with YAP activity in the cells (Figures 2K–N). It has already been shown that cell volume responds to mechanical stimuli and substrate rigidity through the YAP/TAZ dependent pathway; it has not previously been known how it affects mass density (Dasgupta and McCollum, 2019; Pocaterra, Romani and Dupont, 2020). Mass density also changes in global transitions of cell states, such as differentiation and in senescence (Cooper et al., 2013; Okumura et al., 2015; Neurohr et al., 2019; Oh et al., 2022). We have also observed mass density changes when cells enter a different physiological state, such as cell cycle arrest caused by the protein synthesis inhibitor Cycloheximide in NIH3T3 or cell cycle arrest caused by the proteasome inhibitor MG132 in MDCK cells (Figure 6), by serum starvation, and by genotoxic drug-induced senescence (Figure 7). In these circumstances, the perturbations must be able to circumvent whatever homeostatic mechanisms maintaining mass density. We surmise that global cell state changes like cell differentiation can override mass density control and probably reflect discrete changes in the proteome. The tradeoff between maintaining mass density and altering it may ultimately be significant in optimal cell function and may also fail in disease.

Since NoRI is a high-resolution microscopic technique, we have the ability to examine the protein density of subcellular compartments. Nuclear protein density is regulated very similarly to cytoplasmic protein density, but nucleolar protein density is not. We find a very consistent ratio of protein densities in the nucleolus, nucleoplasm, and cytoplasm, of 1.5:1.1:1, in 3 cell lines representing different cell types (Figure 2J). Particularly, the ratio of protein densities in the nucleoplasm and cytoplasm were essentially independent of the osmolarity of the extracellular medium, conditions where cytoplasmic protein density changes over a large range from 0.055 to 0.105 g/ml (Figure 4I). When corrected for the contribution of nucleic acid to the observed nucleoplasmic protein density (about 10%), the ratio indicates that the nucleoplasmic protein density is very close to the cytoplasmic protein density; both change in parallel. The nuclear envelope is known to be permeable to ions, metabolites, and small proteins (Mazzanti, Bustamante and Oberleithner, 2001) but only semi-permeable to larger proteins (larger than 60 kD) (Silver, 1991) and to RNA and, of course, impermeable to chromatin. The changes in osmotic pressure across the nuclear envelope are presumably determined by imbalances caused by active protein transport in and out of the nuclear compartment and less by the osmolarity of the impermeable chromatin and its associated ions (Deviri and Safran, 2022; Lemière et al., 2022). The equal protein densities on both sides of the nuclear envelope demonstrate that, like the plasma membrane, membrane tension on the nuclear envelope is very small. Consistent with the models proposed by Deviri and Safran (2022); Lemière et al. (2022), the ratio between nuclear and cytoplasmic volumes is proportional to the ratio between the number (not mass) of the nuclear and cytoplasmic proteins. Thus, this proportionality should be independent of pressure and tension on the plasma membrane

(Deviri and Safran, 2022; Lemière et al., 2022). This proportionality, determined by the colloidal osmotic pressure inside and outside the nuclear envelope, could serve as the mechanism for maintaining a stable nuclear-cytoplasm (N/C) ratio, as seen in many studies (Trombetta, 1942; Jorgensen et al., 2007; Neumann and Nurse, 2007; Tsichlaki and FitzHarris, 2016). To confirm this conjecture, further studies of nucleoplasmic and cytoplasmic protein densities should be done in other cell types; The 4-band NoRI (Oh et al., 2022), which independently measures protein, lipid, nucleic acid, and water density would be ideal for such studies.

Regulation of lipid density appears quite distinct from regulation of protein density. NoRI separately measures lipid mass density and its spatial distribution relative to protein. We find that lipid mass density is less constrained than protein mass density, with much larger variation in cells of the same cell type. For example, in A7 melanoma cells, the CV of lipid concentrations is 30%, while the CV for protein is 7% (Figure 1J). The CV of cytoplasmic lipid density in live HeLa, NIH3T3, and MDCK cells lies in the range of 14%–17%, while the CV for cytoplasmic protein density is 5%–11% (Figure 2I). Perhaps the lipid distribution should be considered more in terms of a phase separated domain than a solute. Indeed, compared to protein density, lipid density indicated a much larger dispersion in single cross-section vs. whole cell body correlation and a larger pixel-to-pixel variation within a cell (Supplementary Figures S1). Nevertheless, there is a positive correlation between lipid density within a cell type with changes in protein mass density under osmotic stress or cytoskeletal disruption (Figures 3, 4), showing that lipid density may also be affected by cell volume. However, this correlation is inverted when cells are treated with Cycloheximide or Rapamycin (Figure 6). Furthermore, the amplitude of lipid density changes is less consistent among different cell types than the amplitude of protein density changes. The lipid density responses to protein synthesis and mTOR inhibitors are most likely due to the very large differences in the regulation of lipid metabolism and protein with these drugs (Arbogast and Henderson, 1975; García-Sáinz, Piña and Chagoya de Sánchez, 1977; Roberts et al., 1982; Soliman, 2011; Ricoult and Manning, 2013). On the other hand, the lipid distribution can be very sensitive to perturbation in some cell types and may reflect redistribution between the Golgi-ER system and the plasma membrane. Large lipid density increases in cells other than adipocytes are known markers of physiological states, such as senescence, apoptosis, neuron damage, intracellular pathogens, and cancer (Flor et al., 2017; Shyu et al., 2018; Geltinger et al., 2020). Therefore, changes in lipid distribution may be of particular physiological significance and deserve increased attention.

To maintain homeostasis, a cell must have some way to sense protein mass density. Unlike total (dry) mass and total volume, which could in principle be sensed by processes of titration (Amodeo and Skotheim, 2015) or, more generally, by subscaled inhibitors and superscaled activators (Chen et al., 2020; Lanz et al., 2021; Xie, Swaffer and Skotheim, 2022), cells seem to be optimizing and maintaining a constant mass density against fluctuation and perturbation, while at the same time being insensitive to the total dry mass. Perhaps to do this, they utilize reactions that are ultrasensitive to density changes. It is known that the MAPK pathway is the major pathway in mammalian cells that responds to osmotic stress (de Nadal, Alepuz and Posas, 2002; Zhou et al., 2016). It is thought to modulate cell volume, metabolite composition, protein synthesis, and protein degradation (Cargnello and Roux, 2011). Perhaps it may also regulate density. How exactly mass density is sensed, what are the signaling pathways that connect it to the massive biosynthetic control and volume regulation, and how downstream effects of the pathways might compensate for stochastic perturbation are currently the key unanswered questions.

In summary, the uniformity and stability of protein mass density suggests that it may itself be the target of stringent regulation. The variation of mass density in different cell types and in different physiological states suggests it has an important role in cell physiology. How this would work is still completely unknown. For future studies, NoRI, with its vastly improved quality and ease of direct measurement of protein density and its ability to separately measure protein and lipid, would seem to be an important tool for directly reporting on mass density in diverse experimental settings, including living or fixed cultured cells or tissues. Ultimately, we will need to tie the quantitative measurement of mass density to biological circuits that regulate cell volume, metabolism, protein expression, and protein modification and study these in diverse circumstances of differentiation, cell cycle, and pathology.

Data availability statement

The raw data supporting the conclusion of this article will be made available by the authors, without undue reservation. The code used in this work is available at https://github.com/kirschnerlab/NoRI.

Author contributions

XL and SO contributed equally. XL, SO, and MK conceived and designed the research; XL and SO collected the data; XL and SO contributed analysis tools; XL and SO performed the analysis; XL, SO, and MK wrote the paper.

Funding

This research was supported by the Nation Institute of Aging of the NIH under Award 1R01AG073341-01A1.

Acknowledgments

We thank Avik Mukherjee for insightful suggestions, William John Ratzan for proofreading the manuscript and YongKeun Park and Tomocube Inc. for providing the Tomo Chamber stage-top incubator

Conflict of interest

MK and SO hold a patent for Normalized Raman Imaging (NoRI).

The remaining author declares that the research was conducted in the absence of any commercial or financial relationships that could be construed as a potential conflict of interest.

Publisher's note

All claims expressed in this article are solely those of the authors and do not necessarily represent those of their affiliated organizations, or those of the publisher, the editors and the reviewers. Any product that may be evaluated in this article, or claim that may be made by its manufacturer, is not guaranteed or endorsed by the publisher.

Supplementary material

The Supplementary Material for this article can be found online at: https://www.frontiersin.org/articles/10.3389/fcell.2022.1017499/full#supplementary-material

References

Ailenberg, M., and Silverman, M. (2003). Cytochalasin D disruption of actin filaments in 3T3 cells produces an anti-apoptotic response by activating gelatinase A extracellularly and initiating intracellular survival signals. *Biochim. Biophys. Acta* 1593 (2–3), 249–258. doi:10.1016/S0167-4889(02)00395-6

Alberts, B., Johnson, A., Lewis, J., Raff, M., Roberts, K., and Walter, P. (2002). *Molecular Biology of the cell*. 4th edn. New York, NY: Garland Science, Taylor & Francis Group.

Alessio, N., Aprile, D., Cappabianca, S., Peluso, G., Di Bernardo, G., and Galderisi, U. (2021). Different stages of quiescence, senescence, and cell stress identified by molecular algorithm based on the expression of ki67, rps6, and beta-galactosidase activity. *Int. J. Mol. Sci.* 22 (6), 3102–3113. doi:10.3390/ijms22063102

Amodeo, A. A., and Skotheim, J. M. (2015). Cell-size control. *Cold Spring Harb. Perspect. Biol.* 8, a019083. doi:10.1101/cshperspect.a019083

Amodeo, A. A., and Skotheim, J. M. (2016). Cell-size control. *Cold Spring Harb. Perspect. Biol.* 8 (4), a019083. doi:10.1101/cshperspect.a019083

An, H., and Harper, J. W. (2020). Ribosome abundance control via the ubiquitin–proteasome system and autophagy. *J. Mol. Biol.* 432 (1), 170–184. doi:10.1016/j.jmb.2019.06.001

An, H., Ordureau, A., Korner, M., Paulo, J. A., and Harper, J. W. (2020). Systematic quantitative analysis of ribosome inventory during nutrient stress. *Nature* 583 (7815), 303–309. doi:10.1038/s41586-020-2446-y

Arbogast, L. Y., and Henderson, T. O. (1975). Effect of inhibition of protein synthesis on lipid metabolism in Lactobacillus plantarum. *J. Bacteriol.* 123 (3), 962–971. doi:10.1128/jb.123.3.962-971.1975

Atkins, P. W., and De Paula, J. (2006). *Atkins' physical chemistry*. 8th edn. New York, NY: W. H. Freeman and Company.

Bryan, A. K., Hecht, V. C., Shen, W., Payer, K., Grover, W. H., and Manalis, S. R. (2014). Measuring single cell mass, volume, and density with dual suspended microchannel resonators. *Lab. Chip* 14 (3), 569–576. doi:10.1039/c3lc51022k

Cadart, C., Monnier, S., Grilli, J., Sáez, P. J., Srivastava, N., Attia, R., et al. (2018). Size control in mammalian cells involves modulation of both growth rate and cell cycle duration. *Nat. Commun.* 9 (1). doi:10.1038/s41467-018-05393-0

Cadart, C., Venkova, L., Recho, P., Lagomarsino, M., and Piel, M. (2019). The physics of cell-size regulation across timescales. *Nat. Phys.* 15 (10), 993–1004. doi:10.1038/s41567-019-0629-y

Cadart, C., Zlotek-Zlotkiewicz, E., Venkova, L., Thouvenin, O., Racine, V., Le Berre, M., et al. (2017). Fluorescence eXclusion Measurement of volume in live cells. *Methods Cell Biol.* 139, 103–120. doi:10.1016/bs.mcb.2016.11.009

Cargnello, M., and Roux, P. P. (2011). Activation and function of the MAPKs and their substrates, the MAPK-activated protein kinases. *Microbiol. Mol. Biol. Rev.* 75 (1), 50–83. doi:10.1128/MMBR.00031-10

Chen, Y., Zhao, G., Zahumensky, J., Honey, S., and Futcher, B. (2020). Differential scaling of gene expression with cell size may explain size control in budding yeast. *Mol. Cell* 78 (2), 359–370. e6. doi:10.1016/j.molcel.2020.03.012

Cho, S., and Hwang, E. S. (2012). Status of mTOR activity may phenotypically differentiate senescence and quiescence. *Mol. Cells* 33 (6), 597–604. doi:10.1007/s10059-012-0042-1

Choi, W., Fang-Yen, C., Badizadegan, K., Oh, S., Lue, N., Dasari, R. R., et al. (2007). Tomographic phase microscopy. *Nat. Methods* 4 (9), 717–719. doi:10.1038/nmeth1078

Cooper, K. L., Oh, S., Sung, Y., Dasari, R. R., Kirschner, M. W., and Tabin, C. J. (2013). Multiple phases of chondrocyte enlargement underlie differences in skeletal proportions. *Nature* 495 (7441), 375–378. doi:10.1038/nature11940

Dai, J., and Sheetz, M. P. (1999). Membrane tether formation from blebbing cells. *Biophys. J.* 77 (6), 3363–3370. doi:10.1016/S0006-3495(99)77168-7

Dasgupta, I., and McCollum, D. (2019). Control of cellular responses to mechanical cues through YAP/TAZ regulation. *J. Biol. Chem.* 294 (46), 17693–17706. doi:10.1074/jbc.REV119.007963

de Nadal, E., Alepuz, P. M., and Posas, F. (2002). Dealing with osmostress through MAP kinase activation. *EMBO Rep.* 3 (8), 735–740. doi:10.1093/embo-reports/kvf158

Deviri, D., and Safran, S. A. (2022). Balance of osmotic pressures determines the nuclear-to-cytoplasmic volume ratio of the cell. *Proc. Natl. Acad. Sci. U. S. A.* 119 (21), 1–11. doi:10.1073/pnas.2118301119

Dimri, G. P., Lee, X., Basile, G., AcostaM.Scott, G., Roskelley, C., et al. (1995). A biomarker that identifies senescent human cells in culture and in aging skin *in vivo*. *Proc. Natl. Acad. Sci. U. S. A.* 92 (20), 9363–9367. doi:10.1073/pnas.92.20.9363

Downing, K. H. (2000). Structural basis for the interaction of tubulin with proteins and drugs that affect microtubule dynamics. *Annu. Rev. Cell Dev. Biol.* 16 (1), 89–111. doi:10.1146/annurev.cellbio.16.1.89

Ennis, H. L., and Lubin, M. (1964). Cycloheximide: Aspects of inhibition of protein synthesis in mammalian cells. *Science* 146 (3650), 1474–1476. doi:10.1126/science.146.3650.1474

Essig, A. (1968). The "pump-leak" model and exchange diffusion. *Biophys. J.* 8 (1), 53–63. doi:10.1016/S0006-3495(68)86474-4

Feric, M., Vaidya, N., Harmon, T. S., Mitrea, D. M., Zhu, L., Richardson, T. M., et al. (2016). Coexisting liquid phases underlie nucleolar subcompartments. *Cell* 165 (7), 1686–1697. doi:10.1016/j.cell.2016.04.047

Ferrell, J. E., and Ha, S. H. (2014). Ultrasensitivity part III: Cascades, bistable switches, and oscillators. *Trends biochem. Sci.* 39 (12), 612–618. doi:10.1016/j.tibs.2014.10.002

Finan, J. D., and Guilak, F. (2009). The effects of osmotic stress on the structure and function of the cell nucleus. *J. Cell. Biochem.* 109, 460–467. doi:10.1002/jcb.22437

Flor, A. C., Wolfgeher, D., Wu, D., and Kron, S. J. (2017). A signature of enhanced lipid metabolism, lipid peroxidation and aldehyde stress in therapy-induced senescence. *Cell Death Discov.* 3 (1), 17075. doi:10.1038/cddiscovery.2017.75

Fujimaki, K., Li, R., Chen, H., Della Croce, K., Zhang, H. H., Xing, J., et al. (2019). Graded regulation of cellular quiescence depth between proliferation and senescence by a lysosomal dimmer switch. *Proc. Natl. Acad. Sci. U. S. A.* 116 (45), 22624–22634. doi:10.1073/pnas.1915905116

Furcht, L. T., and Wendelschafer-Crabb, G. (1978). Trypsin-induced coordinate alterations in cell shape, cytoskeleton, and intrinsic membrane structure of contact-inhibited cells. *Exp. Cell Res.* 114 (1), 1–14. doi:10.1016/0014-4827(78)90029-0

García-Sáinz, J. A., Piña, E., and Chagoya de Sánchez, V. (1977). Stimulatory action of cycloheximide on glucose metabolism in the rat epididymal fat pad. *J. Lipid Res.* 18 (1), 93–98. doi:10.1016/s0022-2275(20)41719-5

Geltinger, F., Schartel, L., Wiederstein, M., Tevini, J., Aigner, E., Felder, T. K., et al. (2020). Friend or foe: Lipid droplets as organelles for protein and lipid storage in cellular stress response, aging and disease. *Molecules* 25 (21), 5053. doi:10.3390/molecules25215053

Ginzberg, M. B., Kafri, R., and Kirschner, M. (2015). Cell biology. On being the right (cell) size. *Sci. (New York, N.Y.)* 348 (6236), 1245075. doi:10.1126/science.1245075

Gonzalez, N. P., Tao, J., Rochman, N. D., Vig, D., Chiu, E., Wirtz, D., et al. (2018). Cell tension and mechanical regulation of cell volume. *Mol. Biol. Cell* 29 (21), 0–2600. doi:10.1091/mbc.E18-04-0213

Grover, W. H., Bryan, A. K., Diez-Silva, M., Suresh, S., Higgins, J. M., and Manalis, S. R. (2011). Measuring single-cell density. *Proc. Natl. Acad. Sci. U. S. A.* 108 (27), 10992–10996. doi:10.1073/pnas.1104651108

Guo, M., Pegoraro, A. F., Mao, A., Zhou, E. H., Arany, P. R., Han, Y., et al. (2017). Cell volume change through water efflux impacts cell stiffness and stem cell fate. *Proc. Natl. Acad. Sci. U. S. A.* 114 (41), E8618–E8627. doi:10.1073/pnas.1705179114

Han, Y. H., Moon, H. J., You, B. R., and Park, W. H. (2009). The effect of MG132, a proteasome inhibitor on HeLa cells in relation to cell growth, reactive oxygen species and GSH. *Oncol. Rep.* 22 (1), 215–221. doi:10.3892/or_00000427

Haralick, R. M., and Shapiro, L. G. (1993). *Computer and robot vision*. Boston, MA: Addison-Wesley Longman Publishing Co., Inc.

Hoffmann, E. K., Lambert, I. H., and Pedersen, S. F. (2009). Physiology of cell volume regulation in vertebrates. *Physiol. Rev.* 89 (1), 193–277. doi:10.1152/physrev.00037.2007

Inoki, K., Ouyang, H., Li, Y., and Guan, K. L. (2005). Signaling by target of rapamycin proteins in cell growth control. *Microbiol. Mol. Biol. Rev.* 69 (1), 79–100. doi:10.1128/MMBR.69.1.79-100.2005

Jorgensen, P., Edgington, N. P., Schneider, B. L., Rupes, I., Tyers, M., and Futcher, B. (2007). The size of the nucleus increases as yeast cells grow. *Mol. Biol. Cell* 18 (9), 3523–3532. doi:10.1091/mbc.e06-10-0973

Kafri, R., Levy, J., Ginzberg, M. B., Oh, S., Lahav, G., and Kirschner, M. W. (2013). Dynamics extracted from fixed cells reveal feedback linking cell growth to cell cycle. *Nature* 494 (7438), 480–483. doi:10.1038/nature11897

Kay, A. R., and Blaustein, M. P. (2019). Evolution of our understanding of cell volume regulation by the pump-leak mechanism. *J. Gen. Physiol.* 151 (4), 407–416. doi:10.1085/jgp.201812274

Kay, A. R. (2017). How cells can control their size by pumping ions. *Front. Cell Dev. Biol.* 5, 41. doi:10.3389/fcell.2017.00041

Kim, K., and Guck, J. (2020). The relative densities of cytoplasm and nuclear compartments are robust against strong perturbation. *Biophys. J.* 119 (10), 1946–1957. doi:10.1016/j.bpj.2020.08.044

Kim, Y. S., Lee, S., Jung, J., Shin, S., Choi, H. G., Cha, G. H., et al. (2018). Combining three-dimensional quantitative phase imaging and fluorescence microscopy for the study of cell pathophysiology. *Yale J. Biol. Med.* 91 (3), 267–277.

Kulms, D., Dussmann, H., Poppelmann, B., Stander, S., SchwArz, A., and Schwarz, T. (2002). Apoptosis induced by disruption of the actin cytoskeleton is mediated via activation of CD95 (Fas/APO-1). *Cell Death Differ.* 9 (6), 598–608. doi:10.1038/sj.cdd.4401002

Kwon, H., Kim, J., and Jho, E. (2021). Role of the Hippo pathway and mechanisms for controlling cellular localization of YAP/TAZ. *FEBS J.* 2021, 16091. doi:10.1111/febs.16091

Lafontaine, D. L. J., Riback, J. A., Bascetin, R., and Brangwynne, C. P. (2021). The nucleolus as a multiphase liquid condensate. *Nat. Rev. Mol. Cell Biol.* 22 (3), 165–182. doi:10.1038/s41580-020-0272-6

Lanz, M. C., Zatulovskiy, E., Swaffer, M. P., Zhang, L., Ilerten, I., Zhang, S., et al. (2021). *Increasing cell size remodels the proteome and promotes senescence*. Cold Spring Harbor, NY: bioRxiv is hosted by Cold Spring Harbor Laboratory, 1–50. doi:10.1101/2021.07.29.454227

Le Roux, A.-L., Quiroga, X., Walani, N., Arroyo, M., and Roca-Cusachs, P. (2019). The plasma membrane as a mechanochemical transducer. *Philos. Trans. R. Soc. Lond. B Biol. Sci.* 374 (1779), 20180221. doi:10.1098/rstb.2018.0221

Lecinski, S., Shepherd, J. W., Frame, L., Hayton, I., MacDonald, C., and Leake, M. C. (2021). Investigating molecular crowding during cell division and hyperosmotic stress in budding yeast with FRET. *Curr. Top. Membr.* 88, 75–118. doi:10.1016/bs.ctm.2021.09.001

Lee, B. Y., Han, J. A., Im, J. S., Morrone, A., Johung, K., Goodwin, E. C., et al. (2006). Senescence-associated β-galactosidase is lysosomal β-galactosidase. *Aging Cell* 5 (2), 187–195. doi:10.1111/j.1474-9726.2006.00199.x

Lemière, J., Real-Calderon, P., Holt, L. J., Fai, T. G., and Chang, F. (2022). Control of nuclear size by osmotic forces in *Schizosaccharomyces pombe*. *eLife* 11, e76075. doi:10.7554/eLife.76075

Liu, A. X., Yan, J., and Kirschner, M. W. (2022). *Beyond G1/S regulation : How cell size homeostasis is tightly controlled throughout the cell cycle ?*. Cold Spring Harbor, NY: bioRxiv is hosted by Cold Spring Harbor Laboratory. doi:10.1101/2022.02.03.478996

Liu, X., Oh, S., Peshkin, L., and Kirschner, M. W. (2020). Computationally enhanced quantitative phase microscopy reveals autonomous oscillations in mammalian cell growth. *Proc. Natl. Acad. Sci. U. S. A.* 117 (44), 27388–27399. doi:10.1073/pnas.2002152117

Mazzanti, M., Bustamante, J. O., and Oberleithner, H. (2001). Electrical dimension of the nuclear envelope. *Physiol. Rev.* 81 (1), 1–19. doi:10.1152/physrev.2001.81.1.1

Meek, W. D., and Davis, W. L. (1986). Cytochalasin D and cationized ferritin as probes for the morphological investigation of blebbing in two human cell lines. *Vitro Cell. Dev. Biol.* 22 (12), 725–737. doi:10.1007/BF02621090

Merriam, R. W., and Koch, W. E. (1960). The relative concentration of solids in the nucleolus, nucleus, and cytoplasm of the developing nerve cell of the chick. *J. Biophys. Biochem. Cytol.* 7 (1), 151–160. doi:10.1083/jcb.7.1.151

Miettinen, T. P., Ly, K. S., Lam, A., and Manalis, S. R. (2022). Single-cell monitoring of dry mass and dry mass density reveals exocytosis of cellular dry contents in mitosis. *eLife* 11, 1–20. doi:10.7554/eLife.76664

Neumann, F. R., and Nurse, P. (2007). Nuclear size control in fission yeast. *J. Cell Biol.* 179 (4), 593–600. doi:10.1083/jcb.200708054

Neurohr, G. E., and Amon, A. (2020). Relevance and regulation of cell density. *Trends Cell Biol.* 30 (3), 213–225. doi:10.1016/j.tcb.2019.12.006

Neurohr, G. E., Terry, R. L., Lengefeld, J., Bonney, M., Brittingham, G. P., Moretto, F., et al. (2019). Excessive cell growth causes cytoplasm dilution and contributes to senescence. *Cell* 176 (5), 1083–1097. e18. doi:10.1016/j.cell.2019.01.018

Nofal, M., Zhang, K., Han, S., and Rabinowitz, J. D. (2017). mTOR inhibition restores amino acid balance in cells dependent on catabolism of extracellular protein. *Mol. Cell* 67 (6), 936–946. e5. doi:10.1016/j.molcel.2017.08.011

Odermatt, P. D., Miettinen, T. P., Lemiere, J., Kang, J. H., Bostan, E., Manalis, S. R., et al. (2021). Variations of intracellular density during the cell cycle arise from tip-growth regulation in fission yeast. *eLife* 10, e64901. doi:10.7554/eLife.64901

Oh, S., Lee, C., Yang, W., Li, A., Mukherjee, A., Basan, M., et al. (2022). Protein and lipid mass concentration measurement in tissues by stimulated Raman scattering microscopy. *Proc. Natl. Acad. Sci. U. S. A.* 119 (17), 1–11. doi:10.1073/pnas.2117938119

Okumura, N., Kusakabe, A., Hirano, H., Inoue, R., Okazaki, Y., Nakano, S., et al. (2015). Density-gradient centrifugation enables the purification of cultured corneal endothelial cells for cell therapy by eliminating senescent cells. *Sci. Rep.* 5 (1), 15005. doi:10.1038/srep15005

Otsu, N. (1979). A threshold selection method from gray-level histograms. *IEEE Trans. Syst. Man. Cybern.* 9 (1), 62–66. doi:10.1109/TSMC.1979.4310076

Perez-Gonzalez, N. A., Rochman, N. D., Yao, K., Tao, J., Le, M. T., Flanary, S., et al. (2019). YAP and TAZ regulate cell volume. *J. Cell Biol.* 218 (10), 3472–3488. doi:10.1083/JCB.201902067

Peukes, J., and Betz, T. (2014). Direct measurement of the cortical tension during the growth of membrane blebs. *Biophys. J.* 107 (8), 1810–1820. doi:10.1016/j.bpj.2014.07.076

Platonova, A., Koltsova, S., Maksimov, G. V., Grygorczyk, R., and Orlov, S. N. (2011). The death of ouabain-treated renal epithelial C11-MDCK cells is not mediated by swelling-induced plasma membrane rupture. *J. Membr. Biol.* 241 (3), 145–154. doi:10.1007/s00232-011-9371-9

Pocaterra, A., Romani, P., and Dupont, S. (2020). YAP/TAZ functions and their regulation at a glance. *J. Cell Sci.* 133 (2), jcs230425–9. doi:10.1242/jcs.230425

Pradeep, S., and Zangle, T. A. (2022). Quantitative phase velocimetry measures bulk intracellular transport of cell mass during the cell cycle. *Sci. Rep.* 12 (1), 1–14. doi:10.1038/s41598-022-10000-w

Ricoult, S. J. H., and Manning, B. D. (2013). The multifaceted role of mTORC1 in the control of lipid metabolism. *EMBO Rep.* 14 (3), 242–251. doi:10.1038/embor.2013.5

Roberts, A. F. C., Vina, J. R., Munday, M. R., FaRRell, R., and Williamson, D. H. (1982). Effects of inhibition of protein synthesis by cycloheximide on lipogenesis in mammary gland and liver of lactating rats. *Biochem. J.* 204 (2), 417–423. doi:10.1042/bj2040417

Roffay, C., Molinard, G., Kim, K., Urbanska, M., Andrade, V., Barbarasa, V., et al. (2021). Passive coupling of membrane tension and cell volume during active response of cells to osmosis. *Proc. Natl. Acad. Sci. U. S. A.* 118 (47), e2103228118. doi:10.1073/pnas.2103228118

Rollin, R., Joanny, J.-F., and Sens, P. (2022). *Cell size scaling laws: A unified theory*. Cold Spring Harbor, NY: bioRxiv is hosted by Cold Spring Harbor Laboratory. doi:10.1101/2022.08.01.502021

Roos, S., Kanai, Y., Prasad, P. D., Powell, T. L., and Jansson, T. (2009). Regulation of placental amino acid transporter activity by mammalian target of rapamycin. *Am. J. Physiol. Cell Physiol.* 296 (1), C142–C150. doi:10.1152/ajpcell.00330.2008

Santos, D. A., Shi, L., Tu, B. P., and Weissman, J. S. (2019). Cycloheximide can distort measurements of mRNA levels and translation efficiency. *Nucleic Acids Res.* 47 (10), 4974–4985. doi:10.1093/nar/gkz205

Schliwa, M. (1982). Action of cytochalasin D on cytoskeletal networks. *J. Cell Biol.* 92 (1), 79–91. doi:10.1083/jcb.92.1.79

Shyu, P., Wong, X. F. A., Crasta, K., and Thibault, G. (2018). Dropping in on lipid droplets: Insights into cellular stress and cancer. *Biosci. Rep.* 38 (5), BSR20180764. doi:10.1042/BSR20180764

Silver, P. A. (1991). How proteins enter the nucleus. *Cell* 64 (3), 489–497. doi:10.1016/0092-8674(91)90233-O

Sitarska, E., and Diz-Muñoz, A. (2020). Pay attention to membrane tension: Mechanobiology of the cell surface. *Curr. Opin. Cell Biol.* 66, 11–18. doi:10.1016/j.ceb.2020.04.001

Soliman, G. A. (2011). The integral role of mTOR in lipid metabolism. *Cell Cycle* 10 (6), 861–862. doi:10.4161/cc.10.6.14930

Son, S., Kang, J. H., Oh, S., Kirschner, M. W., Mitchison, T. J., and Manalis, S. (2015). Resonant microchannel volume and mass measurements show that suspended cells swell during mitosis. *J. Cell Biol.* 211 (4), 757–763. doi:10.1083/jcb.201505058

Swain, B. M., Guo, D., Singh, H., Rawlins, P. B., McAlister, M., and van Veen, H. W. (2020). Complexities of a protonatable substrate in measurements of Hoechst 33342 transport by multidrug transporter LmrP. *Sci. Rep.* 10 (1), 20026. doi:10.1038/s41598-020-76943-0

Tao, J., and Sun, S. X. (2015). Active biochemical regulation of cell volume and a simple model of cell tension response. *Biophys. J.* 109 (8), 1541–1550. doi:10.1016/j.bpj.2015.08.025

Tinevez, J.-Y., Schulze, U., Salbreux, G., Roensch, J., Joanny, J. F., and Paluch, E. (2009). Role of cortical tension in bleb growth. *Proc. Natl. Acad. Sci. U. S. A.* 106 (44), 18581–18586. doi:10.1073/pnas.0903353106

Trombetta, V. V. (1942). The cytonuclear ratio. *Bot. Rev.* 8 (5), 317–336. doi:10.1007/bf02882227

Tsichlaki, E., and FitzHarris, G. (2016). Nucleus downscaling in mouse embryos is regulated by cooperative developmental and geometric programs. *Sci. Rep.* 6 (1), 28040. doi:10.1038/srep28040

Tucci, P., Porta, G., Agostini, M., Antonov, A., Garabadgiu, A. V., Melino, G., et al. (2013). Rapamycin regulates biochemical metabolites. *Cell Cycle* 12 (15), 2454–2467. doi:10.4161/cc.25450

Venkova, L., Vishen, A. S., Lembo, S., Srivastava, N., Duchamp, B., Ruppel, A., et al. (2022). A mechano-osmotic feedback couples cell volume to the rate of cell deformation. *eLife* 11, 1–41. doi:10.7554/eLife.72381

Wang, P., Zhang, Q., Fang, X., Lin, F., and Huang, J. (2021). Mechanical regulation of cell volume in 3D extracellular matrices. *Extreme Mech. Lett.* 49, 101498. doi:10.1016/j.eml.2021.101498

White, S. R., Williams, P., Wojcik, K. R., Sun, S., Hiemstra, P. S., Rabe, K. F., et al. (2001). Initiation of apoptosis by actin cytoskeletal derangement in human airway epithelial cells. *Am. J. Respir. Cell Mol. Biol.* 24 (3), 282–294. doi:10.1165/ajrcmb.24.3.3995

Xie, K., Yang, Y., and Jiang, H. (2018). Controlling cellular volume via mechanical and physical properties of substrate. *Biophys. J.* 114 (3), 675–687. doi:10.1016/j.bpj.2017.11.3785

Xie, S., Swaffer, M., and Skotheim, J. M. (2022). Eukaryotic cell size control and its relation to biosynthesis and senescence. *Annu. Rev. Cell Dev. Biol.* 38 (1), 1–29. doi:10.1146/annurev-cellbio-120219-040142

Yamamoto, J., Matsui, A., Gan, F., Oura, M., Ando, R., Matsuda, T., et al. (2021). Quantitative evaluation of macromolecular crowding environment based on translational and rotational diffusion using polarization dependent fluorescence correlation spectroscopy. *Sci. Rep.* 11 (1), 1–11. doi:10.1038/s41598-021-89987-7

Zangle, T. A., and Teitell, M. A. (2014). Live-cell mass profiling: An emerging approach in quantitative biophysics. *Nat. Methods* 11 (12), 1221–1228. doi:10.1038/nmeth.3175

Zhang, T., Shen, S., Qu, J., and Ghaemmaghami, S. (2016). Global analysis of cellular protein flux quantifies the selectivity of basal autophagy. *Cell Rep.* 14 (10), 2426–2439. doi:10.1016/j.celrep.2016.02.040

Zhao, J., Zhai, B., Gygi, S. P., and Goldberg, A. L. (2015). mTOR inhibition activates overall protein degradation by the ubiquitin proteasome system as well as by autophagy. *Proc. Natl. Acad. Sci. U. S. A.* 112 (52), 15790–15797. doi:10.1073/pnas.1521919112

Zhou, X., Naguro, I., Ichijo, H., and Watanabe, K. (2016). Mitogen-activated protein kinases as key players in osmotic stress signaling. *Biochim. Biophys. Acta* 1860 (9), 2037–2052. doi:10.1016/j.bbagen.2016.05.032

Zieve, G. W., Turnbull, D., Mullins, J. M., and McIntosh, J. R. (1980). Production of large numbers of mitotic mammalian cells by use of the reversible microtubule inhibitor nocodazole. Nocodazole accumulated mitotic cells. *Exp. Cell Res.* 126 (2), 397–405. doi:10.1016/0014-4827(80)90279-7

Zlotek-Zlotkiewicz, E., Monnier, S., Cappello, G., Le Berre, M., and Piel, M. (2015). Optical volume and mass measurements show that mammalian cells swell during mitosis. *J. Cell Biol.* 211 (4), 765–774. doi:10.1083/jcb.201505056

frontiers | Frontiers in Cell and Developmental Biology

TYPE Original Research
PUBLISHED 26 October 2022
DOI 10.3389/fcell.2022.1030338

OPEN ACCESS

EDITED BY
Jette Lengefeld,
University of Helsinki, Finland

REVIEWED BY
Rohit Anthony Sinha,
Sanjay Gandhi Post Graduate Institute of Medical Sciences (SGPGI), India
Shuyuan Zhang,
Stanford University, United States

*CORRESPONDENCE
Ai-Min Huang,
aimin@fjmu.edu.cn

SPECIALTY SECTION
This article was submitted to Cell Growth and Division, a section of the journal Frontiers in Cell and Developmental Biology

RECEIVED 28 August 2022
ACCEPTED 13 October 2022
PUBLISHED 26 October 2022

CITATION
Lian Y-E, Bai Y-N, Lai J-L and Huang A-M (2022), Aberrant regulation of autophagy disturbs fibrotic liver regeneration after partial hepatectomy. *Front. Cell Dev. Biol.* 10:1030338. doi: 10.3389/fcell.2022.1030338

Aberrant regulation of autophagy disturbs fibrotic liver regeneration after partial hepatectomy

Yuan-E. Lian[1,2], Yan-Nan Bai[3], Jian-Lin Lai[3] and Ai-Min Huang[1]*

[1]Department of Pathology and Institute of Oncology, The School of Basic Medical Sciences, Fujian Medical University, Fuzhou, China, [2]Department of Pathology, The Affiliated Union Hospital of Fujian Medical University, Fuzhou, China, [3]Shengli Clinical Medical College of Fujian Medical University, Department of Hepatobiliary and Pancreatic Surgery, Fujian Provincial Hospital, Fuzhou, China

Reports indicate that autophagy is essential for maintaining hepatocyte proliferative capacity during liver regeneration. However, the role of autophagy in fibrotic liver regeneration is incompletely elucidated. We investigated the deregulation of autophagic activities in liver regeneration after partial hepatectomy using a CCl4-induced fibrosis mouse model. The baseline autophagic activity was significantly increased in the fibrotic liver. After 50% partial hepatectomy (PHx), liver regeneration was remarkably decreased, accompanied by increased hepatocyte size and binuclearity ratio. Moreover, the expression of autophagy-related proteins was functionally deregulated and resulted in a reduction in the number of autophagosome and autophagosome–lysosome fusions. We further showed upregulation of autophagy activities through verapamil administration, improved hepatocyte proliferation capacity, and restricted cellular hypertrophy and binuclearity ratio. In conclusion, we demonstrated that the impairment of liver regeneration is associated with aberrant autophagy in fibrotic liver and that enhancing autophagy with verapamil may partially restore the impaired liver regeneration following PHx.

KEYWORDS

autophagy, liver regeneration, fibrotic liver, partial hepatectomy, verapamil

Introduction

The understanding of liver regeneration has considerably improved over the past decades. Liver regeneration is characterized by an extraordinary and well-orchestrated regenerative process following partial hepatectomy (PHx) in a normal liver (Fausto et al., 2012; Tanaka and Miyajima, 2016; Michalopoulos and Bhushan, 2021). Liver fibrosis is the most common pathological alteration when the liver is insulted by numerous etiologies (e.g., drugs, alcohol, and viruses). The regeneration capacity of the fibrotic liver sharply declines yet the underlying mechanisms remain poorly understood (Andıran et al., 2000; Mann et al., 2001; Kele et al., 2013). Either in experimental or clinical studies, the poor outcome is generally attributed to compromised hepatocyte proliferation (Nagasue et al., 1987; Andiran et al., 2000; Kuramitsu et al., 2013; Aierken et al., 2020). As the fibrotic liver has a reduced regeneration capacity, the

extent of the hepatectomy is limited in terms of its clinical application due to the potential risk of acute liver failure and death.

Autophagy, an evolutionarily well-conserved catabolic pathway in processing self-degradation of intracellular material, physiologically maintains cellular homeostasis and remodeling. Autophagy acts ubiquitously at a basal level and can be induced in response to intra- or extra-cellular stimuli (Klionsky et al., 2021). Pathologically, the autophagic activity is remarkably upregulated in patients with liver cirrhosis or in experimental models with liver fibrosis (Hernandez-Gea et al., 2012; Hung et al., 2015). The autophagic activity may be induced for profibrogenesis in the liver. In zebrafish caudal fin regeneration, the autophagic activity significantly increases and plays an indispensable role in cell fate determination and proliferation (Varga et al., 2014). In the liver, the autophagic regulation of regeneration is important for maintaining metabolic balance and pre-venting hepatocyte senescence (Toshima et al., 2014). A plethora of evidence indicates that the depletion of the protein products of some critical autophagy-related genes, including Atg5 (Toshima et al., 2014), Atg7 (Lin et al., 2015; Romermann et al., 2020), and cathepsin L (Sato et al., 2019), leads to impairment of hepatocyte mitosis and proliferation. By contrast, liver regeneration can be improved through stimulation of autophagic promoters (Lin et al., 2015; Romermann et al., 2020; Lai et al., 2021).

It is paradoxical that the upregulation of the autophagic activity in liver regeneration and liver fibrosis is uninformative to interpret the impaired regeneration capacity in the fibrotic liver. Although the molecular mechanisms of autophagy in regulating the liver regeneration process were described based on the normal liver, an investigation of autophagic regulation in fibrotic liver regeneration is still lacking. In this study, we developed a murine model of liver regeneration with mild or moderate degree of liver fibrosis. We observed that liver regeneration gradually declined with the increasing severity of fibrosis. In moderate liver fibrosis after 50% PHx, hepatocyte proliferation sharply decreased, accompanied with the apparent enlargement of hepatocytes, which was a sign of hepatocyte hypertrophy (Miyaoka et al., 2012). Unexpectedly, the expression of autophagy-related proteins in the moderate fibrotic liver significantly differed from that of the liver under normal or mild fibrotic contexts. These results indicate that aberrant autophagic activities may have a poor impact on the process of liver regeneration. We also investigated whether the corrected autophagic activity by verapamil administration can partially restore the regeneration capacity.

Materials and methods

Construction of carbon tetrachloride-induced fibrotic mice

All the mice used in this study were of C57BL/6 background and were raised at the Animal Experimental Center of Fujian Medical University under previously described conditions (Lai et al., 2021).

Carbon tetrachloride (CCl4) liver fibrosis was induced in male C57BL/6 mice weighing 21.3 ± 0.2 g using previously described CCl4 mixture regimen (intraperitoneal injection with 20% CCl4 at 100 or 150 mg dosage twice a week for seven consecutive weeks). Mild and moderate liver fibrosis were set according to the proposed fibrosis staging criteria (Zhao et al., 2008). Mice with moderate fibrosis were further intraperitoneally injected with verapamil (5 mg per kg bodyweight for 10 days) prior to 50% PHx for the induction of autophagy (Lai et al., 2021).

Partial hepatectomy

PHx was performed in mice 1 week after CCL4 injection. Mice were anesthetized with 2% isoflurane continuous inhalation and subjected to approximately 50% PHx by removing the left lateral lobe, superior and inferior right lobes, or 70% PHx by removing the left lateral and median lobes, after midventral laparotomy (Martins et al., 2008). The residual liver was obtained from defined time points after PHx: 0, 6, 12, 24, 36, 48, and 72 h.

Western blot analysis

Frozen liver tissues were homogenized, and the total protein extracts were prepared according. SDS-PAGE was performed using standard western blotting protocols. The antibodies used in this study are listed in Supplementary Table S1. The proteins were then scanned using an enhanced chemiluminescence detection system (Thermo Fisher Scientific Inc., Waltham, MA, United States), and the relative density of immunoreactive bands was quantitated using ImageJ (National Institutes of Health, Bethesda, MA, United States).

Histology and immunofluorescence staining

Formalin-fixed liver tissue was processed and stained with hematoxylin and eosin or Masson's trichrome stain for the denotation of liver fibrosis.

Paraffin-fixed sections were subjected to immunofluorescence staining using standard protocols. The primary antibodies used in this study are listed in Supplementary Table S1. Nulcei were stained with Hoechst 33342 (CST, Beverly, MA, United States). Images were obtained using a microscope (ApoTome.2, Zeiss, Jena, Germany) and the accompanying software, Axiovision (version 4.7.2).

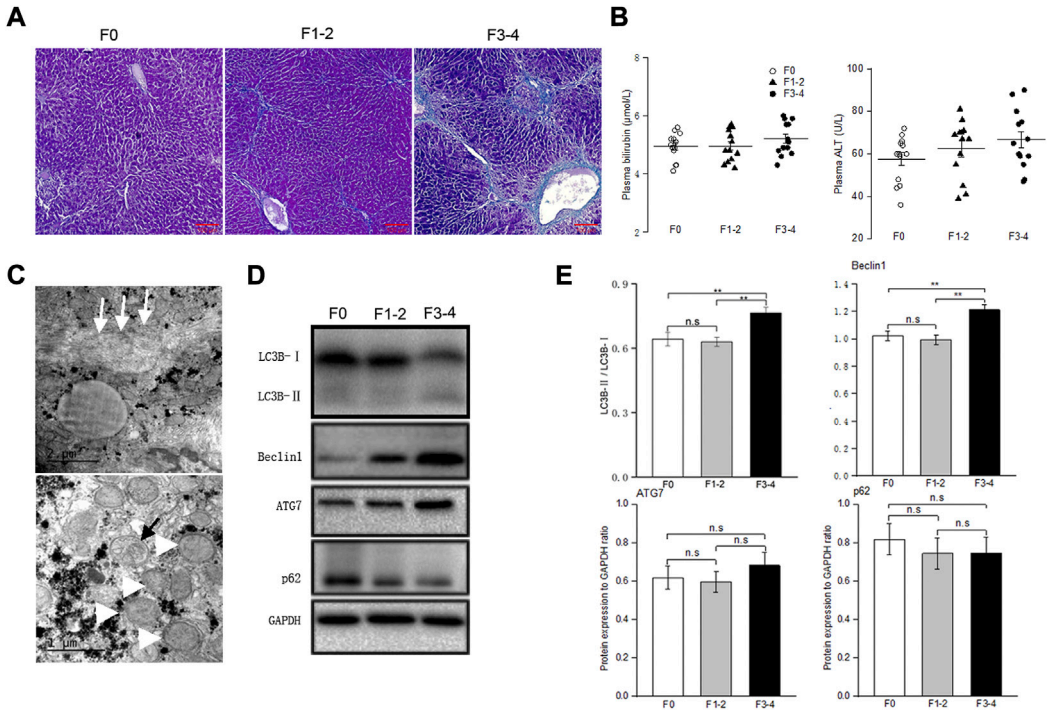

FIGURE 1
Baseline autophagic activities in fibrosis liver. **(A)**, Representative pictures of Masson trichrome staining; scale bar, 100 μm. **(B)**, Plasma bilirubin and alanine transaminase levels were unremarkably changed between groups; n = 10–12. **(C)**, Transmission electron microscopic images of autophagosomes (black arrow) and enlarged mitochondria (white arrowhead) in the fibrotic liver, collagenous fiber (white arrow) may be seen at subcellular level. **(D)**, Representative Western blot analysis depicts fibrosis and autophagic markers, including LC3B, Beclin1, ATG7, p62 (GAPDH used as loading control); GAPDH, glyceraldehyde-3-phosphate dehydrogenase. **(E)**, The intensity of protein bands was quantitated using the ImageJ software version 1.53c (NIH, Bethesda, MD; http://imagej.nih.gov/ij), and normalization of LC3B-II to LC3B-I, and Beclin1, ATG7 and p62 to GAPDH was shown. n.s, non-significance; $^{**}p < 0.01$.

Measurement of cell size and binuclearity ratio

With the combination of nuclei staining and cellular outline staining by Hoechst 33342 and phalloidin-labeled actin, respectively, hepatocytes can be recognized at the threshold of nuclear circularity (≥0.7) by the sectional area of 100–1500 μm^2. The cellular size was calculated in 300–400 individual hepatocytes per mouse using Image J (Miyaoka et al., 2012; Bou-Nader et al., 2020). To determine the number of nuclei, mononuclear and binuclear hepatocytes were quantified on 10 random high-power fields (about 3000 cells in total) on scans of stained sections. The pathologists who performed these calculations were blinded to the treatment group.

Transmission electron microscopy

The methods used for transmission electron microscopy (TEM) were described previously (Lai et al., 2021).

Statistical analysis

All statistical analyses were performed using the "survival" and "ggplot2" packages in R (version 3.6.1). All variables are expressed as the mean ± standard deviation. Continuous variables were compared using the nonparametric Wilcoxon test for independent samples or the parametric paired t-test for paired samples. Survival was calculated using the Kaplan–Meier method, and between-group differences in survival were compared using the log-rank test. Values of $p < 0.05$ were considered to indicate significance.

Results

Increased autophagic activity in the murine fibrotic liver

To determine the basal autophagy of the fibrotic liver, we generated experimental mice in F1–2 or F3–4 stages of liver fibrosis (Figures 1A,C). The severity of the liver fibrosis was

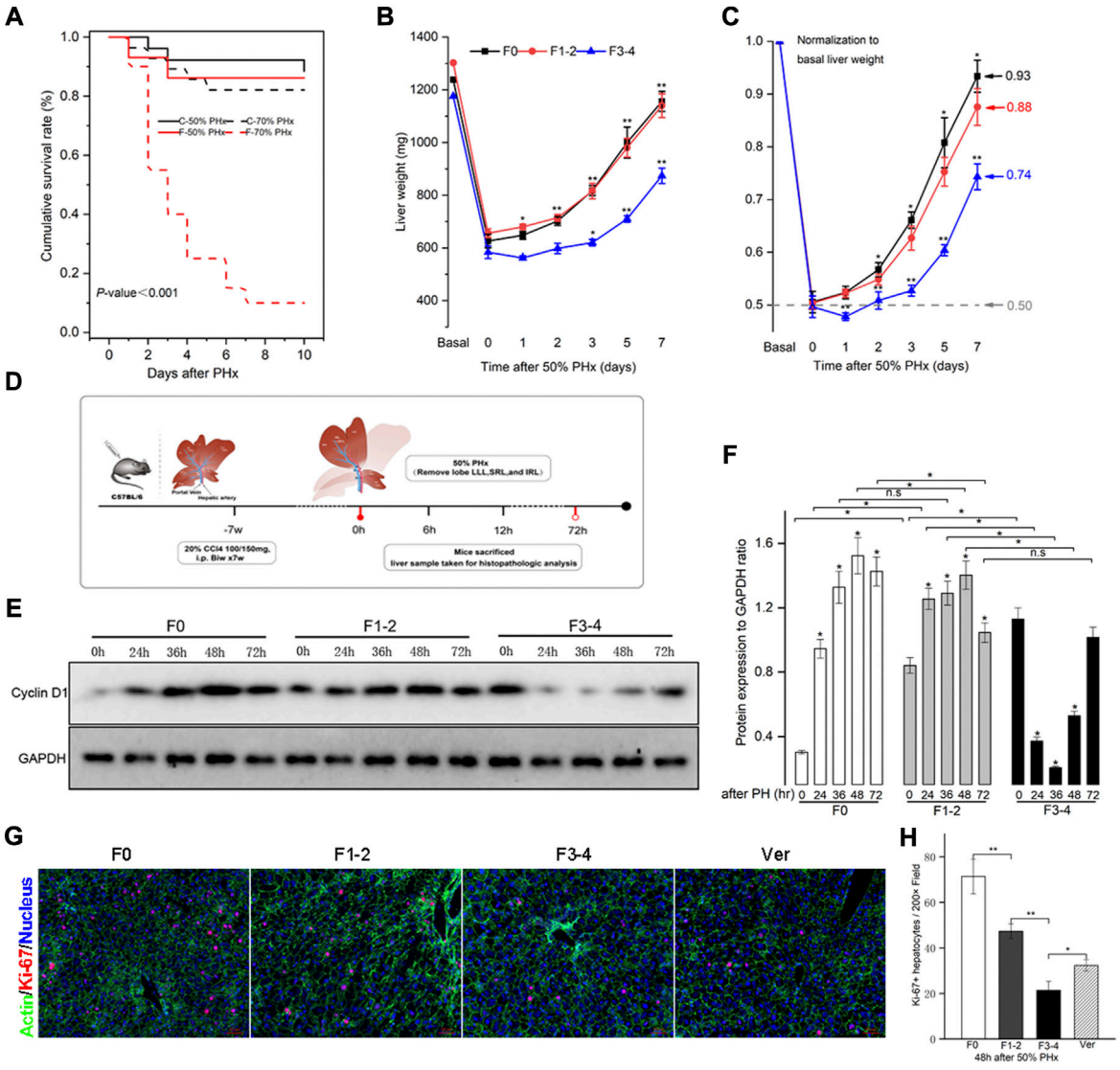

FIGURE 2
Liver fibrosis compromised survival and impaired liver regeneration capacity after PHx. CCl4-induced C57BL/6 fibrotic mouse and their counterpart littermates underwent PHx. **(A)**, Survival rate was comparable except in F3-4 fibrotic mouse underwent 70% PHx. Survival rate was calculated using the Kaplan-Meier method and was 71.8% in total mice (74/103). C, control mice with nonfibrotic liver; F, experimental mice with F3-4 fibrotic liver. **(B)**, Experimental scheme. F1-2 or F3-4 liver fibrosis was induced by chronic CCl4 injections for 7 weeks with twice dosage of 100 mg or 150 mg in C57BL/6 males, respectively. One week after last CCl4 injection, 50% PHx was performed by removing love LLL, SRL and IRL; the liver samples were harvested at the determined time points. LLL, the left lateral lobe; SRL, the superior right lobe; IRL, the inferior inferior right lobe. **(C)**, Liver weight of F0, F1-2 and F3-4 mice after 50% PHx at the determined time points. **(D)**, After normalization to basal liver weight, impaired recovery of liver mass was shown regarding to fibrotic stage. **(E)**, Hepatic cyclin D1 expression after 50% PHx was detected by western blotting. GAPDH, glyceraldehyde-3-phosphate dehydrogenase. **(F)**, The results by densitometry for cyclin D1 expression was plotted. **(G)**, Representative immunofluorescent images from liver sections stained with proliferation marker Ki-67 showed significantly low replicative activity in F1-2 or F3-4 fibrotic versus F0 livers at 48 hours after 50% PHx, while the proliferative activity was partially restored in F3-4 fibrotic mice with verapamil administration. Ver, verapamil; Scale bar, 50 μm **(H)**, Quantification of Ki-67 positive hepatocytes was plotted. Ten randomly HPFs were assessed in sections from five individual mice. HPF, high-power field. h(r), hour; n.s, non-significance; *$p < 0.05$; **$p < 0.01$.

assessed through fibrosis staging criteria that specifically apply to murine CCl4-induced fibrosis models (Zhao et al., 2008). Since there is no universal acceptance of fibrosis staging between species and etiology, liver fibrosis in F1–2 stage is basically equivalent to mild fibrosis, which is characterized by short fibrous tissue in the central venule (C) or C-C fibrotic septa appearance in histopathology. The F3–4 stage is equivalent to moderate fibrosis, which is characterized by multiple C-C fibrotic septa incompletely or completely dividing hepatic lobules into pseudo lobules. The concentration of plasma bilirubin and alanine transaminase in mild or moderate fibrotic mice increased rather unremarkably (Figure 1B). TEM showed

markedly increased number of autophagosomes in fibrotic livers and enlarged mitochondria, compared with those in nonfibrotic livers (F0 group) (Figure 1C). To confirm that the increased autophagosome formation reflects activated autophagy in fibrotic liver tissue, we determined the protein expression beclin 1 through western blotting. As an initial recruiter protein for nucleation of autophagosomes, beclin 1 expression in the F3–4 group was significantly higher than that in the F0 or F1–2 groups (Figures 1D,E). LC3B protein is another autophagosome-related marker, and the conversion of the cytoplasmic isoform LC3B-I to the membrane-associated isoform LC3B-II reflects the induction of the autophagic flux. The abundance of the LC3B-I protein gradually decreased as the liver fibrosis progressed, while the converted LC3B-II/I ratio in F3–4 liver fibrosis significantly increased (Figures 1D,E). The expression of Atg7 and p62 was determined and showed an unremarkable difference between nonfibrotic and fibrotic livers. Collectively, these observations indicated a greater autophagic process in the progression of liver fibrosis.

Impaired regeneration capacity in the murine fibrotic liver

PHx at 70% is the classic stimulating method to induce intense hepatocyte proliferation during normal liver regeneration. This type of major liver volume loss, however, caused unfavorably high mortality in fibrotic mice (Figure 2A). PHx at 50%, triggered liver regeneration less intensely as previously reported and made the postoperative vitality of the fibrotic mice comparable to PHx at 70% in normal littermates (Bonninghoff et al., 2012). Therefore, mice with 50% PHx were eventually selected secondary to the construction of CCl4-induced fibrosis (Figure 2B). As shown in Figure 2C, the usual liver parenchyma in mice with 50% PHx experienced a rapid regeneration process and restored nearly the initial liver weight at postoperative day 7 (Supplementary Table S2). Interestingly, the liver regenerative response and volume restoration of the F1–2 group were comparable to those of the F0 group but, significantly decreased in the F3–4 group. Normalization of the regeneration to basal liver mass was further processed to eliminate the bias from variant liver weight of nonfibrotic and fibrotic mice. As normalized to 0.50 owing to 50% PHx at the 0-day-time point, the regeneration index increased significantly at an early regenerative stage and regained 0.93 and 0.88 of the initial weight 7 days after PHx in F0 and F1–2 groups, respectively (Figure 2C). However, the index curve in the F3–4 group was less steep and only regained 0.74 at the corresponding time points (Figure 2D). These observations indicated impaired regenerative potential as a result of liver fibrosis.

The expression of the cyclin D1 protein is essential for cell cycle transition in the early stages of liver regeneration. As previously reported (Michalopoulos and Bhushan, 2021), cyclin D1 was induced and peaked at 48 h after PHx in F0 as well as in F1–2 groups (Figures 2E,F). In comparison, although the basal level of cyclin D1 in the F3–4 group was higher than that in the other groups, its expression declined during the early stages of liver regeneration, and the peak was delayed at 72 h after PHx. To further check hepatocyte proliferation, the immunofluorescent staining of Ki-67 at 48 h after PHx was performed. Quantification of labeled hepatocytes showed markedly decreased proliferation in the F3–4 group (Figures 2G,H). These observations indicated that the regenerative capacity was impaired and even deteriorated as liver fibrosis progressed.

Hepatocyte enlargement and increased binuclearity ratio number during liver regeneration

Besides hepatocyte proliferation and division—a compensatory response of liver hypertrophy through hepatocyte size enlargement, especially at an early stage after PHx—is of equal importance during liver regeneration (Miyaoka et al., 2012; Romermann et al., 2020). With an appropriate threshold of circularity of nuclei and actin staining, the area of each hepatocyte can be calculated precisely. As expected, hepatocytes became significantly enlarged 72 h after 50% PHx during normal liver regeneration compared to that at the baseline time point (Figures 3A,B and Supplementary Table S3). Hepatocyte enlargement in the F1–2 group was comparable (both $p = 0.04$) but was more evident in the F3–4 group ($p = 0.0001$). During homeostasis, adult hepatocytes maintained a specific and stable proportion of binuclearity; however, during the regeneration process, this proportion markedly declined. Our observation fits well with these reports in that the number of binuclear hepatocytes reduced at 72 h after 50% PHx (Figures 3A,C) (Li et al., 2009; Miyaoka et al., 2012). However, both the cellular size and binuclearity ratio increased in fibrotic liver as a result of CCl4 insult. Interestingly, the number of nuclei in the cell decreased in the F1–2 group but increased in the F3–4 group during liver regeneration. These observations indicated that fibrosis markedly impeded the regeneration process and might contribute to the failure of hepatocyte proliferation in the advanced stage.

Aberrant autophagic activity might be functional during fibrotic liver regeneration

Previous evidence indicated a dual regulatory role of autophagy in liver regeneration and fibrogenesis (Toshima

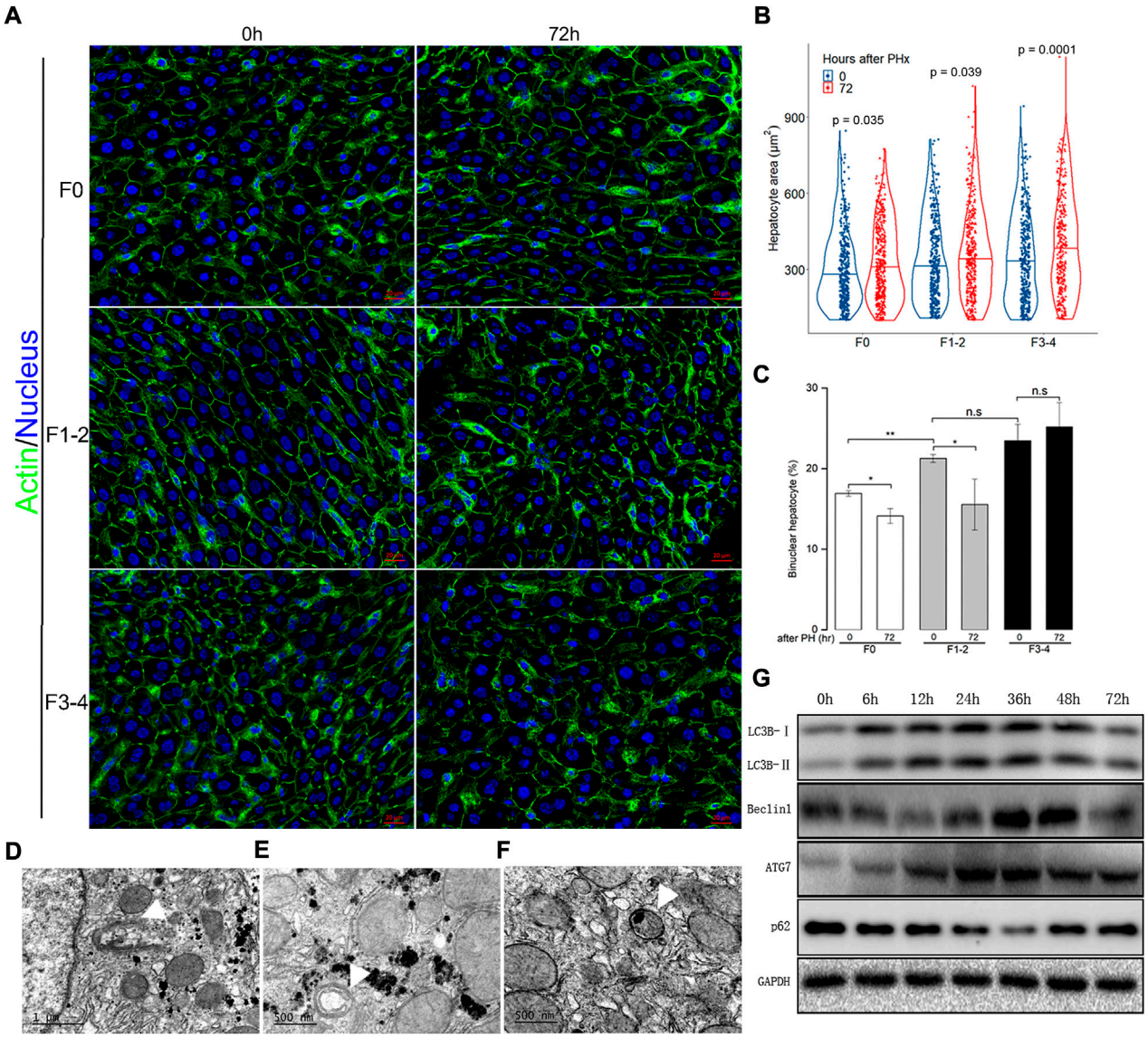

FIGURE 3
Analysis of hepatocyte size and cellular ploidy in F0, F1-2 and F3-4 fibrotic mice 72 hours after 50% PHx, and autophagic activity in the early phase of normal liver regeneration. **(A)**, Representative images of hepatocytes after 50% PHx. Staining of actin (green) and nuclei (blue) of hepatocytes were stained by Hoechst 33342 and Phalloidin respectively. Scale bar, 20 μm. **(B)**, Violin plot of hepatocyte size showed significant cell hypertrophy at 72 hours after 50% PHx, compared to baseline time point. The cellular size was calculated in 300–400 individual hepatocytes per mouse using ImageJ software. **(C)**, The number of binuclear hepatocyte was calculated and the plotted histograms showed insignificantly changed ratio of binuclear hepatocytes in F3-4 fibrotic livers. The mononuclear and binuclear hepatocytes were quantified on 10 random HPFs (about 3000 cells) on scans of stained sections. HPF, high-power field. h(r), hour; n.s, non-significance; $*p < 0.05$; $**p < 0.01$. D-F, Electron-microscopic feature of autophagosome formation (**(D)**, scale bar, 1μm), maturation (**(E)**, scale bar, 500 nm) and fusion with lysosome (**(F)**, scale bar, 500 nm) during F0 fibrotic regeneration at 48 hours after 50% PHx (white arrowhead). **(G)**, Expression of the autophagic proteins was demonstrated in F0 mice at 0-72 hours after 50% PHx.

et al., 2014; Hung et al., 2015). Since aberrant autophagy induced liver hypertrophy and compromised hepatocyte proliferation, there seemed to be a link between regulatory autophagy and hepatocyte enlargement and number of nuclei. The autophagic activity during the regenerative process, including electron microscopic features of autophagosome formation, maturation, fusion with lysosome, and upregulated expression of critical autophagy-related proteins, are presented in Figures 3D–G.

Differences in autophagic activities between the normal and fibrotic regeneration processes were further determined. In F0 mice, the conversion of cytoplasmic LC3B-I to

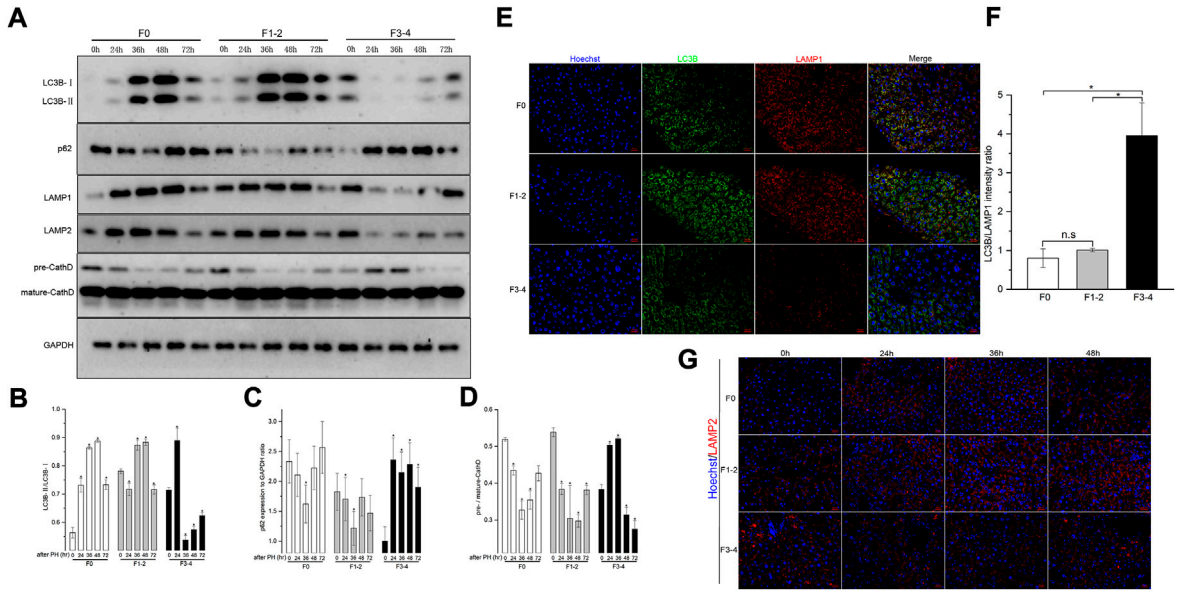

FIGURE 4
Analysis of autophagy levels in fibrotic and nonfibrotic livers. **(A)**, Representative Western blot analysis depicts that expression peak of autophagic proteins (LC3B, p62, LAMP1, LAMP2, Cathepsin D) was basically delayed as fibrosis progressed. **(B–D)**, The results by densitometry for LC3B-II/LC3B-I **(B)**, p62 **(C)**, and pre-/mature-Cathepsin D **(D)** was plotted respectively. The comparison was performed in each post-PHx time point versus baseline 0 hour. CathD, Cathepsin D; GAPDH, glyceraldehyde-3-phosphate dehydrogenase. **(E)**, Dual-immunofluorescence staining of LC3B (green) and LAMP-1 (red) in F0, F1-2 and F3-4 fibrotic livers. Nuclei (blue) of hepatocytes was stained by Hoechst 33342. Scale bar, 20 μm. **(F)**, The plotted Histograms for LC3B/LAMP1 immunofluorescent intensity ratio indicated relatively small number of autophagosome-lysosome fusions in F3-4 fibrotic livers. **(G)**, Immunofluorescence staining of LAMP2 (red) and nuclei (blue) in F0, F1-2 and F3-4 fibrotic livers. Nuclei (blue) of hepatocytes was stained by Hoechst 33342. Scale bar, 20 μm; n.s, non-significance; *$p < 0.05$.

autophagosome-bound LC3B-II and the expression of p62 protein peaked at 48 h after 50% PHx, and indicated upregulation of the autophagic flux during the regeneration process (Figures 4A–D). A similar pattern of LAMP-2 and cathepsin D expression indicated an increase in lysosome numbers and activated lysosomal function. To assess the autophagosome–lysosome fusion step, subcellular localization of the lysosomal marker LAMP-1 and the autophagosomal marker LC3B was performed at the same time points using dual immunofluorescence labeling. The immunofluorescent colocalization of punctate LC3B and LAMP-1 staining with an intensity ratio of 0.80 indicated an appropriate fusion into autolysosome at the final stage of autophagy (Figures 4E,F). In the F1–2 group, the corresponding autophagy expression during liver regeneration showed a comparable tendency to that of the F0 group. In the F3–4 group, the expression pattern showed evident differences, including delayed peak of LC3B and other proteins at 72 h after 50% PHx; this indicated delayed formation of the autophagosome and reduced immunofluorescent colocalization intensity of LC3B and LAMP-1 staining, which indicated relatively small number of autophagosome–lysosome fusions (Figure 4). Through TEM, although the formation of autophagosomes and autolysosomes reflected an autophagic process during F3–4 fibrotic liver regeneration, accompanied events of apoptotic bodies and increased flattening of mitochondria implied the presence of impaired autophagy (Figure 5A). These observations indicated that aberrant autophagic signals in the moderate fibrotic liver might account for hepatocyte enlargement and increased binuclearity ration.

Inhibition of mitotic responses during fibrotic liver regeneration

Autophagy has been found to be involved in the mitotic response of hepatocytes during the regeneration process (Toshima et al., 2014). To better understand the hepatocyte enlargement caused by aberrant autophagy, we focused on mitosis in hepatocytes during liver regeneration through examining the expression of Aurora B, which plays a centrally kinase-activated role in mitotic progression and cell division (Ruchaud et al., 2007). At 48 h after 50% PHx, the expression of Aurora B protein significantly increased in F0 and F1–2 groups, compared with its level before hepatectomy (Figures 5B,C). Conversely, the expression of Aurora B in the F3–4 group significantly decreased as expected. Regarding the critical time of the maximal entry into mitosis during liver regeneration, the

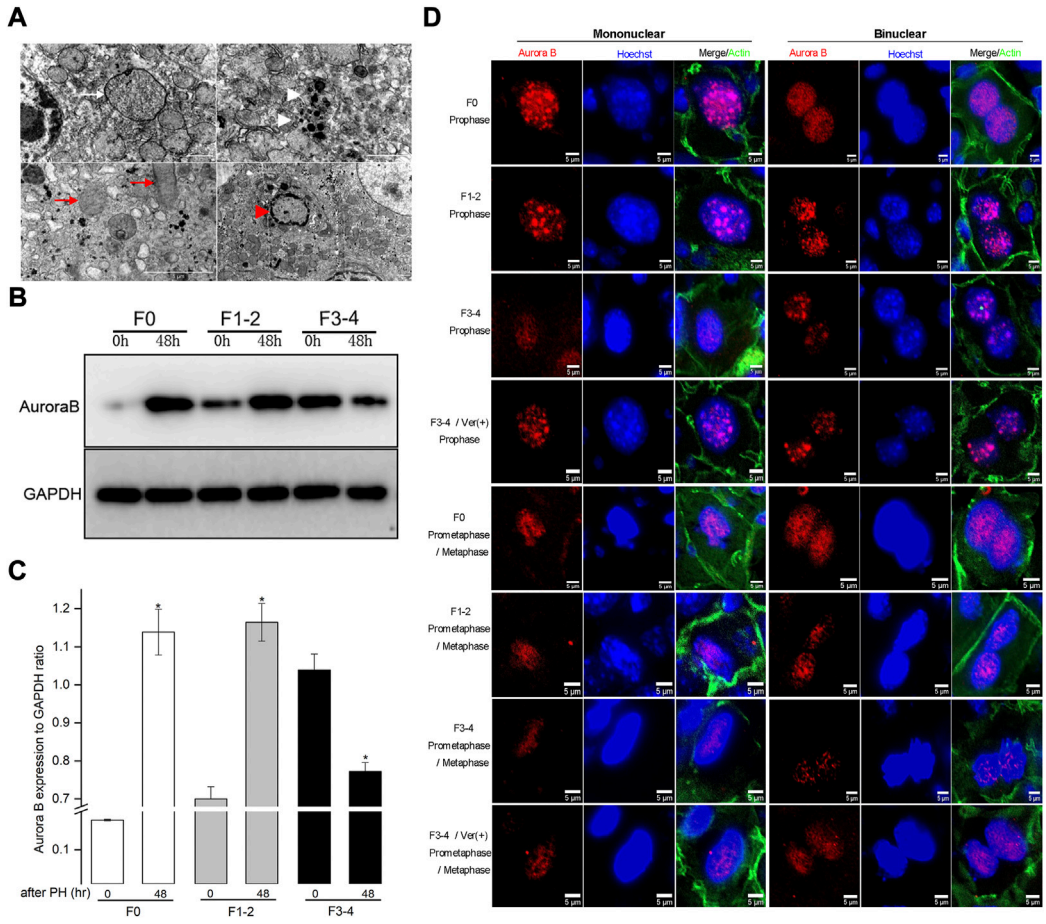

FIGURE 5
Impaired autophagic activities in F3-4 fibrotic liver regeneration and its association with mitosis. **(A)**, Representative features of impaired autophagic activities by electron-microscopically, formation of autophagosome (white arrow), autolysosome (white arrowhead), flatten mitochondria (red arrows) and apoptotic body (red arrowhead). **(B)**, Representative Western blot analysis depicts the expression of mitotic Aurora B protein in F0, F1-2, and F3-4 fibrotic mice. **(C),** The results by densitometry for Aurora B expression was plotted respectively. The comparison was performed at 48 hours after 50% PHx versus baseline 0 hour. GAPDH, glyceraldehyde-3-phosphate dehydrogenase; $*p < 0.05$. **(D)**, Immunofluorescent staining of Aurora B (red) in mononuclear (left panel) and binuclear hepatocytes (right panel) in F0, F1-2, and F3-4 fibrotic livers. Representative images at prophase (upper four rows) and prometaphase/metaphase (lower four rows) of mitosis were shown. The images of 4th and 8th row represented Aurora B staining after verapamil administration in F3-4 fibrotic mice. Nuclei (blue) of hepatocytes was stained by Hoechst 33342. Ver, verapamil; Scale bar, 5 μm.

intracellular distribution of Aurora B and morphology of nuclei can be used to represent each mitotic stage (Ruchaud et al., 2007; Miyaoka et al., 2012; Miyaoka and Miyajima, 2013). We investigated the expression of Aurora B in hepatocytes 48 h after 50% PHx using immunofluorescence (Figure 5D). In F0 pro- and prometaphase hepatocytes, the punctuated distribution of Aurora B at the chromosomes was clearly visible, for both mononuclear and binuclear hepatocytes. Aurora B remained well detectable with a slight decline in F1–2 mitotic hepatocytes. Interestingly, as liver fibrosis progressed, an obvious decline in the signals for Aurora B in F3–4 mitotic hepatocytes was observed. These observations indicated that Aurora B may be functionally affected, resulting in enlarged volume and declined proliferation of hepatocytes in fibrotic background due to aberrant autophagy.

Impaired liver regeneration could be partially restored through increased autophagy

Based on the findings presented above, we hypothesized that autophagy induction might be beneficial in improving the impaired regenerative capacity of hepatocytes in mice with moderate fibrosis. Thus, verapamil, which has been shown to pharmacologically restore the autophagosome–lysosome fusion

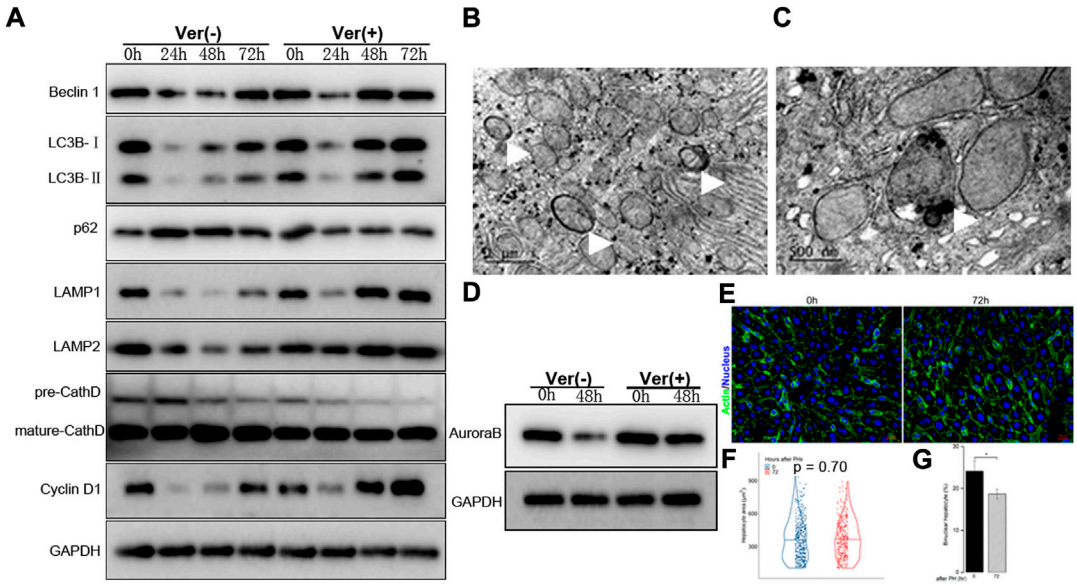

FIGURE 6
Liver regeneration capacity was partially restored under corrected autophagy after 50% PHx. **(A)**, Representative Western blot analysis depicts that expression of autophagic proteins (Beclin1, LC3B, p62, LAMP1, LAMP2, Cathepsin D) and cyclin D1 in the F3-4 fibrotic liver of mice with or without verapamil administration. **(B–C)**, Representative features of upregulated autophagy by electron-microscopically, including increased formation of autophagosome ((**B**), white arrows), autolysosome ((**C**), white arrow). **(D)**, Representative Western blot analysis depicts that expression of Aurora B. **(E)**, Representative images of hepatocytes in the F3-4 fibrotic liver of mice with or without verapamil administration. Staining of actin (green) and nuclei (blue) of hepatocytes were stained by Hoechst 33342 and Phalloidin respectively. Scale bar, 20 μm. **(F)**, Violin plot of hepatocyte size showed insignificant cell hypertrophy at 72 hours after 50% PHx, compared to baseline time point. **(G)**, The number of binuclear hepatocyte was calculated and the plotted histograms showed a significantly declined ratio of binuclear hepatocytes after verapamil administration. Ver, verapamil; GAPDH, glyceraldehyde-3-phosphate dehydrogenase; h, hour; *$p < 0.05$.

among other benefits, was administered prior to 50% PHx in F3–4 mice (Park et al., 2014; Lai et al., 2021). Remarkably, the verapamil treatment induced Atg-related protein expression earlier than that in the non-treated mice; the peak of beclin 1, LC3B, and LAMP-1/2 expression occurred 48 h after 50% PHx (Figure 6A). Through electron microscopy, the number of autophagosomes and autolysosomes were observed to increase, but there were virtually no diseased mitochondria or apoptotic bodies (Figures 6B,C and data not shown). These observations indicated that verapamil administration improved the aberrant autophagy activity in the fibrotic liver.

Accordingly, we explored whether the corrected autophagy would improve regenerative capacity. No mortality was caused by the verapamil treatment, and the expression of cyclin D1 protein increased from 48 to 72 h after 50% PHx (Figure 6A). In verapamil-treated mice, the Ki-67 labeling index was significantly higher than that in non-treated mice (Figures 2G,H). Similarly, the expression of Aurora B (Figure 6D) and immunofluorescent punctuated Aurora B signals (Figure 5D) were partially recovered, for both mononuclear and binuclear pro-/prometaphase hepatocytes. Based on micro-morphology, the hepatocyte size in verapamil-treated mice was insignificantly enlarged, and hepatocytes exhibited a descending binuclearity ratio postoperatively (Figures 6F,G and Supplementary Table S3) compared to those of non-treated mice. These observations indicated that hepatocyte proliferation was partially restored as a result of autophagy enhancement by verapamil during liver regeneration.

Discussion

In this study, we investigate the relationship between autophagy and liver regeneration in 50% PHx models with different degrees of fibrosis. To the best of our knowledge, we found, for the first time, that fibrotic mice have reduced autophagic activity in the early stages of liver regeneration (Figure 4). The suppression of autophagy is intensified when liver fibrosis progresses. In fact, the tendency of autophagic activity in mice with mild fibrosis was generally consistent with that in normal mice, which is upregulated in the early stages of liver regeneration and is critical for the protection of hepatocyte proliferation and organ homeostasis (Toshima et al., 2014; Sato et al., 2019; Romermann et al., 2020). By contrast,

downregulated autophagy was observed in mice with moderate fibrosis with hepatocyte enlargement and increased binuclearity ratio, which indicated impaired regeneration capacity (Figure 3). Surprisingly, the impaired regeneration could be partially restored through pharmacological autophagic induction (Figure 6). In mice with moderate liver fibrosis, we found that corrected autophagy causes Aurora B expression of mononuclear or binuclear pro-/prometaphase hepatocytes to increase, which mechanistically indicated the entry into mitosis (Figures 5, 6). Furthermore, corrected autophagy increased the expression of proliferation-related proteins (cyclin D1 and Ki-67) and improved hepatocyte enlargement and binuclearity ratio (Figures 2, 6). Thus, aberrant autophagy in mice with liver fibrosis impaired hepatocyte proliferation during liver regeneration and could be partially ameliorated through pharmacological autophagic induction.

Liver fibrosis is an adaptive response attributed to chronic hepatic insults with drugs, alcohol, and viruses. Unlike normal liver regeneration, the pathophysiology of fibrotic liver regeneration, characterized by comprehensive failure of hepatocytes to replicate, remained to be elucidated. In agreement with previous reports (Hernandez-Gea et al., 2012; Kuramitsu et al., 2013; Hung et al., 2015), the baseline upregulation of autophagy in CCl4-induced liver fibrosis and impairment of liver regeneration after 50% PHx in the fibrotic mouse was indicated (Figures 1. In that context, alteration of autophagy seems to play a "double-edged sword" role in the pathogenesis of liver diseases. In patients with α1-antitrypsin deficiency, autophagy is specifically triggered for the intracellular degradation of the misfolded AT proteins to prevent cellular enlargement and hepatomegaly (Marciniak and Lomas, 2010). The activation of autophagy is similarly triggered by insults with alcohol (Gual et al., 2017), CCl4 (Hernandez-Gea et al., 2012), and steatosis (Singh et al., 2009; Czaja, 2011), whereas the hepatic depletion of autophagy causes metabolic and energetic dysfunction of hepatocytes, which can lead to hepatomegaly, fibrosis, or carcinogenesis. In another study, the activation of autophagy was identified as a profibrogenic factor in activated hepatic stellate cells (Hung et al., 2015). Accordingly, autophagy may be a protective or non-protective mechanism depending on the functional effects of each liver cell type (Hung et al., 2020). Thus, as the predominant parenchymal cell, previous studies indicated that hepatocytes play a central role in liver regeneration through upregulated autophagy (Toshima et al., 2014; Lin et al., 2015; Sato et al., 2019; Romermann et al., 2020). The reversal of the autophagy tendency was immensely different from the normal progression after hepatectomy in our F3–4 fibrotic mice, indicating suppression of autophagic signals in the hepatocyte in the fibrotic microenvironment during liver regeneration.

The deletion of autophagy-related genes prominently decreases hepatocyte proliferation (Toshima et al., 2014; Sato et al., 2019; Romermann et al., 2020). Our results showing decreased cyclin D1 and Ki-67 expression together with impaired autophagy were similar to previous observations during regeneration in the moderate fibrotic mice (Figures 2E–G). Furthermore, hepatocyte size enlargement (hypertrophy) and increased number of binuclear hepatocytes were observed (Figures 3A,B). Unconventionally, hypertrophy was an alternative regeneration pathway such as hepatocyte proliferation in liver regeneration (Miyaoka et al., 2012). It was claimed that size enlargement of hepatocytes is the first process by which liver regenerates, especially in PHx with less resected liver volume, hypertrophy of hepatocytes plays critical, even solely role on liver regenerative process before cell division. The enlargement of hepatocytes could be attributed to dysregulation of autophagy (Toshima et al., 2014; Romermann et al., 2020). In normal liver regeneration, cell size grew larger as regeneration proceeding. Hepatocytes are prevented from becoming senescent and intracellular organelles are functional well under upregulated autophagy in the early phase of liver regeneration. Rationally, hypertrophy is a compensatory response as physiological levels of autophagy are required for normal cell size. However, in L-Atg5 KO mice, this responsive hypertrophy was more severe which might suggest problematic degradation of cumulatively dysfunctional organelles in the status of defective autophagy (Toshima et al., 2014). This phenomenon was indicated in another Atg7-deficient PHx mice model (Romermann et al., 2020), as well as by patients with α1-antitrypsin deficiency for the autophagic inability of degradation of the misfolded AT proteins (Marciniak and Lomas, 2010). In our study, obvious enlargement of hepatocytes and downregulated autophagy coexisted in F3-4 fibrotic mice. It is interesting to note that enlargement of hepatocytes can be partly reversed by enhanced autophagy with verapamil administration. Liver regeneration is improved through upregulated autophagy which might hint reversely problematic disposal of damaged intracellular organelles; thus, cell size was normally enlarged rather than excessively hypertrophic (Toshima et al., 2014; Sato et al., 2019; Romermann et al., 2020). Unlike physiological status, insufficient or excessive levels of autophagy would lead to mismatch in cell enlargement (Vellai et al., 2008; Neufeld, 2012).

The profile for hepatocyte binuclearity ratio reflects its proliferation and differentiation status in various physiological process (Toyoda et al., 2005). In livers from adults, approximately 20% of hepatocytes have double nuclei (Li et al., 2009). The binuclearity ratio remains stable in dormant mature hepatocytes but declines in normal regenerative process apparently owing to replicative response from binuclear hepatocytes to mononuclear daughter cells (Gerlyng et al., 1993; Li et al., 2009). Our results in F0 regenerative liver are consistent with those of previous reports (Figures 3A–C; and Supplementary Table S3). Unlike in F0 regenerative liver, the ratio of binuclear hepatocytes increased instead in F3–4 regenerative liver at 72 h after 50% PHx. In this regard, the hepatocyte entering into the cell cycle does not necessarily indicate cell division; insufficient cytokinesis would

prevent the conversion of polyploidization and cause a decrease in the number of binuclear hepatocytes (Guidotti et al., 2003; Miyaoka et al., 2012). The proliferation status of hepatocytes can be further revealed by investigating the expression of Aurora B between mitotic phases. According to the intracellular distribution of Aurora B and morphology of nuclei of hepatocytes, the punctuated distribution of Aurora B remarkably declined in F3–4 mitotic hepatocytes for both mononuclear and binuclear hepatocytes (Figure 5D).

As downregulated autophagy is associated with declined proliferation of hepatocytes during fibrotic liver regeneration, pharmacological restoration of autophagic signals was induced through verapamil administration (Park et al., 2014; Lai et al., 2021). The corrected autophagy included earlier expression of Atg-related proteins at 48 h after 50% PHx, increased number of autophagosomes and autolysosomes, and decreased numbers of diseased mitochondria or apoptotic bodies (Figures 6A–C). As a result, proliferative indices improved, especially the reduced number and degree of hypertrophic and polyploid hepatocytes (Figures 6D–G). Hepatocyte enlargement and descreasing number of binuclear hepatocyte suggested that hypertrophy together with proliferation jointly contribute to liver regeneration (Minamishima et al., 2002; Haga et al., 2005; Miyaoka et al., 2012; Miyaoka and Miyajima, 2013).

Two main factors challenge the experimental results and their robustness. The resection volume of the liver is the first affected factor. When 40%–70% of the liver is removed, the hepatocyte proliferation response is linearly correlated with the extent of volume loss (Bonninghoff et al., 2012). Thus, mice with 70% PHx constitute the classic murine model because this procedure produces a strong regenerative response postoperatively. Liver fibrosis is another factor; accumulating evidence indicates the impaired regeneration capacity of hepatocytes in fibrotic liver (Cao et al., 2009; Bonninghoff et al., 2012). Under preestablished experimental liver fibrosis, primary replication of hepatocytes is substantially impaired, and alternative regenerative pathways of intrahepatic or extrahepatic stem cells would be activated in mice with excessive liver volume loss (Kuramitsu et al., 2013). Nonetheless, most of the mice died postoperatively (Figure 2). Since the aim of our study was to explore the potential regenerative mechanism of mature hepatocytes under fibrotic conditions, limited hepatectomy (50%) triggered regeneration response although less intensely, and the postoperative vitality was maintained stably, which would have avoided positive selection of experimental animals. Hence, a more clinically relevant condition, such as 50% PHx, was eventually chosen as an experimental model.

In conclusion, we have demonstrated that the aberrant regulation of autophagy disturbs fibrotic liver regeneration after 50% PHx. Hepatocyte proliferation improved with verapamil by pharmacologically modulating autophagy, thereby reducing the number and degree of hypertrophic and polyploid hepatocytes.

Data availability statement

The raw data supporting the conclusions of this article will be made available by the authors, without undue reservation.

Ethics statement

All animal care and experiments were carried out in accordance with the ethical guidelines of the 1975 Helsinki Declaration. All animal experiments were performed according to the ethical review requirements and protocols of animal experiments at Fujian Medical University (Fuzhou, Fujian, China). The animal study was reviewed and approved by the Ethics Committee of the Fujian Medical University.

Author contributions

Conceptualization, A-MH and Y-NB; methodology, J-LL; draft-original draft preparation, Y-EL and Y-NB; writing—review and editing, Y-EL and A-MH. All authors have read and agreed to the published version of the manuscript.

Acknowledgments

We thank professor Lian-huang Li (Fujian Normal University) for technical assistance with image processing and analysis.

Conflict of interest

The authors declare that the research was conducted in the absence of any commercial or financial relationships that could be construed as a potential conflict of interest.

Publisher's note

All claims expressed in this article are solely those of the authors and do not necessarily represent those of their affiliated organizations, or those of the publisher, the editors and the reviewers. Any product that may be evaluated in this article, or claim that may be made by its manufacturer, is not guaranteed or endorsed by the publisher.

Supplementary material

The Supplementary Material for this article can be found online at: https://www.frontiersin.org/articles/10.3389/fcell.2022.1030338/full#supplementary-material

References

Aierken, Y., Kong, L. X., Li, B., Liu, X. J., Lu, S., and Yang, J. Y. (2020). Liver fibrosis is a major risk factor for liver regeneration: A comparison between healthy and fibrotic liver. *Med. Baltim.* 99, e20003. doi:10.1097/MD.0000000000020003

Andiran, F., Ayhan, A., Tanyel, F. C., Abbasoglu, O., and Sayek, I. (2000). Regenerative capacities of normal and cirrhotic livers following 70% hepatectomy in rats and the effect of alpha-tocopherol on cirrhotic regeneration. *J. Surg. Res.* 89, 184–188. doi:10.1006/jsre.2000.5825

Andıran, F., Ayhan, A., Tanyel, F. C., Abbasoğlu, O., and Sayek, İ. (2000). Regenerative capacities of normal and cirrhotic livers following 70% hepatectomy in rats and the effect of α-tocopherol on cirrhotic regeneration. *J. Surg. Res.* 89, 184–188.

Bonninghoff, R., Schwenke, K., Keese, M., Magdeburg, R., Bitter-Suermann, H., Otto, M., et al. (2012). Effect of different liver resection methods on liver damage and regeneration factors VEGF and FGF-2 in mice. *Can. J. Surg.* 55, 389–393. doi:10.1503/cjs.007911

Bou-Nader, M., Caruso, S., Donne, R., Celton-Morizur, S., Calderaro, J., Gentric, G., et al. (2020). Polyploidy spectrum: A new marker in HCC classification. *Gut* 69, 355–364. doi:10.1136/gutjnl-2018-318021

Cao, H., Yu, J., Xu, W., Jia, X., Yang, J., Pan, Q., et al. (2009). Proteomic analysis of regenerating mouse liver following 50% partial hepatectomy. *Proteome Sci.* 7, 48. doi:10.1186/1477-5956-7-48

Czaja, M. J. (2011). Functions of autophagy in hepatic and pancreatic physiology and disease. *Gastroenterology* 140, 1895–1908. doi:10.1053/j.gastro.2011.04.038

Fausto, N., Campbell, J. S., and Riehle, K. J. (2012). Liver regeneration. *J. Hepatol.* 57, 692–694. doi:10.1016/j.jhep.2012.04.016

Gerlyng, P., Abyholm, A., Grotmol, T., Erikstein, B., Huitfeldt, H. S., Stokke, T., et al. (1993). Binucleation and polyploidization patterns in developmental and regenerative rat liver growth. *Cell Prolif.* 26, 557–565. doi:10.1111/j.1365-2184.1993.tb00033.x

Gual, P., Gilgenkrantz, H., and Lotersztajn, S. (2017). Autophagy in chronic liver diseases: The two faces of janus. *Am. J. Physiol. Cell Physiol.* 312, C263–C273. doi:10.1152/ajpcell.00295.2016

Guidotti, J. E., Bregerie, O., Robert, A., Debey, P., Brechot, C., and Desdouets, C. (2003). Liver cell polyploidization: A pivotal role for binuclear hepatocytes. *J. Biol. Chem.* 278, 19095–19101. doi:10.1074/jbc.M300982200

Haga, S., Ogawa, W., Inoue, H., Terui, K., Ogino, T., Igarashi, R., et al. (2005). Compensatory recovery of liver mass by Akt-mediated hepatocellular hypertrophy in liver-specific STAT3-deficient mice. *J. Hepatol.* 43, 799=807. doi:10.1016/j.jhep.2005.03.027

Hernandez-Gea, V., Ghiassi-Nejad, Z., Rozenfeld, R., Gordon, R., Fiel, M. I., Yue, Z., et al. (2012). Autophagy releases lipid that promotes fibrogenesis by activated hepatic stellate cells in mice and in human tissues. *Gastroenterology* 142, 938–946. doi:10.1053/j.gastro.2011.12.044

Hung, T. M., Hsiao, C. C., Lin, C. W., and Lee, P. H. (2020). Complex cell type-specific roles of autophagy in liver fibrosis and cirrhosis. *Pathogens* 9. doi:10.3390/pathogens9030225

Hung, T. M., Yuan, R. H., Huang, W. P., Chen, Y. H., Lin, Y. C., Lin, C. W., et al. (2015). Increased autophagy markers are associated with ductular reaction during the development of cirrhosis. *Am. J. Pathol.* doi:10.1016/j.ajpath.2015.05.010

Kele, P. G., Van Der Jagt, E. J., Gouw, A. S. H., Lisman, T., Porte, R. J., and De Boer, M. T. (2013). The impact of hepatic steatosis on liver regeneration after partial hepatectomy. *Liver Int.* 33, 469–475. doi:10.1111/liv.12089

Klionsky, D. J., Abdel-Aziz, A. K., Abdelfatah, S., Abdellatif, M., Abdoli, A., Abel, S., et al. (2021). Guidelines for the use and interpretation of assays for monitoring autophagy (4th edition)(1). *Autophagy* 17, 1–382. doi:10.1080/15548627.2020.1797280

Kuramitsu, K., Sverdlov, D. Y., Liu, S. B., Csizmadia, E., Burkly, L., Schuppan, D., et al. (2013). Failure of fibrotic liver regeneration in mice is linked to a severe fibrogenic response driven by hepatic progenitor cell activation. *Am. J. Pathol.* 183, 182–194. doi:10.1016/j.ajpath.2013.03.018

Lai, J. L., Lian, Y. E., Wu, J. Y., Wang, Y. D., and Bai, Y. N. (2021). Verapamil induces autophagy to improve liver regeneration in non-alcoholic fatty liver mice. *Adipocyte* 10, 532–545. doi:10.1080/21623945.2021.1983241

Li, C. C., Chu, H. Y., Yang, C. W., Chou, C. K., and Tsai, T. F. (2009). Aurora-A overexpression in mouse liver causes p53-dependent premitotic arrest during liver regeneration. *Mol. Cancer Res.* 7, 678–688. doi:10.1158/1541-7786.MCR-08-0483

Lin, C. W., Chen, Y. S., Lin, C. C., Chen, Y. J., Lo, G. H., Lee, P. H., et al. (2015). Amiodarone as an autophagy promoter reduces liver injury and enhances liver regeneration and survival in mice after partial hepatectomy. *Sci. Rep.* 5, 15807. doi:10.1038/srep15807

Mann, D. V., Lam, W. W., Hjelm, N. M., So, N. M., Yeung, D. K., Metreweli, C., et al. (2001). Human liver regeneration: Hepatic energy economy is less efficient when the organ is diseased. *Hepatology* 34, 557–565. doi:10.1053/jhep.2001.27012

Marciniak, S. J., and Lomas, D. A. (2010). Alpha1-Antitrypsin deficiency and autophagy. *N. Engl. J. Med.* 363, 1863–1864. doi:10.1056/NEJMcibr1008007

Martins, P. N. A., Theruvath, T. P., and Neuhaus, P. (2008). Rodent models of partial hepatectomies. *Liver Int.* 28, 3–11. doi:10.1111/j.1478-3231.2007.01628.x

Michalopoulos, G. K., and Bhushan, B. (2021). Liver regeneration: Biological and pathological mechanisms and implications. *Nat. Rev. Gastroenterol. Hepatol.* 18, 40–55. doi:10.1038/s41575-020-0342-4

Minamishima, Y. A., Nakayama, K., and Nakayama, K. (2002). Recovery of liver mass without proliferation of hepatocytes after partial hepatectomy in Skp2-deficient mice. *Cancer Res.* 62, 995–999.

Miyaoka, Y., Ebato, K., Kato, H., Arakawa, S., Shimizu, S., and Miyajima, A. (2012). Hypertrophy and unconventional cell division of hepatocytes underlie liver regeneration. *Curr. Biol. CB* 22, 1166–1175. doi:10.1016/j.cub.2012.05.016

Miyaoka, Y., and Miyajima, A. (2013). To divide or not to divide: Revisiting liver regeneration. *Cell Div.* 8, 8. doi:10.1186/1747-1028-8-8

Nagasue, N., Yukaya, H., Ogawa, Y., Kohno, H., and Nakamura, T. (1987). Human liver regeneration after major hepatic resection. A study of normal liver and livers with chronic hepatitis and cirrhosis. *Ann. Surg.* 206, 30–39. doi:10.1097/00000658-198707000-00005

Neufeld, T. P. (2012). Autophagy and cell growth--the yin and yang of nutrient responses. *J. Cell Sci.* 125, 2359–2368. doi:10.1242/jcs.103333

Park, H. W., Park, H., Semple, I. A., Jang, I., Ro, S. H., Kim, M., et al. (2014). Pharmacological correction of obesity-induced autophagy arrest using calcium channel blockers. *Nat. Commun.* 5, 4834. doi:10.1038/ncomms5834

Romermann, D., Ansari, N., Schultz-Moreira, A. R., Michael, A., Marhenke, S., Hardtke-Wolenski, M., et al. (2020). Absence of Atg7 in the liver disturbed hepatic regeneration after liver injury. *Liver Int.* doi:10.1111/liv.14425

Ruchaud, S., Carmena, M., and Earnshaw, W. C. (2007). Chromosomal passengers: Conducting cell division. *Nat. Rev. Mol. Cell Biol.* 8, 798. doi:10.1038/nrm2257

Sato, T., Yamashina, S., Izumi, K., Ueno, T., Koike, M., Ikejima, K., et al. (2019). Cathepsin L-deficiency enhances liver regeneration after partial hepatectomy. *Life Sci.* doi:10.1016/j.lfs.2019.02.040

Singh, R., Kaushik, S., Wang, Y., Xiang, Y., Novak, I., Komatsu, M., et al. (2009). Autophagy regulates lipid metabolism. *Nature* 458, 1131–1135. doi:10.1038/nature07976

Tanaka, M., and Miyajima, A. (2016). Liver regeneration and fibrosis after inflammation. *Inflamm. Regen.* 36, 19. doi:10.1186/s41232-016-0025-2

Toshima, T., Shirabe, K., Fukuhara, T., Ikegami, T., Yoshizumi, T., Soejima, Y., et al. (2014). Suppression of autophagy during liver regeneration impairs energy charge and hepatocyte senescence in mice. *Hepatology* 60, 290–300. doi:10.1002/hep.27140

Toyoda, H., Bregerie, O., Vallet, A., Nalpas, B., Pivert, G., Brechot, C., et al. (2005). Changes to hepatocyte ploidy and binuclearity profiles during human chronic viral hepatitis. *Gut* 54, 297–302. doi:10.1136/gut.2004.043893

Varga, M., Sass, M., Papp, D., Takacs-Vellai, K., Kobolak, J., Dinnyes, A., et al. (2014). Autophagy is required for zebrafish caudal fin regeneration. *Cell Death Differ.* 21, 547–556. doi:10.1038/cdd.2013.175

Vellai, T., Bicsak, B., Toth, M. L., Takacs-Vellai, K., and Kovacs, A. L. (2008). Regulation of cell growth by autophagy. *Autophagy* 4, 507–509. doi:10.4161/auto.5670

Zhao, X. Y., Wang, B. E., Li, X. M., and Wang, T. L. (2008). Newly proposed fibrosis staging criterion for assessing carbon tetrachloride- and albumin complex-induced liver fibrosis in rodents. *Pathol. Int.* 58, 580–588. doi:10.1111/j.1440-1827.2008.02274.x

frontiers | Frontiers in Cell and Developmental Biology

TYPE Review
PUBLISHED 01 November 2022
DOI 10.3389/fcell.2022.949382

OPEN ACCESS

EDITED BY
Jette Lengefeld,
University of Helsinki, Finland

REVIEWED BY
Xili Liu,
Harvard Medical School, United States
Attila Csikász-Nagy,
Pázmány Péter Catholic University, Hungary

*CORRESPONDENCE
Shixuan Liu,
shixuan@stanford.edu
Ran Kafri,
ran.kafri@sickkids.ca

†These authors have contributed equally to this work

SPECIALTY SECTION
This article was submitted to Cell Growth and Division, a section of the journal Frontiers in Cell and Developmental Biology

RECEIVED 20 May 2022
ACCEPTED 07 September 2022
PUBLISHED 01 November 2022

CITATION
Liu S, Tan C, Tyers M, Zetterberg A and Kafri R (2022), What programs the size of animal cells?
Front. Cell Dev. Biol. 10:949382.
doi: 10.3389/fcell.2022.949382

What programs the size of animal cells?

Shixuan Liu[1,2,3*†], Ceryl Tan[1,2†], Mike Tyers[4], Anders Zetterberg[5] and Ran Kafri[1,2*]

[1]Department of Molecular Genetics, University of Toronto, Toronto, ON, Canada, [2]Program in Cell Biology, The Hospital for Sick Children, Toronto, ON, Canada, [3]Department of Chemical and Systems Biology, Stanford University, Stanford, CA, United States, [4]Institute for Research in Immunology and Cancer, University of Montréal, Montréal, QC, Canada, [5]Department of Oncology-Pathology, Karolinska Institutet, Stockholm, Sweden

The human body is programmed with definite quantities, magnitudes, and proportions. At the microscopic level, such definite sizes manifest in individual cells - different cell types are characterized by distinct cell sizes whereas cells of the same type are highly uniform in size. How do cells in a population maintain uniformity in cell size, and how are changes in target size programmed? A convergence of recent and historical studies suggest - just as a thermostat maintains room temperature - the size of proliferating animal cells is similarly maintained by homeostatic mechanisms. In this review, we first summarize old and new literature on the existence of cell size checkpoints, then discuss additional advances in the study of size homeostasis that involve feedback regulation of cellular growth rate. We further discuss recent progress on the molecules that underlie cell size checkpoints and mechanisms that specify target size setpoints. Lastly, we discuss a less-well explored teleological question: why does cell size matter and what is the functional importance of cell size control?

KEYWORDS

cell size, cell size checkpoint, cell cycle, cell size homeostasis, cell growth, target size, cell size sensing

Introduction

Leonardo da Vinci's *Vitruvian man* stands as a monument to the innate curiosity of humanity to uncover the code that reproducibly programs the quantities and proportions of life. Advances in modern biology have uncovered networks of gene regulation and signal transduction, yet it remains unknown how definite values and quantities are programmed and measured by these complex networks. Reproducible size differences over orders of magnitude distinguish animal species (Bonner, 2006). Within a given species, size differences characterize organs and cell types (Figure 1A). In the murine pancreas, for example, β cells are roughly half the size of their neighboring acinar cells (Figure 1B). These differences in cell size suggest that, during differentiation, different cell types are programmed with a specific target size (Figure 1C). At the molecular level, growth in cell size is often attributed to the conserved mTORC1 growth factor and nutrient sensing network (Fingar et al., 2002; Sabatini, 2017), but it remains unknown

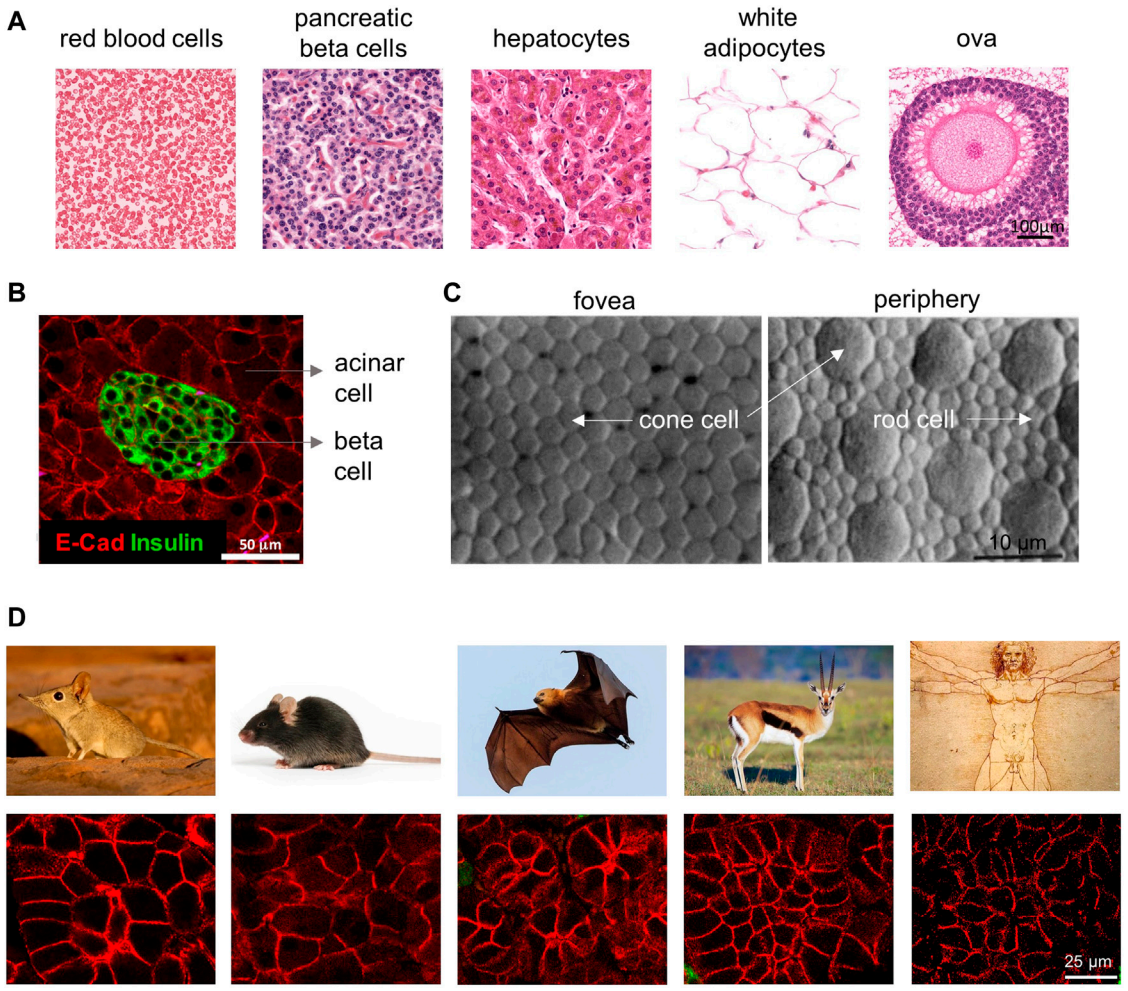

FIGURE 1
Cell size differences among different cell types and species. **(A)** In the human body, cells of different cell types can vary significantly in their size. Cell images are shown at the same magnification, adapted with permission from HistologyGuide.org. **(B)** Cell size differences in murine pancreatic cells. Note the pancreatic beta cells in the islet (insulin positive) have much smaller size than the surrounding acinar cells (insulin negative). Adapted from (Anzi et al., 2018). **(C)** Cell size in the retina not only differs by cell type (cone vs. rod) but also by the location in the tissue (fovea vs. periphery). Note that the cone cells are smaller in the fovea than ones in the periphery, which directly corresponds with the retina's local visual resolution. Image is from (Curcio et al., 1990). **(D)** Pancreatic acinar cells vary in size in different mammalian species, from left to right are the Etruscan shrew, mouse, fruit bat, mountain gazelle, and human (tissue section images from Yuval Dor's lab and animal images searched from Google).

whether or how mTORC1 functions to specify a characteristic size for each of the many different cell types in the body.

Questions on cell size have been investigated for over a century since the start of modern cytology (Jorgensen and Tyers, 2004). Yet, molecular mechanisms that program the size of animal cells are only starting to be revealed. Until recently, a major focus of the field had been to resolve whether "active" homeostatic control of cell size exists for proliferating mammalian cells, i.e., whether cells actively monitor and adjust their cell size as opposed to size merely being a passive consequence of cell growth and division. Conversely, although less well-studied, size changes in non-proliferating cells are by definition the result of an active process that is independent of division. Reflecting on both old and recent literature, we present a convergence of evidence to suggest that individual cells actively maintain size homeostasis by regulating both the speed of cell cycle progression (i.e., cell cycle duration) and the rate of cell size growth (i.e., cellular growth rate). We further discuss recent advances on the molecular mechanisms underlying homeostatic control of cell size as well as target size specification. Last, we discuss the functional relevance of cell size

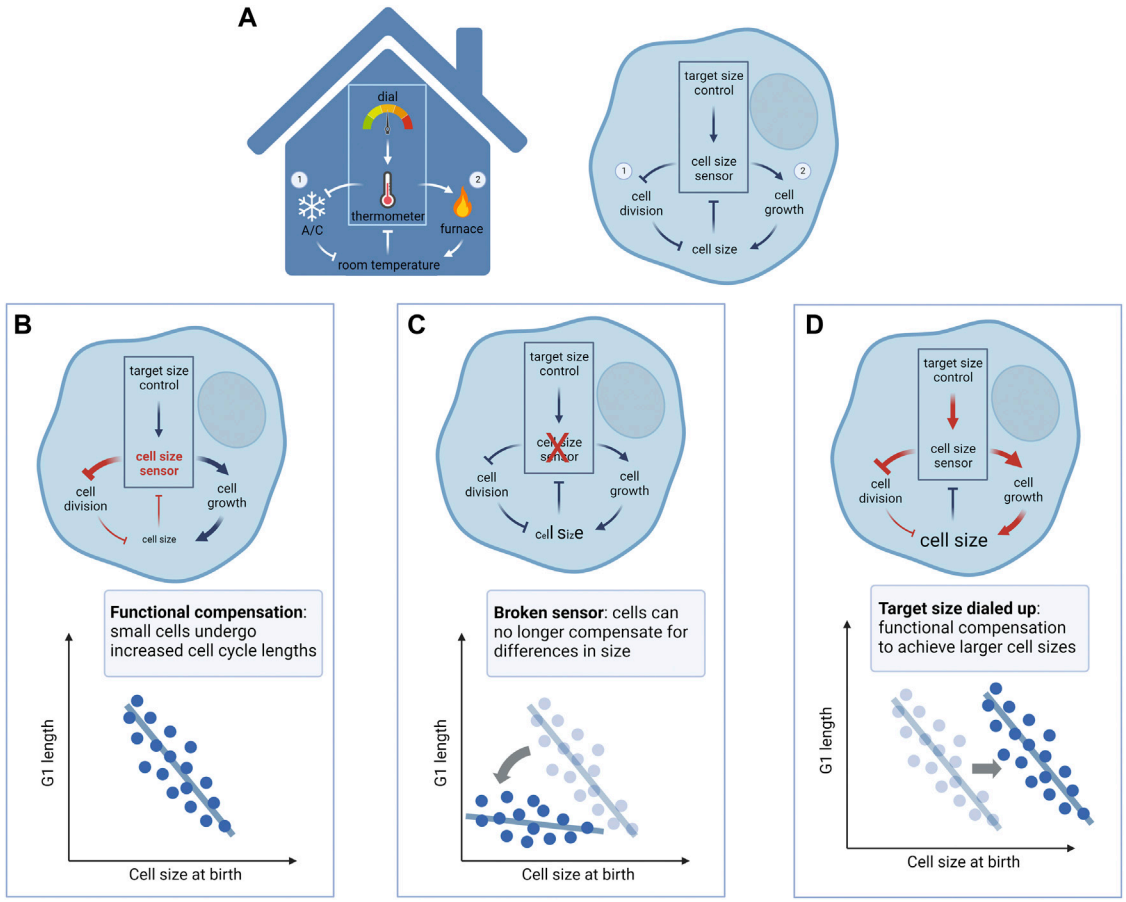

FIGURE 2
A model for mammalian cell size control. **(A)** Cell size regulation shares similar control circuits as a thermostat that controls the temperature of a room. Note that analogies between circuit components are based on the direction of regulation, i.e., faster cell division/cell cycle alone reduces cell size (turning on/up the air conditioner reduces room temperature), and faster cell growth alone increases cell size (turning on/up the furnace increases room temperature). Left panel: A thermometer measures the temperature of the room and compares it to the setpoint determined by the dial. If the room temperature is lower than the setpoint, the thermostat turns on the furnace and turns off the air conditioner to heat up the room. Conversely, if the room temperature is higher than the setpoint, the thermostat turns off the furnace and turns on the air conditioner to cool the room down. This dual-arm negative feedback regulation on the furnace and air conditioner maintains the room temperature at the setpoint. Right panel: Cell size control may involve a cell size sensor, relating a cell's actual size with a "programmed" target size value, to regulate cell cycle progression (① cell size checkpoint) and cellular growth (② size-dependent regulation of growth rate), respectively. Cells that are smaller than their target size mainly compensate with a longer cell cycle mediated by size-dependent G1 extension, whereas cells that are larger than their target size mainly compensate with slowed cell growth, mediated by the upregulation of global protein degradation. This dual-arm negative feedback regulation on cell cycle and cellular growth maintains cell size relatively stable at the target size value. **(B)** With a properly functional size control mechanism (e.g., cell size checkpoint), small cells compensate with a longer period of growth in G1, allowing all cells to reach similar sizes at S phase entry. **(C)** When the homeostatic size control is perturbed (e.g., p38 inhibition, Rb1 knockout), cells would fail to compensate for their small size with a G1 extension, resulting in increased size heterogeneity. **(D)** When the target size is changed to a different level without perturbing the homeostatic control mechanism, cell size is shifted to the new setpoint while maintaining the compensatory G1 extension (e.g., CDK4 inhibition). Diagrams created using BioRender.com.

and how cell size affects cellular, tissue and organismal level functions. While we mainly focus on proliferating mammalian cells, we also highlight examples of size control in terminally differentiated cells under physiological or pathological conditions for which mechanistic insights are less explored. We hope this review inspires more mechanistic and functional studies of cell size control in the future.

The thermostat analogy of cell size control

At an EMBO workshop on cell size regulation in 2016, Wallace Marshall suggested an interesting analogy for cell size regulation. Size control, according to Marshall's analogy, may be compared to a thermostat in the maintenance of room

temperature (Figure 2). A thermostat (cell size homeostasis) comprises a thermometer (cell size sensor) that senses the room temperature (current cell size) and adjusts the activity of the furnace and/or air conditioner (cell growth and cell cycle machineries, respectively) to reach and maintain room temperature at the setpoint level (target size). However, when one observes a change in the room temperature, this can result from perturbations to the thermometer, to the furnace/air conditioner, or to the set point temperature. Similarly, in an experiment where one observes a change in cell size, it may reflect: 1) perturbations to size sensing/homeostatic control (broken thermometer or thermostat circuit), 2) perturbations to the cell growth or cell cycle machinery (broken furnace/air conditioner), such as diminished mTORC1 signaling or a prolonged G1, or 3) a reprogrammed target size (thermostat dialed to a lower or higher set point temperature).

Although not a perfect comparison, we find this thermostat analogy helps to clarify certain conceptual ambiguities regarding cell size regulation and may help resolve some of the historical debates in the field (see next section). In particular, this model highlights the importance of distinguishing different types of cell size perturbations when interpreting experimental results. The analogy also offers a useful conceptual framework to dissect different aspects of cell size control.

Historical and recent studies on the existence of the mammalian cell size checkpoint

Emergence of the cell size checkpoint concept

The cell size checkpoint refers to a size control point in the cell cycle that restricts cell cycle progression of cells that are too small or too large. The term checkpoint is drawn from its original use by Hartwell and Weinert to describe control mechanisms that enforce dependency in the cell cycle (Hartwell and Weinert, 1989). By analogy to a thermostat, the cell size checkpoint represents not a single module but a part of the homeostasis circuit: the cell size checkpoint involves active size sensing (thermometer) and corresponding modulation of the cell cycle machinery (air conditioner) to maintain size at the setpoint level. In mammalian cells, the most prominent and well-studied size checkpoint exists at the G1/S transition, where we focus our discussion.

Compelling genetic experiments in both the fission yeast *Schizosaccharomyces pombe* and the budding yeast *Saccharomyces cerevisiae* established the existence of cell size checkpoints in single-celled organisms in the 1970s, either at the G1/S transition in budding yeast or the G2/M transition in fission yeast (Nurse, 1975; Fantes and Nurse, 1977; Johnston et al., 1977). In contrast, the literature on animal cell size control has posited conflicting models for decades (Conlon and Raff, 2003; Sveiczer et al., 2004; Lloyd, 2013). And yet, ironically, it was in animal cells that the cell size checkpoint was first discovered. In 1965, Zetterberg and Killander reported evidence suggesting that individual mouse fibroblasts are programmed with a definite size (Killander and Zetterberg, 1965a; 1965b). To quantify cell growth along the cell cycle, Zetterberg et al. developed a sophisticated experimental assay in which cells were photographed every 45 min for 30 h to track cell division. Then, cells were fixed, stained with Feulgen dye, and scanned by microinterferometry to measure cellular dry mass and by microspectrophotometry to measure DNA and RNA content. The live-cell tracking allowed the estimation of a cell's division age, i.e., the time period since its last mitotic division. This setup produced the first reported single-celled joint measurements of cell size and cell cycle state. Analysis of the data revealed that variability in cell size decreases as cells transition from the G1 phase of cell cycle into S phase (Killander and Zetterberg, 1965a). Indeed, fibroblasts in early S phase are more similar in size than sister cells that just emerged from cell division.

In addition, Zetterberg et al. reported evidence for cell size-dependent regulation of G1 length (Killander and Zetterberg, 1965b). When comparing cell size and cell cycle duration of cells cultured on different slides, they noticed that populations with smaller average sizes at birth grow for longer periods in G1 and accumulated more mass before G1 exit so that all populations enter S phase at a similar size (Figure 2B). This discovery was later supported by other groups working on different cell types (Shields et al., 1978; Darzynkiewicz et al., 1979; Gao and Raff, 1997). However, these observations remained at the population level, as it was technologically impractical to continuously track cell size in live, irregularly-shaped animal cells. In the 1970s, size-dependent control of cell cycle duration was corroborated at single cell resolution in budding yeast (Hartwell et al., 1974; Johnston et al., 1977) and fission yeast (Nurse, 1975; Fantes and Nurse, 1977). Specifically, small cells compensate with longer periods of growth whereas large cells commit to division with little additional growth. These observations supported the notion of a "cell size checkpoint" (Rupes, 2002; Wood and Nurse, 2015). Genetic screens ensued in search for yeast size mutants, which notably yielded the genes *wee1* (Nurse and Thuriaux, 1980), *WHI1* (later renamed *CLN3*) (Sudbery et al., 1980; Nash et al., 1988), and *WHI5* (Jorgensen et al., 2002), all of which were named after the loss- or gain-of-function small size phenotypes. These genetic insights helped lay the foundation for understanding the molecular control of the cell cycle. While Zetterberg's early work suggested a similar cell size checkpoint at the G1/S transition for animal cells, the molecular basis for this checkpoint remained enigmatic. Moreover, in both yeast and mammalian cells, it remains unsettled whether homeostatic size control involves only a single "point" (or a short period of the cell cycle) or is continuously adjusted over an extended cell cycle period (Garmendia-Torres et al., 2018; Liu et al., 2022). In this

review, we define the cell size checkpoint in a broad sense wherein cell cycle progression is regulated in accordance with cell size to maintain size homeostasis.

Historical debates on mammalian cell size checkpoints

Although the pioneering work by Zetterberg et al. presented compelling evidence for a cell size checkpoint that gates the G1/S transition according to cell size, the existence of a mammalian cell size checkpoint remained controversial for many decades (Wells, 2002; Lloyd, 2013). Initially, opposition to the cell size checkpoint (or a cell-intrinsic size control) was motivated by findings showing that cell growth in size and cell cycle progression can be independently influenced by separate types of growth factors (Zetterberg et al., 1984; Conlon et al., 2001; Echave et al., 2007). For example, under certain conditions (e.g., dilution of growth factors), many cell types such as rat Schwann cells show a reduced cell size without triggering an immediate delay in cell cycle entry. However, it is ambiguous as to whether these experimental conditions may have altered the cell's target size. Following the thermostat analogy, if dilution of growth factors changes the cells' target size (e.g., lowering the room's setpoint temperature), one should not expect that a decrease in cell size (e.g., sudden drop of room temperature) would trigger a subsequent cell cycle extension (e.g., shutting down the air conditioner) before the cells reach a new homeostasis. Therefore, we reason that these experiments were not sufficient to either support or refute the cell size checkpoint, i.e., cell-intrinsic size control.

The controversy on the existence of a cell size checkpoint was further fueled by conflicting observations on whether conditions that shift cell size correlate with an *immediate* lengthening/shortening of cell cycle. For example, Conlon and Raff reported that Schwann cells shifted from serum-free to serum-containing medium required more than one cell cycle to equilibrate to their new, larger cell size (Conlon and Raff, 2003). In contrast, Dolznig et al. switched erythroblasts between two conditions that associate with different sizes, a smaller size when under physiological cytokines and a larger size when under constitutively active oncogene expression (Dolznig et al., 2004). This study revealed that erythroblasts immediately adapt in cell cycle length and protein synthesis rates following the switch, resulting in reversible changes in cell size between the two states that were achieved within approximately one cell cycle. The discrepancy in the speed of cell size adaptation may be explained by differences in the stringency of the cell size checkpoint in different cell types or states. A cell type with a stringent size checkpoint should exhibit a faster size adaptation. On the other hand, a cell type with a permissive size checkpoint might allow cells within a wide range of sizes to enter the next cell cycle phase and may take multiple cycles to reach the new size homeostasis. Related to this notion, a series of recent studies have investigated sizer, adder, and timer models of cell size control (Varsano et al., 2017; Cadart et al., 2018; Xie and Skotheim, 2020), originally proposed to explain cell size control in bacteria (Taheri-Araghi et al., 2015; Wallden et al., 2016). The sizer model assumes a strict cell size checkpoint requiring cells to reach an exact size value, such that all cells should end up with identical sizes within one cell cycle. The adder model, however, assumes that no specific target size is required to pass through the cell cycle. Instead, all cells, no matter large or small, accumulate the same amount of growth per cell cycle and therefore require multiple cell cycles to adapt to a new target size. Finally, the timer model assumes that cells grow for a constant period of time, independent of their starting sizes, and thus lack an inherent compensation mechanism. These overly simplified models describe only limited cases and recent studies suggest that size control is more complex (see below).

In addition, the debate on whether mammalian cell growth follows linear or exponential kinetics (Conlon and Raff, 2003; Mitchison, 2003; Sveiczer et al., 2004) also contributed to the controversy regarding the existence of a mammalian cell size checkpoint. This debate was fueled by mathematical calculations showing that stable distributions of cell size are inconsistent with exponential growth (Brooks, 1981; Tyson and Hannsgen, 1985) unless a size checkpoint is invoked. To many, these calculations suggested that if growth is linear, size checkpoints may not be necessary (Lloyd, 2013). Recently, with the development of better experimental methods for measurements of growth dynamics, actual kinetics of cell size growth were found to follow a pattern that is more complex than the simple linear or exponential models initially proposed (see below).

Modern technologies provide further evidence for mammalian cell size checkpoints

In the past decade, new technologies have enabled high-precision and/or high-throughput measurements of cell size, including live-cell tracking of cell growth at single-cell resolution across an entire cell cycle. With these technical advances, a plethora of new data supports the conclusion that individual animal cells do indeed employ cell-intrinsic control to maintain size homeostasis.

Ginzberg et al. (2018) repeated Killander and Zetterberg's time-lapse experimental design in human epithelial cells, measuring cell size and cell cycle stage by single-cell fluorescence microscopy and automated image processing. These modern techniques allowed quantification at a higher throughput and reaffirmed Zetterberg's discovery that cell size variability narrows at S phase entry. Similarly, live-cell tracking of cell size by quantitative phase microscopy revealed that the coefficient of variation of cell dry mass decreases around S

phase entry (Liu et al., 2022). Varsano et al. (2017) devised an experimental system that forces animal cells to grow in narrow channels. By constraining cells in an elongated cylindrical geometry, the authors effectively reduced the cell's three-dimensional volume to a single length scale. Observations obtained with this experimental system are in favour of cell size checkpoints, showing that smaller cells have extended periods of growth in G1. This work also examined channels with different geometry and found that all cells grow to a similar size regardless of the channel geometry. This surprising result suggests that intrinsic cell size control can be independent of cell shape and mechanical forces, at least in the basophil cell lines used in the study. Another study utilized a fluorescence exclusion method and tracked the dynamics of cell volume and cell cycle progression in individual cells (Cadart et al., 2018). Similarly, the authors found a negative correlation between cell size and G1 duration for cultured mammalian cells. In a series of additional studies, we and others measured growth of individual cells throughout the cell cycle, and consistently found that newborn cells with a smaller size compensate with longer periods of G1, giving rise to a size distribution that is stable over generations (D'Ario et al., 2021; Ginzberg et al., 2018; Liu et al., 2018; Liu et al., 2022; Zatulovskiy et al., 2020).

Cell size checkpoints *in vivo* and in exceptional cases

The evidence described above was mostly derived from measurements on cultured proliferating cells, which brings to question whether such size checkpoints are also implemented by cells *in vivo* (Lloyd, 2013). In certain exceptional situations, cell cycle and cell growth are decoupled. For example, during early embryogenesis before access to external nutrients, cleavage cycles entail cell division without growth. However, such physiological contexts likely represent a specific adaptation to achieve unique biological ends than the general rule. For example, the embryonic cell cycle lacks G1 and G2 phases and only consists of S phase and mitosis such that cell cycle checkpoints are absent (Finkielstein et al., 2001). It is reasonable to suspect that during later phases of development (e.g., post-implantation embryogenesis and postnatal growth), tissue renewal, and regeneration, cell size checkpoints possibly function to maintain cell size uniformity that is common in many healthy tissues. Indeed, careful measurements of cell size and cell cycle progression in plant meristem cells (Jones et al., 2017; Serrano-Mislata et al., 2015) and mouse skin epidermis (Xie and Skotheim, 2020) reported similar cell size checkpoints *in vivo*. To date, such single-cell measurements of cell growth and division *in vivo* are still sparse in the literature. Future research should examine additional cell types and/or species to test the generality of the cell size checkpoint. In addition, it is also worth examining whether the cell size checkpoint also functions in endoreplication cycles that generate polyploid cells such as hepatocytes, pancreatic acinar cells, trophoblasts, and osteoclasts (Edgar and Orr-Weaver, 2001; Anzi et al., 2018). Endocycles use similar G1/S regulatory machinery as mitotic cycles (Edgar and Orr-Weaver, 2001). Therefore, the G1/S size checkpoint may exist in endocycles to maintain stable cellular content per genome to ensure balanced transcriptional and translational activities (Marguerat and Bähler, 2012; Neurohr et al., 2019; Mu et al., 2020).

Cell size homeostasis is further regulated by a cell-autonomous feedback control of growth rate

Evidence for size-dependent regulation of cellular growth rate

In proliferating cells, a cell's size (s) is the integral of the cellular growth rate (v) over the duration of the cell cycle (t), i.e., $s = \int_t v \cdot dt$. In addition to the size-dependent modulation of cell cycle length that is characteristic of cell size checkpoints, recent work suggests that the control of size homeostasis also involves cell-autonomous feedback control of cellular growth rate, i.e., the rate of volume or mass change (Figure 2A). Following the thermostat analogy, a thermometer (cell size hemostatic control) can employ parallel circuits involving both a furnace (cell growth rate regulation) and an air conditioner (cell cycle machinery) to reach and maintain homeostasis. Kafri et al. developed a novel analytic method, termed ergodic rate analysis (ERA), to extract dynamics of cell size growth from fixed epithelial cell populations for differently sized cells along a pseudotime cell cycle trajectory (Kafri et al., 2013). This analysis revealed that the estimated cell growth rate (rate of mass accumulation) is negatively correlated with size before the G1/S transition, possibly contributing to the decrease in cell size variability occurring concomitantly. In addition, Son et al. (2012) used a suspended microfluidic resonator (SMR) to quantify the instantaneous growth rates of individual mouse lymphoblasts with a precision of ~3%. This study provided the first direct, high-precision measurements of single cell growth curves and revealed a decrease in growth rate variability at the G1/S transition. Following this work, two studies used different approaches to measure cellular growth rate in adherent mammalian cells of different sizes across the cell cycle (Cadart et al., 2018; Ginzberg et al., 2018). Ginzberg et al. (2018) estimated cell size from microscopy images of nuclear area and cell mass (total protein content), and Cadart et al. (2018) estimated cell size from single cell measurements on cell volume. Despite the differences in experimental methods, these two studies converged to conclude that individual cells modulate not only growth duration (e.g., G1 length) but also growth rate to maintain size homeostasis. These findings were also supported by

recent work that measured dynamics of cellular dry mass by quantitative phase microscopy (Liu et al., 2022). Ginzberg et al. and Cadart et al. further independently showed that genetic and/or pharmacological perturbations to cell cycle duration triggered reciprocal and compensatory adjustments in cellular growth rate. In cultured RPE1 cells, Ginzberg et al. (2018) demonstrated that doxycycline-induced expression of cyclin E or p27 results in shorter or longer periods of growth in G1, respectively. Yet, these changes in growth duration are compensated by reciprocal changes in growth rate, such that cell size remains relatively constant. Cadart et al. (2018) showed that when treated with the CDK inhibitor Roscovitine, larger HeLa cells at birth compensate with slower rates of growth.

It is worth noting that the regulation on growth rate likely differs by cell types and cell cycle stages (Liu et al., 2022). For example, measurements on cellular growth by SMR found that cultured lymphocytes exhibit exponential growth kinetics where cell size positively scales with growth rate in a cell cycle-dependent manner (Son et al., 2012; Mu et al., 2020). There is also substantial literature that reported linear growth kinetics for size in certain cell types, but it has been controversial whether the measurements were accurate enough and/or correctly interpreted to make the claim (Conlon and Raff, 2003; Mitchison, 2003; Cooper, 2004, 2006; Sveiczer et al., 2004). To date, it remains a non-trivial task to generate high-quality measurements of growth dynamics in single mammalian cells. SMR, for example, is only compatible with suspended cells, whereas growth rate derived from time-lapse size measurements of nuclear size, cell volume (e.g., by fluorescence exclusion), or cell mass (quantitative phase microscopy) is very noisy at the single cell level and requires averaging across a large population to see a trend. Nevertheless, studies using these techniques have revealed interesting patterns of growth rate regulation and the underlying molecular mechanisms are starting to be revealed.

Active proteolysis underpins size-dependent regulation of cellular growth rate

What is the mechanism of such size-dependent regulation of cellular growth rate? Recent evidence suggests that the underlying driver unexpectedly involves proteasome-mediated global protein degradation, rather than protein synthesis (Liu et al., 2021). This study compared global rates of protein synthesis and degradation in differently sized cells across cell cycle stages in both unperturbed conditions or conditions that trigger a size-dependent compensation in cellular growth. These experiments demonstrated that the rate of protein synthesis scales linearly with cell size whereas the rate of protein degradation scales superlinearly, suggesting an activation of protein degradation pathways in large cells. For example, reducing the activity of cyclinE/CDK2 extends the cell cycle and subsequently triggers a compensatory slowdown of cellular growth, which involves upregulated proteasome-mediated global protein degradation. This finding suggests that the growth rate regulation in G1 mainly involves control of protein degradation, which was further supported by an independent study by Liu et al. (2022). Interestingly, it was found that large cells at the G1/S transition demonstrate hyperactivated protein degradation, even when compared to similarly-sized or larger cells at S or G2 phases (Liu et al., 2021). Taken together, these new discoveries suggest that the homeostatic size control at G1/S transition involves both the cell size checkpoint and protein degradation-mediated growth rate regulation.

Molecular control of cell size checkpoints and the hunt for cell size sensors

In the past decade, the field has started to discern the molecular mechanisms underlying the cell size checkpoint and cell size sensing. Studies on different systems yielded different models for cell size sensing. Systematic screens on cell size have revealed many critical genes and proteins involved in size regulation in different yeast species (Jorgensen et al., 2002; Zhang et al., 2002; Navarro and Nurse, 2012; Soifer and Barkai, 2014; Sellam et al., 2019) as well as mammalian cells (Liu et al., 2018). Yet, it remains unsettled whether a single molecule or pathway functions as a ruler to measure cell size, and whether different species and/or cell types share a conserved mechanism or have evolved distinct adaptive mechanisms for size checkpoint and sensing. Below we discuss progress made in different systems.

Budding and fission yeast

These two yeast model systems have pioneered the discovery of genes that activate or inhibit cell division, typically manifest as large or small sized cells in loss-of-function strains, respectively. As a primary countervailing force that balances growth, division may be triggered by the accumulation of cell cycle activators or the dilution of cell cycle inhibitors. Evidence exists for both mechanisms in both yeasts.

In the fission yeast *S. pombe*, size-dependent expression of phosphatase Cdc25, which activates the cyclin-dependent kinase Cdc2 to initiate mitosis, appears to link cell size at division (Keifenheim et al., 2017). Conversely, a potential cell size sensing mechanism based on inhibitor dilution involves the spatially restricted proteins Pom1 and Cdr2 (Martin and Berthelot-Grosjean, 2009; Moseley et al., 2009). Cdr2 is medially bound and promotes mitotic entry, whereas Pom1 localizes at the two poles and inhibits Cdr2 when cells are small. As cells elongate, Pom1 concentration at the medial zone drops, releasing cells

from Pom1 inhibition, triggering mitotic entry. Follow-up work from both groups later found that Pom1 levels at the cell median was constant regardless of cell length, and that deletion mutants of Pom1 and Cdr2 nevertheless retain cell size homeostasis, suggesting the existence of additional or compensatory size-control mechanisms (Bhatia et al., 2014; Wood and Nurse, 2013). Interestingly, Facchetti et al. (2019) reported that *S. pombe* mutants of different widths divided at the same surface area as control, but at different lengths or volumes, suggesting that cells may directly sense cell surface area or surface-to-volume ratio rather than cell size.

In the budding yeast *S. cerevisiae*, the G1 cyclin Cln3 and the G1/S transcriptional inhibitor Whi5 were identified as strong size regulators from genetic screens (Nash et al., 1988; Jorgensen et al., 2002). Cln3 has long been implicated as a critical upstream activator of cell division based on its potent dosage-dependent ability to initiate the G1/S transition and commitment to division, called Start in yeast (Nash et al., 1988; Tyers et al., 1993). The Cln3-Cdc28 (Cdk1) kinase is thought to phosphorylate both Whi5 and the SBF transcription factor complex in late G1 phase, thereby alleviating Whi5 repression and activating G1/S transcription (Costanzo et al., 2004; de Bruin et al., 2004; Wagner et al., 2009). More recently, an inhibitor dilution model has been proposed. Schmoller et al. (2015) reported that while other G1/S regulators appear to maintain a constant concentration as cells grow in G1 phase, Whi5 is subject to attenuated synthesis in G1 and is therefore diluted in concentration as cells grow in size. This dilution may trigger Start once the Whi5 concentration drops below a critical threshold in late G1 phase. However, other quantitative studies have reported that the concentration of Whi5 is independent of cell size and time, i.e., Whi5 continues to be synthesized throughout G1 phase in concert with cell growth (Dorsey et al., 2018; Litsios et al., 2019; Sommer et al., 2021; Litsios et al., 2022). Genetic evidence suggests that constitutive expression of Whi5 at physiological levels does not alter the coupling of size with passage through Start (Barber et al., 2020). In contrast to Whi5 dilution, recent single cell measurements suggest that a burst in global protein synthesis in late G1 phase results in the rapid accumulation of the highly unstable G1 cyclin Cln3, which then triggers Start and G1/S transcription by the phosphorylation-dependent inactivation of Whi5 (Litsios et al., 2019; Liu et al., 2015; Sommer et al., 2021). The Whi5 dilution model remains contentious as the critical underlying quantitative measurements depend heavily on appropriate controls for Whi5 signal loss (Litsios et al., 2022; Schmoller et al., 2022). Additional regulators and mechanisms may couple cell size, growth, and Start in budding yeast. For example, quantitative single cell analysis suggested that the SBF subunit Swi4 is initially limiting in early G1 phase with respect to its binding sites in G1/S promoters but accumulates as cells grow (Dorsey et al., 2018) and may titrate available binding sites as cells approach Start (Wang et al., 2009). Intriguingly, super-resolution microscopy studies suggest that Swi4 and other G1/S transcription factors form discrete clusters of fixed size that increase in number as cells grow throughout G1 phase (Black et al., 2020). In another example, the Aldea group uncovered a potential role for Ydj1, a chaperone regulating Cln3 degradation and localization (Ferrezuelo et al., 2012). Another recent study proposed that Cln3-Cdc28 may directly phosphorylate and activate RNA Poll II to initiate G1/S transcription (Kõivomägi et al., 2021). Work by Chen et al. (2020) suggests that size homeostasis in the budding yeast likely involves changes in the concentrations of multiple proteins. This study found that a set of cell cycle activators increase in concentration as cells grow in size while another set of cell cycle inhibitors tend to decrease in concentration, and that the countervailing effects of these positive and negative regulators determines the size of cells at S phase entry (Chen et al., 2020). Similar differential scaling of macromolecular concentrations and organelle content over cell size as a function of senescence has been recently reported in human cells (Cheng et al., 2021; Lanz et al., 2021). Beyond cell size regulation under homeostatic conditions, many studies have investigated how nutrient conditions alter cell size in yeast, and multiple factors have been implicated as nutrient sensors or effectors, including Cln3, Whi5, G1/S transcription factors, nutrient-sensing kinases, and metabolic status (Dorsey et al., 2018; Litsios et al., 2019; Qu et al., 2019; Sommer et al., 2021; Tollis et al., 2022). Despite the powerful molecular genetics of yeast models, it is clear that further quantitative experiments will be needed to discriminate between countervailing models and to understand how different signals are integrated to effect robust yet adaptive size homeostasis.

Mammalian cells

To probe the factors underlying the cell size checkpoint in mammalian cells, Liu et al. (2018) employed a high-throughput screening approach to systematically search for perturbations that result in loss of cell size (total protein mass) control. Specifically, the authors looked for perturbations that increase cell size variability and also disrupt the function of the G1/S size checkpoint, resulting in the loss of G1 length compensation in small cells (Figure 2C). It was found that components of the p38 MAPK pathway were highly enriched among the top hits of the screen. In contrast, the mTOR pathway, a master regulator of cell growth, is not required for the proper function of the checkpoint, i.e., small cells under mTOR inhibition still compensate with longer G1. The work further demonstrated that small cells undergo p38 activation, which delays their G1/S transition. Inhibition of p38 MAPKs by either chemical inhibitors or genetic knockdown leads to the loss of the

compensatory G1 extension in small cells, resulting in faster proliferation, smaller cell sizes, and increased size heterogeneity. It was later independently reported by Sellam et al. (2019) that Hog1, a yeast homolog of mammalian p38 MAPK, similarly underlies the G1/S cell size checkpoint in the opportunistic yeast pathogen *Candida albicans*. This result suggests that the p38 MAPK may be an evolutionarily conserved regulator of cell size across eukaryotes. However, it remains to be discovered how p38 MAPK or its upstream regulators biophysically 'sense' cell size. The p38 MAPK pathway is canonically viewed as a stress response pathway that is activated by multiple types of stress stimuli, including cytokines, heat shock, and osmotic shock; notably, the latter induces fast and often drastic changes in cell volume (Han et al., 2020). This suggests an interesting possibility that changes in cell mass and volume are sensed, at least in part, through a shared mechanism. It is also possible that deviations in size homeostasis activates stress sensing pathways, which then integrate to activate the p38 MAPK and inhibit cell cycle progression.

In parallel, inhibitor dilution mechanisms have been reported for Rb in mammalian cells (Zatulovskiy et al., 2020), and for KRP4, a plant-specific G1/S inhibitor, in plant shoot meristem cells (D'Ario et al., 2021). The p16-cyclin D-CDK4/6 axis that mediates the phosphorylation-dependent inactivation of the Rb tumor suppressor, which inhibits the E2F family of G1/S transcription factors, has long been implicated in cell cycle commitment and, by extension, size control in mammalian cells (Sherr, 1996). This conventional view of phosphorylation-mediated inactivation of Rb has been challenged recently, however, in that size-dependent G1/S transition may not require progressive phosphorylation of Rb by cyclin/CDKs but is instead driven by size-associated Rb dilution (Zatulovskiy et al., 2020). It was suggested that Rb phosphorylation possibly remains constant throughout most of G1 and that the G1/S transition may be initiated before Rb hyperphosphorylation occurs (Rubin et al., 2020; Zatulovskiy et al., 2020). Analogous to the proposed Whi5 dilution mechanism in yeast (Schmoller et al., 2015), Zatulovskiy et al. (2020) reported that the amount of Rb is maintained relatively constant in the G1 phase and should therefore be diluted as cells grow in size. Rb synthesis was found to be restricted to the S and G2 phases, and mother cells were observed to partition equal amounts of Rb to both daughter cells in a size-independent manner, but the specific mechanisms are unknown. Knocking out Rb results in smaller cell sizes, higher cell size variability, and disruption of the size-dependency in G1 duration, similarly to the previously reported p38 inhibition phenotype (Liu et al., 2018; Zatulovskiy et al., 2020). Given that the p38 MAPK pathway is upstream of Rb in the regulation of G1/S transition (Thornton and Rincon, 2009; Tomás-Loba et al., 2019), it is plausible that both proteins function in a shared pathway downstream of cell size sensing to regulate cell size-dependent S phase entry.

Cells in tissues and of other systems

Past pursuits for cell size sensors concentrated on single-celled yeast or cultured cells. Do animal cells in an *in vivo* tissue context employ further size sensing mechanisms? Mechanosensing is a likely candidate. A study by Boehlke et al. (2010) showed that kidney epithelial cells regulate their size in response to the flow of extracellular fluid (i.e., urine flow *in vivo*) through activation of the LKB1-mTORC1 pathway induced by the primary cilia. Additionally, cardiac muscles are known to undergo hypertrophy under excessive mechanical load from high blood pressure or volume overload (Pitoulis and Terracciano, 2020). Studies on mechanobiology have revealed that mammalian cells can sense mechanical forces and regulate the cell cycle accordingly. High local mechanical stress was found to inhibit cell proliferation through the Hippo-YAP pathway (Pan et al., 2016); conversely, exerting a stretching force promotes cell proliferation (Streichan et al., 2014). A recent study on growing epithelial cell monolayer sheets also found that mechanical tension more strongly predicts a cell's G1 duration compared to the cell area and area growth rate, suggesting that cells may directly sense mechanical forces to determine the timing of G1/S transition (Uroz et al., 2018). In addition to its role in regulating the cell cycle, it is possible that mechanical forces also regulate cellular growth: pushing forces may inhibit cell growth and therefore alleviate local mechanical stresses, whereas stretching forces may promote cell growth to reduce the initial stretch. Such a biophysical negative feedback regulation between mechanical forces and cell size may be critical for cell size uniformity at the tissue level. Direct experimental evidence for this hypothesis is still lacking, but recent work from different groups suggest that the Hippo-YAP pathway may function as a mechanotransducer to regulate cell size and volume independent of its role in the cell cycle (Gonzalez et al., 2018; Perez-Gonzalez et al., 2019; Mugahid et al., 2020).

In addition, others have developed mathematical models on axon length sensing in neurons (Rishal et al., 2012; Perry et al., 2016) and flagellum length sensing in *Chlamydomonas reinhardtii* (Hendel et al., 2018). These models suggest that size sensing may be an emergent phenomenon of a biochemical network instead of relying on a single sensor molecule. Interestingly, a study using cell-free droplets of *Xenopus* egg extracts recapitulated chemical oscillations of the embryonic cell cycle in oil-encapsulated droplets and found that smaller droplets had longer cycle period, resembling that of yeast and animal cells (Guan et al., 2018). Another study on a non-cell-cycle transcription oscillator also observed that smaller droplets had longer cycle periods (Weitz et al., 2014). As these droplets were generated from the same extract preparation, they should have the same expected concentrations of different types of molecules. Why do smaller droplets have longer cycle periods? A possible explanation is that smaller droplets have higher stochasticity in the number of different types of encapsulated molecules (Box 1).

Box 1 Why do smaller cell-free droplets have longer cycle periods?

Consider the chemical oscillation (e.g., cell cycle) in the droplets as a biochemical reaction of *N* rate limiting steps, and that in each step, a gene is translated in a linear rate to reach a normalized threshold 1 to activate the next reaction. In the embryonic cell cycle, for example, it can be considered to have one rate limiting step of cyclin B translation. Assume that the translation rate has a normal distribution *X(u,v)*, where *u* represents the distribution mean and *v* the standard deviation. Then for any cell, the cell cycle duration is *N*E(1/X)*, where *E* represents the expectation (mean). When the cell is large enough, the translation rate equals *E(X)=u*, and the cycle duration is *N/u*. When the cell is small, the average duration of the cell cycle is *N*E(1/X)*. According to Jensen's inequality, $N*E(1/X) \geq N/E(X)=N/u$.

Mechanisms that determine target size

The cell size checkpoint contributes to the control of size homeostasis. However, the setpoint of such a checkpoint can be dynamically adjusted during cellular differentiation and under different environmental conditions, similar to how the setpoint of a thermostat can be dialed. What is the mechanism that programs target size? Indications for roles of the CDK4-cyclin D1/Rb pathway in cell size control have previously been identified. CDK4/cyclin D1 functions to promote cell growth independently of cell cycle progression in both *Drosophila* and *C. elegans* (Datar et al., 2000; Korzelius et al., 2011), while the size of isolated murine hepatocytes scales with the number of *Rb1* alleles (Zatulovskiy et al., 2020). Tan et al. (2021) recently identified that CDK4 is involved in the target size specification of mammalian cells. In previous work on cell size checkpoint (Liu et al., 2018), the same group developed an experimental assay that quantifies the level of compensation (i.e., G1 length extension) in small cells under different levels of mTORC1 inhibition. This assay revealed two types of cell size regulators, which were termed sensors and dials, following the thermostat analogy. Perturbing sensors, such as p38 MAPK, disrupts the G1 length compensation (i.e., small cells do not compensate with longer G1), implicating their role in the cell size checkpoint. In contrast, perturbing dials, such as CDK4, shifts cells to a different size without interfering with the G1 length compensation, indicating a reprogramming of target size (Figure 2D). Using the same assay, Tan et al. (2021) characterized hits from a previously published cell size screen (Liu et al., 2018). Among all hits analyzed, CDK4 inhibitors produced the biggest shift in size (up to ~80%) while still maintaining the size-dependent checkpoint at G1/S transition. Moreover, the observed influence on cell size is dose-dependent, suggesting that CDK4 activity fine tunes target size in a continuous manner. Interestingly, knockdown of CDK2 or CDK6 also results in a dial phenotype but has a much smaller influence on cell size (~10%–20%), highlighting a distinct role for CDK4 in target size specification.

The strong influence of CDK4 on cell size suggests that in addition to its role in cell cycle progression, CDK4 also regulates growth rate. Indeed, its cyclin partner, cyclin D, has been shown to be a key mediator of cell growth in both plant and animal cells (Cockcroft et al., 2000; Nelsen et al., 2003). Decreases in CDK4 activity are also associated with increased rates of protein synthesis, activities of growth-promoting pathways (e.g., mTORC1, c-Myc, ERK), and overall bioenergetic capacity (Tan et al., 2021). Previously, p38 activity was found to be selectively upregulated in cells that are smaller than a given size threshold (Liu et al., 2018). Tan et al. (2021) further found that this threshold is determined by CDK4 activity. While links between p38 and CDK4 have been identified (Casanovas et al., 2000; Thoms et al., 2007), it remains unexplored how these two signaling pathways are coupled to maintain cell size homeostasis at a given CDK4-determined target size. Interestingly, genetic knockdown of *Rb1*, a direct downstream target of CDK4, results in perturbations to the G1/S size checkpoint and homeostatic control of cell size (Zatulovskiy et al., 2020). These studies show different influences for CDK4 and Rb1 on cell size - while perturbations to CDK4 activity in RPE1 cells and primary human fibroblasts result in shifts in cell size with minimal influence on size homeostasis (Tan et al., 2021), perturbing Rb1 in mouse hepatocytes leads to an increase in size heterogeneity (Zatulovskiy et al., 2020). The differential size effects of CDK4 and Rb1 may be explained by their tissue- and cell type-specific growth effects (Lin et al., 1996; Datar et al., 2000). Alternatively, it may suggest that CDK4 regulates cell growth through both Rb1-dependent and Rb1-independent mechanisms, as hinted by previous studies in *Drosophila* (Datar et al., 2000; Emmerich et al., 2004), *C. elegans* (Korzelius et al., 2011), and mammalian cells (Lee et al., 2014).

It is important to note that perturbations to either the cell size checkpoint, target size specification mechanism, or cell cycle progression can result in significant changes in cell size, particularly when probed at a population-averaged level. It is well recognized in the field that one needs to delineate a gene's influence on the cell cycle from that on cell size. This is because perturbations to the cell cycle may affect cells' distribution across cell cycle stages. Therefore, cell size may have appeared different at the population average yet remained identical when comparing the same cell cycle stage. Just as how cell size relates to the cell cycle, the control of cell size homeostasis and target size specification are two separate but coupled processes. It is therefore necessary to delineate the two to identify specific factors that separately control each, ones that regulate both, and those that coordinate the two processes.

Cell size and function: Why does cell size matter?

Despite much recent work on the mechanisms of size control, past research has skirted the key question of the biological significance of cell size (Lloyd, 2013; Björklund and Marguerat,

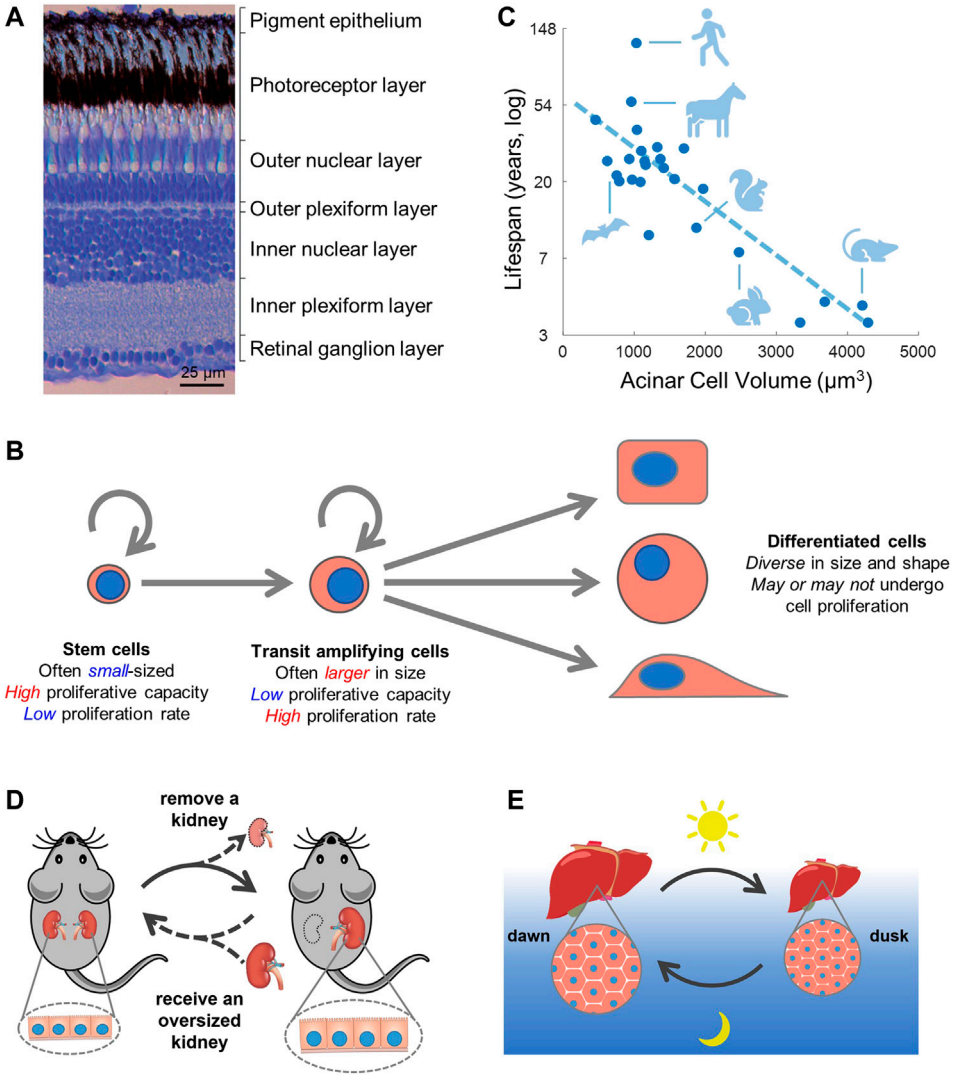

FIGURE 3
Cell size and function. **(A)** In the retina, cell size is tightly regulated to match the layered tissue structure. Image is from (Gramage et al., 2014). **(B,C)** Small cell size is correlated with stemness **(B)** and longer lifespan **(C)**. Panel **(C)** is adapted from (Anzi et al., 2018), which examined the size of pancreatic acinar cells among 24 mammalian species and identified a negative correlation between cell size and animal lifespan. **(D,E)** Cell size regulation as a general strategy to modulate organ size and function. **(D)** Animals removed of one kidney experience compensatory growth in the remaining kidney mainly through increases in cell size (Johnson and Vera Roman, 1966). Conversely, replacing a normal sized kidney with an oversized one induces a regression in kidney size (Churchill et al., 1991; Salvatierra et al., 1998), potentially through changes in cell size. **(E)** Murine hepatocytes oscillate in size from dawn to dusk following a circadian rhythm (Sinturel et al., 2017). Note that the mouse is nocturnal and eats at night.

2017; Miettinen et al., 2017). Nevertheless, various studies have identified interesting links between cell size and animal physiology/pathology (see below). In humans, deregulation of cell size and morphology has been associated with various diseases such as breast and small cell lung cancers (Asadullah et al., 2021; Bell and Waizbard, 1986; Lee et al., 1992), hypoinsulinemia (Giordano et al., 1993; Pende et al., 2000), neurological disorders (Kwon et al., 2001, 2003), and aging (Buchwalter and Hetzer, 2017; Tiku et al., 2017; Neurohr et al., 2019). In this section, we discuss this fundamental question and present examples and hypotheses on how cell size may affect different cellular, tissue, and organismal functions.

A structural requirement

Just as all the parts in a physical machine must precisely match in size for the machine to function properly, it is likely

critical for cells in the body to coordinate in size with each other and with the tissue structure. For example, skeletal muscle fibers usually span the entire length of a muscle (Heidlauf and Röhrle, 2014) and many neurons also extend a long distance from the central nervous system to peripheral target tissues (Rich and Terman, 2018). The nervous system provides a particularly compelling example in which function depends on precise size control to match the tissue structure (Figure 3A).

Early research on cell size control in neurons found that neuronal size is regulated by extrinsic signals, such as nerve growth factors, secreted by peripheral targets that couple rates of protein synthesis with degradation (Purves et al., 1988; Franklin and Johnson, 1998). Such extrinsic size control allows neurons to adjust in size in accordance with its surrounding tissues during development and regeneration. In addition to extrinsic size control, several recent studies also proposed intrinsic mechanisms of axon length control (Lallemend et al., 2012; Rishal et al., 2012; Perry et al., 2016). Interestingly, a systematic analysis of dendrite morphology in cortical neurons revealed that the size of dendrites (length and number of branches) is cell-autonomously controlled, such that fluctuations in one region of a neuron are systematically counterbalanced by the remaining dendrites in the same cell (Samsonovich and Ascoli, 2006).

To maintain proper tissue structure, cells need to coordinate their size and shape but are not necessarily required to be at certain absolute sizes. In 1945, Gerhard Fankhauser published a fascinating paper showing an almost perfect maintenance of organ size and function in the salamander larvae despite significant changes in cell size (Fankhauser, 1945). In this study, haploid or polyploid animals that have smaller or larger cell sizes, respectively, maintained similar organ and body sizes as normal diploids by adjusting cell number and shape. While this seems to suggest that cell size does not necessarily impact overt physiological function, it raises the question of why cells in normal diploids have specific characteristic sizes. Resolution of this question remains an outstanding problem.

An optimal cell size for growth and metabolism

While it is evident that certain cell types need to be of certain sizes, it is less obvious how cell size matters for others. One hypothesis is that there may exist an optimal size for particular functions. Supporting this notion, a study quantified mitochondrial activity across cells of different sizes and found that size-normalized mitochondrial level peaks at an intermediate cell size and drops in either large or small cells (Miettinen and Björklund, 2016). This observation suggests that an optimal cell size exists to maximize mitochondrial metabolism, which would be important for metabolically demanding processes such as cellular growth. Indeed, a similar trend has been observed for cellular growth rates. Although rates of cellular growth (in cell mass or volume) tend to increase with cell size (with the exception of G1/S transition), recent studies revealed a decline in growth rate and/or efficiency (size-normalized growth rate) in exceedingly large cells (Cadart et al., 2018; Ginzberg et al., 2018; Goranov et al., 2013; Liu et al., 2021; Neurohr et al., 2019; Son et al., 2012; Varsano et al., 2017), implying an optimal cell size range for tissues that undergo rapid growth. In microorganisms, optimal sizes may depend on nutrient conditions. For example, budding yeast show a reduced size upon nutrient limitation (Johnston et al., 1977). Interestingly, a multi-decade experiment that grew *E. coli* on rich media over 50,000 generations has found that cells consistently evolved larger sizes, suggesting higher fitness for large cells under rich nutrients (Grant et al., 2021).

What is the biophysical and biochemical basis for the existence of an optimal cell size? A well-known mechanism is that large cells have reduced surface area to volume ratio, which negatively impacts cross-membrane absorption and secretion (Miettinen and Björklund, 2017; Björklund, 2019). DNA content is also a potential limiting factor for cellular growth and function in large diploid cells. It was suggested that in both yeast and mammalian cells, a low DNA:cytoplasm ratio contributes to functional decline and senescence (Neurohr et al., 2019). Another possible mechanism is that the optimal function of a cell requires matched sizes and/or numbers of different intracellular molecules and structures, but these quantities may not always scale linearly with cell size. For example, many organelles have larger sizes in larger cells (Marshall, 2020), such as the nuclei, nucleoli, spindle, mitochondria, and endoplasmic reticulum. However, a recent quantification revealed that the protein content of different organelles scale with cell size at different slopes (Cheng et al., 2021), with the nucleus, lipid droplet, and mitochondrial outer membrane scaling sublinearly and the lysosome, autophagosomes, endoplasmic reticulum, and mitochondrial inner membrane and matrix scaling superlinearly with cell size. Together, these studies suggest that efficient growth is associated with an optimal size; the mechanisms that underlie this control and how various subcellular compartments contribute to this optimality remain to be investigated.

Cell size, stemness, and lifespan

Stem and progenitor cells are critical for tissue homeostasis and regeneration. Interestingly, stem and progenitor cells are generally smaller in size compared to their differentiated progenies (Figure 3B) (Li et al., 2015; Lengefeld et al., 2021). For example, early studies using size elutriation have found that smaller epidermal keratinocytes and fibroblasts had higher proliferative capacity (Barrandon and Green, 1985; Angello

et al., 1987). Smaller keratinocytes also show higher levels of the stem cell marker p63 (Parsa et al., 1999) and lower involucrin synthesis, an indicator of differentiation (Watt and Green, 1981). Hematopoietic stem cells that generate all blood lineages are also characterized by their small size, a property used to isolate hematopoietic stem cells (HSCs) in early studies (Jones et al., 1996; Radley et al., 1999). Additionally, a number of adult stem cell types are commonly described as "small cells" in the literature, such as the intestinal stem cells (Sato et al., 2011), regenerative cells of the fallopian tube (peg cells) (Paik et al., 2012), and stem cells in the rodent incisor (Biehs et al., 2013).

Intriguingly, the link between cell size and proliferative capacity may be evolutionarily conserved. In single-celled budding yeast, smaller cell size is associated with higher replicative capacity since genetic mutations that result in smaller yeast cells have longer replicative lifespans and vice versa (Yang et al., 2011). Similarly, in plants, apical meristem cells located in the shoot or root tips (comparable to stem cells in animals) are smaller in size compared to the more differentiated cells in the developing organs (Laufs et al., 1998; Jones et al., 2017).

On the other hand, senescent cells are usually associated with a large size (Muñoz-Espín and Serrano, 2014). In budding yeast, cells grow >50% larger in size across a replicative lifespan and enter senescence at a relatively constant size (~10 μm) regardless of initial sizes (Mortimer and Johnston, 1958; Yang et al., 2011; Wright et al., 2013). A recent report on mouse HSCs suggested a causal link between cell size and stemness, whereby the enlargement of HSCs reduces their stem cell potential (Lengefeld et al., 2021). These authors also found that HSCs in both mice and humans increase in size during organismal aging, and the prevention of this age-dependent enlargement improves HSC function. Other recent studies examined molecular changes in large cells and proposed that enlarged cell sizes may induce senescence rather than simply being a phenotypic hallmark of senescence (Neurohr et al., 2019; Cheng et al., 2021; Lanz et al., 2021). For example, two independent papers reported upregulation of certain ER and lysosome-resident proteins in large mammalian cells (Cheng et al., 2021; Lanz et al., 2021), which has been known to induce a senescent phenotype (Lee et al., 2006; Ziegler et al., 2021).

Interestingly, the function of mTORC1, a major regulator of cell size and growth, was shown to be necessary for senescence (Demidenko et al., 2009; Laberge et al., 2015; Park et al., 2020). Aside from being a central regulator of cell growth, the mTORC1 pathway is also one of the key regulators of organismal aging. In fact, mTOR remains one of the few evolutionarily conserved pathways whose inhibition was found to extend the lifespan of all model organisms tested thus far, including yeast (Kaeberlein et al., 2005), *C. elegans* (Vellai et al., 2003), *Drosophila* (Kapahi et al., 2004), zebrafish (Khor et al., 2019), and mouse (Harrison et al., 2009). Together, these studies pose an interesting association between cell size and animal lifespan as both have links to the mTOR pathway. Indeed, two recent studies have revealed striking inverse correlations between cell size and animal lifespan in multicellular organisms. One study examined the size of adult pancreatic acinar cells across 24 mammalian species and identified a negative correlation between acinar cell size and animal lifespan (Figure 3C), independent of animal body size or metabolic rate (Anzi et al., 2018). Another study demonstrated that larger nucleoli are implicated with accelerated aging in worms, mice, and humans (Tiku et al., 2017). In addition, $p16^{INK4a}$/CDK4 may be another pathway that regulates both cell size and animal longevity. p16 is a major driver of senescence (Coppé et al., 2011). In mice, aging is reversed by the clearance of p16 expressing cells and accelerated by the overexpression of p16 (Boquoi et al., 2015; Baker et al., 2016) as well as by mutation of multiple Rb phosphorylation sites (Jiang et al., 2022). p16 may also regulate cell size through its canonical function as an inhibitor of CDK4/6 (Tan et al., 2021). However, the correlation between cell size and longevity do not necessarily imply causation or directionality, and future work should therefore investigate the mechanistic drivers that link the two processes.

Organ size control by cellular hypertrophy and atrophy

Growth (hypertrophy) and shrinkage (atrophy) in cell size is a common strategy of organ size regulation. Even in adulthood, tissue and organ sizes are dynamically controlled in response to the fluctuating environment. A larger organ size is generally associated with higher functional capacity. Many organs such as the liver, pancreas, kidney, lung, heart, and skeletal muscle undergo compensatory growth when experiencing increased functional demand (Goss, 1965). The liver, for example, can regenerate after partial hepatectomy by cell hypertrophy and increased polyploidy when cell division is inhibited (Diril et al., 2012). Pregnant mothers (of rodents and humans) that face elevated metabolic demand also experience significant cell hypertrophy in the liver (Milona et al., 2010) and pancreas (Rieck et al., 2009; Rieck and Kaestner, 2010). For cell types with limited proliferative capability, cell hypertrophy and atrophy can be readily used to regulate organ size. For example, the adult kidney has a low regenerative capacity. Human subjects or animals that have lost one kidney (e.g., for a kidney donation) experience rapid growth of the remaining kidney mostly through an increase in cell size (Johnson and Vera Roman, 1966) (Figure 3D). Even more surprisingly, transplanting an oversized kidney into a small-sized recipient (e.g., from adult to infants) results in regression of the transplanted kidney to match the size of the recipient (Churchill et al., 1991; Salvatierra et al., 1998), a process possibly accomplished through atrophy in cell size.

Growth and regression in organ size by changes in cell size maintains the overall organ structure and is likely more energy efficient than drastic alterations in cell number. The advantage of cell hypertrophy over hyperplasia can be important for tissues that undergo repeated cycles of growth and regression, such as the circadian/daily and circannual/seasonal cycles. Murine hepatocytes, for example, can experience daily oscillations in size of over 30% between dawn and dusk (Figure 3E) (Sinturel et al., 2017). In seasonal animals (e.g., seasonal breeders and hibernators), many organs undergo dramatic changes in size (Hindle et al., 2015) and cell types including adipocytes and different endocrine cells have been reported to display seasonal cell size variations (Klonisch et al., 2006; Wood et al., 2015). The mechanisms that account for cell division-independent control of cell size remain to be explored but will almost certainly depend on catabolic processes such as proteasome-mediated protein degradation (Acebron et al., 2014; Liu et al., 2021; Liu et al., 2022) and the manifold forms of autophagy (Miettinen and Björklund, 2015; Orhon et al., 2016).

Perspectives on future cell size research

The past decade has seen rapid advances in mammalian cell size research, much of which was motivated by the original evidence for the cell size checkpoint first published in 1965 by Killander and Zetterberg. Over recent years, a number of independent labs have developed new methods to accurately and efficiently measure cell size (Cadart et al., 2018; Godin et al., 2010; Kafri et al., 2013; Liu et al., 2020; Serrano-Mislata et al., 2015; Son et al., 2012; Varsano et al., 2017). These efforts have delivered evidence that not only confirms the original seminal observation (Killander and Zetterberg, 1965a), but have further shown that size homeostasis in animal cells arise from regulation of both the duration and rate of cellular growth (Cadart et al., 2018; Ginzberg et al., 2018; Liu et al., 2022). Initial insights into the signal transduction pathways that underlie mammalian cell size checkpoint (Liu et al., 2018; Zatulovskiy et al., 2020) and target size specification (Tan et al., 2021) have begun to emerge.

Despite recent progress, our understanding of cell size control *in vivo* remains limited. In this review, we discussed the physiological importance of cell size. To date, quantification of cell size in tissues remains limited. With advances in 3D live-cell and deep tissue imaging, we expect more reports on measurements of cell size *in vivo* as well as in 3D organoid cultures. We envision that careful measurements of cell size in different tissue types and in different mutant contexts will reveal further interesting links between cell size and function, and shed light on how cell growth and size regulate and are regulated by animal physiology.

Author contributions

All authors listed have made a substantial, direct, and intellectual contribution to the work and approved it for publication.

Funding

The Kafri lab team was supported by the Canada Research Chair (CRC) Program (Chair in Quantitative Cell Biology) and the Canadian Institutes of Health Research (CIHR) (FRN: MOP-142194). SL was supported by the SickKids Restracomp Graduate Fellowship and the Wu Tsai Neurosciences Institute Interdisciplinary Scholar Award. CT was supported by a University of Toronto Open Fellowship. MT was supported by a CRC Chair in Systems and Synthetic Biology and a grant from the CIHR (FDN-167277). AZ was supported by the Swedish Cancer Society "Cancerfonden".

Acknowledgments

We thank Wallace Marshall for inspiration on the thermostat model of cell size control, Jan Skotheim for comments on the dilution model, Zhengda Li for input on the theory of how droplet size affects cell cycle length (Box 1), Shona Wood for input on the circannual rhythm, Yuval Dor and colleagues for the histological images of pancreata, www.HistologyGuide.org, T. Clark Brelje and Robert L. Sorenson (University of Minnesota, Minneapolis, MN) for the histological images presented in Figure 1A, as well as Teemu Miettinen, Catherine Royer, Andreas Milias-Argeitis, and Kafri lab members for helpful discussions of the manuscript.

Conflict of interest

The authors declare that the research was conducted in the absence of any commercial or financial relationships that could be construed as a potential conflict of interest.

Publisher's note

References

Acebron, S. P., Karaulanov, E., Berger, B. S., Huang, Y.-L., and Niehrs, C. (2014). Mitotic wnt signaling promotes protein stabilization and regulates cell size. *Mol. Cell.* 54 (4), 663–674. doi:10.1016/j.molcel.2014.04.014

Angello, J. C., Pendergrass, W. R., Norwood, T. H., and Prothero, J. (1987). Proliferative potential of human fibroblasts: An inverse dependence on cell size. *J. Cell. Physiol.* 132 (1), 125–130. doi:10.1002/jcp.1041320117

Anzi, S., Stolovich-Rain, M., Klochendler, A., Fridlich, O., Helman, A., Paz-Sonnenfeld, A., et al. (2018). Postnatal exocrine pancreas growth by cellular hypertrophy correlates with a shorter lifespan in mammals. *Dev. Cell.* 45 (6), 726–737. e3. doi:10.1016/j.devcel.2018.05.024

AsadullahKumar, S., Saxena, N., Sarkar, M., Barai, A., and Sen, S. (2021). Combined heterogeneity in cell size and deformability promotes cancer invasiveness. *J. Cell. Sci.* 134 (7), jcs250225. doi:10.1242/jcs.250225

Baker, D. J., Childs, B. G., Durik, M., Wijers, M. E., Sieben, C. J., Zhong, J., et al. (2016). Naturally occurring p16Ink4a-positive cells shorten healthy lifespan. *Nature* 530 (7589), 184–189. doi:10.1038/nature16932

Barber, F., Amir, A., and Murray, A. W. (2020). Cell-size regulation in budding yeast does not depend on linear accumulation of Whi5. *Proc. Natl. Acad. Sci. U. S. A.* 117 (25), 14243–14250. doi:10.1073/pnas.2001255117

Barrandon, Y., and Green, H. (1985). Cell size as a determinant of the clone-forming ability of human keratinocytes. *Proc. Natl. Acad. Sci. U. S. A.* 82 (16), 5390–5394. doi:10.1073/pnas.82.16.5390

Bell, C. D., and Waizbard, E. (1986). Variability of cell size in primary and metastatic human breast carcinoma. *Invasion Metastasis* 6 (1), 11–20.

Biehs, B., Hu, J. K.-H., Strauli, N. B., Sangiorgi, E., Jung, H., Heber, R.-P., et al. (2013). BMI1 represses Ink4a/Arf and Hox genes to regulate stem cells in the rodent incisor. *Nat. Cell. Biol.* 15 (7), 846–852. doi:10.1038/ncb2766

Björklund, M. (2019). Cell size homeostasis: Metabolic control of growth and cell division. *Biochim. Biophys. Acta. Mol. Cell. Res.* 1866 (3), 409–417. doi:10.1016/j.bbamcr.2018.10.002

Björklund, M., and Marguerat, S. (2017). Editorial: Determinants of cell size. *Front. Cell. Dev. Biol.* 5, 115. doi:10.3389/fcell.2017.00115

Bhatia, P., Hachet, O., Hersch, M., Rincon, S. A., Berthelot-Grosjean, M., Dalessi, S., et al. (2014). Distinct levels in Pom1 gradients limit Cdr2 activity and localization to time and position division. *Cell Cycle* 13 (4), 538–552. doi:10.4161/cc.27411

Black, L., Tollis, S., Fu, G., Fiche, J.-B., Dorsey, S., Cheng, J., et al. (2020). G1/S transcription factors assemble in increasing numbers of discrete clusters through G1 phase. *J. Cell. Biol.* 219 (9), e202003041. doi:10.1083/jcb.202003041

Boehlke, C., Kotsis, F., Patel, V., Braeg, S., Voelker, H., Bredt, S., et al. (2010). Primary cilia regulate mTORC1 activity and cell size through Lkb1. *Nat. Cell. Biol.* 12 (11), 1115–1122. doi:10.1038/ncb2117

Bonner, J. T. (2006). *Why size matters*. Princeton University Press.

Boquoi, A., Arora, S., Chen, T., Litwin, S., Koh, J., and Enders, G. H. (2015). Reversible cell cycle inhibition and premature aging features imposed by conditional expression of p16Ink4a. *Aging Cell.* 14 (1), 139–147. doi:10.1111/acel.12279

Brooks, R. F. (1981). in *Variability in the cell cycle and the control of proliferation*. *The cell cycle*. Editor P. C. L. John (Cambridge University Press).

Buchwalter, A., and Hetzer, M. W. (2017). Nucleolar expansion and elevated protein translation in premature aging. *Nat. Commun.* 8 (1), 328. doi:10.1038/s41467-017-00322-z

Cadart, C., Monnier, S., Grilli, J., Sáez, P. J., Srivastava, N., Attia, R., et al. (2018). Size control in mammalian cells involves modulation of both growth rate and cell cycle duration. *Nat. Commun.* 9 (1), 3275. doi:10.1038/s41467-018-05393-0

Casanovas, O., Miró, F., Estanyol, J. M., Itarte, E., Agell, N., and Bachs, O. (2000). Osmotic stress regulates the stability of cyclin D1 in a p38SAPK2-dependent manner. *J. Biol. Chem.* 275 (45), 35091–35097. doi:10.1074/jbc.M006324200

Chen, Y., Zhao, G., Zahumensky, J., Honey, S., and Futcher, B. (2020). Differential scaling of gene expression with cell size may explain size control in budding yeast. *Mol. Cell.* 78 (2), 359–370. e6. doi:10.1016/j.molcel.2020.03.012

Cheng, L., Chen, J., Kong, Y., Tan, C., Kafri, R., and Bjorklund, M. (2021). Size-scaling promotes senescence-like changes in proteome and organelle content. *bioRxiv*. doi:10.1101/2021.08.05.455193

Churchill, M., Churchill, P. C., Schwartz, M., Bidani, A., and McDonald, F. (1991). Reversible compensatory hypertrophy in transplanted Brown Norway rat kidneys. *Kidney Int.* 40 (1), 13–20. doi:10.1038/ki.1991.173

Cockcroft, C. E., den Boer, B. G., Healy, J. M., and Murray, J. A. (2000). Cyclin D control of growth rate in plants. *Nature* 405 (6786), 575–579. doi:10.1038/35014621

Conlon, I., Dunn, G. A., Mudge, A. W., and Raff, M. (2001). Extracellular control of cell size. *Nat. Cell. Biol.* 3 (10), 918–921. doi:10.1038/ncb1001-918

Conlon, I., and Raff, M. (2003). Differences in the way a mammalian cell and yeast cells coordinate cell growth and cell-cycle progression. *J. Biol.* 2 (1), 7. doi:10.1186/1475-4924-2-7

Cooper, S. (2004). Control and maintenance of mammalian cell size. *BMC Cell. Biol.* 5 (1), 35–21. doi:10.1186/1471-2121-5-35

Cooper, S. (2006). Distinguishing between linear and exponential cell growth during the division cycle: Single-cell studies, cell-culture studies, and the object of cell-cycle research. *Theor. Biol. Med. Model.* 3, 10. doi:10.1186/1742-4682-3-10

Coppé, J.-P., Rodier, F., Patil, C. K., Freund, A., Desprez, P.-Y., and Campisi, J. (2011). Tumor suppressor and aging biomarker p16(INK4a) induces cellular senescence without the associated inflammatory secretory phenotype. *J. Biol. Chem.* 286 (42), 36396–36403. doi:10.1074/jbc.M111.257071

Costanzo, M., Nishikawa, J. L., Tang, X., Millman, J. S., Schub, O., Breitkreuz, K., et al. (2004). CDK activity antagonizes Whi5, an inhibitor of G1/S transcription in yeast. *Cell.* 117 (7), 899–913. doi:10.1016/j.cell.2004.05.024

Curcio, C. A., Sloan, K. R., Kalina, R. E., and Hendrickson, A. E. (1990). Human photoreceptor topography. *J. Comp. Neurol.* 292 (4), 497–523. doi:10.1002/cne.902920402

D'Ario, M., Tavares, R., Schiessl, K., Desvoyes, B., Gutierrez, C., Howard, M., et al. (2021). Cell size controlled in plants using DNA content as an internal scale. *Science* 372 (6547), 1176–1181. doi:10.1126/science.abb4348

Darzynkiewicz, Z., Evenson, D. P., Staiano-Coico, L., Sharpless, T. K., and Melamed, M. L. (1979). Correlation between cell cycle duration and RNA content. *J. Cell. Physiol.* 100 (3), 425–438. doi:10.1002/jcp.1041000306

Datar, S. A., Jacobs, H. W., de la Cruz, A. F. A., Lehner, C. F., and Edgar, B. A. (2000). The Drosophila Cyclin D–Cdk4 complex promotes cellular growth. *EMBO J.* 19 (17), 4543–4554. doi:10.1093/emboj/19.17.4543

de Bruin, R. A., McDonald, W. H., Kalashnikova, T. I., Yates, J., and Wittenberg, C. (2004). Cln3 activates G1-specific transcription via phosphorylation of the SBF bound repressor Whi5. *Cell.* 117 (7), 887–898. doi:10.1016/j.cell.2004.05.025

Demidenko, Z. N., Zubova, S. G., Bukreeva, E. I., Pospelov, V. A., Pospelova, T. V., and Blagosklonny, M. V. (2009). Rapamycin decelerates cellular senescence. *Cell. Cycle* 8 (12), 1888–1895. doi:10.4161/cc.8.12.8606

Diril, M. K., Ratnacaram, C. K., Padmakumar, V. C., Du, T., Wasser, M., Coppola, V., et al. (2012). Cyclin-dependent kinase 1 (Cdk1) is essential for cell division and suppression of DNA re-replication but not for liver regeneration. *Proc. Natl. Acad. Sci. U. S. A.* 109 (10), 3826–3831. doi:10.1073/pnas.1115201109

Dolznig, H., Grebien, F., Sauer, T., Beug, H., and Müllner, E. W. (2004). Evidence for a size-sensing mechanism in animal cells. *Nat. Cell. Biol.* 6 (9), 899–905. doi:10.1038/ncb1166

Dorsey, S., Tollis, S., Cheng, J., Black, L., Notley, S., Tyers, M., et al. (2018). G1/S transcription factor copy number is a growth-dependent determinant of cell cycle commitment in yeast. *Cell. Syst.* 6 (5), 539–554. doi:10.1016/j.cels.2018.04.012

Echave, P., Conlon, I. J., and Lloyd, A. C. (2007). Cell size regulation in mammalian cells. *Cell. Cycle* 6 (2), 218–224. doi:10.4161/cc.6.2.3744

Edgar, B. A., and Orr-Weaver, T. L. (2001). Endoreplication cell cycles: More for less. *Cell.* 105 (3), 297–306. doi:10.1016/s0092-8674(01)00334-8

Emmerich, J., Meyer, C. A., de la Cruz, A. F. A., Edgar, B. A., and Lehner, C. F. (2004). Cyclin D does not provide essential Cdk4-independent functions in Drosophila. *Genetics* 168 (2), 867–875. doi:10.1534/genetics.104.027417

Facchetti, G., Knapp, B., Flor-Parra, I., Chang, F., and Howard, M. (2019). Reprogramming cdr2-dependent geometry-based cell size control in fission yeast. *Curr. Biol.* 29 (2), 350–358. e4. doi:10.1016/j.cub.2018.12.017

Fankhauser, G. (1945). Maintenance of normal structure in heteroploid salamander larvae, through compensation of changes in cell size by adjustment of cell number and cell shape. *J. Exp. Zool.* 100, 445–455. doi:10.1002/jez.1401000310

Fantes, P., and Nurse, P. (1977). Control of cell size at division in fission yeast by a growth-modulated size control over nuclear division. *Exp. Cell. Res.* 107 (2), 377–386. doi:10.1016/0014-4827(77)90359-7

Ferrezuelo, F., Colomina, N., Palmisano, A., Garí, E., Gallego, C., Csikász-Nagy, A., et al. (2012). The critical size is set at a single-cell level by growth rate to attain homeostasis and adaptation. *Nat. Commun.* 3 (1), 1012. doi:10.1038/ncomms2015

Fingar, D. C., Salama, S., Tsou, C., Harlow, E., and Blenis, J. (2002). Mammalian cell size is controlled by mTOR and its downstream targets S6K1 and 4EBP1/eIF4E. *Genes. Dev.* 16 (12), 1472–1487. doi:10.1101/gad.995802

Finkielstein, C. V., Lewellyn, A. L., and Maller, J. L. (2001). The midblastula transition in *Xenopus* embryos activates multiple pathways to prevent apoptosis in response to DNA damage. *Proc. Natl. Acad. Sci. U. S. A.* 98 (3), 1006–1011. doi:10.1073/pnas.98.3.1006

Franklin, J. L., and Johnson, E. M. (1998). Control of neuronal size homeostasis by trophic factor-mediated coupling of protein degradation to protein synthesis. *J. Cell. Biol.* 142 (5), 1313–1324. doi:10.1083/jcb.142.5.1313

Gao, F.-B., and Raff, M. (1997). Cell size control and a cell-intrinsic maturation program in proliferating oligodendrocyte precursor cells. *J. Cell. Biol.* 138 (6), 1367–1377. doi:10.1083/jcb.138.6.1367

Garmendia-Torres, C., Tassy, O., Matifas, A., Molina, N., and Charvin, G. (2018). Multiple inputs ensure yeast cell size homeostasis during cell cycle progression. *eLife* 7, e34025. doi:10.7554/eLife.34025

Ginzberg, M. B., Chang, N., D'Souza, H., Patel, N., Kafri, R., and Kirschner, M. W. (2018). Cell size sensing in animal cells coordinates anabolic growth rates and cell cycle progression to maintain cell size uniformity. *eLife* 7, e26957. doi:10.7554/eLife.26957

Giordano, E., Cirulli, V., Bosco, D., Rouiller, D., Halban, P., and Meda, P. (1993). B-cell size influences glucose-stimulated insulin secretion. *Am. J. Physiol.* 265 (2), C358–C364. doi:10.1152/ajpcell.1993.265.2.C358

Godin, M., Delgado, F. F., Son, S., Grover, W. H., Bryan, A. K., Tzur, A., et al. (2010). Using buoyant mass to measure the growth of single cells. *Nat. Methods* 7 (5), 387–390. doi:10.1038/nmeth.1452

Gonzalez, N. P., Tao, J., Rochman, N. D., Vig, D., Chiu, E., Wirtz, D., et al. (2018). Cell tension and mechanical regulation of cell volume Molecular Biology of the Cell 29 (21). doi:10.1091/mbc.e18-04-0213

Goranov, A. I., Gulati, A., Dephoure, N., Takahara, T., Maeda, T., Gygi, S. P., et al. (2013). Changes in cell morphology are coordinated with cell growth through the TORC1 pathway. *Curr. Biol.* 23 (14), 1269–1279. doi:10.1016/j.cub.2013.05.035

Goss, R. J. (1965). Kinetics of compensatory growth. *Q. Rev. Biol.* 40, 123–146. doi:10.1086/404538

Gramage, E., Li, J., and Hitchcock, P. (2014). The expression and function of midkine in the vertebrate retina. *Br. J. Pharmacol.* 171 (4), 913–923. doi:10.1111/bph.12495

Grant, N. A., Abdel Magid, A., Franklin, J., Dufour, Y., and Lenski, R. E. (2021). Changes in cell size and shape during 50, 000 generations of experimental evolution with *Escherichia coli*. *J. Bacteriol.* 203 (10), e00469-20. doi:10.1128/JB.00469-20

Guan, Y., Li, Z., Wang, S., Barnes, P. M., Liu, X., Xu, H., et al. (2018). A robust and tunable mitotic oscillator in artificial cells. *eLife* 7, e33549. doi:10.7554/eLife.33549

Han, J., Wu, J., and Silke, J. (2020). An overview of mammalian p38 mitogen-activated protein kinases, central regulators of cell stress and receptor signaling. *F1000Res.*, F1000 Faculty Rev-653. doi:10.12688/f1000research.22092.1

Harrison, D. E., Strong, R., Sharp, Z. D., Nelson, J. F., Astle, C. M., Flurkey, K., et al. (2009). Rapamycin fed late in life extends lifespan in genetically heterogeneous mice. *Nature* 460 (7253), 392–395. doi:10.1038/nature08221

Hartwell, L. H., Culotti, J., Pringle, J. R., and Reid, B. J. (1974). Genetic control of the cell division cycle in yeast. *Science* 183 (4120), 46–51. doi:10.1126/science.183.4120.46

Hartwell, L. H., and Weinert, T. A. (1989). Checkpoints: Controls that ensure the order of cell cycle events. *Science* 246 (4930), 629–634. doi:10.1126/science.2683079

Heidlauf, T., and Röhrle, O. (2014). A multiscale chemo-electro-mechanical skeletal muscle model to analyze muscle contraction and force generation for different muscle fiber arrangements. *Front. Physiol.* 5, 498. doi:10.3389/fphys.2014.00498

Hendel, N. L., Thomson, M., and Marshall, W. F. (2018). Diffusion as a ruler: Modeling kinesin diffusion as a length sensor for intraflagellar transport. *Biophys. J.* 114 (3), 663–674. doi:10.1016/j.bpj.2017.11.3784

Hindle, A. G., Otis, J. P., Epperson, L. E., Hornberger, T. A., Goodman, C. A., Carey, H. V., et al. (2015). Prioritization of skeletal muscle growth for emergence from hibernation. *J. Exp. Biol.* 218 (2), 276–284. doi:10.1242/jeb.109512

Jiang, Z., Li, H., Schroer, S. A., Voisin, V., Ju, Y., Pacal, M., et al. (2022). Hypophosphorylated pRb knock-in mice exhibit hallmarks of aging and vitamin C-preventable diabetes. *EMBO J.* 41 (4), e106825. doi:10.15252/embj.2020106825

Johnson, H. A., and Vera Roman, J. M. (1966). Compensatory renal enlargement. Hypertrophy versus hyperplasia. *Am. J. Pathol.* 49 (1), 1–13.

Johnston, G. C., Pringle, J. R., and Hartwell, L. H. (1977). Coordination of growth with cell division in the yeast *Saccharomyces cerevisiae*. *Exp. Cell. Res.* 105 (1), 79–98. doi:10.1016/0014-4827(77)90154-9

Jones, R. J., Collector, M. I., Barber, J. P., Vala, M. S., Fackler, M. J., May, W. S., et al. (1996). Characterization of mouse lymphohematopoietic stem cells lacking spleen colony-forming activity. *Blood* 88 (2), 487–491. doi:10.1182/blood.v88.2.487.bloodjournal882487

Jones, R., Jones, A. R., Forero-Vargas, M., Withers, S. P., Smith, R. S., Traas, J., et al. (2017). Cell-size dependent progression of the cell cycle creates homeostasis and flexibility of plant cell size. *Nat. Commun.* 8, 15060. doi:10.1038/ncomms15060

Jorgensen, P., Nishikawa, J. L., Breitkreutz, B.-J., and Tyers, M. (2002). Systematic identification of pathways that couple cell growth and division in yeast. *Science* 297 (5580), 395–400. doi:10.1126/science.1070850

Jorgensen, P., and Tyers, M. (2004). How cells coordinate growth and division. *Curr. Biol.* 14 (23), R1014–R1027. doi:10.1016/j.cub.2004.11.027

Kaeberlein, M., Powers, R. W., 3rd, Steffen, K. K., Westman, E. A., Hu, D., Dang, N., et al. (2005). Regulation of yeast replicative life span by TOR and Sch9 in response to nutrients. *Science* 310 (5751), 1193–1196. doi:10.1126/science.1115535

Kafri, R., Levy, J., Ginzberg, M. B., Oh, S., Lahav, G., and Kirschner, M. W. (2013). Dynamics extracted from fixed cells reveal feedback linking cell growth to cell cycle. *Nature* 494 (7438), 480–483. doi:10.1038/nature11897

Kapahi, P., Zid, B. M., Harper, T., Koslover, D., Sapin, V., and Benzer, S. (2004). Regulation of lifespan in Drosophila by modulation of genes in the TOR signaling pathway. *Curr. Biol.* 14 (10), 885–890. doi:10.1016/j.cub.2004.03.059

Keifenheim, D., Sun, X.-M., D'Souza, E., Ohira, M. J., Magner, M., Mayhew, M. B., et al. (2017). Size-dependent expression of the mitotic activator Cdc25 suggests a mechanism of size control in fission yeast. *Curr. Biol.* 27 (10), 1491–1497. e4. doi:10.1016/j.cub.2017.04.016

Khor, E.-S., Noor, S. M., and Wong, P.-F. (2019). Understanding the role of ztor in aging-related diseases using the zebrafish model. *Vivo* 33 (6), 1713–1720. doi:10.21873/invivo.11661

Killander, D., and Zetterberg, A. (1965b). A quantitative cytochemical investigation of the relationship between cell mass and initiation of DNA synthesis in mouse fibroblasts *in vitro*. *Exp. Cell. Res.* 40 (1), 12–20. doi:10.1016/0014-4827(65)90285-5

Killander, D., and Zetterberg, A. (1965a). Quantitative cytochemical studies on interphase growth. *Exp. Cell. Res.* 38 (2), 272–284. doi:10.1016/0014-4827(65)90403-9

Klonisch, T., Schön, J., Hombach-Klonisch, S., and Blottner, S. (2006). The roe deer as a model for studying seasonal regulation of testis function. *Int. J. Androl.* 29 (1), 122–128. doi:10.1111/j.1365-2605.2005.00603.x

Kõivomägi, M., Swaffer, M. P., Turner, J. J., Marinov, G., and Skotheim, J. M. (2021). G_1 cyclin-Cdk promotes cell cycle entry through localized phosphorylation of RNA polymerase II. *Science* 374 (6565), 347–351. doi:10.1126/science.aba5186

Korzelius, J., The, I., Ruijtenberg, S., Prinsen, M. B. W., Portegijs, V., Middelkoop, T. C., et al. (2011). *Caenorhabditis elegans* cyclin D/CDK4 and cyclin E/CDK2 induce distinct cell cycle re-entry programs in differentiated muscle cells. *PLoS Genet.* 7 (11), e1002362. doi:10.1371/journal.pgen.1002362

Kwon, C.-H., Zhu, X., Zhang, J., and Baker, S. J. (2003). mTor is required for hypertrophy of Pten-deficient neuronal soma *in vivo*. *Proc. Natl. Acad. Sci. U. S. A.* 100 (22), 12923–12928. doi:10.1073/pnas.2132711100

Kwon, C.-H., Zhu, X., Zhang, J., Knoop, L. L., Tharp, R., Smeyne, R. J., et al. (2001). Pten regulates neuronal soma size: A mouse model of lhermitte-duclos disease. *Nat. Genet.* 29 (4), 404–411. doi:10.1038/ng781

Laberge, R.-M., Sun, Y., Orjalo, A. V., Patil, C. K., Freund, A., Zhou, L., et al. (2015). MTOR regulates the pro-tumorigenic senescence-associated secretory phenotype by promoting IL1A translation. *Nat. Cell. Biol.* 17 (8), 1049–1061. doi:10.1038/ncb3195

Lallemend, F., Sterzenbach, U., Hadjab-Lallemend, S., Aquino, J. B., Castelo-Branco, G., Sinha, I., et al. (2012). Positional differences of axon growth rates between sensory neurons encoded by Runx3. *EMBO J.* 31 (18), 3718–3729. doi:10.1038/emboj.2012.228

Lanz, M. C., Zatulovskiy, E., Swaffer, M. P., Zhang, L., Zhang, S., You, D. S., et al. (2021). Increasing cell size remodels the proteome and promotes senescence. *bioRxiv*. doi:10.1101/2021.07.29.454227

Laufs, P., Grandjean, O., Jonak, C., Kiêu, K., and Traas, J. (1998). Cellular parameters of the shoot apical meristem in Arabidopsis. *Plant Cell.* 10 (8), 1375–1390. doi:10.1105/tpc.10.8.1375

Lee, B. Y., Han, J. A., Im, J. S., Morrone, A., Johung, K., Goodwin, E. C., et al. (2006). Senescence-associated beta-galactosidase is lysosomal beta-galactosidase. *Aging Cell.* 5 (2), 187–195. doi:10.1111/j.1474-9726.2006.00199.x

Lee, T. K., Esinhart, J. D., Blackburn, L. D., and Silverman, J. F. (1992). The size of small cell lung carcinoma cells. Ratio to lymphocytes and correlation with specimen size and crush artifact. *Anal. Quant. Cytol. Histol.* 14 (1), 32–34.

Lee, Y., Dominy, J. E., Choi, Y. J., Jurczak, M., Tolliday, N., Camporez, J. P., et al. (2014). Cyclin D1-Cdk4 controls glucose metabolism independently of cell cycle progression. *Nature* 510 (7506), 547–551. doi:10.1038/nature13267

Lengefeld, J., Cheng, C.-W., Maretich, P., Blair, M., Hagen, H., McReynolds, M. R., et al. (2021). Cell size is a determinant of stem cell potential during aging. *Sci. Adv.* 7 (46), eabk0271. doi:10.1126/sciadv.abk0271

Li, Q., Rycaj, K., Chen, X., and Tang, D. G. (2015). Cancer stem cells and cell size: A causal link? *Semin. Cancer Biol.* 35, 191–199. doi:10.1016/j.semcancer.2015.07.002

Lin, S.-C. J., Skapek, S. X., and Lee, E. Y.-H. P. (1996). Genes in the RB pathway and their knockout in mice. *Semin. Cancer Biol.* 7 (5), 279–289. doi:10.1006/scbi.1996.0036

Litsios, A., Goswami, P., Terpstra, H. M., Coffin, C., Vuillemenot, L.-A., Rovetta, M., et al. (2022). The timing of Start is determined primarily by increased synthesis of the Cln3 activator rather than dilution of the Whi5 inhibitor. *Mol. Biol. Cell.* 33 (5), rp2. doi:10.1091/mbc.E21-07-0349

Litsios, A., Huberts, D. H. E. W., Terpstra, H. M., Guerra, P., Schmidt, A., Buczak, K., et al. (2019). Differential scaling between G1 protein production and cell size dynamics promotes commitment to the cell division cycle in budding yeast. *Nat. Cell. Biol.* 21 (11), 1382–1392. doi:10.1038/s41556-019-0413-3

Liu, S., Ginzberg, M. B., Patel, N., Hild, M., Leung, B., Li, Z., et al. (2018). Size uniformity of animal cells is actively maintained by a p38 MAPK-dependent regulation of G1-length. *eLife* 7, e26947. doi:10.7554/eLife.26947

Liu, S., Tan, C., Melo-Gavin, C., Mark, K. G., Ginzberg, M. B., Blutrich, R., et al. (2021). Large cells activate global protein degradation to maintain cell size homeostasis. *bioRxiv*. doi:10.1101/2021.11.09.467936

Liu, X., Oh, S., Peshkin, L., and Kirschner, M. W. (2020). Computationally enhanced quantitative phase microscopy reveals autonomous oscillations in mammalian cell growth. *Proc. Natl. Acad. Sci. U. S. A.* 117 (44), 27388–27399. doi:10.1073/pnas.2002152117

Liu, X., Wang, X., Yang, X., Liu, S., Jiang, L., Qu, Y., et al. (2015). Reliable cell cycle commitment in budding yeast is ensured by signal integration. *eLife* 4. doi:10.7554/eLife.03977

Liu, X., Yan, J., and Kirschner, M. W. (2022). Beyond G1/S regulation: How cell size homeostasis is tightly controlled throughout the cell cycle? *bioRxiv*. doi:10.1101/2022.02.03.478996

Lloyd, A. C. (2013). The regulation of cell size. *Cell.* 154 (6), 1194–1205. doi:10.1016/j.cell.2013.08.053

Marguerat, S., and Bähler, J. (2012). Coordinating genome expression with cell size. *Trends Genet.* 28 (11), 560–565. doi:10.1016/j.tig.2012.07.003

Marshall, W. F. (2020). Scaling of subcellular structures. *Annu. Rev. Cell. Dev. Biol.* 36, 219–236. doi:10.1146/annurev-cellbio-020520-113246

Martin, S. G., and Berthelot-Grosjean, M. (2009). Polar gradients of the DYRK-family kinase Pom1 couple cell length with the cell cycle. *Nature* 459 (7248), 852–856. doi:10.1038/nature08054

Miettinen, T. P., and Björklund, M. (2016). Cellular allometry of mitochondrial functionality establishes the optimal cell size. *Dev. Cell.* 39 (3), 370–382. doi:10.1016/j.devcel.2016.09.004

Miettinen, T. P., and Björklund, M. (2015). Mevalonate pathway regulates cell size homeostasis and proteostasis through autophagy. *Cell. Rep.* 13 (11), 2610–2620. doi:10.1016/j.celrep.2015.11.045

Miettinen, T. P., and Björklund, M. (2017). Mitochondrial function and cell size: An allometric relationship. *Trends Cell. Biol.* 27 (6), 393–402. doi:10.1016/j.tcb.2017.02.006

Miettinen, T. P., Caldez, M. J., Kaldis, P., and Björklund, M. (2017). Cell size control - a mechanism for maintaining fitness and function. *BioEssays* 39 (9), 1700058. doi:10.1002/bies.201700058

Milona, A., Owen, B. M., van Mil, S., Dormann, D., Mataki, C., Boudjelal, M., et al. (2010). The normal mechanisms of pregnancy-induced liver growth are not maintained in mice lacking the bile acid sensor Fxr. *Am. J. Physiol. Gastrointest. Liver Physiol.* 298 (2), G151–G158. doi:10.1152/ajpgi.00336.2009

Mitchison, J. M. (2003). "Growth during the cell cycle," in *International review of cytology*, 165–258.

Mortimer, R. K., and Johnston, J. R. (1958). Life span of individual yeast cells. doi:10.2172/4329664

Moseley, J. B., Mayeux, A., Paoletti, A., and Nurse, P. (2009). A spatial gradient coordinates cell size and mitotic entry in fission yeast. *Nature* 459 (7248), 857–860. doi:10.1038/nature08074

Mu, L., Kang, J. H., Olcum, S., Payer, K. R., Calistri, N. L., Kimmerling, R. J., et al. (2020). Mass measurements during lymphocytic leukemia cell polyploidization decouple cell cycle- and cell size-dependent growth. *Proc. Natl. Acad. Sci. U. S. A.* 117 (27), 15659–15665. doi:10.1073/pnas.1922197117

Mugahid, D., Kalocsay, M., Liu, X., Gruver, J. S., Peshkin, L., and Kirschner, M. W. (2020). YAP regulates cell size and growth dynamics via non-cell autonomous mediators. *eLife* 9, e53404. doi:10.7554/eLife.53404

Muñoz-Espín, D., and Serrano, M. (2014). Cellular senescence: From physiology to pathology. *Nat. Rev. Mol. Cell. Biol.* 15 (7), 482–496. doi:10.1038/nrm3823

Nash, R., Tokiwa, G., Anand, S., Erickson, K., and Futcher, A. B. (1988). The WHI1+ gene of *Saccharomyces cerevisiae* tethers cell division to cell size and is a cyclin homolog. *EMBO J.* 7 (13), 4335–4346. doi:10.1002/j.1460-2075.1988.tb03332.x

Navarro, F. J., and Nurse, P. (2012). A systematic screen reveals new elements acting at the G2/M cell cycle control. *Genome Biol.* 13 (5), R36. doi:10.1186/gb-2012-13-5-r36

Nelsen, C. J., Rickheim, D. G., Tucker, M. M., Hansen, L. K., and Albrecht, J. H. (2003). Evidence that cyclin D1 mediates both growth and proliferation downstream of TOR in hepatocytes. *J. Biol. Chem.* 278 (6), 3656–3663. doi:10.1074/jbc.M209374200

Neurohr, G. E., Terry, R. L., Lengefeld, J., Bonney, M., Brittingham, G. P., Moretto, F., et al. (2019). Excessive cell growth causes cytoplasm dilution and contributes to senescence. *Cell.* 176 (5), 1083–1097. doi:10.1016/j.cell.2019.01.018

Nurse, P. (1975). Genetic control of cell size at cell division in yeast. *Nature* 256 (5518), 547–551. doi:10.1038/256547a0

Nurse, P., and Thuriaux, P. (1980). Regulatory genes controlling mitosis in the fission yeast *Schizosaccharomyces pombe*. *Genetics* 96 (3), 627–637. doi:10.1093/genetics/96.3.627

Orhon, I., Dupont, N., and Codogno, P. (2016). Primary cilium and autophagy: The avengers of cell-size regulation. *Autophagy* 12 (11), 2258–2259. doi:10.1080/15548627.2016.1212790

Paik, D. Y., Janzen, D. M., Schafenacker, A. M., Velasco, V. S., Shung, M. S., Cheng, D., et al. (2012). Stem-like epithelial cells are concentrated in the distal end of the fallopian tube: A site for injury and serous cancer initiation. *Stem Cells* 30 (11), 2487–2497. doi:10.1002/stem.1207

Pan, Y., Heemskerk, I., Ibar, C., Shraiman, B. I., and Irvine, K. D. (2016). Differential growth triggers mechanical feedback that elevates Hippo signaling. *Proc. Natl. Acad. Sci. U. S. A.* 113 (45), E6974-E6983–E6983. doi:10.1073/pnas.1615012113

Park, J. H., Lee, N. K., Lim, H. J., Ji, S. T., Kim, Y.-J., Jang, W. B., et al. (2020). Pharmacological inhibition of mTOR attenuates replicative cell senescence and improves cellular function via regulating the STAT3-PIM1 axis in human cardiac progenitor cells. *Exp. Mol. Med.* 52 (4), 615–628. doi:10.1038/s12276-020-0374-4

Parsa, R., Yang, A., McKeon, F., and Green, H. (1999). Association of p63 with proliferative potential in normal and neoplastic human keratinocytes. *J. Investig. Dermatol.* 113 (6), 1099–1105. doi:10.1046/j.1523-1747.1999.00780.x

Pende, M., Kozma, S. C., Jaquet, M., Oorschot, V., Burcelin, R., Le Marchand-Brustel, Y., et al. (2000). Hypoinsulinaemia, glucose intolerance and diminished beta-cell size in S6K1-deficient mice. *Nature* 408 (6815), 994–997. doi:10.1038/35050135

Perez-Gonzalez, N. A., Rochman, N. D., Yao, K., Tao, J., Le, M.-T. T., Flanary, S., et al. (2019). YAP and TAZ regulate cell volume. *J. Cell. Biol.* 218 (10), 3472–3488. doi:10.1083/jcb.201902067

Perry, R. B.-T., Rishal, I., Doron-Mandel, E., Kalinski, A. L., Medzihradszky, K. F., Terenzio, M., et al. (2016). Nucleolin-mediated RNA localization regulates neuron growth and cycling cell size. *Cell. Rep.* 16 (6), 1664–1676. doi:10.1016/j.celrep.2016.07.005

Pitoulis, F. G., and Terracciano, C. M. (2020). Heart plasticity in response to pressure- and volume-overload: A review of findings in compensated and decompensated phenotypes. *Front. Physiol.* 0, 92. doi:10.3389/fphys.2020.00092

Purves, D., Snider, W. D., and Voyvodic, J. T. (1988). Trophic regulation of nerve cell morphology and innervation in the autonomic nervous system. *Nature* 336 (6195), 123–128. doi:10.1038/336123a0

Qu, Y., Jiang, J., Liu, X., Wei, P., Yang, X., and Tang, C. (2019). Cell cycle inhibitor Whi5 records environmental information to coordinate growth and division in yeast. *Cell. Rep.* 29 (4), 987–994. doi:10.1016/j.celrep.2019.09.030

Radley, J. M., Ellis, S., Palatsides, M., Williams, B., and Bertoncello, I. (1999). Ultrastructure of primitive hematopoietic stem cells isolated using probes of functional status. *Exp. Hematol.* 27 (2), 365–369. doi:10.1016/s0301-472x(98)00017-4

Rich, S. K., and Terman, J. R. (2018). Axon formation, extension, and navigation: Only a neuroscience phenomenon? *Curr. Opin. Neurobiol.* 53, 174–182. doi:10.1016/j.conb.2018.08.004

Rieck, S., and Kaestner, K. H. (2010). Expansion of β-cell mass in response to pregnancy. *Trends Endocrinol. Metab.* 21 (3), 151–158. doi:10.1016/j.tem.2009.11.001

Rieck, S., White, P., Schug, J., Fox, A. J., Smirnova, O., Gao, N., et al. (2009). The transcriptional response of the islet to pregnancy in mice. *Mol. Endocrinol.* 23 (10), 1702–1712. doi:10.1210/me.2009-0144

Rishal, I., Kam, N., Perry, R. B.-T., Shinder, V., Fisher, E. M. C., Schiavo, G., et al. (2012). A motor-driven mechanism for cell-length sensing. *Cell. Rep.* 1 (6), 608–616. doi:10.1016/j.celrep.2012.05.013

Rubin, S. M., Sage, J., and Skotheim, J. M. (2020). Integrating old and new paradigms of G1/S control. *Mol. Cell.* 80 (2), 183–192. doi:10.1016/j.molcel.2020.08.020

Rupes, I. (2002). Checking cell size in yeast. *Trends Genet.* 18 (9), 479–485. doi:10.1016/s0168-9525(02)02745-2

Sabatini, D. M. (2017). Twenty-five years of mTOR: Uncovering the link from nutrients to growth. *Proc. Natl. Acad. Sci. U. S. A.* 114 (45), 11818–11825. doi:10.1073/pnas.1716173114

Salvatierra, O., Jr, Singh, T., Shifrin, R., Conley, S., Alexander, S., Tanney, D., et al. (1998). Successful transplantation of adult-sized kidneys into infants requires maintenance of high aortic blood flow. *Transplantation* 66 (7), 819–823. doi:10.1097/00007890-199810150-00001

Samsonovich, V., and Ascoli, G. A. (2006). Morphological homeostasis in cortical dendrites. *Proc. Natl. Acad. Sci. USA* 103 (5), 1569–1514. doi:10.1073/pnas.0510057103

Sato, T., van Es, J. H., Snippert, H. J., Stange, D. E., Vries, R. G., van den Born, M., et al. (2011). Paneth cells constitute the niche for Lgr5 stem cells in intestinal crypts. *Nature* 469 (7330), 415–418. doi:10.1038/nature09637

Schmoller, K. M., Lanz, M. C., Kim, J., Koivomagi, M., Qu, Y., Tang, C., et al. (2022). Whi5 is diluted and protein synthesis does not dramatically increase in pre-*Start* G1. *Mol. Biol. Cell.* 33 (5), lt1. doi:10.1091/mbc.E21-01-0029

Schmoller, K. M., Turner, J. J., Kõivomägi, M., and Skotheim, J. M. (2015). Dilution of the cell cycle inhibitor Whi5 controls budding-yeast cell size. *Nature* 526 (7572), 268–272. doi:10.1038/nature14908

Sellam, A., Chaillot, J., Mallick, J., Tebbji, F., Richard Albert, J., Cook, M. A., et al. (2019). The p38/HOG stress-activated protein kinase network couples growth to division in Candida albicans. *PLoS Genet.* 15 (3), e1008052. doi:10.1371/journal.pgen.1008052

Serrano-Mislata, A., Schiessl, K., and Sablowski, R. (2015). Active control of cell size generates spatial detail during plant organogenesis. *Curr. Biol.* 25 (22), 2991–2996. doi:10.1016/j.cub.2015.10.008

Sherr, C. J. (1996). Cancer cell cycles. *Science* 274 (5293), 1672–1677. doi:10.1126/science.274.5293.1672

Shields, R., Brooks, R. F., Riddle, P. N., Capellaro, D. F., and Delia, D. (1978). Cell size, cell cycle and transition probability in mouse fibroblasts. *Cell.* 15 (2), 469–474. doi:10.1016/0092-8674(78)90016-8

Sinturel, F., Gerber, A., Mauvoisin, D., Wang, J., Gatfield, D., Stubblefield, J. J., et al. (2017). Diurnal oscillations in liver mass and cell size accompany ribosome assembly cycles. *Cell.* 169 (4), 651–663. e14. doi:10.1016/j.cell.2017.04.015

Soifer, I., and Barkai, N. (2014). Systematic identification of cell size regulators in budding yeast. *Mol. Syst. Biol.* 10 (11), 761. doi:10.15252/msb.20145345

Sommer, R. A., DeWitt, J. T., Tan, R., and Kellogg, D. R. (2021). Growth-dependent signals drive an increase in early G1 cyclin concentration to link cell cycle entry with cell growth. *eLife* 10, e64364. doi:10.7554/eLife.64364

Son, S., Tzur, A., Weng, Y., Jorgensen, P., Kim, J., Kirschner, M. W., et al. (2012). Direct observation of mammalian cell growth and size regulation. *Nat. Methods* 9 (9), 910–912. doi:10.1038/nmeth.2133

Streichan, S. J., Hoerner, C. R., Schneidt, T., Holzer, D., and Hufnagel, L. (2014). Spatial constraints control cell proliferation in tissues. *Proc. Natl. Acad. Sci. U. S. A.* 111 (15), 5586–5591. doi:10.1073/pnas.1323016111

Sudbery, P. E., Goodey, A. R., and Carter, B. L. (1980). Genes which control cell proliferation in the yeast *Saccharomyces cerevisiae*. *Nature* 288 (5789), 401–404. doi:10.1038/288401a0

Sveiczer, A., Novak, B., and Mitchison, J. M. (2004). Size control in growing yeast and mammalian cells. *Theor. Biol. Med. Model.* 1, 12. doi:10.1186/1742-4682-1-12

Taheri-Araghi, S., Bradde, S., Sauls, J. T., Hill, N. S., Levin, P. A., Paulsson, J., et al. (2015). Cell-size control and homeostasis in bacteria. *Curr. Biol.* 25 (3), 385–391. doi:10.1016/j.cub.2014.12.009

Talarek, N., Gueydon, E., and Schwob, E. (2017). Homeostatic control of START through negative feedback between Cln3-Cdk1 and Rim15/Greatwall kinase in budding yeast. *eLife* 6, e26233. doi:10.7554/eLife.26233

Tan, C., Ginzberg, M. B., Webster, R., Iyengar, S., Liu, S., Papadopoli, D., et al. (2021). Cell size homeostasis is maintained by CDK4-dependent activation of p38 MAPK. *Dev. Cell.* 56 (12), 1756–1769.e7. e7. doi:10.1016/j.devcel.2021.04.030

Thoms, H. C., Dunlop, M. G., and Stark, L. A. (2007). p38-mediated inactivation of cyclin D1/cyclin-dependent kinase 4 stimulates nucleolar translocation of RelA and apoptosis in colorectal cancer cells. *Cancer Res.* 67 (4), 1660–1669. doi:10.1158/0008-5472.CAN-06-1038

Thornton, T. M., and Rincon, M. (2009). Non-classical P38 map kinase functions: Cell cycle checkpoints and survival. *Int. J. Biol. Sci.* 5, 44–51. doi:10.7150/ijbs.5.44

Tiku, V., Jain, C., Raz, Y., Nakamura, S., Heestand, B., Liu, W., et al. (2017). Small nucleoli are a cellular hallmark of longevity. *Nat. Commun.* 8, 16083. doi:10.1038/ncomms16083

Tomás-Loba, A., Manieri, E., González-Terán, B., Mora, A., Leiva-Vega, L., Santamans, A. M., et al. (2019). p38γ is essential for cell cycle progression and liver tumorigenesis. *Nature* 568 (7753), 557–560. doi:10.1038/s41586-019-1112-8

Tollis, S., Singh, J., Palou, R., Thattikota, Y., Ghazal, G., Coulombe-Huntington, J., et al. (2022). The microprotein Nrs1 rewires the G1/S transcriptional machinery during nitrogen limitation in budding yeast. *PLoS Biol.* 20 (3), e3001548. doi:10.1371/journal.pbio.3001548

Tyers, M., Tokiwa, G., and Futcher, B. (1993). Comparison of the *Saccharomyces cerevisiae* G1 cyclins: Cln3 may be an upstream activator of Cln1, Cln2 and other cyclins. *EMBO J.* 12 (5), 1955–1968. doi:10.1002/j.1460-2075.1993.tb05845.x

Tyson, J. J., and Hannsgen, K. B. (1985). Global asymptotic stability of the size distribution in probabilistic models of the cell cycle. *J. Math. Biol.* 22 (1), 61–68. doi:10.1007/BF00276546

Uroz, M., Wistorf, S., Serra-Picamal, X., Conte, V., Sales-Pardo, M., Roca-Cusachs, P., et al. (2018). Regulation of cell cycle progression by cell–cell and cell–matrix forces. *Nat. Cell. Biol.* 20 (6), 646–654. doi:10.1038/s41556-018-0107-2

Varsano, G., Wang, Y., and Wu, M. (2017). Probing mammalian cell size homeostasis by channel-assisted cell reshaping. *Cell. Rep.* 20 (2), 397–410. doi:10.1016/j.celrep.2017.06.057

Vellai, T., Takacs-Vellai, K., Zhang, Y., Kovacs, A. L., Orosz, L., and Müller, F. (2003). Genetics: Influence of TOR kinase on lifespan in *C. elegans*. *Nature* 426 (6967), 620. doi:10.1038/426620a

Wagner, M. V., Smolka, M. B., de Bruin, R. A. M., Zhou, H., Wittenberg, C., and Dowdy, S. F. (2009). Whi5 regulation by site specific CDK-phosphorylation in *Saccharomyces cerevisiae*. *PloS One* 4 (1), e4300. doi:10.1371/journal.pone.0004300

Wallden, M., Fange, D., Lundius, E. G., Baltekin, Ö., and Elf, J. (2016). The synchronization of replication and division cycles in individual *E. coli* cells. *Cell.* 166 (3), 729–739. doi:10.1016/j.cell.2016.06.052

Wang, H., Carey, L. B., Cai, Y., Wijnen, H., and Futcher, B. (2009). Recruitment of Cln3 cyclin to promoters controls cell cycle entry via histone deacetylase and other targets. *PLoS Biol.* 7 (9), e1000189. doi:10.1371/journal.pbio.1000189

Watt, F. M., and Green, H. (1981). Involucrin synthesis is correlated with cell size in human epidermal cultures. *J. Cell. Biol.* 90 (3), 738–742. doi:10.1083/jcb.90.3.738

Weitz, M., Kim, J., Kapsner, K., Winfree, E., Franco, E., and Simmel, F. C. (2014). Diversity in the dynamical behaviour of a compartmentalized programmable biochemical oscillator. *Nat. Chem.* 6 (4), 295–302. doi:10.1038/nchem.1869

Wells, W. A. (2002). Does size matter? *J. Cell. Biol.* 158 (7), 1156–1159. doi:10.1083/jcb.200209042

Wood, E., and Nurse, P. (2013). Pom1 and cell size homeostasis in fission yeast. *Cell. Cycle* 12 (19), 3228–3236. doi:10.4161/cc.26462

Wood, E., and Nurse, P. (2015). Sizing up to divide: Mitotic cell-size control in fission yeast. *Annu. Rev. Cell. Dev. Biol.* 31, 11–29. doi:10.1146/annurev-cellbio-100814-125601

Wood, S. H., Christian, H. C., Miedzinska, K., Saer, B. R. C., Johnson, M., Paton, B., et al. (2015). Binary switching of calendar cells in the pituitary defines the phase of the circannual cycle in mammals. *Curr. Biol.* 25 (20), 2651–2662. doi:10.1016/j.cub.2015.09.014

Wright, J., Dungrawala, H., Bright, R. K., and Schneider, B. L. (2013). A growing role for hypertrophy in senescence. *FEMS Yeast Res.* 13 (1), 2–6. doi:10.1111/1567-1364.12015

Xie, S., and Skotheim, J. M. (2020). A G1 sizer coordinates growth and division in the mouse epidermis. *Curr. Biol.* 30 (5), 916–924. e2. doi:10.1016/j.cub.2019.12.062

Yang, J., Dungrawala, H., Hua, H., Manukyan, A., Abraham, L., Lane, W., et al. (2011). Cell size and growth rate are major determinants of replicative lifespan. *Cell. Cycle* 10 (1), 144–155. doi:10.4161/cc.10.1.14455

Zatulovskiy, E., Zhang, S., Berenson, D. F., Topacio, B. R., and Skotheim, J. M. (2020). Cell growth dilutes the cell cycle inhibitor Rb to trigger cell division. *Science* 369 (6502), 466–471. doi:10.1126/science.aaz6213

Zetterberg, A., Engström, W., and Dafgård, E. (1984). The relative effects of different types of growth factors on DNA replication, mitosis, and cellular enlargement. *Cytometry* 5 (4), 368–375. doi:10.1002/cyto.990050413

Zhang, J., Schneider, C., Ottmers, L., Rodriguez, R., Day, A., Markwardt, J., et al. (2002). Genomic scale mutant hunt identifies cell size homeostasis genes in *S. cerevisiae*. *Curr. Biol.* 12 (23), 1992–2001. doi:10.1016/s0960-9822(02)01305-2

Ziegler, D. V., Martin, N., and Bernard, D. (2021). Cellular senescence links mitochondria-ER contacts and aging. *Commun. Biol.* 4 (1), 1323. doi:10.1038/s42003-021-02840-5

frontiers | Frontiers in Cell and Developmental Biology

TYPE Review
PUBLISHED 10 November 2022
DOI 10.3389/fcell.2022.1036602

OPEN ACCESS

EDITED BY
Jan M. Skotheim,
Stanford University, United States

REVIEWED BY
Akshay Narkar,
United States Food and Drug Administration, United States
Robert Antonius Maria De Bruin,
University College London, United Kingdom
Gabriel Neurohr,
ETH Zürich, Switzerland

*CORRESPONDENCE
Jette Lengefeld,
jette.lengefeld@helsinki.fi

SPECIALTY SECTION
This article was submitted to Cell Growth and Division, a section of the journal Frontiers in Cell and Developmental Biology

RECEIVED 04 September 2022
ACCEPTED 17 October 2022
PUBLISHED 10 November 2022

CITATION
Davies DM, van den Handel K, Bharadwaj S and Lengefeld J (2022), Cellular enlargement - A new hallmark of aging?
Front. Cell Dev. Biol. 10:1036602.
doi: 10.3389/fcell.2022.1036602

Cellular enlargement - A new hallmark of aging?

Daniel M. Davies[1], Kim van den Handel[1], Soham Bharadwaj[1] and Jette Lengefeld[1,2]*

[1]Institute of Biotechnology, HiLIFE, University of Helsinki, Helsinki, Finland, [2]Center for Hematology and Regenerative Medicine, Department of Medicine Huddinge, Karolinska Institutet, Stockholm, Sweden

Years of important research has revealed that cells heavily invest in regulating their size. Nevertheless, it has remained unclear why accurate size control is so important. Our recent study using hematopoietic stem cells (HSCs) *in vivo* indicates that cellular enlargement is causally associated with aging. Here, we present an overview of these findings and their implications. Furthermore, we performed a broad literature analysis to evaluate the potential of cellular enlargement as a new aging hallmark and to examine its connection to previously described aging hallmarks. Finally, we highlight interesting work presenting a correlation between cell size and age-related diseases. Taken together, we found mounting evidence linking cellular enlargement to aging and age-related diseases. Therefore, we encourage researchers from seemingly unrelated areas to take a fresh look at their data from the perspective of cell size.

KEYWORDS

Cellular enlargement, hallmarks of aging, cell size physiology, aging-related diseases, stem cells

1 Introduction

Aging is the time-dependent loss of physiological integrity (Lopez-Otin et al., 2013) that can lead to numerous diseases like neurodegenerative diseases, cardiovascular disease, autoimmune diseases and cancer (Sadighi Akha, 2018; Stauder et al., 2018; Hou Y. et al., 2019; Rodgers et al., 2019; Zjablovskaja and Florian, 2019). The appearance of some of these diseases is facilitated by aging-related stem cell dysfunction. One of the most significant examples of this are HSCs. HSCs possess the ability to self-renew and are multipotent, thereby giving rise to the multiple different cell types of the blood. A healthy blood system requires HSCs to balance and maintain both these abilities, which decline with age. This leads to stem cell exhaustion and biased lineage differentiation (Yamashita and Iwama, 2022), which can contribute to the development of anemia, leukemia and a compromised immune system (Dykstra and de Haan, 2008; Hill et al., 2017; Chen et al., 2019; Chopra and Bohlander, 2019; Anurogo et al., 2021).

Our current understanding of aging splits into nine categories known as the hallmarks of aging (Lopez-Otin et al., 2013): cellular senescence, mitochondrial dysfunction, stem cell exhaustion, telomere attrition, altered intercellular communication, deregulated nutrient sensing, loss of proteostasis, chromatin remodeling, and genomic instability.

Each category represents a factor that 1) manifests during aging, 2) upon accumulation accelerates aging 3) and upon removal slows down aging (Lopez-Otin et al., 2013). By now these hallmarks are almost a decade old, and it is unclear whether additional hallmarks of aging exist.

Since the 1960s, it has been known that cells become large *in vitro* when entering the senescent state (Hayflick and Moorhead, 1961). Several researchers also observed that cells *in vitro* and *in vivo* enlarge during aging (Hayflick and Moorhead, 1961; Mitsui and Schneider, 1976a; Mitsui and Schneider, 1976b; Treton and Courtois, 1981; Martinelli et al., 2006a; Mammoto et al., 2019). Since then, tremendous efforts have been made towards understanding how cells regulate their size. However, it was not until recently that we gained a deeper understanding of why cells regulate their size (Miettinen and Bjorklund, 2016; Neurohr et al., 2019; Lengefeld et al., 2021). Focusing on HSCs, we discuss the implications of these recent findings and the potential of cellular enlargement as a new hallmark of aging (Lengefeld et al., 2021). Then, we highlight numerous publications reporting a correlation between cell size and diseases of old age. We expose the need for future research to address whether these correlations are reflecting a causal relationship between enlargement and function, and the implication this has on research areas that have so far not considered the importance of cell size.

2 Cellular enlargement: A new hallmark of aging?

A large body of literature highlights two important findings: 1) Different cell types display different average sizes (Ginzberg et al., 2015) and 2) cells maintain a uniform size by using several regulatory pathways (Lloyd, 2013; Cadart et al., 2014; Schmoller et al., 2015; Amodeo and Skotheim, 2016; Schmoller, 2017; Bjorklund, 2019). This raises the question of why cells invest in maintaining their size. Therefore, understanding what happens when cells fail to regulate their size is important. While the first findings around this topic led to controversial conclusions (Bilinski, 2012; Ganley et al., 2012; Kaeberlein, 2012), budding yeast has been a key model organism to provide the first evidence that cellular enlargement could be directly linked to cellular dysfunction during aging (Bilinski and Bartosz, 2006; Zadrag-Tecza et al., 2009; Yang et al., 2011; Bilinski et al., 2012; Neurohr et al., 2019). It is known that budding yeast cells enlarge during aging (Mortimer and Johnston, 1959; Yang et al., 2011; Bilinski, 2012; Lee et al., 2012; Denoth Lippuner et al., 2014). Preventing this enlargement with drugs preserves their replicative age (Johnson et al., 2013; Neurohr et al., 2019). Similarly, preventing cellular enlargement *in vitro* in primary human cells has been shown to maintain their capacity to enter the cell cycle thereby avoiding cellular senescence (Demidenko and Blagosklonny, 2008; Demidenko et al., 2009; Neurohr et al., 2019; Lanz et al., 2022).

Our recent publication dissected whether the role of cell size on cell function is based on correlation or causation. An intrinsic challenge was to manipulate cell size without targeting other pathways, and to delineate that the observed changes are causal and not correlative. This hurdle was tackled using HSCs *in vivo* (Lengefeld et al., 2021; Strzyz, 2022):

- Six orthogonal approaches were examined under which HSCs became larger. In each of these conditions, HSC function was also compromised. HSC function was determined as their ability to form a blood system after transplantation into recipient mice. While it could be argued that each single manipulation affected HSC function unrelated to cell size, together these experiments suggest that the dysfunction was not driven by an unaccounted variable. Furthermore, alternate causes were excluded by analyzing other parameters of the hematopoietic system: homing, stem cell identity, differentiation potential and cell cycle state. Therefore, the simplest explanation is that enlargement of HSCs reduces their functionality.
- Treatment with a Cdk4/6 inhibitor (palbociclib-PD) caused artificial HSC enlargement and dysfunction. In PD-treated animals, not all HSCs became larger and those HSCs that stayed small displayed higher functionality than large HSCs from PD- or vehicle-treated mice. This indicates that PD-induced enlargement, rather than PD-treatment *per se*, causes HSC dysfunction.

Further lines of experimental evidence from this study support the conclusion that cellular enlargement causally decreases HSC function (Lengefeld et al., 2021):

- Preventing HSC enlargement by inhibiting macromolecule biosynthesis (rapamycin treatment) during insults that enlarge HSCs (DNA damage, successive divisions and aging), protected HSCs from losing their stem cell function.
- Reducing the large size of non-functional HSCs by shortening G_1 (*RB* mutation) restored their functionality. Removal of *RB* does not improve the function of control or small HSCs (Walkley and Orkin, 2006; Lengefeld et al., 2021), indicating that the lack *RB* does not improve stem cell function *per se*, but restores it specifically by reducing cell size.

Together these data make a strong case that enlargement drives the dysfunction of murine HSCs *in vivo*.

In addition to the above-listed observations, cellular enlargement also qualifies as a novel aging factor for HSCs

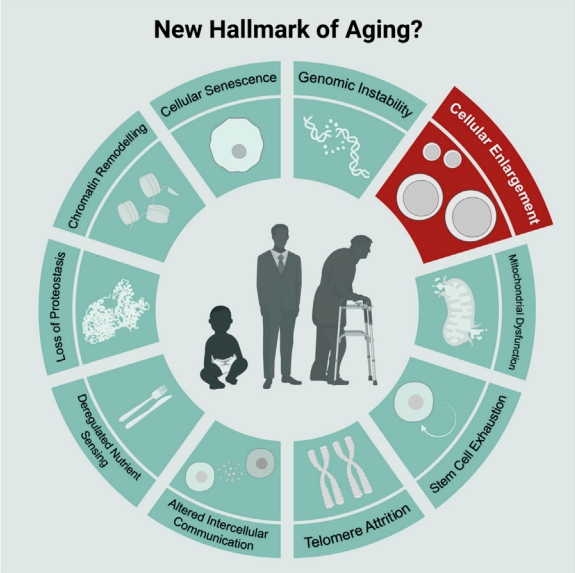

FIGURE 1
Scheme of commonly known nine hallmarks of aging in light-green and the new hallmark "Cellular Enlargement." Scheme adopted from Lopez-Otin et al. (2013) and created with BioRender.com.

(Figure 1): 1) HSCs naturally enlarge during aging, 2) artificially increasing cell size reduces HSC function and induces the appearance of aging characteristics and 3) preventing HSC enlargement during aging using rapamycin preserves the function of HSCs (Lengefeld et al., 2021). To thoroughly evaluate whether cell enlargement qualifies as an *bona fide* aging factor/hallmark, it will be important generalize these studies by testing for a causal relationship between enlargement and dysfunction also in other stem cells and even differentiated cells.

Of note, accumulating evidence suggest that small size is important for stem cells in general. Like HSCs, mesenchymal stem cells enlarge during aging *in vitro* (Oja et al., 2018), intestinal stem cells display size dependent functions (Lengefeld et al., 2021) and numerous stem cell types are small in size (Colter et al., 2000; Colter et al., 2001; Smith et al., 2004; Young et al., 2004; Virant-Klun et al., 2008; Zuba-Surma et al., 2008; Virant-Klun and Stimpfel, 2016). Thus, it is likely that mechanisms connecting cellular size with aging-related function are conserved in other stem cell types as well.

How do HSCs enlarge during aging? To explain the process of HSC enlargement and the consequent loss of their function during aging we proposed the following model (Lengefeld et al., 2021): As HSCs divide and age, they experience conditions that cause cell cycle arrest. For example, DNA damage incurred during replication (Geiger et al., 2013; Flach et al., 2014; Walter et al., 2015) activates cell cycle checkpoints that transiently halt division until the DNA damage is repaired (Sperka et al., 2012; Moehrle et al., 2015). During arrest phases, cell growth continues leading to increased HSC size (Fingar et al., 2002; Neurohr et al., 2019; Padovani et al., 2022). The enlarged HSCs become dysfunctional. Indeed, inhibition with rapamycin prevents enlargement during these arrests thereby preserving the function of HSCs (Lengefeld et al., 2021). This adds to our current understanding of the role of DNA damage and cellular dysfunction: In addition to DNA damage causing HSC dysfunction directly, DNA damage also drives HSC enlargement, which renders HSCs dysfunctional (Figure 2). Of note, DNA damage itself is not needed for the dysfunction of large HSCs, as increasing HSC size without DNA damage (e.g., mTOR overexpression) also drives the loss of function (Lengefeld et al., 2021). Overall, HSCs enlarge during aging after a series of transient cell cycle arrests, which ultimately causes their dysfunction.

Under physiological conditions, cells are able to return to their original size after size fluctuations by adjusting cellular growth and division speed (Cadart et al., 2018; Ginzberg et al., 2018; Bjorklund, 2019; Xie and Skotheim, 2020). Unexpectedly, like large HSCs (Lengefeld et al., 2021), yeast cells and primary human cells *in vitro* become larger with every division (Mortimer and Johnston, 1959; Mitsui and Schneider, 1976a; Mitsui and Schneider, 1976b; Bemiller and Miller, 1979; Yang et al., 2011; Lee et al., 2012) and do not shrink back to their original size. This is in line with the observation that many cell types enlarge with age *in vivo* and *vitro* (Roth et al., 1976; Treton and Courtois, 1981;

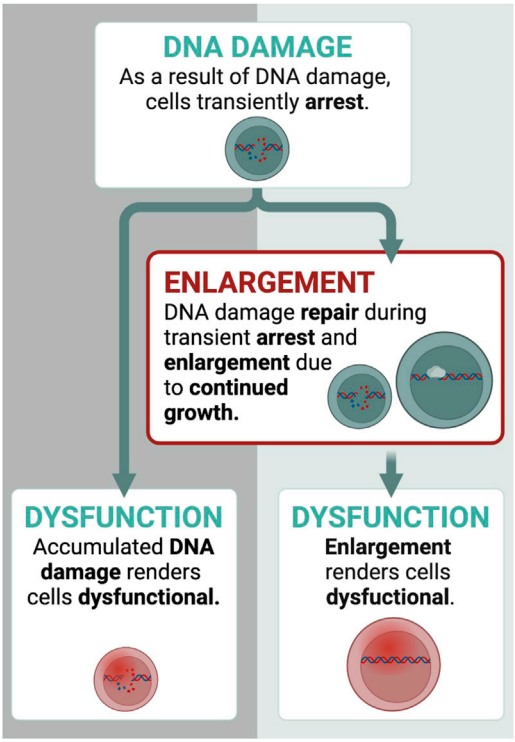

FIGURE 2
How do HSCs enlarge? Transient cell cycle arrests drive enlargement of HSCs. Here, we display an example with DNA damage. DNA damage affects HSCs in two ways: 1) it causes dysfunction directly 2) and transiently arrest HSCs for DNA damage repair, during which growth continues. This leads to the enlargement of HSCs. Once they are too large, they become dysfunctional. Thus, DNA damage contributes to dysfunction also indirectly by enlarging HSCs. Created with BioRender.com.

Anversa et al., 1986; Melissari et al., 1991; Horsfall et al., 1994; Dyachenko etal., 2006; Martinelli et al., 2006a; Helms et al., 2010; Roh et al., 2013; Pucker et al., 2015; Mammoto et al., 2019; Delgado-González et al., 2020; Lengefeld et al., 2021; Yako et al., 2021). It is unclear why mechanisms of size homeostasis fail to reduce the size of these enlarging cell types.

In summary, an emerging picture in the field suggests a causal link between cell size and function in yeast, *in vitro* cell lines and *in vivo* systems. Furthermore, cellular enlargement aligns with the criteria of an aging hallmark. This highlights the importance of cell size for consideration in the design of aging studies.

3 Interplay between cellular enlargement of hematopoietic stem cells and other hallmarks of aging

Increased cell size was previously assumed to be a consequence of aging, rather than a causal factor (Johnson et al., 2013). Therefore, studies on aging may have overlooked cellular enlargement and did not evaluate a connection to other aging hallmarks. In this section, we discuss potential intersections between HSC enlargement and other hallmarks of aging, highlighting their overlaps and differences.

3.1 Cellular senescence

Senescent cells are irreversibly arrested in the cell cycle and are usually large in size (Biran et al., 2017). Large HSCs are always dysfunctional as they fail to build a blood system *in vivo* and display proliferative defects. This raises the question whether large HSCs are senescent and whether enlargement facilitates the senescent state (Lanz et al., 2022; Xie et al., 2022)? While little is known about this connection in HSCs, it has been shown that not all large HSCs are also senescent based on SA-β-gal production (Lengefeld et al., 2021). This indicates that HSC enlargement does not strictly induce cellular senescence. Nevertheless, based on the observation that senescent HSCs are always large, we speculate that large HSCs may be more prone to acquire the senescent program when exposed to additional damage. This is

supported by the observation that larger human cells *in vitro* are as well more prone to senescence potentially *via* expansion of lysosomes and the endoplasmic reticulum (Cheng et al., 2021; Lanz et al., 2022). Overall, it will be important to further investigate how HSC enlargement increases the likelihood of entering the senescent state.

3.2 Telomere attrition and DNA damage

Telomere shortening and the accumulation of DNA damage during aging contribute to cellular dysfunction (Lopez-Otin et al., 2013). Are telomere shortening and DNA damage also contributing to the dysfunction of large HSCs? As outlined above, DNA damage contributes to enlargement as it transiently halts HSC division to repair the DNA damage (Sperka et al., 2012). During this arrest, cell growth continues leading to HSC enlargement (Fingar et al., 2002; Neurohr et al., 2019). This enlargement drives dysfunction of HSCs. When growth is inhibited with rapamycin during this DNA damage, HSCs maintain their functionality (Lengefeld et al., 2021). Thus, if telomere shortening during DNA damage induced enlargement is crucial for their dysfunction, then we expect rapamycin to prevent telomere shortening and the associated accumulation of DNA damage. This is not the case. Rapamycin does not prevent DNA damage in HSCs and, so far, no protective effect of rapamycin on telomere length has been reported (Kawauchi et al., 2005; Qi et al., 2008; Ungar et al., 2011; Gopalakrishnan et al., 2018; Ferrara-Romeo et al., 2020). Additionally, other studies have indicated that it is still unclear whether telomere length plays a crucial role in HSC exhaustion (Allsopp et al., 2003): Telomeres become shorter during divisions of HSCs (Allsopp et al., 2001). However, at least in mice, HSCs become exhausted even when telomere shortening is prevented by telomerase overexpression (Allsopp et al., 2003) arguing that there are telomere-independent barriers to HSC function. Furthermore, we would like to speculate about the possible protective feature of enlargement. DNA-damage leads to enlargement and potentially permanent gene mutations and chromosomal aberrations. However, this enlargement in turn reduces the proliferation potential of these cells and thereby may prevent the propagation of potentially harmful features in the tissue that could facilitate, for example, a malignant transformation. In summary, DNA damage contributes to HSC dysfunction by enlarging their size, while telomere attrition seems to play a less dominant role than enlargement in causing HSC dysfunction.

3.3 Mitochondrial dysfunction

Mitochondrial volume typically scales with cell size in dividing cells supporting faithful cellular functions (Posakony et al., 1977; Rafelski et al., 2012; Miettinen and Bjorklund, 2016; Cheng et al., 2021; Lanz et al., 2021; Seel et al., 2022). For example, HSCs are able to scale mitochondria upon their activation (Ho et al., 2017). Changes in mitochondrial morphology and volume beyond this scaling are associated with cellular dysfunction (Chistiakov et al., 2014). Mitochondrial number and volume have often been quantified in old cells, but the results have been inconsistent. *In vitro*, some cell types display decreased mitochondrial volume (Stoll et al., 2011; Yako et al., 2021; Barilani et al., 2022), but most human cell lines increase their mitochondrial volume as they become larger and senescent (Lee et al., 2002; Passos et al., 2007; Koziel et al., 2011; Xie et al., 2011; Correia-Melo et al., 2016; Stab et al., 2016). It is noteworthy that increased mitochondrial volume does not necessarily translate into increased mitochondrial functions *in vitro* (Passos et al., 2007; Passos et al., 2010; Miettinen and Bjorklund, 2016). Furthermore, *in vivo* studies often reported decreased mitochondrial volume during aging (Markowska et al., 1994; Navarro and Boveris, 2004; Mathieu-Costello et al., 2005; Martinelli et al., 2006a; Addabbo et al., 2009; Leduc-Gaudet et al., 2015; Del Campo et al., 2018; Brown et al., 2021; Lengefeld et al., 2021). For example, in large HSCs mitochondrial volume decreases per unit volume (Lengefeld et al., 2021). Currently, the underlying reasons for these differences *in vitro* and *in vivo* are unclear. One possibility is that they are facilitated by different oxygen levels *in vivo* (hypoxic) and *in vitro* (hyperoxic). Nevertheless, these changes in mitochondrial volume during aging are associated with a decline in mitochondrial function, potentially driven by differences in fusion, fission and mitophagy (Mai et al., 2010; Korolchuk et al., 2017; Yako et al., 2021). Whether changes in mitochondrial morphology, volume and number during aging are the cause or consequence of cellular enlargement remains to be determined. In summary, while mitochondria volume and function scale with cellular size during faithful divisions, these parameters become uncoupled when cells enlarge during aging.

3.4 Loss of proteostasis

The scaling of protein levels with cell size is important for cellular function (Fraser and Nurse, 1978; Padovan-Merhar et al., 2015; Schmoller and Skotheim, 2015; Sun et al., 2020; Cheng et al., 2021; Lanz et al., 2021). Upon substantial enlargement of primary human cells *in vitro*, protein synthesis rates and ribosome levels decrease (Delarue et al., 2018; Neurohr et al., 2019). However, considering that disruptions of proteostasis contribute to HSC aging (Signer et al., 2014; Kruta et al., 2021), it was surprising that measurements of nucleolar size, cellular density, mTOR activity and protein synthesis in large HSCs indicated no loss of protein synthesis capacity (Lengefeld et al., 2021). While protein synthesis was unaffected by large HSC size, whether protein turn-over, folding state, aggregation and

protein-protein interactions were impaired is unknown. Indeed, during aging, misfolded proteins contribute to the loss of cellular function (Lopez-Otin et al., 2013) and it will be important to analyze whether large stem cell size affects the accumulation of these misfolded proteins.

How enlargement of HSCs is related to the remaining hallmarks of aging like chromatin remodeling, genomic instability, nutrient sensing and intercellular communication is at this point unclear. It will be important to understand which aging hallmarks act in the same pathways as cellular enlargement to build a holistic picture of aging. Furthermore, initial experimental evidence suggests that enlargement can be reversed, which improved stem cell function (Lengefeld et al., 2021). This may open the possibility that other aging factors that are connected to cell size can be improved when shrinking stem cells.

4 Relation between cell size and aging-related functions: A fresh look at old studies

As mentioned above, to evaluate whether cell enlargement qualifies as an aging factor/hallmark, it will be important to test for a causal relationship between enlargement and cellular dysfunction during aging in various different cell types. Interestingly, we can extract clues from numerous studies for how cell size potentially affects various cellular functions. Here, we present publications showing examples of cell size in association with different aspects of aging and pathologies (Figure 3). Whether size is causally associated with the corresponding changes is not addressed in these studies. Nevertheless, considering the recent findings that cellular enlargement manifests itself an aging factor, we take a fresh look at these studies in the next sections.

4.1 Enlargements as part of faithful cellular functions

Before we dive into the literature evaluating cellular size and age-related dysfunctions, we would like to point out examples of enlargement that are not associated with dysfunction.

Cell cycle - Cells usually double in size during the cell cycle to ensure that their daughter cells are the same size as the original mother cell after symmetric cell division (Lloyd, 2013). In muscle satellite cells, this enlargement can happen already prior to cell cycle entry and is called the G_{alert} state. This enables an accelerated entry into a proliferating state after repeated muscle injury (Rodgers et al., 2014).

Differentiation - Another example of enlargement as part of faithful cellular processes is differentiation, in particularly during development. For example, 1) keratinocyte enlargement during differentiation is proposed to enable the formation of an insoluble protein envelope at the plasma membrane (Watt and Green, 1981), 2) terminal differentiation drives enlargement of chondrocytes (hypertrophy) as part of skeletal tissue elongation (Cooper et al., 2013), 3) cardiomyocytes increase in size during heart development (Knaapen et al., 1996; Li et al., 1996), and 4) T cell activation requires profound changes in cell size (Kaesler et al., 2012). Furthermore, during cell manipulations that trigger differentiation, cells not only acquire a new cell identity but also a new cell size, which is optimal for this cell type. For example, overexpression of *RUNX3*, results in an increase in cell size and a block in faithful differentiation of erythrocytes (Menezes et al., 2022).

Ploidy - Changes in ploidy are generally associated with enlargement, but do not necessarily lead to dysfunction (Gillooly et al., 2015; Mu et al., 2020). For example, during adolescence, mouse acinar cells often become tetraploid and increase in size without losing their function (Xanthopoulos et al., 2008). On the other hand, polyploidization of hepatocytes occurs successively during postnatal development and again during advanced aging. The latter being associated with senescence, progressive loss of cell pluripotency and decreased replication capacity (Celton-Morizur and Desdouets, 2010; Wang et al., 2017).

Apoptosis - Cell volume decrease is characteristic of apoptotic cell death (Bortner and Cidlowski, 2002; Núñez et al., 2010). Cancer cells are able to prevent apoptotic shrinking by modulating the activity of ion channels (Lehen'kyi et al., 2011).

In conclusion, changes in cell volume are part of cellular processes and not necessarily associated with dysfunction. In the next part of this section, we will highlight findings, in which cellular enlargement is associated with aging, dysfunction and disease.

4.2 The mechanical microenvironment and cell size

Cell size is influenced by matrix stiffness, osmotic pressure and mechanical forces (Wang et al., 2020a). For example, cells substantially shrink when cultivated on substrates of increased stiffness (Guo et al., 2017; Xie et al., 2018; Yang et al., 2020). Interestingly, modulation of the external stiffness, and thereby cellular size, affects cellular function. For example, mesenchymal stem cells (MSCs) enlarge during aging *in vitro* and *in vivo*, which is accompanied by a senescent phenotype including high levels of p21, β-galactosidase, and SASP (Block et al., 2017; Yin et al., 2020; Liu et al., 2021). When MSCs are cultivated at an optimal substrate stiffness, they maintain their small size and proliferation capacity and do not become senescent (Kureel et al., 2019). Furthermore, cultivating large aged endothelial

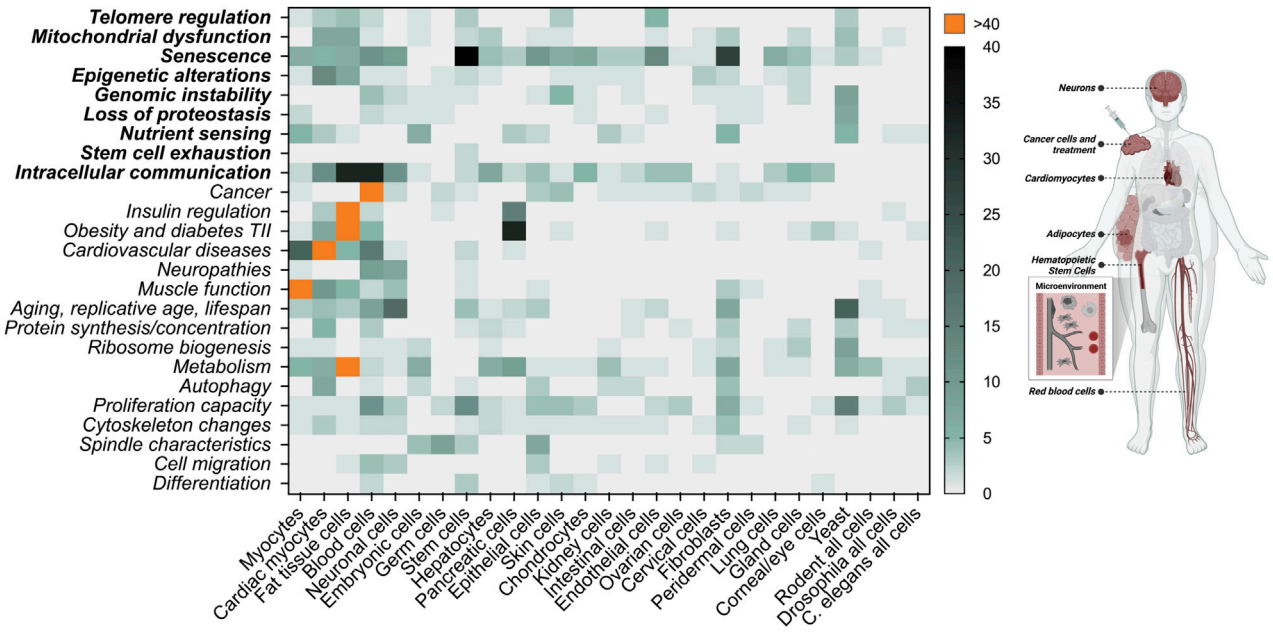

FIGURE 3
Literature research of connections between cell size and various cellular functions associated with aging. A total of 1,626 publications were manually collected using PubMed.gov and keywords related to cellular functions in combination with cell size in the abstract ["cell size" OR "cell volume" AND (category)]. These publications were categorized based on cell type and cellular function and presented as heat map. Aging factors are displayed in bold. AI methods for computation abstract search were considered, however this technology is currently limited for this purpose. We do not differentiate whether cellular size changes are associated with polyploidy, osmolarity or *in vivo/in vitro* studies. This figure is not a complete representation of the literature but gives the first unbiased insight that cellular size is connected to a large variety of cellular functions. On the left side of the image, we highlight the areas that we focus on in the main text. Created with BioRender.com.

cells on substrate with increased stiffness rejuvenates these cells and reduces their size (Mammoto et al., 2019). The underlying mechanism is unknown. Together, this suggests that the environmental stiffness can modulate cellular size and thereby cellular functionality *in vitro*.

It is important to note that cells in 2D monocultures are exposed to a different microenvironment than in the *in vivo* 3D tissue context. *In vivo*, cells face the extracellular matrix (ECM), neighboring cells, biochemical and physical cues (Barthes et al., 2014), which all affect the environmental stiffness. As tissues have different solidity states, it is expected that stiffness varies between tissues and organs (Butcher et al., 2009). During aging *in vivo*, increased stiffness is associated with malignancy (Lieber et al., 2004; Butcher et al., 2009; Stearns-Reider et al., 2017; Segel et al., 2019; Ghosh et al., 2020), while stiffness decreases in some organs like the skin (Tissot et al., 2018; Runel et al., 2020; Lynch et al., 2022) and muscle tissues (Akagi et al., 2015; Yoshida et al., 2017; Alfuraih et al., 2019). We speculate that reduced stiffness contributes to cellular enlargement during aging. It will be of critical interest to analyze how microenvironmental forces affect cellular size and thereby cellular function during aging *in vivo*. In summary, the microenvironment modulates cell size and therefore likely cell function as well.

4.3 Cell size of red blood cells

Red blood cell distribution width (RDW) represents variability of the size distribution of red blood cells and has been used as a marker for multiple aging-related pathologies (Salvagno et al., 2015). RDW involves a change in mean corporal volume (MCV). An increase in MCV, meaning increase in red blood cell volume, correlates with aging (Hoffmann et al., 2015; Lippi et al., 2018) and numerous diseases like anemia, autoimmune diseases, cancer types, and cardio- and cerebrovascular diseases (Bessman et al., 1983; Li et al., 2017; Lippi et al., 2018; Katsaros et al., 2020). Interestingly, not only enlargement, but a deviation from optimal red blood cell size in general is associated with diseases, for example, various leukemia forms, Alzheimer's disease, Parkinson's disease, autoimmune disease, and macular degeneration (Pilling et al., 2017; Lippi et al., 2018; Katsaros et al., 2020; Kim et al., 2021).

It is unclear why red blood cells of many diseased individuals are large. The fact that red blood cells lack organelles, such as a nucleus and mitochondria, implies that the underlying mechanism driving dysfunction is different from the one in HSCs, in which these organelles are necessary for enlargement and dysfunction (Lengefeld et al., 2021). Furthermore, the

correlation of RDW with aging-associated diseases has not been investigated for a causal relationship. Overall, RDW is a robust indicator of numerous diseases, but the origin of this relationship is insufficiently understood.

4.4 Cell size of adipocytes

Large size of adipocytes is associated with several pathophysiological conditions like reduced response to hormones, increased inflammation, impaired body metabolic regulation and insulin resistance, which is associated with type 2 diabetes (Bjorntorp et al., 1972; Bernstein et al., 1975; Weyer et al., 2000; Lundgren et al., 2007; Lonn et al., 2010; Yang et al., 2012; McLaughlin et al., 2014; Laforest et al., 2015; Stenkula and Erlanson-Albertsson, 2018; Liu et al., 2020). However, it is also suggested that it is the enlargement and not the absolute size that predicts insulin resistance (Johannsen et al., 2014). Interestingly, a recent model proposes that enlargement of adipocytes itself affects the interaction of the cell with the ECM. This activates integrin/Erk signaling and modulates gene expression (Farnier et al., 2002; Farnier et al., 2003). It will be exciting to see further studies evaluating the causality of cellular enlargement on adipocyte function.

Mean adipocyte size increases between middle and old age and then decreases with advanced age (Miller et al., 2017). Interestingly, this correlates with the risk for the onset of type 2 diabetes, which peaks at 45–65 years and lowers afterwards (Plummer et al., 2016; Sattar et al., 2019; Jacobs et al., 2020; Hu et al., 2021). Nevertheless, while smaller adipocyte size during advanced age correlates with a lower onset risk of type 2 diabetes, it coincides also with another unfavorable outcome: A result of decreased adipocyte size is the decline in fat depot size, which leads to the accumulation of fat outside adipose tissue like in the bone marrow, muscle and liver. This is associated with lipotoxic stress in the storage organs and lower organ function with age (Rosen and Bouxsein, 2006; Slawik and Vidal-Puig, 2006). Overall, enlargement of adipocytes predicts obesity-associated pathologies like type 2 diabetes and during aging, the shrinkage of adipocytes is likely associated with other pathologies.

4.5 The aging brain and Alzheimer's disease

At old age, brain volume declines (Haug and Eggers, 1991; Resnick et al., 2003). Studies indicate that this is caused by a shrinking of neuronal cell size (Anderson et al., 1983; Terry et al., 1987; Diaz et al., 1999; Kuwahara et al., 2004; Martinelli et al., 2006b; Fernandez et al., 2007; Stark et al., 2007; Freeman et al., 2008; Verkhratsky et al., 2014; Popov et al., 2021). Nevertheless, in some areas of the brain neurons maintain size or enlarge with age (de Lacalle et al., 1991; Merrill et al., 2000; Martinelli et al., 2006b; Verkhratsky et al., 2014; Thulborn et al., 2016; Delgado-Gonzalez et al., 2020; Yako et al., 2021). Interestingly, during neurodegenerative diseases such as Alzheimer's, neurons enlarge. Overexpression of the amyloid precursor protein causes enlargement of cortical neuron size (Oh et al., 2009) and larger neuronal cell lines are more Aβ-sensitive (Simakova and Arispe, 2007). This causes cellular toxicity and resembles cellular damage in Alzheimer's diseased brains. Furthermore, an increase in cell size or neuronal hypertrophy has been reported in elderly that display no cognitive symptoms yet but markers of Alzheimer's disease (Iacono et al., 2008). At later stages of Alzheimer's disease progression, oligodendrocyte progenitor cells increase in size (Vanzulli et al., 2020) and neocortical neurons are enlarged in Alzheimer patients (Bundgaard et al., 2001; Pakkenberg et al., 2003). In summary, while most neuronal cell types shrink during aging, areas that contain neurons that enlarge might be especially prone to processes that result in symptoms of Alzheimer's disease.

4.6 Cardiomyocyte hypertrophy

As the proliferative capacity of heart cells becomes severely restricted after birth, the postnatal increase of heart volume is achieved by cardiomyocyte hypertrophy (Li et al., 1996; Porrello et al., 2011). Heart hypertrophy coincides at the cellular level with nuclear polyploidization, multinucleation, and cellular growth (Derks and Bergmann, 2020). While cardiomyocyte hypertrophy is associated with development and adjustment to exercise (Ellison et al., 2012), it also predicts numerous cardiovascular diseases like ischemic disease, hypertension, heart failure, and valvular disease (Wang et al., 2013; Akhondzadeh et al., 2020; Peter et al., 2016). This raises an important question: What is the difference between physiological and pathological cellular hypertrophy?

Cellular growth driven by the IGF1/PI3K/Akt1 pathways facilitates heart enlargement after exercise, while signaling *via* G_q protein-coupled receptors, reduced blood supply, oxidative stress, inflammatory processes and Ca^{2+} abnormalities drive cellular growth and enlargement of the heart associated with pathology (Weeks and McMullen, 2011; Oldfield et al., 2020). Thus, in the case of the heart, enlargement is associated with opposite outcomes and thus, it seems unlikely that they are driven by enlargement itself.

Nevertheless, there are some interesting differences to be noted: For example, enlargement after exercise changes the cellular shape in a different way than during disease (Kuo et al., 2012; Peter et al., 2016). Furthermore, it could be that pathological hypertrophy enlarges cardiomyocytes beyond a size-threshold due to extensive growth. This is supported by the observation that cardiomyocytes after exercise are smaller than

cardiomyocytes under diabetic stress (Stolen et al., 2009). While many cardiomyocytes become polyploid during pathological enlargement, whether this enlargement is always accompanied with an increase in DNA copy number is unclear. Interestingly, in yeast, enlargement without increasing DNA copy number results in cytoplasmic dilution and dysfunction (Neurohr et al., 2019). Thus, it will be interesting to investigate whether mechanisms like cytoplasmic dilution contribute to the dysfunction of cardiomyocytes upon pathological enlargement and whether polyploidization is a compensating mechanism to prevent this functional loss. Indeed, polyploidy has been hypothesized as a mechanism to increase metabolic and growth capacity of cells (Frawley and Orr-Weaver, 2015; Mu et al., 2020). Furthermore, if it is true that pathological enlargement facilitates changes in ploidy, this could also include changes like large genomic aberrations and aneuploidy. These genomic defects may also facilitate unwanted downstream effects. Indeed, aneuploidy is a distinct feature of cancer cells (Ben-David and Amon, 2020). Overall, being of the right size is important for cardiomyocytes (Ren and Brown-Borg, 2002) and hypertrophy is a crucial characteristic of adjusting to exercise and pathology.

4.7 Cell volume and cancer

Heterogeneity of cell size and shape are often observed in tumors and referred to as pleomorphism (Manocha et al., 2003; Terzakis et al., 2005). This raises the question of whether a failure of size regulation is facilitating cancer progression. Some research suggests that size heterogeneity of cancer cells provides the highest malignant potential (Kawada et al., 1994; Manukyan et al., 2021). Furthermore, the population of small cells within tumors raise attention. Small prostate cancer cells build more malignant tumors than large ones (Li et al., 2015). Mutated *STAT3* is a crucial cancer facilitator and leukemia patients with *STAT3* mutations carry smaller blood cells than patients without these mutations (Tanahashi et al., 2016) suggesting that the smaller cells might facilitate cancer progression. It is also speculated that cancer stem cells are small, just like most stem cells (Berardi et al., 1995; Colter et al., 2001; Young et al., 2004; Virant-Klun and Stimpfel, 2016). The small size could result from the fast proliferation of cancer cells, leaving little time for growth during these short cell cycle durations (Lloyd, 2013; Wright and Schneider, 2014). On the other hand, a small size might support the cancerous potential of the cells. One possibility is that size affects the migration behavior of cancer cells (Leal-Egana et al., 2017; Wang et al., 2020b). Overall, the literature provides interesting clues that a deviation from the optimal cell size is associated with cancer, but whether and how size modulates malignancy is unclear.

Solid tumors are usually an assembly of distinct cell types including infiltrating immune cells, each owning their own cell size (Ginzberg et al., 2015). Thus, the size heterogeneity found in cancer tissues could reflect the tumor's composition of various cell types (Shembrey et al., 2019) and not a failure in size regulation of the cells that originated the cancer. However, cell size could still serve as a diagnostic marker for certain types of cancers. For example, for acute lymphoblastic leukemia, the significance of cell size as a prognostic indicator is heavily investigated (Mathe et al., 1971; Pantazopoulos and Sinks, 1974; Murphy et al., 1975; Oster et al., 1976; Dubner et al., 1978; Ghani and Krause, 1986; Olcay et al., 1999). Further research is needed to determine whether cell size is a reliable predictor of malignancy. Investigating the potential link between cellular size and cancer potential will be crucial for the development of new therapies for cancer treatments.

4.8 Effect of cell cycle inhibitors on cell size during treatment approaches

As discussed, an arrest in cell cycle causes cellular enlargement (Fingar et al., 2002; Neurohr et al., 2019; Lengefeld et al., 2021). Cell cycle inhibitors like palbociclib, dinaciclib, seliciclib, ribociclib, and abemaciclib therefore enlarge cell size. These kinds of drugs are already successfully used in clinical trials or are even FDA-approved for cancer treatment. As enlargement can cause dysfunction, this could contribute to the inhibitory success of these cell cycle inhibitors in cancer treatments. Recent studies provide important insights into this topic. Uncoupling cell growth and proliferation in cancer cells by arresting them in G_1 phase leads to toxic overgrowth and senescence (Wilson et al., 2021; Crozier et al., 2022; Foy et al., 2022; Manohar et al., 2022). Furthermore, keeping patient-derived glioma stem cells small (rapamycin treatment) during cell cycle arrest (palbociclib) prevents their entry into a senescence state (Morris-Hanon et al., 2019). Thus, growth and enlargement, in addition to cell cycle arrest, effectively inhibit cancer cells from proliferating and cancer treatments using cell cycle inhibitors may therefore not be combined with rapamycin.

Cell cycle inhibitors like palbociclib have also been investigated as treatment for other pathologies: mast cell-mediated allergy (Hou Y. B. et al., 2019), diabetic cardiomyopathy (Wang et al., 2019), pulmonary arterial hypertension (Weiss et al., 2019), replication of herpes virus (Badia et al., 2016), systemic sclerosis (Yamamoto et al., 2022) and spinal muscular atrophy (Hor et al., 2018). It will be important to evaluate how arrest-induced growth and enlargement affect the outcome of these diseases. Overall, this highlights the importance of understanding how growth and

enlargement contribute to the multilayered effects of treatment drugs.

4.9 Cell size and lifespan

Cell enlargement is associated with cellular aging. Does cell size also influence organismal lifespan? A recent study found a reliable predictor of lifespan across 24 mammalian species: Pancreatic acinar cell volume inversely correlates with lifespan of different species (Anzi et al., 2018). Noting that ploidy was not accounted for in this correlation, the study suggests that these results might apply to multiple other tissues. Mice with a reduced body size and hereditary dwarfism are longer-lived than larger mice (Roberts, 1961; Eklund and Bradford, 1977; Brown-Borg et al., 1996; Miller et al., 2000; Flurkey et al., 2002; Miller et al., 2002). Interestingly, cardiomyocytes from old dwarf mice are smaller compared to their wild-type counterparts (Helms et al., 2010). While these smaller cardiomyocytes are associated with cardiac contractile defects (Ren and Brown-Borg, 2002), they also display reduced extracellular collagen, which is protective against heart disease (Helms et al., 2010) and may have improved cardiac function during aging (Li et al., 2007; Reddy et al., 2007). It remains to be determined whether small cardiomyocyte size is contributing to longevity. We note that there are cell types that are exceptions: for example, human neurons and astrocytes are larger than the ones in mice (Herculano-Houzel et al., 2006; Oberheim et al., 2009; Rostock et al., 2018), yet humans live longer than mice. Overall, cellular size could serve as an indicator of lifespan when choosing the correct cell type.

5 Summary and outlook

Researchers unraveling the process of aging and its associated diseases have revealed that aging is associated with great phenotypic variation, which is driven by several aging hallmarks. Now, it crystalizes that one of these hallmarks is cellular enlargement, at least for HSCs. Recent data suggest that cellular enlargement is not only correlated with aging, but also causally contributes to the functional decline of HSCs during aging. While cells have an innate ability to regulate their cell size, upon age-dependent enlargement this regulatory mechanism fails. This new concept of cellular enlargement driving dysfunction during aging has been tested for HSCs. Interestingly, numerous other cell types have also been observed to enlarge during aging (Hayflick and Moorhead, 1961; Mitsui and Schneider, 1976a; Mitsui and Schneider, 1976b; Treton and Courtois, 1981; Martinelli et al., 2006a; Mammoto et al., 2019). This raises the possibility that cellular enlargement contributes to aging in other cell types. Moving forward, the research community will benefit from further experiments providing critical evidence of whether cellular enlargement is cause or consequence of aging in other stem cell types and differentiating cells. Furthermore, 1) researchers working with rare clinical samples should consider whether a simple measurement of cellular size will lead to important insights on aging, 2) categorizing cell types by cell size might explain ageing-related heterogeneity of samples and even reveal new pathways, 3) cancer treatments might cause the desired effect or undesired side-effects by changing cell size, and 4) enlargement of certain cell types might explain aging-associated cellular dysfunctions. As a result, cellular enlargement might affect several processes related to physiology, aging and disease that have so far not been connected to cell size. Understanding how cellular enlargement relates to aging and disease will help to explain previous observations, direct research, and support the development of new therapies for aging-related diseases.

Changes in the cell's volume during various processes are necessary for the cell to function, for example during the cell cycle, development, and differentiation. Interestingly, the literature also provides an overwhelming number of publications reporting a correlation between cell size and various cellular dysfunctions. Our literature analysis revealed areas, which are connected to cell size like cancer, cardiovascular diseases, obesity, autoimmune diseases and Alzheimer's disease. Other factors, like the ECM stiffness, caught our attention for having a potential effect on cell size *in vivo*. Interestingly, not only enlargement of cells is associated with dysfunctions, but a general deviation from the optimal cell size affects cancer progression, diseases associated with red blood cells and potentially neurodegenerative aging. Furthermore, cell size might be a predictor of lifespan, cancer, type 2 diabetes, heart failure and Alzheimer's disease. A systematic documentation of cell size of different cell types during health, disease and aging may allow to define a threshold beyond which cells are more likely dysfunctional. Overall, this could indicate that there is a relationship between cell size and cellular failure in different cell types of multicellular systems. However, this hypothesis needs testing. Now, we encourage researchers to test a potential causal connection between cell size, pathology and aging, to analyze the value of cell size as a prognostic marker for diseases, and to evaluate whether cellular enlargement qualifies as a new aging hallmark. These new insights will affect research areas that have so far not considered the importance of cell size.

Author contributions

DD and JL wrote the manuscript, all authors edited the manuscript and created the figures.

Funding

JL was supported by the Academy of Finland and Instrufoundation fellow grant.

Acknowledgments

We are grateful to the members of the Lengefeld lab, E. Cerezo, K. Schmoller, J. Kamenz, A. X. Su, F. Padovani, and J. Saarikangas for discussion and feedback. We apologize to the authors of studies that we were not able to mention here due to space restrictions.

Conflict of interest

The authors declare that the research was conducted in the absence of any commercial or financial relationships that could be construed as a potential conflict of interest.

Publisher's note

References

Addabbo, F., Ratliff, B., Park, H. C., Kuo, M. C., Ungvari, Z., Csiszar, A., et al. (2009). The krebs cycle and mitochondrial mass are early victims of endothelial dysfunction: Proteomic approach. *Am. J. Pathol.* 174, 34–43. doi:10.2353/ajpath.2009.080650

Akagi, R., Yamashita, Y., and Ueyasu, Y. (2015). Age-related differences in muscle shear moduli in the lower extremity. *Ultrasound Med. Biol.* 41, 2906–2912. doi:10.1016/j.ultrasmedbio.2015.07.011

Akhondzadeh, F., Astani, A., Najjari, R., Samadi, M., Rezvani, M. E., Zare, F., et al. (2020). Resveratrol suppresses interleukin-6 expression through activation of sirtuin 1 in hypertrophied H9c2 cardiomyoblasts. *J. Cell. Physiol.* 235, 6969–6977. doi:10.1002/jcp.29592

Alfuraih, A. M., Tan, A. L., O'Connor, P., Emery, P., and Wakefield, R. J. (2019). The effect of ageing on shear wave elastography muscle stiffness in adults. *Aging Clin. Exp. Res.* 31, 1755–1763. doi:10.1007/s40520-019-01139-0

Allsopp, R. C., Cheshier, S., and Weissman, I. L. (2001). Telomere shortening accompanies increased cell cycle activity during serial transplantation of hematopoietic stem cells. *J. Exp. Med.* 193, 917–924. doi:10.1084/jem.193.8.917

Allsopp, R. C., Morin, G. B., Horner, J. W., DePinho, R., Harley, C. B., and Weissman, I. L. (2003). Effect of TERT over-expression on the long-term transplantation capacity of hematopoietic stem cells. *Nat. Med.* 9, 369–371. doi:10.1038/nm0403-369

Amodeo, A. A., and Skotheim, J. M. (2016). Cell-size control. *Cold Spring Harb. Perspect. Biol.* 8, a019083. doi:10.1101/cshperspect.a019083

Anderson, J. M., Hubbard, B. M., Coghill, G. R., and Slidders, W. (1983). The effect of advanced old age on the neurone content of the cerebral cortex. Observations with an automatic image analyser point counting method. *J. Neurol. Sci.* 58, 235–246. doi:10.1016/0022-510x(83)90220-4

Anurogo, D., Yuli Prasetyo Budi, N., Thi Ngo, M. H., Huang, Y. H., and Pawitan, J. A. (2021). Cell and gene therapy for anemia: Hematopoietic stem cells and gene editing. *Int. J. Mol. Sci.* 22, 6275. doi:10.3390/ijms22126275

Anversa, P., Hiler, B., Ricci, R., Guideri, G., and Olivetti, G. (1986). Myocyte cell loss and myocyte hypertrophy in the aging rat heart. *J. Am. Coll. Cardiol.* 8 (6), 1441–8. doi:10.1016/s0735-1097(86)80321-7

Anzi, S., Stolovich-Rain, M., Klochendler, A., Fridlich, O., Helman, A., Paz-Sonnenfeld, A., et al. (2018). Postnatal exocrine pancreas growth by cellular hypertrophy correlates with a shorter lifespan in mammals. *Dev. Cell.* 45, 726–737. doi:10.1016/j.devcel.2018.05.024

Badia, R., Angulo, G., Riveira-Munoz, E., Pujantell, M., Puig, T., Ramirez, C., et al. (2016). Inhibition of herpes simplex virus type 1 by the CDK6 inhibitor PD-0332991 (palbociclib) through the control of SAMHD1. *J. Antimicrob. Chemother.* 71, 387–394. doi:10.1093/jac/dkv363

Barilani, M., Lovejoy, C., Piras, R., Abramov, A. Y., Lazzari, L., and Angelova, P. R. (2022). Age-related changes in the energy of human mesenchymal stem cells. *J. Cell. Physiol.* 237, 1753–1767. doi:10.1002/jcp.30638

Barthes, J., Ozcelik, H., Hindie, M., Ndreu-Halili, A., Hasan, A., and Vrana, N. E. (2014). Cell microenvironment engineering and monitoring for tissue engineering and regenerative medicine: The recent advances. *Biomed. Res. Int.* 2014, 921905. doi:10.1155/2014/921905

Bemiller, P. M., and Miller, J. E. (1979). Cytological changes senescing WI-38 cells: A statistical analysis. *Mech. Ageing Dev.* 10, 1–15. doi:10.1016/0047-6374(79)90066-6

Ben-David, U., and Amon, A. (2020). Context is everything: Aneuploidy in cancer. *Nat. Rev. Genet.* 21, 44–62. doi:10.1038/s41576-019-0171-x

Berardi, A. C., Wang, A., Levine, J. D., Lopez, P., and Scadden, D. T. (1995). Functional isolation and characterization of human hematopoietic stem cells. *Science* 267, 104–108. doi:10.1126/science.7528940

Bernstein, R. S., Grant, N., and Kipnis, D. M. (1975). Hyperinsulinemia and enlarged adipocytes in patients with endogenous hyperlipoproteinemia without obesity or diabetes mellitus. *Diabetes* 24, 207–213. doi:10.2337/diab.24.2.207

Bessman, J. D., Gilmer, P. R., Jr., and Gardner, F. H. (1983). Improved classification of anemias by MCV and RDW. *Am. J. Clin. Pathol.* 80, 322–326. doi:10.1093/ajcp/80.3.322

Bilinski, T., and Bartosz, G. (2006). Hypothesis: Cell volume limits cell divisions. *Acta Biochim. Pol.* 53, 833–835. doi:10.18388/abp.2006_3313

Bilinski, T. (2012). Hypertrophy, replicative ageing and the ageing process. *FEMS Yeast Res.* 12, 739–740. doi:10.1111/j.1567-1364.2012.00843.x

Bilinski, T., Zadrag-Tecza, R., and Bartosz, G. (2012). Hypertrophy hypothesis as an alternative explanation of the phenomenon of replicative aging of yeast. *FEMS Yeast Res.* 12, 97–101. doi:10.1111/j.1567-1364.2011.00759.x

Biran, A., Zada, L., Abou Karam, P., Vadai, E., Roitman, L., Ovadya, Y., et al. (2017). Quantitative identification of senescent cells in aging and disease. *Aging Cell.* 16, 661–671. doi:10.1111/acel.12592

Bjorklund, M. (2019). Cell size homeostasis: Metabolic control of growth and cell division. *Biochim. Biophys. Acta. Mol. Cell. Res.* 1866, 409–417. doi:10.1016/j.bbamcr.2018.10.002

Bjorntorp, P., Grimby, G., Sanne, H., Sjostrom, L., Tibblin, G., and WiLheLmsen, L. (1972). Adipose tissue fat cell size in relation to metabolism in weight-stabile, physically active men. *Horm. Metab. Res.* 4, 182–186. doi:10.1055/s-0028-1094045

Block, T. J., Marinkovic, M., Tran, O. N., Gonzalez, A. O., Marshall, A., Dean, D. D., et al. (2017). Restoring the quantity and quality of elderly human mesenchymal stem cells for autologous cell-based therapies. *Stem Cell. Res. Ther.* 8, 239. doi:10.1186/s13287-017-0688-x

Bortner, C. D., and Cidlowski, J. A. (2002). Apoptotic volume decrease and the incredible shrinking cell. *Cell. Death Differ.* 9, 1307–1310. doi:10.1038/sj.cdd.4401126

Brown, A. D., Davis, L. A., Fogarty, M. J., and Sieck, G. C. (2021). Mitochondrial fragmentation and dysfunction in type IIx/IIb diaphragm muscle fibers in 24-month old fischer 344 rats. *Front. Physiol.* 12, 727585. doi:10.3389/fphys.2021.727585

Brown-Borg, H. M., Borg, K. E., Meliska, C. J., and Bartke, A. (1996). Dwarf mice and the ageing process. *Nature* 384, 33. doi:10.1038/384033a0

Bundgaard, M. J., Regeur, L., Gundersen, H. J., and Pakkenberg, B. (2001). Size of neocortical neurons in control subjects and in Alzheimer's disease. *J. Anat.* 198, 481–489. doi:10.1046/j.1469-7580.2001.19840481.x

Butcher, D. T., Alliston, T., and Weaver, V. M. (2009). A tense situation: Forcing tumour progression. *Nat. Rev. Cancer* 9, 108–122. doi:10.1038/nrc2544

Cadart, C., Monnier, S., Grilli, J., Saez, P. J., Srivastava, N., Attia, R., et al. (2018). Size control in mammalian cells involves modulation of both growth rate and cell cycle duration. *Nat. Commun.* 9, 3275. doi:10.1038/s41467-018-05393-0

Cadart, C., Zlotek-Zlotkiewicz, E., Le Berre, M., Piel, M., and Matthews, H. K. (2014). Exploring the function of cell shape and size during mitosis. *Dev. Cell.* 29, 159–169. doi:10.1016/j.devcel.2014.04.009

Celton-Morizur, S., and Desdouets, C. (2010). Polyploidization of liver cells. *Adv. Exp. Med. Biol.* 676, 123–135. doi:10.1007/978-1-4419-6199-0_8

Chen, J., Kao, Y. R., Sun, D., Todorova, T. I., Reynolds, D., Narayanagari, S. R., et al. (2019). Myelodysplastic syndrome progression to acute myeloid leukemia at the stem cell level. *Nat. Med.* 25, 103–110. doi:10.1038/s41591-018-0267-4

Cheng, L., Chen, J., Kong, Y., Tan, C., Kafri, R., and Bjorklund, M. (2021). Size-scaling promotes senescence-like changes in proteome and organelle content. *bioRxiv* 2021, 455193. 2008.2005. doi:10.1101/2021.08.05.455193

Chistiakov, D. A., Sobenin, I. A., Revin, V. V., Orekhov, A. N., and Bobryshev, Y. V. (2014). Mitochondrial aging and age-related dysfunction of mitochondria. *Biomed. Res. Int.* 2014, 238463. doi:10.1155/2014/238463

Chopra, M., and Bohlander, S. K. (2019). The cell of origin and the leukemia stem cell in acute myeloid leukemia. *Genes. Chromosom. Cancer* 58, 850–858. doi:10.1002/gcc.22805

Colter, D. C., Class, R., DiGirolamo, C. M., and Prockop, D. J. (2000). Rapid expansion of recycling stem cells in cultures of plastic-adherent cells from human bone marrow. *Proc. Natl. Acad. Sci. U. S. A.* 97, 3213–3218. doi:10.1073/pnas.070034097

Colter, D. C., Sekiya, I., and Prockop, D. J. (2001). Identification of a subpopulation of rapidly self-renewing and multipotential adult stem cells in colonies of human marrow stromal cells. *Proc. Natl. Acad. Sci. U. S. A.* 98, 7841–7845. doi:10.1073/pnas.141221698

Cooper, K. L., Oh, S., Sung, Y., Dasari, R. R., Kirschner, M. W., and Tabin, C. J. (2013). Multiple phases of chondrocyte enlargement underlie differences in skeletal proportions. *Nature* 495, 375–378. doi:10.1038/nature11940

Correia-Melo, C., Marques, F. D. M., Anderson, R., Hewitt, G., Hewitt, R., Cole, J., et al. (2016). Mitochondria are required for pro-ageing features of the senescent phenotype. *EMBO J.* 35, 724–742. doi:10.15252/embj.201592862

Crozier, L., Foy, R., Adib, R., Badonyi, M., Kar, A., Holt, J. A., et al. (2022). Cell overgrowth during G1 arrest triggers an osmotic stress response and chronic p38 activation to promote cell cycle exit. *bioRxiv* 2022, 506843. 2009.2008. doi:10.1101/2022.09.08.506843

de Lacalle, S., Iraizoz, I., and Ma Gonzalo, L. (1991). Differential changes in cell size and number in topographic subdivisions of human basal nucleus in normal aging. *Neuroscience* 43, 445–456. doi:10.1016/0306-4522(91)90307-a

Del Campo, A., Contreras-Hernandez, I., Castro-Sepulveda, M., Campos, C. A., Figueroa, R., Tevy, M. F., et al. (2018). Muscle function decline and mitochondria changes in middle age precede sarcopenia in mice. *Aging (Albany NY)* 10, 34–55. doi:10.18632/aging.101358

Delarue, M., Brittingham, G. P., Pfeffer, S., Surovtsev, I. V., Pinglay, S., Kennedy, K. J., et al. (2018). mTORC1 controls phase separation and the biophysical properties of the cytoplasm by tuning crowding. *Cell.* 174, 338–349. doi:10.1016/j.cell.2018.05.042

Delgado-Gonzalez, J. C., de la Rosa-Prieto, C., Tarruella-Hernandez, D. L., Vallejo-Calcerrada, N., Cebada-Sanchez, S., Insausti, R., et al. (2020). Neuronal volume of the hippocampal regions in ageing. *J. Anat.* 237, 301–310. doi:10.1111/joa.13189

Demidenko, Z. N., and Blagosklonny, M. V. (2008). Growth stimulation leads to cellular senescence when the cell cycle is blocked. *Cell. Cycle* 7, 3355–3361. doi:10.4161/cc.7.21.6919

Demidenko, Z. N., Zubova, S. G., Bukreeva, E. I., Pospelov, V. A., Pospelova, T. V., and Blagosklonny, M. V. (2009). Rapamycin decelerates cellular senescence. *Cell. Cycle* 8, 1888–1895. doi:10.4161/cc.8.12.8606

Denoth Lippuner, A., Julou, T., and Barral, Y. (2014). Budding yeast as a model organism to study the effects of age. *FEMS Microbiol. Rev.* 38, 300–325. doi:10.1111/1574-6976.12060

Derks, W., and Bergmann, O. (2020). Polyploidy in cardiomyocytes: Roadblock to heart regeneration? *Circ. Res.* 126, 552–565. doi:10.1161/CIRCRESAHA.119.315408

Diaz, F., Villena, A., Gonzalez, P., Requena, V., Rius, F., and Perez De Vargas, I. (1999). Stereological age-related changes in neurons of the rat dorsal lateral geniculate nucleus. *Anat. Rec.* 255, 396–400. doi:10.1002/(SICI)1097-0185(19990801)255:4<396::AID-AR5>3.0.CO;2-M

Dubner, H. N., Crowley, J. J., and Schilling, R. F. (1978). Prognostic value of nucleoli and cell size in chronic lymphocytic leukemia. *Am. J. Hematol.* 4, 337–341. doi:10.1002/ajh.2830040405

Dyachenko, V., Rueckschloss, U., and Isenberg, G. (2006). Aging aggravates heterogeneities in cell-size and stress-intolerance of cardiac ventricular myocytes. *Exp. Gerontol.* 41 (5), 489–96. doi:10.1016/j.exger.2006.03.003

Dykstra, B., and de Haan, G. (2008). Hematopoietic stem cell aging and self-renewal. *Cell. Tissue Res.* 331, 91–101. doi:10.1007/s00441-007-0529-9

Eklund, J., and Bradford, G. E. (1977). Longeveity and lifetime body weight in mice selected for rapid growth. *Nature* 265, 48–49. doi:10.1038/265048b0

Ellison, G. M., Waring, C. D., Vicinanza, C., and Torella, D. (2012). Physiological cardiac remodelling in response to endurance exercise training: Cellular and molecular mechanisms. *Heart* 98, 5–10. doi:10.1136/heartjnl-2011-300639

Farnier, C., Krief, S., BlacheM.Diot-DupuyF.Mory, G., Ferre, P., et al. (2003). Adipocyte functions are modulated by cell size change: Potential involvement of an integrin/ERK signalling pathway. *Int. J. Obes. Relat. Metab. Disord.* 27, 1178–1186. doi:10.1038/sj.ijo.0802399

Farnier, C., Krief, S., BlacheM.Diot-DupuyF.Mory, G., Ferre, P., et al. (2002). The signaling pathway for beta1-integrin/ERKs is involved in the adaptation of adipocyte functions to cell size. *Ann. N. Y. Acad. Sci.* 973, 594–597. doi:10.1111/j.1749-6632.2002.tb04706.x

Fernandez, J. A., Suarez, C., NavArro, A., Diaz, C., Alvarez, J. C., Gonzalez del Rey, C., et al. (2007). Aging in the vestibular nuclear complex of the male golden hamster (*Mesocricetus auratus*): Anatomic and morphometric study. *Histol. Histopathol.* 22, 855–868. doi:10.14670/HH-22.855

Ferrara-Romeo, I., Martinez, P., Saraswati, S., Whittemore, K., Grana-Castro, O., Thelma Poluha, L., et al. (2020). The mTOR pathway is necessary for survival of mice with short telomeres. *Nat. Commun.* 11, 1168. doi:10.1038/s41467-020-14962-1

Fingar, D. C., Salama, S., Tsou, C., Harlow, E., and Blenis, J. (2002). Mammalian cell size is controlled by mTOR and its downstream targets S6K1 and 4EBP1/eIF4E. *Genes. Dev.* 16, 1472–1487. doi:10.1101/gad.995802

Flach, J., Bakker, S. T., Mohrin, M., Conroy, P. C., Pietras, E. M., Reynaud, D., et al. (2014). Replication stress is a potent driver of functional decline in ageing haematopoietic stem cells. *Nature* 512, 198–202. doi:10.1038/nature13619

Flurkey, K., Papaconstantinou, J., and Harrison, D. E. (2002). The Snell dwarf mutation Pit1(dw) can increase life span in mice. *Mech. Ageing Dev.* 123, 121–130. doi:10.1016/s0047-6374(01)00339-6

Foy, R., Crozier, L., Pareri, A. U., Park, B. H., and Saurin, A. T. (2022). Oncogenic signals prime cancer cells for toxic cell growth during a G1 cell cycle arrest. *bioRxiv* 2022, 506962. 2009.2008. doi:10.1101/2022.09.08.506962

Fraser, R. S., and Nurse, P. (1978). Novel cell cycle control of RNA synthesis in yeast. *Nature* 271, 726–730. doi:10.1038/271726a0

Frawley, L. E., and Orr-Weaver, T. L. (2015). Polyploidy. *Curr. Biol.* 25, R353–R358. doi:10.1016/j.cub.2015.03.037

Freeman, S. H., Kandel, R., Cruz, L., Rozkalne, A., Newell, K., Frosch, M. P., et al. (2008). Preservation of neuronal number despite age-related cortical brain atrophy in elderly subjects without Alzheimer disease. *J. Neuropathol. Exp. Neurol.* 67, 1205–1212. doi:10.1097/NEN.0b013e31818fc72f

Ganley, A. R., Breitenbach, M., Kennedy, B. K., and Kobayashi, T. (2012). Yeast hypertrophy: Cause or consequence of aging? Reply to Bilinski et al. *FEMS Yeast Res.* 12, 267–268. doi:10.1111/j.1567-1364.2012.00796.x

Geiger, H., de Haan, G., and Florian, M. C. (2013). The ageing haematopoietic stem cell compartment. *Nat. Rev. Immunol.* 13, 376–389. doi:10.1038/nri3433

Ghani, A. M., and Krause, J. R. (1986). Investigation of cell size and nuclear clefts as prognostic parameters in chronic lymphocytic leukemia. *Cancer* 58, 2233–2238.

Ghosh, D., Mejia Pena, C., Quach, N., Xuan, B., Lee, A. H., and Dawson, M. R. (2020). Senescent mesenchymal stem cells remodel extracellular matrix driving breast cancer cells to a more-invasive phenotype. *J. Cell. Sci.* 133, jcs232470. doi:10.1242/jcs.232470

Gillooly, J. F., Hein, A., and Damiani, R. (2015). Nuclear DNA content varies with cell size across human cell types. *Cold Spring Harb. Perspect. Biol.* 7, a019091. doi:10.1101/cshperspect.a019091

Ginzberg, M. B., Chang, N., D'Souza, H., Patel, N., Kafri, R., and Kirschner, M. W. (2018). Cell size sensing in animal cells coordinates anabolic growth rates and cell cycle progression to maintain cell size uniformity. *Elife* 7, e26957. doi:10.7554/eLife.26957

Ginzberg, M. B., Kafri, R., and Kirschner, M. (2015). Cell biology. On being the right (cell) size. *Science* 348, 1245075. doi:10.1126/science.1245075

Gopalakrishnan, K., Venkatesan, S., Low, E. S. H., and Hande, M. P. (2018). Effects of rapamycin on the mechanistic target of rapamycin (mTOR) pathway and telomerase in breast cancer cells. *Mutat. Res. Genet. Toxicol. Environ. Mutagen.* 836, 103–113. doi:10.1016/j.mrgentox.2018.03.008

Guo, M., Pegoraro, A. F., Mao, A., Zhou, E. H., Arany, P. R., Han, Y., et al. (2017). Cell volume change through water efflux impacts cell stiffness and stem cell fate. *Proc. Natl. Acad. Sci. U. S. A.* 114, E8618–E8627. doi:10.1073/pnas.1705179114

Haug, H., and Eggers, R. (1991). Morphometry of the human cortex cerebri and corpus striatum during aging. *Neurobiol. Aging* 12, 336–338. discussion 352-335. doi:10.1016/0197-4580(91)90013-a

Hayflick, L., and Moorhead, P. S. (1961). The serial cultivation of human diploid cell strains. *Exp. Cell. Res.* 25, 585–621. doi:10.1016/0014-4827(61)90192-6

Helms, S. A., Azhar, G., Zuo, C., Theus, S. A., Bartke, A., and Wei, J. Y. (2010). Smaller cardiac cell size and reduced extra-cellular collagen might be beneficial for hearts of Ames dwarf mice. *Int. J. Biol. Sci.* 6, 475–490. doi:10.7150/ijbs.6.475

Herculano-Houzel, S., Mota, B., and Lent, R. (2006). Cellular scaling rules for rodent brains. *Proc. Natl. Acad. Sci. U. S. A.* 103, 12138–12143. doi:10.1073/pnas.0604911103

Hill, A., DeZern, A. E., Kinoshita, T., and Brodsky, R. A. (2017). Paroxysmal nocturnal haemoglobinuria. *Nat. Rev. Dis. Prim.* 3, 17028. doi:10.1038/nrdp.2017.28

Ho, T. T., Warr, M. R., Adelman, E. R., Lansinger, O. M., Flach, J., Verovskaya, E. V., et al. (2017). Autophagy maintains the metabolism and function of young and old stem cells. *Nature* 543, 205–210. doi:10.1038/nature21388

Hoffmann, J. J., Nabbe, K. C., and van den Broek, N. M. (2015). Effect of age and gender on reference intervals of red blood cell distribution width (RDW) and mean red cell volume (MCV). *Clin. Chem. Lab. Med.* 53, 2015–2019. doi:10.1515/cclm-2015-0155

Hor, J. H., Soh, E. S., Tan, L. Y., Lim, V. J. W., Santosa, M. M., Winanto, et al. (2018). Cell cycle inhibitors protect motor neurons in an organoid model of Spinal Muscular Atrophy. *Cell. Death Dis.* 9 (11), 1100. doi:10.1038/s41419-018-1081-0

Horsfall, D. J., Mayne, K., Ricciardelli, C., Rao, M., Skinner, J. M, Henderson, D. W., et al. (1994). Age-related changes in guinea pig prostatic stroma. *Lab Invest.* 70 (5), 753–63.

Hou, Y. B., Ji, K., Sun, Y. T., Zhang, L. N., and Chen, J. J. (2019). CDK4/6 inhibitor palbociclib suppresses IgE-mediated mast cell activation. *J. Transl. Med.* 17, 276. doi:10.1186/s12967-019-2026-9

Hou, Y., Dan, X., Babbar, M., Wei, Y., Hasselbalch, S. G., Croteau, D. L., et al. (2019). Ageing as a risk factor for neurodegenerative disease. *Nat. Rev. Neurol.* 15, 565–581. doi:10.1038/s41582-019-0244-7

Hu, C., Lin, L., Zhu, Y., Zhang, Y., Wang, S., Zhang, J., et al. (2021). Association between age at diagnosis of type 2 diabetes and cardiovascular diseases: A nationwide, population-based, cohort study. *Front. Endocrinol.* 12, 717069. doi:10.3389/fendo.2021.717069

Iacono, D., O'Brien, R., Resnick, S. M., Zonderman, A. B., Pletnikova, O., Rudow, G., et al. (2008). Neuronal hypertrophy in asymptomatic Alzheimer disease. *J. Neuropathol. Exp. Neurol.* 67, 578–589. doi:10.1097/NEN.0b013e3181772794

Jacobs, E., Rathmann, W., Tonnies, T., ArenDt, D., MarchowezM.Veith, L., et al. (2020). Age at diagnosis of type 2 diabetes in Germany: A nationwide analysis based on claims data from 69 million people. *Diabet. Med.* 37, 1723–1727. doi:10.1111/dme.14100

Johannsen, D. L., Tchoukalova, Y., Tam, C. S., Covington, J. D., Xie, W., Schwarz, J. M., et al. (2014). Effect of 8 weeks of overfeeding on ectopic fat deposition and insulin sensitivity: Testing the "adipose tissue expandability" hypothesis. *Diabetes Care* 37, 2789–2797. doi:10.2337/dc14-0761

Johnson, S. C., Rabinovitch, P. S., and Kaeberlein, M. (2013). mTOR is a key modulator of ageing and age-related disease. *Nature* 493, 338–345. doi:10.1038/nature11861

Kaeberlein, M. (2012). Hypertrophy and senescence factors in yeast aging. A reply to Bilinski et al. *FEMS Yeast Res.* 12, 269–270. doi:10.1111/j.1567-1364.2012.00798.x

Kaesler, S., Sobiesiak, M., Kneilling, M., Volz, T., Kempf, W. E., Lang, P. A., et al. (2012). Effective T-cell recall responses require the taurine transporter Taut. *Eur. J. Immunol.* 42, 831–841. doi:10.1002/eji.201141690

Katsaros, M., Paschos, P., and Giouleme, O. (2020). Red cell distribution width as a marker of activity in inflammatory bowel disease: A narrative review. *Ann. Gastroenterol.* 33, 348–354. doi:10.20524/aog.2020.0486

Kawada, H., Ichikawa, Y., Watanabe, S., Nagao, T., and Arimori, S. (1994). Flow cytometric analysis of cell-surface antigen expressions on acute myeloid leukemia cell populations according to their cell-size. *Leuk. Res.* 18, 29–35. doi:10.1016/0145-2126(94)90006-x

Kawauchi, K., Ihjima, K., and Yamada, O. (2005). IL-2 increases human telomerase reverse transcriptase activity transcriptionally and posttranslationally through phosphatidylinositol 3'-kinase/Akt, heat shock protein 90, and mammalian target of rapamycin in transformed NK cells. *J. Immunol.* 174, 5261–5269. doi:10.4049/jimmunol.174.9.5261

Kim, K. M., Lui, L. Y., Browner, W. S., Cauley, J. A., Ensrud, K. E., Kado, D. M., et al. (2021). Association between variation in red cell size and multiple aging-related outcomes. *J. Gerontol. A Biol. Sci. Med. Sci.* 76, 1288–1294. doi:10.1093/gerona/glaa217

Knaapen, M. W., Vrolijk, B. C., and Wenink, A. C. (1996). Nuclear and cellular size of myocytes in different segments of the developing rat heart. *Anat. Rec.* 244, 118–125. doi:10.1002/(SICI)1097-0185(199601)244:1<118:AID-AR12>3.0.CO;2-S

Korolchuk, V. I., Miwa, S., Carroll, B., and von Zglinicki, T. (2017). Mitochondria in cell senescence: Is mitophagy the weakest link? *EBioMedicine* 21, 7–13. doi:10.1016/j.ebiom.2017.03.020

Koziel, R., Greussing, R., Maier, A. B., Declercq, L., and Jansen-Durr, P. (2011). Functional interplay between mitochondrial and proteasome activity in skin aging. *J. Invest. Dermatol.* 131, 594–603. doi:10.1038/jid.2010.383

Kruta, M., Sunshine, M. J., Chua, B. A., Fu, Y., Chawla, A., Dillingham, C. H., et al. (2021). Hsf1 promotes hematopoietic stem cell fitness and proteostasis in response to *ex vivo* culture stress and aging. *Cell. Stem Cell.* 28, 1950–1965.e6. doi:10.1016/j.stem.2021.07.009

Kuo, P. L., Lee, H., Bray, M. A., Geisse, N. A., Huang, Y. T., Adams, W. J., et al. (2012). Myocyte shape regulates lateral registry of sarcomeres and contractility. *Am. J. Pathol.* 181, 2030–2037. doi:10.1016/j.ajpath.2012.08.045

Kureel, S. K., Mogha, P., Khadpekar, A., Kumar, V., Joshi, R., Das, S., et al. (2019). Soft substrate maintains proliferative and adipogenic differentiation potential of human mesenchymal stem cells on long-term expansion by delaying senescence. *Biol. Open* 8, bio039453. doi:10.1242/bio.039453

Kuwahara, S., Kesuma Sari, D., Tsukamoto, Y., Tanaka, S., and Sasaki, F. (2004). Age-related changes in growth hormone (GH)-releasing hormone and somatostatin neurons in the hypothalamus and in GH cells in the anterior pituitary of female mice. *Brain Res.* 1025, 113–122. doi:10.1016/j.brainres.2004.08.012

Laforest, S., Labrecque, J., Michaud, A., Cianflone, K., and Tchernof, A. (2015). Adipocyte size as a determinant of metabolic disease and adipose tissue dysfunction. *Crit. Rev. Clin. Lab. Sci.* 52, 301–313. doi:10.3109/10408363.2015.1041582

Lanz, M. C., Zatulovskiy, E., Swaffer, M. P., Zhang, L., Ilerten, I., Zhang, S., et al. (2021). Increasing cell size remodels the proteome and promotes senescence. *bioRxiv* 2021, 454227. 2007.2029. doi:10.1101/2021.07.29.454227

Lanz, M. C., Zatulovskiy, E., Swaffer, M. P., Zhang, L., Ilerten, I., Zhang, S., et al. (2022). Increasing cell size remodels the proteome and promotes senescence. *Mol. Cell.* 82, 3255–3269.e8. doi:10.1016/j.molcel.2022.07.017

Leal-Egana, A., Letort, G., Martiel, J. L., Christ, A., Vignaud, T., Roelants, C., et al. (2017). The size-speed-force relationship governs migratory cell response to tumorigenic factors. *Mol. Biol. Cell.* 28, 1612–1621. doi:10.1091/mbc.E16-10-0694

Leduc-Gaudet, J. P., Picard, M., St-Jean Pelletier, F., Sgarioto, N., Auger, M. J., Vallee, J., et al. (2015). Mitochondrial morphology is altered in atrophied skeletal muscle of aged mice. *Oncotarget* 6, 17923–17937. doi:10.18632/oncotarget.4235

Lee, H. C., Yin, P. H., Chi, C. W., and Wei, Y. H. (2002). Increase in mitochondrial mass in human fibroblasts under oxidative stress and during replicative cell senescence. *J. Biomed. Sci.* 9, 517–526. doi:10.1007/BF02254978

Lee, S. S., Avalos Vizcarra, I., Huberts, D. H., Lee, L. P., and Heinemann, M. (2012). Whole lifespan microscopic observation of budding yeast aging through a microfluidic dissection platform. *Proc. Natl. Acad. Sci. U. S. A.* 109, 4916–4920. doi:10.1073/pnas.1113505109

Lehen'kyi, V., Shapovalov, G., Skryma, R., and Prevarskaya, N. (2011). Ion channnels and transporters in cancer. 5. Ion channels in control of cancer and cell apoptosis. *Am. J. Physiol. Cell. Physiol.* 301, C1281–C1289. doi:10.1152/ajpcell.00249.2011

Lengefeld, J., Cheng, C. W., Maretich, P., Blair, M., Hagen, H., McReynolds, M. R., et al. (2021). Cell size is a determinant of stem cell potential during aging. *Sci. Adv.* 7, eabk0271. doi:10.1126/sciadv.abk0271

Li, F., Wang, X., Capasso, J. M., and Gerdes, A. M. (1996). Rapid transition of cardiac myocytes from hyperplasia to hypertrophy during postnatal development. *J. Mol. Cell. Cardiol.* 28, 1737–1746. doi:10.1006/jmcc.1996.0163

Li, N., Zhou, H., and Tang, Q. (2017). Red blood cell distribution width: A novel predictive indicator for cardiovascular and cerebrovascular diseases. *Dis. Markers* 2017, 7089493. doi:10.1155/2017/7089493

Li, Q., Rycaj, K., Chen, X., and Tang, D. G. (2015). Cancer stem cells and cell size: A causal link? *Semin. Cancer Biol.* 35, 191–199. doi:10.1016/j.semcancer.2015.07.002

Li, Q., Yang, X., Sreejayan, N., and Ren, J (2007). Insulin-like growth factor I deficiency prolongs survival and antagonizes paraquat-induced cardiomyocyte dysfunction: Role of oxidative stress. *Rejuvenation Res.* 10, 501–512. doi:10.1089/rej.2007.0552

Lieber, S. C., Aubry, N., Pain, J., Diaz, G., Kim, S. J., and Vatner, S. F. (2004). Aging increases stiffness of cardiac myocytes measured by atomic force microscopy nanoindentation. *Am. J. Physiol. Heart Circ. Physiol.* 287, H645–H651. doi:10.1152/ajpheart.00564.2003

Lippi, G., Turcato, G., Cervellin, G., and Sanchis-Gomar, F. (2018). Red blood cell distribution width in heart failure: A narrative review. *World J. Cardiol.* 10, 6–14. doi:10.4330/wjc.v10.i2.6

Liu, F., He, J., Wang, H., Zhu, D., and Bi, Y. (2020). Adipose morphology: A critical factor in regulation of human metabolic diseases and adipose tissue dysfunction. *Obes. Surg.* 30, 5086–5100. doi:10.1007/s11695-020-04983-6

Liu, Z., Screven, R., Yu, D., Boxer, L., Myers, M. J., Han, J., et al. (2021). Microfluidic separation of canine adipose-derived mesenchymal stromal cells. *Tissue Eng. Part C Methods* 27, 445–461. doi:10.1089/ten.TEC.2021.0082

Lloyd, A. C. (2013). The regulation of cell size. *Cell.* 154, 1194–1205. doi:10.1016/j.cell.2013.08.053

Lonn, M., Mehlig, K., Bengtsson, C., and Lissner, L. (2010). Adipocyte size predicts incidence of type 2 diabetes in women. *FASEB J.* 24, 326–331. doi:10.1096/fj.09-133058

Lopez-Otin, C., Blasco, M. A., Partridge, L., Serrano, M., and Kroemer, G. (2013). The hallmarks of aging. *Cell.* 153, 1194–1217. doi:10.1016/j.cell.2013.05.039

Lundgren, M., SvenssonM.Lindmark, S., RenstromF.Ruge, T., and Eriksson, J. W. (2007). Fat cell enlargement is an independent marker of insulin resistance and 'hyperleptinaemia. *Diabetologia* 50, 625–633. doi:10.1007/s00125-006-0572-1

Lynch, B., Pageon, H., Le Blay, H., Brizion, S., Bastien, P., Bornschlogl, T., et al. (2022). A mechanistic view on the aging human skin through *ex vivo* layer-by-layer analysis of mechanics and microstructure of facial and mammary dermis. *Sci. Rep.* 12, 849. doi:10.1038/s41598-022-04767-1

Mai, S., Klinkenberg, M., Auburger, G., Bereiter-Hahn, J., and Jendrach, M. (2010). Decreased expression of Drp1 and Fis1 mediates mitochondrial elongation in senescent cells and enhances resistance to oxidative stress through PINK1. *J. Cell. Sci.* 123, 917–926. doi:10.1242/jcs.059246

Mammoto, T., Torisawa, Y. S., Muyleart, M., Hendee, K., Anugwom, C., Gutterman, D., et al. (2019). Effects of age-dependent changes in cell size on endothelial cell proliferation and senescence through YAP1. *Aging (Albany NY)* 11, 7051–7069. doi:10.18632/aging.102236

Manocha, S., Matrai, Z., Osthoff, M., Carter, A., and Pettitt, A. R. (2003). Correlation between cell size and CD38 expression in chronic lymphocytic leukaemia. *Leuk. Lymphoma* 44, 797–800. doi:10.1080/1042819031000068034

Manohar, S., Estrada, M. E., Uliana, F., and Neurohr, G. E. (2022). Cell cycle progression defects and impaired DNA damage signaling drive enlarged cells into senescence. *bioRxiv* 2022, 506740. 2009.2008. doi:10.1101/2022.09.08.506740

Manukyan, G., Mikulkova, Z., Turcsanyi, P., Savara, J., Trajerova, M., Kubova, Z., et al. (2021). Towards a better characterisation of leukemic cells in chronic lymphocytic leukaemia: Cell-size heterogeneity reflects their activation status and migratory abilities. *Cancers (Basel)* 13, 4922. doi:10.3390/cancers13194922

Markowska, A., Rebuffat, P., Gottardo, G., Mazzochi, G., and Nussdorfer, G. G. (1994). Age-dependent changes in the function and morphology of mitochondria of rat adrenal zona fasciculata. *Histol. Histopathol.* 9, 263–268.

Martinelli, C., Sartori, P., De Palo, S., Ledda, M., and Pannese, E. (2006). The perineuronal glial tissue of spinal ganglia. Quantitative changes in the rabbit from youth to extremely advanced age. *Anat. Embryol.* 211, 455–463. doi:10.1007/s00429-006-0097-x

Martinelli, C., Sartori, P., Ledda, M., and Pannese, E. (2006). A study of mitochondria in spinal ganglion neurons during life: Quantitative changes from youth to extremely advanced age. *Tissue Cell.* 38, 93–98. doi:10.1016/j.tice.2005.12.002

Mathe, G., Pouillart, P., SterescuM.Amiel, J. L., Schwarzenberg, L., SchneiderM., et al. (1971). Subdivision of classical varieties of acute leukemia. Correlation with prognosis and cure expectancy. *Rev. Eur. Etud. Clin. Biol.* 16, 554–560.

Mathieu-Costello, O., Ju, Y., Trejo-Morales, M., and Cui, L. (2005). Greater capillary-fiber interface per fiber mitochondrial volume in skeletal muscles of old rats. *J. Appl. Physiol.* 99, 281–289. doi:10.1152/japplphysiol.00750.2004

McLaughlin, T., Lamendola, C., CoghlaNN.Liu, T. C., Lerner, K., ShermAn, A., et al. (2014). Subcutaneous adipose cell size and distribution: Relationship to insulin resistance and body fat. *Obes. (Silver Spring)* 22, 673–680. doi:10.1002/oby.20209

Menezes, A. C., Dixon, C., Scholz, A., Nicholson, R., Leckenby, A., Azevedo, A., et al. (2022). RUNX3 overexpression inhibits normal human erythroid development. *Sci. Rep.* 12, 1243. doi:10.1038/s41598-022-05371-z

Merrill, D. A., Roberts, J. A., and Tuszynski, M. H. (2000). Conservation of neuron number and size in entorhinal cortex layers II, III, and V/VI of aged primates. *J. Comp. Neurol.* 422, 396–401. doi:10.1002/1096-9861(20000703)422:3<396::aid-cne6>3.0.co;2-r

Melissari, M., Balbi, T., Gennari, M., and Olivetti, G. (1991). L'invecchiamento del cuore: modificazioni ponderali e strutturali del ventricolo sinistro con l'età [The aging of the heart: weight and structural changes in the left ventricle with age]. *G. Ital. Cardiol.* 21 (2), 119–30.

Miettinen, T. P., and Bjorklund, M. (2016). Cellular allometry of mitochondrial functionality establishes the optimal cell size. *Dev. Cell.* 39, 370–382. doi:10.1016/j.devcel.2016.09.004

Miller, K. N., Burhans, M. S., Clark, J. P., Howell, P. R., Polewski, M. A., DeMuth, T. M., et al. (2017). Aging and caloric restriction impact adipose tissue, adiponectin, and circulating lipids. *Aging Cell.* 16, 497–507. doi:10.1111/acel.12575

Miller, R. A., Chrisp, C., and Atchley, W. (2000). Differential longevity in mouse stocks selected for early life growth trajectory. *J. Gerontol. A Biol. Sci. Med. Sci.* 55, B455–B461. doi:10.1093/gerona/55.9.b455

Miller, R. A., Harper, J. M., Galecki, A., and Burke, D. T. (2002). Big mice die young: Early life body weight predicts longevity in genetically heterogeneous mice. *Aging Cell.* 1, 22–29. doi:10.1046/j.1474-9728.2002.00006.x

Mitsui, Y., and Schneider, E. L. (1976). Increased nuclear sizes in senescent human diploid fibroblast cultures. *Exp. Cell. Res.* 100, 147–152. doi:10.1016/0014-4827(76)90336-0

Mitsui, Y., and Schneider, E. L. (1976). Relationship between cell replication and volume in senescent human diploid fibroblasts. *Mech. Ageing Dev.* 5, 45–56. doi:10.1016/0047-6374(76)90007-5

Moehrle, B. M., Nattamai, K., Brown, A., Florian, M. C., Ryan, M., Vogel, M., et al. (2015). Stem cell-specific mechanisms ensure genomic fidelity within HSCs and upon aging of HSCs. *Cell. Rep.* 13, 2412–2424. doi:10.1016/j.celrep.2015.11.030

Morris-Hanon, O., Marazita, M. C., Romorini, L., Isaja, L., Fernandez-Espinosa, D. D., Sevlever, G. E., et al. (2019). Palbociclib effectively halts proliferation but fails to induce senescence in patient-derived glioma stem cells. *Mol. Neurobiol.* 56, 7810–7821. doi:10.1007/s12035-019-1633-z

Mortimer, R. K., and Johnston, J. R. (1959). Life span of individual yeast cells. *Nature* 183, 1751–1752. doi:10.1038/1831751a0

Mu, L., Kang, J. H., Olcum, S., Payer, K. R., Calistri, N. L., Kimmerling, R. J., et al. (2020). Mass measurements during lymphocytic leukemia cell polyploidization decouple cell cycle- and cell size-dependent growth. *Proc. Natl. Acad. Sci. U. S. A.* 117, 15659–15665. doi:10.1073/pnas.1922197117

Murphy, S. B., Borella, L., Sen, L., and Mauer, A. (1975). Lack of correlation of lymphoblast cell size with presence of T-cell markers or with outcome in childhood acute lymphoblastic leukaemia. *Br. J. Haematol.* 31, 95–101. doi:10.1111/j.1365-2141.1975.tb00836.x

Navarro, A., and Boveris, A. (2004). Rat brain and liver mitochondria develop oxidative stress and lose enzymatic activities on aging. *Am. J. Physiol. Regul. Integr. Comp. Physiol.* 287, R1244–R1249. doi:10.1152/ajpregu.00226.2004

Neurohr, G. E., Terry, R. L., Lengefeld, J., Bonney, M., Brittingham, G. P., Moretto, F., et al. (2019). Excessive cell growth causes cytoplasm dilution and contributes to senescence. *Cell.* 176, 1083–1097. doi:10.1016/j.cell.2019.01.018

Núñez, R., Sancho-Martínez, S. M., Novoa, J. M. L., and López-Hernández, F. J. (2010). Apoptotic volume decrease as a geometric determinant for cell dismantling into apoptotic bodies. *Cell. Death Differ.* 17, 1665–1671. doi:10.1038/cdd.2010.96

Oberheim, N. A., Takano, T., Han, X., He, W., Lin, J. H. C., Wang, F., et al. (2009). Uniquely hominid features of adult human astrocytes. *J. Neurosci.* 29, 3276–3287. doi:10.1523/JNEUROSCI.4707-08.2009

Oh, E. S., Savonenko, A. V., King, J. F., Fangmark Tucker, S. M., Rudow, G. L., Xu, G., et al. (2009). Amyloid precursor protein increases cortical neuron size in transgenic mice. *Neurobiol. Aging* 30, 1238–1244. doi:10.1016/j.neurobiolaging.2007.12.024

Oja, S., Komulainen, P., Penttila, A., Nystedt, J., and Korhonen, M. (2018). Automated image analysis detects aging in clinical-grade mesenchymal stromal cell cultures. *Stem Cell. Res. Ther.* 9, 6. doi:10.1186/s13287-017-0740-x

Olcay, L., Ertem, U., Okur, H., and Tuncer, A. M. (1999). The importance of cell size and surface marker analysis in childhood acute myeloblastic leukemia. *Leuk. Res.* 23, 701–707. doi:10.1016/s0145-2126(99)00053-3

Oldfield, C. J., Duhamel, T. A., and Dhalla, N. S. (2020). Mechanisms for the transition from physiological to pathological cardiac hypertrophy. *Can. J. Physiol. Pharmacol.* 98, 74–84. doi:10.1139/cjpp-2019-0566

Oster, M. W., Margileth, D. A., Simon, R., and Leventhal, B. G. (1976). Lack of prognostic value of lymphoblast size in acute lymphoblastic leukaemia. *Br. J. Haematol.* 33, 131–135. doi:10.1111/j.1365-2141.1976.tb00979.x

Padovan-Merhar, O., Nair, G. P., Biaesch, A. G., Mayer, A., Scarfone, S., Foley, S. W., et al. (2015). Single mammalian cells compensate for differences in cellular volume and DNA copy number through independent global transcriptional mechanisms. *Mol. Cell.* 58, 339–352. doi:10.1016/j.molcel.2015.03.005

Padovani, F., Mairhormann, B., Falter-Braun, P., Lengefeld, J., and Schmoller, K. M. (2022). Segmentation, tracking and cell cycle analysis of live-cell imaging data with Cell-ACDC. *BMC Biol.* 20, 174. doi:10.1186/s12915-022-01372-6

Pakkenberg, B., Pelvig, D., Marner, L., Bundgaard, M. J., Gundersen, H. J. G., Nyengaard, J. R., et al. (2003). Aging and the human neocortex. *Exp. Gerontol.* 38, 95–99. doi:10.1016/s0531-5565(02)00151-1

Pantazopoulos, N., and Sinks, L. F. (1974). Morphological criteria for prognostication of acute lymphoblastic leukaemia. *Br. J. Haematol.* 27, 25–30. doi:10.1111/j.1365-2141.1974.tb06770.x

Passos, J. F., Nelson, G., Wang, C., Richter, T., Simillion, C., Proctor, C. J., et al. (2010). Feedback between p21 and reactive oxygen production is necessary for cell senescence. *Mol. Syst. Biol.* 6, 347. doi:10.1038/msb.2010.5

Passos, J. F., Saretzki, G., Ahmed, S., Nelson, G., Richter, T., Peters, H., et al. (2007). Mitochondrial dysfunction accounts for the stochastic heterogeneity in telomere-dependent senescence. *PLoS Biol.* 5, e110. doi:10.1371/journal.pbio.0050110

Peter, A. K., Bjerke, M. A., and Leinwand, L. A. (2016). Biology of the cardiac myocyte in heart disease. *Mol. Biol. Cell.* 27, 2149–2160. doi:10.1091/mbc.E16-01-0038

Pilling, L. C., Atkins, J. L., Duff, M. O., Beaumont, R. N., Jones, S. E., Tyrrell, J., et al. (2017). Red blood cell distribution width: Genetic evidence for aging pathways in 116, 666 volunteers. *PLoS One* 12, e0185083. doi:10.1371/journal.pone.0185083

Plummer, M. P., Finnis, M. E., Phillips, L. K., Kar, P., Bihari, S., Biradar, V., et al. (2016). Stress induced hyperglycemia and the subsequent risk of type 2 diabetes in survivors of critical illness. *PLoS One* 11, e0165923. doi:10.1371/journal.pone.0165923

Popov, A., Brazhe, A., Denisov, P., Sutyagina, O., Li, L., Lazareva, N., et al. (2021). Astrocyte dystrophy in ageing brain parallels impaired synaptic plasticity. *Aging Cell.* 20, e13334. doi:10.1111/acel.13334

Porrello, E. R., Mahmoud, A. I., Simpson, E., Hill, J. A., Richardson, J. A., Olson, E. N., et al. (2011). Transient regenerative potential of the neonatal mouse heart. *Science* 331, 1078–1080. doi:10.1126/science.1200708

Posakony, J. W., England, J. M., and Attardi, G. (1977). Mitochondrial growth and division during the cell cycle in HeLa cells. *J. Cell. Biol.* 74, 468–491. doi:10.1083/jcb.74.2.468

Pucker, A. D., Jackson, A. R., Morris, H. J., Fischer, A. J., McHugh, K. M., and Mutti, D. O. Ciliary (2015). Muscle cell changes during guinea pig development. *Invest. Ophthalmol. Vis. Sci.* 56 (13), 7691–6. doi:10.1167/iovs.15-17927

Qi, H., Chen, Y., Fu, X., Lin, C. P., Zheng, X. F. S., and Liu, L. F. (2008). TOR regulates cell death induced by telomere dysfunction in budding yeast. *PLoS One* 3, e3520. doi:10.1371/journal.pone.0003520

Rafelski, S. M., Viana, M. P., Zhang, Y., Chan, Y. H. M., Thorn, K. S., Yam, P., et al. (2012). Mitochondrial network size scaling in budding yeast. *Science* 338, 822–824. doi:10.1126/science.1225720

Reddy, A. K., Amador-Noguez, D., Darlington, G. J., Scholz, B. A., Michael, L. H., Hartley, C. J., et al. (2007). Cardiac function in young and old Little mice. *J. Gerontol. A Biol. Sci. Med. Sci.* 62, 1319–1325. doi:10.1093/gerona/62.12.1319

Ren, J., and Brown-Borg, H. M. (2002). Impaired cardiac excitation-contraction coupling in ventricular myocytes from Ames dwarf mice with IGF-I deficiency. *Growth Horm. IGF Res.* 12, 99–105. doi:10.1054/ghir.2002.0267

Resnick, S. M., Pham, D. L., Kraut, M. A., Zonderman, A. B., and Davatzikos, C. (2003). Longitudinal magnetic resonance imaging studies of older adults: A shrinking brain. *J. Neurosci.* 23, 3295–3301. doi:10.1523/jneurosci.23-08-03295.2003

Roberts, R. C. (1961). The lifetime growth and reproduction of selected strains of mice. *Heredity* 16, 369–381. doi:10.1038/hdy.1961.46

Rodgers, J. L., Jones, J., Bolleddu, S. I., Vanthenapalli, S., Rodgers, L. E., Shah, K., et al. (2019). Cardiovascular risks associated with gender and aging. *J. Cardiovasc. Dev. Dis.* 6, E19. doi:10.3390/jcdd6020019

Rodgers, J. T., King, K. Y., Brett, J. O., Cromie, M. J., Charville, G. W., Maguire, K. K., et al. (2014). mTORC1 controls the adaptive transition of quiescent stem cells from G0 to G(Alert). *Nature* 510, 393–396. doi:10.1038/nature13255

Roh, D. S., Du, Y., Gabriele, M. L., Robinson, A. R., Niedernhofer, L. J., and Funderburgh, J. L. (2013). Age-related dystrophic changes in corneal endothelium from DNA repair-deficient mice. *Aging Cell.* 12 (6), 1122–31. doi:10.1111/acel.12143

Rosen, C. J., and Bouxsein, M. L. (2006). Mechanisms of disease: Is osteoporosis the obesity of bone? *Nat. Clin. Pract. Rheumatol.* 2, 35–43. doi:10.1038/ncprheum0070

Rostock, C., Schrenk-Siemens, K., Pohle, J., and Siemens, J. (2018). Human vs. Mouse nociceptors - similarities and differences. *Neuroscience* 387, 13–27. doi:10.1016/j.neuroscience.2017.11.047

Roth, G. S., and Livingston, J. N. (1976). Reductions in glucocorticoid inhibition of glucose oxidation and presumptive glucocorticoid receptor content in rat adipocytes during aging. *Endocrinology.* 99 (3), 831–9. doi:10.1210/endo-99-3-831

Runel, G., Cario, M., Lopez-Ramirez, N., Malbouyres, M., Ruggiero, F., Bernard, L., et al. (2020). Stiffness measurement is a biomarker of skin ageing *in vivo*. *Exp. Dermatol.* 29, 1233–1237. doi:10.1111/exd.14195

Sadighi Akha, A. A. (2018). Aging and the immune system: An overview. *J. Immunol. Methods* 463, 21–26. doi:10.1016/j.jim.2018.08.005

Salvagno, G. L., Sanchis-Gomar, F., Picanza, A., and Lippi, G. (2015). Red blood cell distribution width: A simple parameter with multiple clinical applications. *Crit. Rev. Clin. Lab. Sci.* 52, 86–105. doi:10.3109/10408363.2014.992064

Sattar, N., Rawshani, A., Franzen, S., Rawshani, A., Svensson, A. M., Rosengren, A., et al. (2019). Age at diagnosis of type 2 diabetes mellitus and associations with cardiovascular and mortality risks. *Circulation* 139, 2228–2237. doi:10.1161/CIRCULATIONAHA.118.037885

Schmoller, K. M., and Skotheim, J. M. (2015). The biosynthetic basis of cell size control. *Trends Cell. Biol.* 25, 793–802. doi:10.1016/j.tcb.2015.10.006

Schmoller, K. M. (2017). The phenomenology of cell size control. *Curr. Opin. Cell. Biol.* 49, 53–58. doi:10.1016/j.ceb.2017.11.011

Schmoller, K. M., Turner, J. J., Koivomagi, M., and Skotheim, J. M. (2015). Dilution of the cell cycle inhibitor Whi5 controls budding-yeast cell size. *Nature* 526, 268–272. doi:10.1038/nature14908

Seel, A., Padovani, F., Finster, A., Mayer, M., Bureik, D., Osman, C., et al. (2022). Regulation with cell size ensures mitochondrial DNA homeostasis during cell growth. *bioRxiv*, 471050. 2021.2012.2003. doi:10.1101/2021.12.03.471050

Segel, M., Neumann, B., Hill, M. F. E., Weber, I. P., Viscomi, C., Zhao, C., et al. (2019). Niche stiffness underlies the ageing of central nervous system progenitor cells. *Nature* 573, 130–134. doi:10.1038/s41586-019-1484-9

Shembrey, C., Huntington, N. D., and Hollande, F. (2019). Impact of tumor and immunological heterogeneity on the anti-cancer immune response. *Cancers* 11, 1217. doi:10.3390/cancers11091217

Signer, R. A., Magee, J. A., Salic, A., and Morrison, S. J. (2014). Haematopoietic stem cells require a highly regulated protein synthesis rate. *Nature* 509, 49–54. doi:10.1038/nature13035

Simakova, O., and Arispe, N. J. (2007). The cell-selective neurotoxicity of the Alzheimer's Abeta peptide is determined by surface phosphatidylserine and cytosolic ATP levels. Membrane binding is required for Abeta toxicity. *J. Neurosci.* 27, 13719–13729. doi:10.1523/JNEUROSCI.3006-07.2007

Slawik, M., and Vidal-Puig, A. J. (2006). Lipotoxicity, overnutrition and energy metabolism in aging. *Ageing Res. Rev.* 5, 144–164. doi:10.1016/j.arr.2006.03.004

Smith, J. R., Pochampally, R., Perry, A., Hsu, S. C., and Prockop, D. J. (2004). Isolation of a highly clonogenic and multipotential subfraction of adult stem cells from bone marrow stroma. *Stem Cells* 22, 823–831. doi:10.1634/stemcells.22-5-823

Sperka, T., Wang, J., and Rudolph, K. L. (2012). DNA damage checkpoints in stem cells, ageing and cancer. *Nat. Rev. Mol. Cell. Biol.* 13, 579–590. doi:10.1038/nrm3420

Stab, B. R., Martinez, L., Grismaldo, A., Lerma, A., Gutierrez, M. L., Barrera, L. A., et al. (2016). Mitochondrial functional changes characterization in young and senescent human adipose derived MSCs. *Front. Aging Neurosci.* 8, 299. doi:10.3389/fnagi.2016.00299, 2nd et al

Stark, A. K., Toft, M. H., Pakkenberg, H., Fabricius, K., ErikseNN.Pelvig, D. P., et al. (2007). The effect of age and gender on the volume and size distribution of neocortical neurons. *Neuroscience* 150, 121–130. doi:10.1016/j.neuroscience.2007.06.062

Stauder, R., Valent, P., and Theurl, I. (2018). Anemia at older age: Etiologies, clinical implications, and management. *Blood* 131, 505–514. doi:10.1182/blood-2017-07-746446

Stearns-Reider, K. M., D'Amore, A., Beezhold, K., Rothrauff, B., Cavalli, L., Wagner, W. R., et al. (2017). Aging of the skeletal muscle extracellular matrix drives a stem cell fibrogenic conversion. *Aging Cell.* 16, 518–528. doi:10.1111/acel.12578

Stenkula, K. G., and Erlanson-Albertsson, C. (2018). Adipose cell size: Importance in health and disease. *Am. J. Physiol. Regul. Integr. Comp. Physiol.* 315, R284–R295. doi:10.1152/ajpregu.00257.2017

Stolen, T. O., Hoydal, M. A., Kemi, O. J., Catalucci, D., Ceci, M., Aasum, E., et al. (2009). Interval training normalizes cardiomyocyte function, diastolic Ca2+ control, and SR Ca2+ release synchronicity in a mouse model of diabetic cardiomyopathy. *Circ. Res.* 105, 527–536. doi:10.1161/CIRCRESAHA.109.199810

Stoll, E. A., Cheung, W., Mikheev, A. M., Sweet, I. R., Bielas, J. H., Zhang, J., et al. (2011). Aging neural progenitor cells have decreased mitochondrial content and lower oxidative metabolism. *J. Biol. Chem.* 286, 38592–38601. doi:10.1074/jbc.M111.252171

Strzyz, P. (2022). Big cells, small potential. *Nat. Rev. Mol. Cell. Biol.* 23, 91. doi:10.1038/s41580-021-00439-6

Sun, X. M., Bowman, A., Priestman, M., Bertaux, F., Martinez-Segura, A., Tang, W., et al. (2020). Size-dependent increase in RNA polymerase II initiation rates mediates gene expression scaling with cell size. *Curr. Biol.* 30, 1217–1230. doi:10.1016/j.cub.2020.01.053

Tanahashi, T., Sekiguchi, N., Matsuda, K., Takezawa, Y., Ito, T., Kobayashi, H., et al. (2016). Cell size variations of large granular lymphocyte leukemia: Implication of a small cell subtype of granular lymphocyte leukemia with STAT3 mutations. *Leuk. Res.* 45, 8–13. doi:10.1016/j.leukres.2016.04.001

Terry, R. D., DeTeresa, R., and Hansen, L. A. (1987). Neocortical cell counts in normal human adult aging. *Ann. Neurol.* 21, 530–539. doi:10.1002/ana.410210603

Terzakis, J. A., Santagada, E., Hernandez, A., and Taskin, M. (2005). Scanning electron microscopy of peripheral blood smears: Comparison of normal blood with some common leukemias. *Ultrastruct. Pathol.* 29, 19–28. doi:10.1080/01913120490903459

Thulborn, K., Lui, E., Guntin, J., Jamil, S., Sun, Z., Claiborne, T. C., et al. (2016). Quantitative sodium MRI of the human brain at 9.4 T provides assessment of tissue sodium concentration and cell volume fraction during normal aging. *NMR Biomed.* 29, 137–143. doi:10.1002/nbm.3312

Tissot, F. S., Estrach, S., Boulter, E., Cailleteau, L., Tosello, L., Seguin, L., et al. (2018). Dermal fibroblast SLC3A2 deficiency leads to premature aging and loss of epithelial homeostasis. *J. Invest. Dermatol.* 138, 2511–2521. doi:10.1016/j.jid.2018.05.026

Treton, J. A., and Courtois, Y. (1981). Evolution of the distribution, proliferation and ultraviolet repair capacity of rat lens epithelial cells as a function of maturation and aging. *Mech. Ageing Dev.* 15, 251–267. doi:10.1016/0047-6374(81)90134-2

Ungar, L., Harari, Y., Toren, A., and Kupiec, M. (2011). Tor complex 1 controls telomere length by affecting the level of Ku. *Curr. Biol.* 21, 2115–2120. doi:10.1016/j.cub.2011.11.024

Vanzulli, I., Papanikolaou, M., De-La-Rocha, I. C., Pieropan, F., Rivera, A. D., Gomez-Nicola, D., et al. (2020). Disruption of oligodendrocyte progenitor cells is an early sign of pathology in the triple transgenic mouse model of Alzheimer's disease. *Neurobiol. Aging* 94, 130–139. doi:10.1016/j.neurobiolaging.2020.05.016

Verkhratsky, A., Rodriguez, J. J., and Parpura, V. (2014). Neuroglia in ageing and disease. *Cell. Tissue Res.* 357, 493–503. doi:10.1007/s00441-014-1814-z

Virant-Klun, I., and Stimpfel, M. (2016). Novel population of small tumour-initiating stem cells in the ovaries of women with borderline ovarian cancer. *Sci. Rep.* 6, 34730. doi:10.1038/srep34730

Virant-Klun, I., Zech, N., Rozman, P., Vogler, A., Cvjeticanin, B., Klemenc, P., et al. (2008). Putative stem cells with an embryonic character isolated from the ovarian surface epithelium of women with no naturally present follicles and oocytes. *Differentiation.* 76, 843–856. doi:10.1111/j.1432-0436.2008.00268.x

Walkley, C. R., and Orkin, S. H. (2006). Rb is dispensable for self-renewal and multilineage differentiation of adult hematopoietic stem cells. *Proc. Natl. Acad. Sci. U. S. A.* 103, 9057–9062. doi:10.1073/pnas.0603389103

Walter, D., Lier, A., Geiselhart, A., Thalheimer, F. B., Huntscha, S., Sobotta, M. C., et al. (2015). Exit from dormancy provokes DNA-damage-induced attrition in haematopoietic stem cells. *Nature* 520, 549–552. doi:10.1038/nature14131

Wang, M. J., Chen, F., Lau, J. T. Y., and Hu, Y. P. (2017). Hepatocyte polyploidization and its association with pathophysiological processes. *Cell. Death Dis.* 8, e2805. doi:10.1038/cddis.2017.167

Wang, M., Yang, Y., Han, L., Han, S., Liu, N., Xu, F., et al. (2020a). Effect of three-dimensional ECM stiffness on cancer cell migration through regulating cell volume homeostasis. *Biochem. Biophys. Res. Commun.* 528, 459–465. doi:10.1016/j.bbrc.2020.05.182

Wang, M., Yang, Y., Han, L., Xu, F., and Li, F. (2020a). Cell mechanical microenvironment for cell volume regulation. *J. Cell. Physiol.* 235, 4070–4081. doi:10.1002/jcp.29341

Wang, R. H., He, J. P., Su, M. L., Luo, J., Xu, M., Du, X. D., et al. (2013). The orphan receptor TR3 participates in angiotensin II-induced cardiac hypertrophy by controlling mTOR signalling. *EMBO Mol. Med.* 5, 137–148. doi:10.1002/emmm.201201369

Wang, Z., Li, J., Wang, Y., and Liu, Q. (2019). Palbociclib improves cardiac dysfunction in diabetic cardiomyopathy by regulating Rb phosphorylation. *Am. J. Transl. Res.* 11, 3481–3489.

Watt, F. M., and Green, H. (1981). Involucrin synthesis is correlated with cell size in human epidermal cultures. *J. Cell. Biol.* 90, 738–742. doi:10.1083/jcb.90.3.738

Weeks, K. L., and McMullen, J. R. (2011). The athlete's heart vs. the failing heart: Can signaling explain the two distinct outcomes? *Physiol. (Bethesda)* 26, 97–105. doi:10.1152/physiol.00043.2010

Weiss, A., Neubauer, M. C., Yerabolu, D., Kojonazarov, B., Schlueter, B. C., Neubert, L., et al. (2019). Targeting cyclin-dependent kinases for the treatment of pulmonary arterial hypertension. *Nat. Commun.* 10, 2204. doi:10.1038/s41467-019-10135-x

Weyer, C., Foley, J. E., Bogardus, C., Tataranni, P. A., and Pratley, R. E. (2000). Enlarged subcutaneous abdominal adipocyte size, but not obesity itself, predicts type II diabetes independent of insulin resistance. *Diabetologia* 43, 1498–1506. doi:10.1007/s001250051560

Wilson, G. A., Sava, G., Vuina, K., Huard, C., Meneguello, L., Coulombe-Huntington, J., et al. (2021). Active growth signalling promotes cancer cell sensitivity to the CDK7 inhibitor ICEC0942. *bioRxiv* 2021, 459733. 2009.2010. doi:10.1101/2021.09.10.459733

Wright, J., and Schneider, B. L. (2014). Cell growth: When less means more. *Curr. Biol.* 24, R283–R285. doi:10.1016/j.cub.2014.02.044

Xanthopoulos, J. M., Gorelick, F. S., and Swenson, E. S. (2008). AGE-DEPENDENT polyploidization in mouse exocrine pancreas. *Pancreas* 37, 502. doi:10.1097/01.MPA.0000335419.46283.0e

Xie, K., Yang, Y., and Jiang, H. (2018). Controlling cellular volume via mechanical and physical properties of substrate. *Biophys. J.* 114, 675–687. doi:10.1016/j.bpj.2017.11.3785

Xie, S., and Skotheim, J. M. (2020). A G1 sizer coordinates growth and division in the mouse epidermis. *Curr. Biol.* 30, 916–924. doi:10.1016/j.cub.2019.12.062

Xie, S., Swaffer, M., and Skotheim, J. M. (2022). Eukaryotic cell size control and its relation to biosynthesis and senescence. *Annu. Rev. Cell. Dev. Biol.* 38, 291–319. doi:10.1146/annurev-cellbio-120219-040142

Xie, X., Hiona, A., Lee, A. S., Cao, F., Huang, M., Li, Z., et al. (2011). Effects of long-term culture on human embryonic stem cell aging. *Stem Cells Dev.* 20, 127–138. doi:10.1089/scd.2009.0475

Yako, T., Nakamura, M., Otsu, W., Nakamura, S., Shimazawa, M., and Hara, H. (2021). Mitochondria dynamics in the aged mice eye and the role in the RPE phagocytosis. *Exp. Eye Res.* 213, 108800. doi:10.1016/j.exer.2021.108800

Yamamoto, A., Saito, T., Hosoya, T., Kawahata, K., Asano, Y., Sato, S., et al. (2022). Therapeutic effect of cyclin-dependent kinase 4/6 inhibitor on dermal fibrosis in murine models of systemic sclerosis. *Arthritis Rheumatol.* 74, 860–870. doi:10.1002/art.42042

Yamashita, M., and Iwama, A. (2022). Aging and clonal behavior of hematopoietic stem cells. *Int. J. Mol. Sci.* 23, 1948. doi:10.3390/ijms23041948

Yang, J., Dungrawala, H., Hua, H., Manukyan, A., Abraham, L., Lane, W., et al. (2011). Cell size and growth rate are major determinants of replicative lifespan. *Cell. Cycle* 10, 144–155. doi:10.4161/cc.10.1.14455

Yang, J., Eliasson, B., Smith, U., Cushman, S. W., and Sherman, A. S. (2012). The size of large adipose cells is a predictor of insulin resistance in first-degree relatives of type 2 diabetic patients. *Obes. (Silver Spring)* 20, 932–938. doi:10.1038/oby.2011.371

Yang, Y., Xie, K., and Jiang, H. (2020). Durotaxis index of 3T3 fibroblast cells scales with stiff-to-soft membrane tension polarity. *Biophys. J.* 119, 1427–1438. doi:10.1016/j.bpj.2020.07.039

Yin, L., Yang, Z., Wu, Y., Denslin, V., Yu, C. C., Tee, C. A., et al. (2020). Label-free separation of mesenchymal stem cell subpopulations with distinct differentiation

potencies and paracrine effects. *Biomaterials* 240, 119881. doi:10.1016/j.biomaterials.2020.119881

Yoshida, K., Itoigawa, Y., Maruyama, Y., Saita, Y., Takazawa, Y., Ikeda, H., et al. (2017). Application of shear wave elastography for the gastrocnemius medial head to tennis leg. *Clin. Anat.* 30, 114–119. doi:10.1002/ca.22788

Young, H. E., Duplaa, C., Yost, M. J., Henson, N. L., Floyd, J. A., Detmer, K., et al. (2004). Clonogenic analysis reveals reserve stem cells in postnatal mammals. II. Pluripotent epiblastic-like stem cells. *Anat. Rec. A Discov. Mol. Cell. Evol. Biol.* 277, 178–203. doi:10.1002/ar.a.20000

Zadrag-Tecza, R., Kwolek-Mirek, M., Bartosz, G., and Bilinski, T. (2009). Cell volume as a factor limiting the replicative lifespan of the yeast *Saccharomyces cerevisiae*. *Biogerontology* 10, 481–488. doi:10.1007/s10522-008-9192-0

Zjablovskaja, P., and Florian, M. C. (2019). Acute myeloid leukemia: Aging and epigenetics. *Cancers (Basel)* 12, E103. doi:10.3390/cancers12010103

Zuba-Surma, E. K., Kucia, M., Abdel-Latif, A., Dawn, B., Hall, B., Singh, R., et al. (2008). Morphological characterization of very small embryonic-like stem cells (VSELs) by ImageStream system analysis. *J. Cell. Mol. Med.* 12, 292–303. doi:10.1111/j.1582-4934.2007.00154.x

frontiers | Frontiers in Cell and Developmental Biology

TYPE Original Research
PUBLISHED 12 April 2023
DOI 10.3389/fcell.2023.1118766

OPEN ACCESS

EDITED BY
Jette Lengefeld,
University of Helsinki, Finland

REVIEWED BY
Bruce Futcher,
Stony Brook University, United States
Tony Ly,
University of Dundee, United Kingdom

*CORRESPONDENCE
Gabriel E. Neurohr,
gabriel.neurohr@bc.biol.ethz.ch

‡These authors have contributed equally to this work

†Deceased

SPECIALTY SECTION
This article was submitted to Cell Growth and Division, a section of the journal Frontiers in Cell and Developmental Biology

RECEIVED 07 December 2022
ACCEPTED 21 March 2023
PUBLISHED 12 April 2023

CITATION
Terhorst A, Sandikci A, Whittaker CA, Szórádi T, Holt LJ, Neurohr GE and Amon A (2023), The environmental stress response regulates ribosome content in cell cycle-arrested *S. cerevisiae*. *Front. Cell Dev. Biol.* 11:1118766. doi: 10.3389/fcell.2023.1118766

The environmental stress response regulates ribosome content in cell cycle-arrested *S. cerevisiae*

Allegra Terhorst[1‡], Arzu Sandikci[1‡], Charles A. Whittaker[1], Tamás Szórádi[2], Liam J. Holt [2], Gabriel E. Neurohr [1,3]* and Angelika Amon[1†]

[1]David H. Koch Institute for Integrative Cancer Research, Howard Hughes Medical Institute, Massachusetts Institute of Technology, Cambridge, MA, United States, [2]Institute for Systems Genetics, New York University Langone Health, New York City, NY, United States, [3]Institute of Biochemistry, ETH Zurich, Zurich, Switzerland

Prolonged cell cycle arrests occur naturally in differentiated cells and in response to various stresses such as nutrient deprivation or treatment with chemotherapeutic agents. Whether and how cells survive prolonged cell cycle arrests is not clear. Here, we used *S. cerevisiae* to compare physiological cell cycle arrests and genetically induced arrests in G1-, meta- and anaphase. Prolonged cell cycle arrest led to growth attenuation in all studied conditions, coincided with activation of the Environmental Stress Response (ESR) and with a reduced ribosome content as determined by whole ribosome purification and TMT mass spectrometry. Suppression of the ESR through hyperactivation of the Ras/PKA pathway reduced cell viability during prolonged arrests, demonstrating a cytoprotective role of the ESR. Attenuation of cell growth and activation of stress induced signaling pathways also occur in arrested human cell lines, raising the possibility that the response to prolonged cell cycle arrest is conserved.

KEYWORDS

environmental stress response (ESR), cell cycle arrest, cytoplasm dilution, ribosome fraction, growth law

Introduction

Cell size homeostasis is a conserved feature of all cells, and failure to control cell size correlates with reduced cell fitness and cell senescence (Demidenko and Blagosklonny, 2008; Yang et al., 2011; Neurohr et al., 2019; Lanz et al., 2022). In proliferating cells, size homeostasis requires a tight coordination between biomass accumulation and cell division (Turner et al., 2012; Lloyd, 2013). The presence of growth signals, amino acids, and glucose stimulates macromolecule biosynthesis leading to an increase in cell mass and volume. In budding and fission yeast, cell division is linked to cell growth because cells need to reach a critical minimal size before progressing through the G1/S or G2/M transition, respectively (Jorgensen and Tyers, 2004; Dechant and Peter, 2008). However, many cells are non-proliferating and remain in a prolonged cell cycle arrest. This is the case for terminally differentiated cells in multicellular organisms, or for cells exposed to external signals that halt cell division, such as the presence of pheromone or different forms of stress. How cells regulate their size and maintain viability during prolonged periods without proliferation is unclear.

Saccharomyces cerevisiae, or budding yeast, has proven to be a valuable tool in the study of the relationship between cell growth and cell cycle progression because cell growth and division can be uncoupled using temperature-sensitive cell division cycle (*cdc-ts*) mutants, which have mutations in genes required for cell cycle progression (Hartwell et al., 1970). At the restrictive temperature, the *cdc-ts* mutants are unable to progress through the cell cycle but continue to accumulate biomass and thus increase in size, in some mutant strains up to 16 times the size of a wild-type cell (Johnston et al., 1977; Goranov et al., 2009). Previous work from our lab determined that, at the restrictive temperature, the size of many *cdc-ts* mutants eventually plateaus (Goranov et al., 2009). Attenuation of cell growth in large cells has also been observed in cycling and arrested human cells (Cadart et al., 2018; Ginzberg et al., 2018; Liu et al., 2022; Zatulovskiy et al., 2022). In one of the yeast *cdc-ts* mutants, attenuation of cell growth in oversized cells correlated with an unusual dilution of the cytoplasm, suggesting that reduced overall biomass production might cause attenuation of growth during prolonged cell cycle arrests (Neurohr et al., 2019). What causes cytoplasm dilution and growth attenuation is unclear.

The ability or inability to produce ribosomes strongly affects cell size (Jorgensen and Tyers, 2004), and the ribosomal fraction of the proteome correlates with growth rate (Metzl-Raz et al., 2017). As a significant portion of a cells energy is used for biomass accumulation through protein synthesis, the biogenesis of ribosomes is highly regulated to prevent cells from unnecessarily expending energy (Warner, 1999). We hypothesized that cell cycle arrested cells would shift energy expenditure from growth to maintenance of viability.

Here we used different *cdc-ts* mutants as a model system to determine how cells regulate growth and biomass production during prolonged cell cycle arrests in budding yeast. Using ribosome purification and Tandem Mass Tag (TMT) proteomics, we found that ribosomes were specifically downregulated during cell cycle arrests in *cdc-ts* mutants. We saw a similar downregulation of ribosome biogenesis by direct inhibition of TORC1 and in physiological cell cycle arrests induced by pheromone treatment and starvation. All investigated cell cycle arrests led to activation of the Environmental Stress Response (ESR), a transcriptional response to stress in *S. cerevisiae* that decreases translational capacity (Gasch et al., 2000). Hyperactivation of the Ras/PKA pathway increased the ribosome fraction of the proteome, but this was not sufficient to increase the total cellular protein content and did not prevent cytoplasm dilution. This observation suggests that ribosomes are not rate limiting for protein production in arrested cells. Furthermore, constitutive activation of PKA reduced cell survival during the cell cycle arrest and suppressed ESR activation, suggesting that the ESR orchestrates the reallocation of cellular resources from biomass production to cell survival during periods without proliferation.

Results

Growth attenuation occurs in *cdc-ts* arrested cells

In order determine the effect of prolonged cell cycle arrests on cell growth, we studied three independent *cdc-ts* mutants: *cdc28-13*, *cdc20-1*, and *cdc15-2*. We decided to examine these three mutants because they arrest in three distinct phases of the cell cycle and grow to different maximum cell volumes. This allowed us to distinguish between global, size-specific, and cell cycle phase-specific observations. Cdc28 is the main cyclin-dependent kinase that drives the yeast cell cycle and *cdc28-13* cells arrest in G1 when shifted to the restrictive temperature (Nasmyth, 1993). Cdc20 is the activating subunit of the anaphase promoting complex that drives the metaphase-anaphase transition and *cdc20-1* mutants at the restrictive temperature arrest in metaphase (Visintin et al., 1979). Cdc15 is a kinase required for mitotic exit, and *cdc15-2* mutants arrest in late anaphase when shifted to the restrictive temperature (Visintin and Amon, 2001).

We measured the mean cell volume of all three *cdc-ts* strains after shift to the restrictive temperature using a Coulter Counter. As a control, a *WT* strain was grown concurrently at the same temperature and was kept at a low cell density by repeated dilution of the culture to avoid confounding factors caused by nutrient deprivation (Terhorst et al., 2020). In agreement with our previous findings (Goranov et al., 2009), the mean cell volume of all three *cdc-ts* strains increased over 9 h and eventually plateaued (Figure 1A). Arrested *cdc28-13* and *cdc15-2* mutant cells grew exponentially during the first phase of the arrest, transitioned to a more linear mode of growth before reaching a plateau at 800 fL and 500 fL, respectively (Figure 1A). *cdc20-1* cells were already larger at the permissive temperature and cell size plateaued at 450 fL after 9 h of cell cycle arrest (Figure 1A). Thus, compared to the exponential cell growth observed in cycling wild type cells (Godin et al., 2010), cell growth is attenuated during prolonged genetically induced cell cycle arrests, independent of which cell cycle phase cells arrest in.

Ribosomes are downregulated in arrested cells leading to increased cytoplasmic diffusion

We hypothesized that growth attenuation was caused by a reduced cellular ribosome content because ribosomes are rate-limiting for growth in proliferating yeast cells (Metzl-Raz et al., 2017). To test this hypothesis, we measured the protein and ribosome content of the *cdc-ts* mutant strains during 9-h cell cycle arrests to determine protein and ribosome concentrations as cell growth slowed down. Cells were lysed, and protein concentration in the lysates was measured with a Bradford Assay. To determine the concentration of ribosomes, we used a sucrose-cushion centrifugation protocol to enrich for assembled (80S) ribosomal particles and measured rRNA concentration using a spectrophotometer (Terhorst et al., 2020). The ribosomal fraction of the proteome was then determined by normalizing ribosome concentration to total protein concentration. Because the arrest of *cdc-ts* strains requires a temperature shift from 25°C to 37°C, we began protein and ribosome measurements after 2h at 37°C and normalized our measurements to a *WT* cycling culture at 37°C to avoid confounding effects of heat shock (Verghese et al., 2012; Zakhartsev and Reuss, 2018). The ribosomal fraction of the

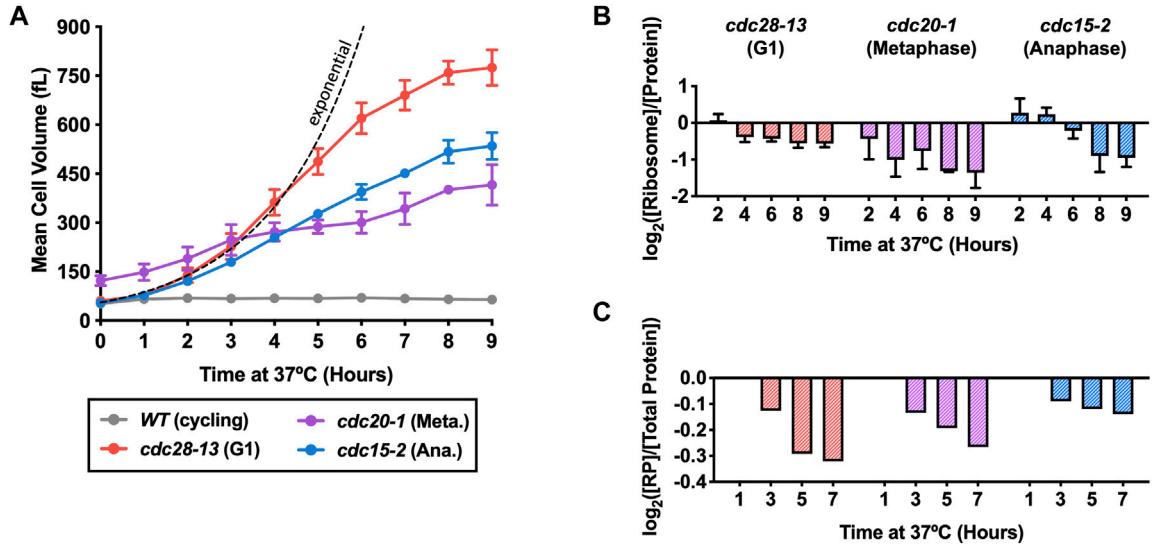

FIGURE 1
Ribosome concentrations decrease during prolonged cell cycle arrest. *WT* (A2587), *cdc28-13* (A39000), *cdc20-1* (A937), and *cdc15-2* (A2596) cells were grown to log phase in YEPD at 25°C and then shifted to 37°C for 9 h. *WT* cultures were kept in log phase (cycling) at OD_{600nm} 0.2–0.8, by diluting with pre-warmed (37°C) YEPD. **(A)** Mean cell volume (fL) was measured on a Coulter Counter. Error bars represent standard deviations of ≥3 biological replicates and the range of two replicates in *cdc20-1* mutants. The dashed black line indicates theoretical perfect exponential volume growth (90-min doubling time). **(B)** Protein and ribosome concentrations were quantified using a quantitative ribosome purification method as described in the method section. Values were normalized to those of the *WT* cycling samples at each time point and subsequently $\log_2$ transformed. Error bars represent the range of two biological replicates. **(C)** TMT Proteomics was performed on the *cdc-ts* strains as described in the methods except for the *cdc28-13* arrest, where our previously published TMT proteomics data were used to quantify the ribosomal proteome fraction (Neurohr et al., 2019). The fraction of ribosomal proteins (RP) in total protein extracts ([RP]/[Total Protein]) was determined. Values were normalized to the 1-h time point in each experiment and subsequently $\log_2$ transformed.

proteome decreased over the 9-h cell cycle arrests in all three *cdc-ts* strains (Figure 1B).

To validate this data, we compared the measured 80S ribosome concentrations to the abundance of ribosomal proteins determined by TMT proteomics. We used our previously published TMT data in *cdc28-13* arrested cells (Neurohr et al., 2019) and generated new data sets for *cdc20-1* and *cdc15-2* arrested cells (Supplementary Table S1). In agreement with our measurements of intact ribosomes, the fraction of peptides from ribosomal proteins continuously decreased over the course of the *cdc-ts* arrests (Figure 1C). However, the detected magnitude of ribosome downregulation differs substantially between the two methods. We cannot exclude that this difference reflects a technical issue, such as, for example, the fact that many proteins are not detected in our proteomics experiment. On the other hand, the two methods report on different ribosome populations: TMT proteomics detects all ribosome subunits while the ribosome purification method only detects assembled 80S ribosomes. Despite the quantitative differences, the data from these two experiments consistently show a specific downregulation of ribosomes during *cdc-ts* cell cycle arrests, which is independent of the cell cycle stage in which cells are arrested. We hypothesize that the resulting decreased translational capacity contributes to attenuation of cell volume increase after prolonged cell cycle arrest.

Cytoplasmic ribosome concentration not only affects translational capacity but also contributes to molecular crowding and thereby indirectly influences important processes, such as phase separation and cytoplasmic diffusion (Delarue et al., 2018). To determine whether cytoplasmic crowding was affected in *cdc-ts* cell cycle arrests, we used genetically encoded multimeric nanoparticles (GEMs) to probe the mesoscale diffusivity of the cytoplasm (Delarue et al., 2018). The median effective diffusion coefficients of GEMs in *cdc-ts* and *WT* cycling cells were measured at different time points over 6 h, at which point ribosome and protein content are downregulated in *cdc-ts* mutants. The median effective diffusion coefficients of the *cdc-ts* and *WT* cycling cells increased considerably between 0 h and 2 h, during which they were shifted to 37°C (Supplementary Figure S1). We attribute this increase to heat shock, which has been previously shown to increase cytoplasmic diffusion (Persson et al., 2020). After the initial heat shock, the median diffusion coefficients of all three *cdc-ts* mutants remained above the median diffusion coefficient of the *WT* cycling cells (Supplementary Figure S1), which decreased gradually after heat shock as previously described (Persson et al., 2020). *cdc20-1* cells had the highest median diffusion coefficient initially and throughout the experiment, in agreement with our observation that *cdc20-1* cells are already downregulating ribosomes at the permissive temperature (Figure 1B). We conclude that ribosome downregulation causes decreased macromolecular crowding of the cytoplasm in *cdc-ts* cells arrested in different cell cycle phases.

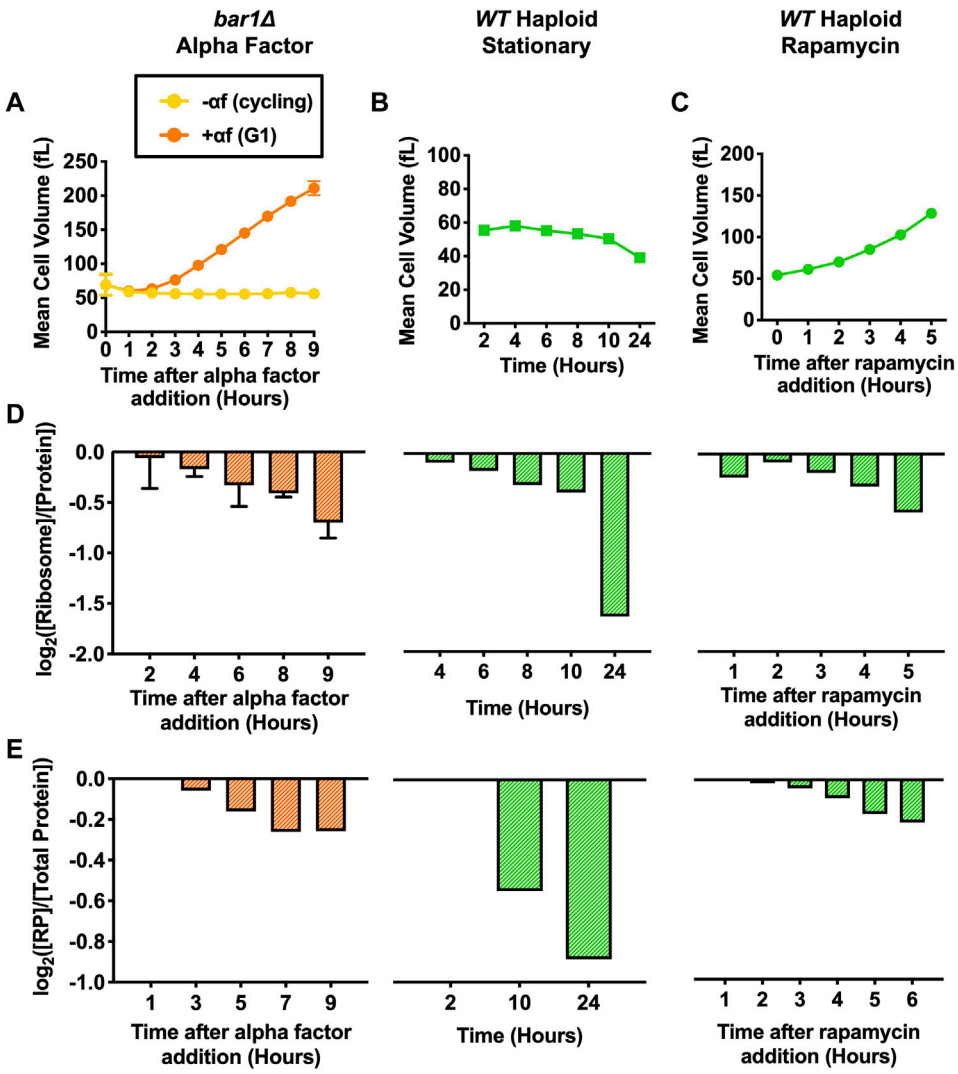

FIGURE 2
Protein and ribosome quantification of cells arrested in G1 with various methods. For alpha factor experiments, *bar1Δ* (A2589) cells were grown to log phase in YEPD at 30˚C. Cells were then divided into two cultures and grown for 9 h at 30˚C. 5 μg/mL alpha factor was added to one culture (+αf) while the equivalent volume of DMSO was added to the other (-αf). 2 μg/mL of alpha factor (+αf) or the equivalent volume of DMSO (-αf) was re-added every 2 h. For stationary phase experiments, *WT* haploid (A2587) cells were grown in YEPD for 24 h at 30˚C. For rapamycin experiments, *WT* haploid (A2587) cells were grown to log phase in YEPD at 30˚C. 5 nM rapamycin was added, and cells were grown for 5 h at 30˚C. **(A-C)** Mean cell volume (fL) was measured for **(A)** bar1Δ cells with (+αf) and without (-αf), **(B)** WT haploid cells grown into stationary phase, and **(C)** *WT* haploid cells with added rapamycin (5 nM). For alpha factor experiments, error bars represent standard deviations of three experimental replicates. For the stationary phase and rapamycin experiments, one experimental replicate was performed. **(D)** Protein and intact ribosome concentrations were quantified using the method described in (Terhorst et al., 2020). [Ribosome]/[Protein] was determined. Values were normalized to those of the cycling samples in each experiment (-αf in alpha factor experiments, 2-h time point in stationary phase experiments, and 0-h time point in rapamycin experiments) and subsequently $\log_2$ transformed. For alpha factor experiments, error bars represent standard deviations of three experimental replicates. The stationary phase and rapamycin experiments were performed once. **(E)** TMT Proteomics was performed for each indicated condition. The fraction of ribosomal proteins (RP) in total protein extracts ([RP]/[Total Protein]) was determined. Values were normalized to the 1-h time point in each experiment and subsequently $\log_2$ transformed.

Downregulation of ribosome biogenesis effectively reduces cell growth during physiological cell cycle arrests

Prolonged cell cycle arrests occur naturally when budding yeast cells are exposed to mating pheromone or when nutrients become limiting. As excessive cell growth is detrimental for cell function (Neurohr et al., 2019), we wondered whether downregulation of ribosome content in naturally occurring cell cycle arrests contributes to growth attenuation. We investigated the growth of cells arrested with alpha factor pheromone addition and nutrient starvation. Alpha factor (αf) is a pheromone that arrests mating-type a (*MATa*) yeast cells in G1 until mating is completed (Bardwell, 2004). While this arrest is similar to the genetically induced G1 arrest using *cdc28-ts* mutant strains described in Figure 1A, pheromone exposure in addition leads to cell polarization, reduces

TORC1 activity, and is cytoprotective during prolonged G1 arrests (Goranov et al., 2013). For practical reasons, the pheromone induced arrest was conducted in *bar1*Δ mutant cells, which are more sensitive to pheromone as BAR1 encodes the protease that degrades alpha factor (Ballensiefen and Schmitt, 1997). Starvation was induced by growing cells to high cell concentrations, which causes nutrient depletion and subsequent cell cycle arrest (Miles et al., 2013). During such stationary growth, both TORC1 and a related nutrient-sensing pathway, the Ras/PKA pathway become inactivated (Conrad et al., 2014; González and Hall, 2017). As comparison, we also treated cells with the TORC1 inhibitor rapamycin, which arrests a majority of cells in G1 (Moreno-Torres et al., 2015).

We first measured mean cell volume throughout each cell cycle arrest. Cells arrested with alpha factor for 9 h reached a maximum mean cell volume of over 200 fL (Figure 2A). WT haploid cells grown into stationary phase reached an OD_{600nm} of 8.5 by 10 h and of 20.0 by 24 h. The mean cell volume of these cells decreased as cells became starved for glucose and entered stationary phase (Figure 2B). Previous work by others showed that the observed decrease in mean cell volume as cells enter stationary phase is caused by the accumulation of small daughter cells in the population while arrested mother cells increase in size (Miles et al., 2019). *WT* haploid cells were arrested with rapamycin for 5 h. Although TORC1 inhibition has been shown to decrease cell size in mammalian cells (Fingar et al., 2002), there was a slow increse in mean cell volume throughout the rapamycin arrest in the *S. cerevisiae* cells (Figure 2C), likely reflecting a cell cycle block and continued biomass accumulation. In comparison to *cdc28-13* G1 arrested cells (Figure 1A), biomass accumulation in these physiological G1 cell cycle arrests is much slower, demonstrating efficient attenuation of cell growth.

Alpha factor treatment, stationary phase and rapamycin treatment inactivate major growth regulatory pathways such as TORC1 and PKA, which are both important upstream activators of ribosome biogenesis. We thus determined whether ribosome concentration was decreasing using our ribosome purification protocol and TMT proteomics. Indeed, each arrest caused a decrease in the ribosomal fraction of the proteome (Figures 2D,E). These experiments demonstrate that ribosome biosynthesis is efficiently downregulated in naturally occuring cell cycle arrests, resulting in efficient attenuation of cell growth.

To ensure the accuracy of our protein and ribosome measurements, the protein and ribosome contents of *WT* haploid and *WT* diploid strains were compared in the stationary phase and rapamycin experiments. The mean cell volume of *WT* diploid cells was between 2–3 times that of *WT* haploid cells throughout both experiments, and this difference was maintained when cells reached stationary phase (Supplementary Figures S2A, B). In the two experiments, the ribosomal fraction of the ribosome was the same for WT haploid and *WT* diploid strains at each time point (Supplementary Figures S2C). Taken together, these measurements support the accuracy of our method to determine changes in the ribosomal fraction of the proteome.

Cell cycle arrested cells activate the environmental stress response

We next wanted to understand how cells are able to downregulate ribosomes in response to cell cycle arrests. Previous work showed that slow growing cells activate an Environmental Stress Response (ESR) to a degree that is correlated to their growth rate (Brauer et al., 2008; Sheltzer et al., 2012; O'Duibhir et al., 2014; Terhorst et al., 2020). The ESR was discovered as a common transcriptional signature in cells exposed to a variety of stresses, such as oxidative and reductive stresses, heat shock, hyperosmotic shock, proteotoxic stress, and nutrient limitation (Gasch et al., 2000). There are approximately 300 genes upregulated as part of the ESR, which are involved in promotion of cell survival in stressful conditions by increasing autophagy, DNA damage repair, cell wall reinforcement, protein folding, and degradation. Over 600 genes are downregulated as part of the ESR, many of them encoding proteins required for growth related processes, such as transcription, RNA processing, translation, and ribosome biogenesis (Gasch et al., 2000; Ho et al., 2018). Importantly, slow growth and ESR activation correlate with increased resistance to stress (Elliott and Futcher, 1993; Lu et al., 2009; Guan et al., 2012), indicating that the ESR signature reflects a resource allocation from cell growth to cell maintenance and survival.

Although the ESR can be activated at any cell cycle stage (Ho et al., 2018), slow growth and ESR activation correlate with an increased fraction of cells being in G1 (Brauer et al., 2008; O'Duibhir et al., 2014), and our previous work showed that the ESR continuously increases in strength during prolonged G1 arrests (Neurohr et al., 2019). To investigate whether arrests in other cell cycle phases also lead to activation of an ESR, we performed RNASeq experiments (Supplementary Table S2) in cells arrested in G1-, meta- and anaphase as described above and analyzed the transcriptomes using a single-sample Gene Set Enrichment Analysis (ssGSEA) (Subramanian et al., 2005; Barbie et al., 2009; Tarca et al., 2013; Terhorst et al., 2020). This analysis calculates a ranking-based score for gene sets within individual samples. We used this metric to compare the expression of the stress regulated gene sets identified by Gasch et al. (Gasch et al., 2000). The ssGSEA projection values were calculated separately for stress induced (iESR) and stress repressed ESR (rESR) gene sets. As a point of reference and positive control, we compared ESR activation in cell cycle arrests to our previously published transcriptome data of *WT* cells grown in the presence of 500 mM NaCl for 40 min (Terhorst et al., 2020).

In all three *cdc-ts* arrests, the iESR (Figure 3A) and rESR (Figure 3B) ssGSEA projection values approach or surpass that of the positive control during the 9-h arrests. *cdc20-1* mutant cells already have a high iESR ssGSEA value at the 2-h timepoint, which plateaus after 4 h of arrest at a similar level as the positive control (Figure 3A). In arrested *cdc28-13* and *cdc15-2* mutant cells, the iESR ssGSEA rapidly increases during the first 6 h of the arrest and then plateaus around the same level (Figure 3A). The fact that the iESR ssGSEA plateaus around a maximal value suggests that cells reach a maximal expression level of stress induced genes (Tarca et al., 2013). A similar plateau effect was not observed for the rESR ssGSEA projection (Figure 3B). In particular, in *cdc28-13* and *cdc15-2* mutants the rESR ssGSEA projection continued to decrease

10.3389/fcell.2023.1118766

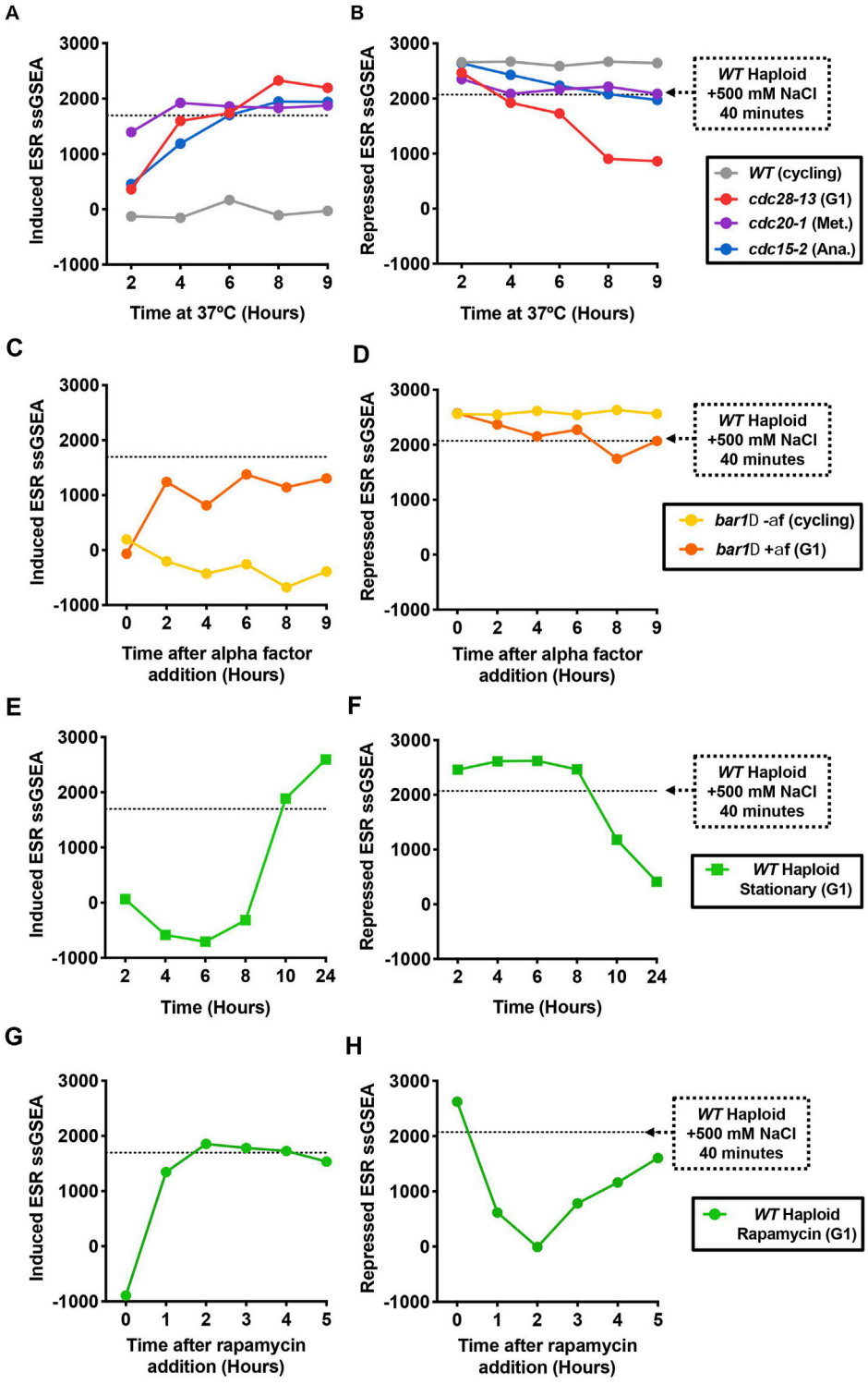

FIGURE 3
The Environmental Stress Response (ESR) is activated in cell cycle arrested cells. **(A, B)** WT haploid (A2587), cdc28-13 (A39000), cdc20-1 (A937), and cdc15-2 (A2596) cells were grown to log phase in YEPD at 25°C and then shifted to 37°C for 9 h. WT cultures were kept in log phase, termed cycling, at OD_{600nm} 0.2–0.8, by diluting with pre-warmed (37°C) YEPD. RNA-Seq samples were collected, and gene expression data were analyzed by calculating ssGSEA projection values for the **(A)** induced ESR and **(B)** repressed ESR. The horizontal lines represent the induced ESR and repressed ESR ssGSEA projection values for *WT* cells (A2587) treated with 500 mM NaCl for 40 min, a positive control for induction of the ESR. These values were taken from data reported in (Terhorst et al., 2020). **(C, D)** Same as in A-B, but for *bar1Δ* (A2589) cells treated with either alpha factor or DMSO as described in Figure 2. **(E, F)** Same as in A-B, but for *WT* haploid (A2587) cells were grown in YEPD for 24 h at 30°C without dilution, reaching an OD_{600nm} of 8.5 by 10 h. **(G, H)** Same as in A-B, but for exponentially growing *WT* haploid (A2587) cells treated with 5 nM rapamycin at t_0.

throughout the arrest and well below the control (Figure 3B). Since a large portion of the rESR genes encode for ribosomal proteins and ribosome biogenesis factors, the ESR signature seen in *cdc-ts* mutants is reflects the selective ribosome downregulation in these strains (Gasch et al., 2000).

We next wanted to confirm whether the ESR also occurs in naturally occurring cell cycle arrests. Indeed, cells grown in the presence of alpha factor exhibit both the induced and repressed ESR (Figures 3C, D) in agreement with previous observations (Ho et al., 2018). Previous work from our lab has shown that alpha factor addition reduces TORC1 activity, raising the possibility that TORC1 inhibition, rather than the cell cycle arrest itself, causes ESR activation in alpha factor-treated cells (Goranov et al., 2013). In support of this idea, direct inhibition of TORC1 with rapamycin or through nutrient depletion leads to strong activation of the ESR (Figures 3E–H) as previously described (Ho and Gasch, 2015; Terhorst et al., 2020). Inhibition of either the TORC1 pathway or the Ras/PKA pathway therefore likely induces the ESR signature in these naturally occurring cell cycle arrests and leads to the downregulation of ribosome biogenesis and growth attenuation.

While it is well understood how nutrient depletion leads to inactivation of the TORC1 and PKA pathways (Conrad et al., 2014; González and Hall, 2017) and thus ESR activation, it is less clear why prolonged cell cycle arrests would lead to a stress response. As growth signaling is highly nutrient sensitive in budding yeast, we hypothesized that the cell surface might become limiting for nutrient import if cells grow too large, causing cells to internally starve. To test this hypothesis, we compared ESR activation in *cdc28-13* G1-arrested cells between an auxotrophic yeast strain, which relies entirely on the import of certain amino acids and nucleobases, and a prototrophic strain, which can produce these nutrients itself. Although the two strains were generally the same size when arrested in G1 at the restrictive temperature of 37°C (Supplementary Figures S3A), ESR activation was weaker in prototrophic *cdc28-13* cells than in auxotrophic *cdc28-13* cells. This difference became more pronounced during the later timepoints of the arrest (Supplementary Figures S3B, C). Thus, inefficient nutrient import contributes to ESR activation in *cdc28-13* G1-arrested cells, potentially as a consequence of a reduced surface to volume ratio. In agreement with this hypothesis, ESR strength correlates strongly with cell size across the different *cdc-ts* arrests (Supplementary Figures S3D, E). As prototrophic strains still elicit an ESR, it is likely that either uptake of additional nutrients, such as glucose, is also limiting in arrested cells or that other arrest associated stresses contribute to ESR activation.

Downregulation of PKA during cell cycle arrests is cytoprotective

To understand the physiological consequences of ESR activation in *cdc-ts* cell cycle arrests, we wanted to observe the effects of preventing ESR activation during these arrests. Nutrient sensing pathways such as the TORC1 and PKA pathway play an important role in the regulation of stress responsive genes. For example, hyperactivation of the Ras/PKA pathway changes the localization of transcription factors that control expression of stress regulated genes (Marion et al., 2004). Because TORC1 and PKA also directly regulate other processes such as protein translation and metabolism (Conrad et al., 2014), the interpretation of experiments involving altered activities of these kinases is not straight forward.

Nevertheless, we wondered whether we could suppress ESR activation by hyperactivating PKA during cell cycle arrests. In order to make PKA constitutively active, we depleted Bcy1 using an auxin-inducible degron (AID) (Nishimura et al., 2009; Morawska and Ulrich, 2013). Bcy1 is a direct inhibitor of the three *S. cerevisiae* PKA isoforms Tpk1-3 (Toda et al., 1987). Previous work from our lab confirmed rapid degradation of AID-Bcy1 within 90 min of auxin addition (Kane et al., 2021). Because inactivation of PKA is required to survive heat shock (Kane et al., 2021) we waited for 2 h after the shift to the restrictive temperature before adding auxin to prevent heat-shock related cell death. RNA samples were taken after auxin addition and processed for RNASeq analysis. Depletion of Bcy1 in cycling *WT AID-BCY1* cells reduced expression of stress-induced genes (Figures 4A–C) and slightly increased expression of stress-repressed genes (Figures 4D–F). Consistent with Bcy1 depletion repressing ESR activation, expression of stress-induced genes was largely suppressed in *cdc28-13 AID-BCY1*, *cdc20-1 AID-BCY1,* and *cdc15-1 AID-BCY1* cells upon auxin addition (Figures 4A–C) and downregulation of stress-repressed genes was prevented (Figures 4D–F). In conclusion, ESR activation was at least partially prevented in all cell cycle arrests when PKA was constitutively active.

We next asked whether constitutive activation of PKA would affect cell viability during prolonged cell cycle arrest. We grew *WT* and *cdc-ts* cells with and without the *AID-BCY1* construct for 9 h at 37°C and plated 300 cells on YPD plates at the permissive temperature to determine the number of cells that can still form a colony. Cell viability was normalized to the 2-h timepoint. Unfortunately, the sonication required to accurately determine cell concentration on the Coulter Counter appeared to separate the bud from the mother cell in *cdc15-2* cells once they began to arrest in anaphase. This caused all cells experiencing the *cdc15-2* arrest to die once sonicated, and therefore, *cdc15-2* and *cdc15-2 AID-BCY1* were not included in this analysis. *WT* and *WT AID-BCY1* did not have significantly different cell viability through the 9-h growth period at 37°C (Figures 4G, H). In contrast, *cdc28-13* cells had a cell viability of above 50% after the 9-h arrest, while viability dropped below 30% after 9 h when Bcy1 was depleted during the arrest (Figure 4G). Similarly, fewer *cdc20-1 AID-BCY1* cells survived throughout the 9-h arrest than *cdc20-1* cells (Figure 4H), but *cdc20-1* cells were less viable than *cdc28-13* cells throughout the arrest. We conclude that the inability to downregulate PKA leads to increased cell death during cell cycle arrest, potentially because cells are unable to activate a stress response.

Constitutive activation of PKA prevents ribosome downregulation but not cytoplasm dilution

ESR activation in arrested *cdc-ts* cells coincides with growth attenuation, a reduced ribosome content (Figures 1A–C) and a reduced overall protein concentration in *cdc28-13* mutant cells (Neurohr et al., 2019). We thus asked whether constitutive PKA activation would prevent these phenotypes. We first analyzed how

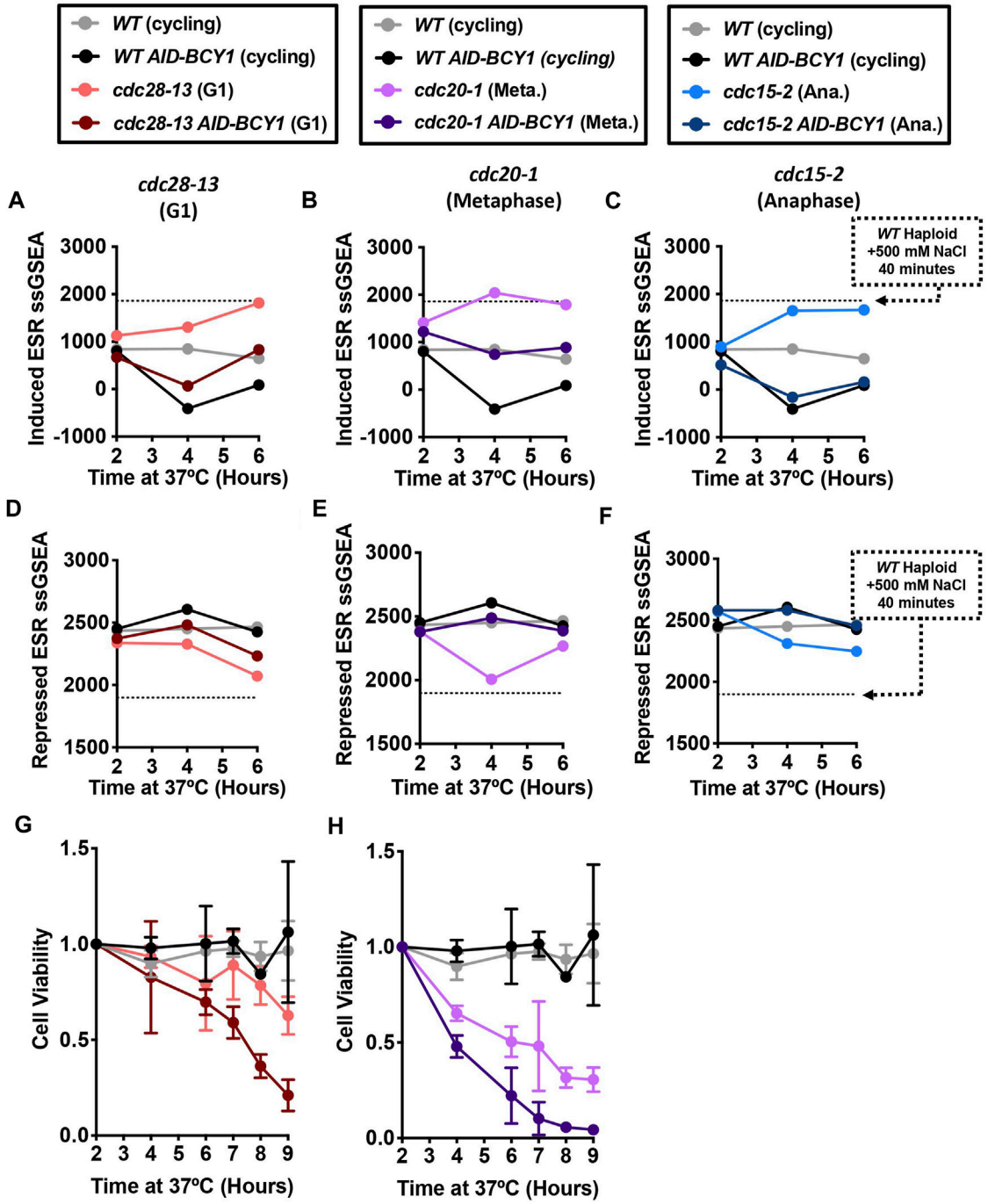

FIGURE 4
Hyperactivation of the Ras/PKA pathway suppresses the ESR and reduces the viability of cell cycle-arrested cells. *WT* (A2587), *WT AID-BCY1* (A40439), *cdc28-13* (A39000), *cdc28-13 AID-BCY1* (A40444), *cdc20-1* (A937), *cdc20-1 AID-BCY1* (A40499), *cdc15-2* (A2596), and *cdc15-2 AID-BCY1* (A40501) cells were grown to log phase in YEPD (supplemented with 138 µL glacial acetic acid for each 1 L YEPD) at 25°C and then shifted to 37°C for 6 h. *WT* and *WT AID-BCY1* cultures were kept in log phase, termed cycling, at OD_{600nm} 0.2–0.8, by diluting with pre-warmed (37°C) YEPD (supplemented with acetic acid). The auxin analogue IAA (500 µM) was added after 2 h and 4 h at 37°C. **(A–C)** Induced ESR ssGSEA projection values calculated from RNA-Seq gene expression data of the indicated strains and arrest timepoints. **(D–F)** Repressed ESR ssGSEA projection values calculated from RNA-Seq gene expression data of the indicated strains and arrest timepoints. WT ad WT AID-BCY1 data shown in A-F are from the same experiment. **(G–H)** Cell viability was measured for the indicated strains during a 9 h cell cycle arrest. Cells were plated and colony forming units were determined for each timepoint and normalized to the 0-h time point of each experiment. Error bars represent range of two experimental replicates. The same data for WT ad WT AID-BCY1 are shown in G-H for comparison.

Bcy1 depletion affects cell volume. *WT AID-BCY1* cells grew larger than *WT* cycling cells (Figures 5A–C) upon auxin addition, for reasons we do not fully understand. *cdc20-1* strains carrying the *AID-BCY1* allele were larger to begin with, and auxin addition did not lead to a significant increase in growth rate (Figures 5A–C). In arrested *cdc28-13* and *cdc15-2* cells, depletion of Bcy1 accelerated

10.3389/fcell.2023.1118766

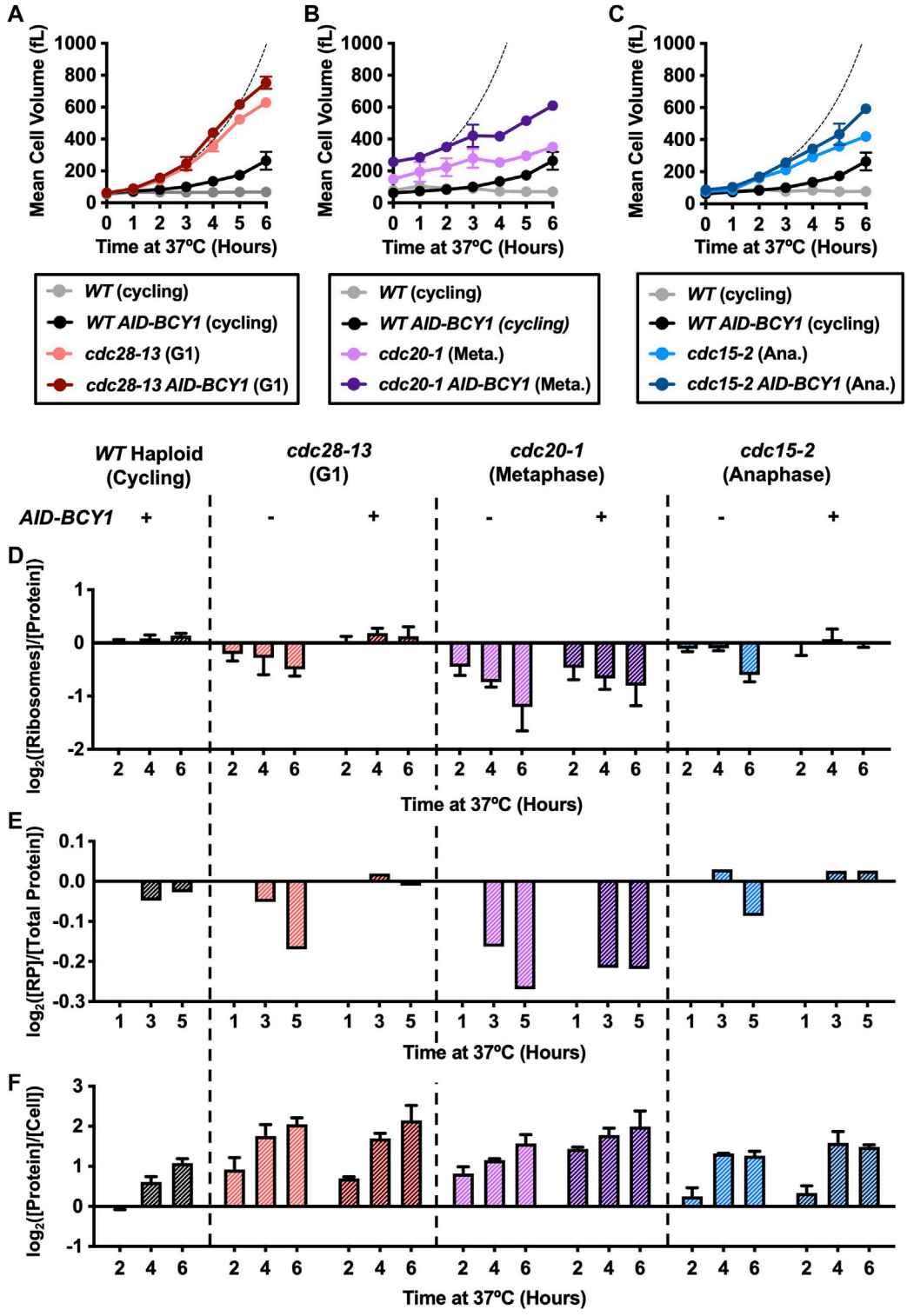

FIGURE 5
Hyperactivation of the Ras/PKA pathway attenuates ribosome depletion during cell cycle arrest. *WT* (A2587), *WT AID-BCY1* (A40439), *cdc28-13* (A39000), *cdc28-13 AID-BCY1* (A40444), *cdc20-1* (A937), *cdc20-1 AID-BCY1* (A40499), *cdc15-2* (A2596), and *cdc15-2 AID-BCY1* (A40501) cells were grown to log phase in YEPD (supplemented with 138 µL glacial acetic acid for each 1 L YEPD) at 25°C and then shifted to 37°C for 9 h. *WT* and *WT AID-BCY1* (cycling) cultures were kept at an OD_{600nm} between 0.2–0.8, by diluting with pre-warmed (37°C) YEPD (supplemented glacial acetic acid). The auxin analogue IAA (500 µM) was added after 2 h and 4 h at 37°C. **(A–C)** Mean cell volume (fL) was measured on a coulter counter for the indicated genotype. The same WT AID-BCY1 data is shown in A-C for comparison. The dashed line indicates theoretical exponential volume growth after BCY1 depletion (90-min doubling time). Error bars represent range of two experimental replicates. **(D)** Protein and intact ribosome concentrations were quantified as described in the method section and [Ribosome]/[Protein] was determined. Values were normalized to those of the WT cycling samples at each time point and subsequently $\log_2$ transformed. Error bars represent range of two experimental replicates. **(E)** TMT Proteomics was performed as described in the methods. The fraction of ribosomal proteins (RP) in total protein extracts ([RP]/[Total Protein]) was calculated. Values were normalized to the 1-h time point in each experiment and subsequently $\log_2$

(*Continued*)

FIGURE 5 (Continued)
transformed. **(F)** Protein concentration was quantified as above normalized to cell number determined using a coulter counter. Values were normalized to those of the WT cycling samples at each time point and subsequently log_2 transformed. Error bars represent range of two experimental replicates.

volume increase (Figures 5A–C). Thus, all three *cdc-ts* strains attenuate growth less efficiently during cell cycle arrests when PKA is constitutively active, but Bcy1 depletion is not sufficient to fully restore exponential growth, indicating that other processes also contribute to growth attenuation during cell cycle arrests.

As genes encoding ribosomal proteins and ribosome biogenesis factors are downregulated as part of the ESR, we next determined whether constitutive activation of PKA prevented the selective downregulation of ribosomes in arrested *cdc-ts* strains. There was no change in the ribosome fraction for *WT AID-BCY1* cells in comparison to *WT* cells, suggesting that PKA activation does not cause an increase in ribosome biogenesis in unstressed cells (Figures 5D, E). A decrease in the ribosomal proteome fraction was no longer observed in arrested *cdc28-13* and *cdc15-2* cells upon Bcy1 depletion (Figures 5D, E). In contrast, hyperactivation of PKA did not prevent the reduction in ribosome content in *cdc20-1* cells (Figures 5D, E), despite efficient suppression of the ESR at the transcriptional level (Figure 4B). While we do not understand the basis of this observation, it is consistent with the fact that Bcy1 depletion does not accelerate growth in arrested *cdc20-1* mutant cells. This observation also demonstrates the importance of directly analyzing ribosome content instead of relying on transcriptome data only. Importantly, the increase in the ribosomal proteome fraction did not fully restore exponential growth as described above and did not result in a substantial increase in overall cellular protein content (Figure 5F). As a consequence, the uncoupling of volume increase and protein synthesis we previously described in arrested *cdc28-13* cells is still observed when PKA is constitutively active (Supplementary Figure S4). We conclude that ribosomes are not the limiting factor for overall protein synthesis in arrested *cdc-ts* cells and that cytoplasm dilution is therefore not a consequence of ESR activation in oversized cells.

Discussion

Previous work from our lab had thoroughly investigated the change in cell volume of *cdc-ts* mutants that were arrested in the cell cycle, but how cells regulate growth during these arrests and ensure survival remained unlcear (Goranov et al., 2009). Here we confirmed that after prolonged cell cycle arrest, cells of three independent *cdc-ts* strains attenuate growth. Growth attenuation coincided with a selective downregulation of ribosomes and reduced crowding in the cytoplasm, and this observation was evident in all described cell cycle arrests. In addition, cell cycle arrest coincided with activation of the ESR, a transcriptional signature indicative of reduced ribosome production. ESR strength correlates with cell volume across all cell cycle arrests and can be partially suppressed when cells are not dependent on importing essential amino acids from the environment. Hyperactivation of PKA prevents ESR activation in *cdc-ts* cells and decreases cell viability during long arrests. Additionally, cells with constitutively active PKA attenuated growth less efficiently during prolonged arrests. Constitutive activation of PKA prevented the selective downregulation of ribosomes but did not increase the overall cellular protein content in arrested cells. Taken together, we conclude that a reduction in PKA activity is required to survive long cell cycle arrests, potentially due to its central role in orchestrating stress response and cell growth through the environmental stress response.

The cause of ESR activation in *cdc-ts* arrests remains unknown but poses an important yet complex question to answer. It is possible that each strain studied may activate the ESR through a different mechanism, which might be related to the stage in which the cells are arrested or the mutation itself. Therefore, it is important to continue to study multiple *cdc-ts* strains in comparison to other cell cycle arrests, as we have done here. The fact that the extent of stress response activation correlates with cell volume across different cell cycle arrests (Supplementary Figures S3D, E) however suggests that the ESR is activated by a common arrest-associated stress (increasd cell size) rather than by arrest-specific stresses.

There are several possible mechanisms of ESR activation in *cdc-ts* cells. It is likely that ESR activation is mediated at least at some level by altered activity of the major growth regulatory pathways Ras/PKA and TORC1. For example, internal starvation for amino acids or glucose could result in reduced TORC1 or PKA activity. In addition, there are multiple MAP kinase pathways that are implicated in ESR activation in response to different stresses. Specifically, the cell wall integrity pathway may be activated in *cdc-ts* arrests when cells grow large, since cell volume increase would automatically lead to increased cell wall tension if turgor pressure remains constant (Laplace-law). Osmotic or oxidative stress could also activate a stress response through MAP kinase pathways, similar to human cells that activate the stress-induced MAP kinase p38 after prolonged G1 cell cycle arrests (Crozier et al., 2022). As these pathways are highly interconnected, it would not be surprising if multiple pathways were involved (Chasman et al., 2014). Further studies will be necessary to identify the upstream signal that activates the ESR in cell cycle arrested cells.

We found that constitutive activation of PKA suppresses activation of the ESR and increases the ribosome fraction of the proteome. Increasing ribosome concentration did however not increase the overall protein content of arrested *cdc-ts* cells (*Figure 5D-F, S4*), which suggests that ribosomes are not the limiting factor for protein synthesis in these cells. Ribosomes have been proposed to limit cell growth because growth rate and the ribosome fraction correlate in free living unicellular organisms (Metzl-Raz et al., 2017). Previous observations however indicate that when cells grow too large, DNA becomes limiting for macromolecule synthesis (Zhurinsky et al., 2010; Neurohr et al., 2019). This could explain why increasing ribosome content does not lead to an overall increase in protein production. If DNA were the only factor limiting protein synthesis in arrested *cdc-ts*

mutants however, one would expect that cells arrested in metaphase (*cdc20-1*) or anaphase (*cdc15-2*) accumulate twice as much protein as cells arrested in G1 (*cdc28-13*), which is not the case (Figure 5F). Thus, other factors than DNA content must influence overall protein production capacity in these *cdc-ts* arrests.

Finally, questions remain concerning the mechanism by which cells maintain viability during a prolonged cell cycle arrest. When arrested cells were no longer able to downregulate PKA activity after Bcy1 depletion, cell viability decreased dramatically (Figures 4G, H). We do not know which PKA targets are critical for maintaining cell viability or what their respective contributions to survival are. Because large cell size reduces cell fitness (Neurohr et al., 2019), attenuation of cell growth through downregulation of ribosome biogenesis might contribute to survival in *cdc-ts* arrests. On the other hand, induction of protective stress-induced genes could contribute to survival. Understanding whether and how ESR activation protects arrested cells will require further studies.

In conclusion we have shown that cell cycle arrests lead to the activation of a canonical stress response, irrespective of the cell cycle phase in which cells are arrested. ESR activation correlates with growth attenuation and long term viability during prolonged cell cycle arrests. Our results are in agreement with the idea that the ESR orchestrates the reallocation of resources from cell growth to long term cell survival when cell proliferation is blocked.

Materials and methods

Yeast strains and growth conditions

Yeast strains used in this study are of the W303 background and described in the Supplementary Table S3. Unless otherwise noted, strains were grown in YEPD complete media at 30 °C. For stationary phase experiments, overnight cultures of *WT* cells were diluted to OD_{600} 0.1 and inucculated at 30°C. exponentially growing *cdc-ts* strains were grown at 25°C and shifted to 37°C for the experiments. For pheromone arrest experiments, cells were treated with 5 μg/mL alpha factor and 2 μg/mL alpha factor was added every 2 h throughout prolonged arrests. Rapamycin was used at a concentration of 5 nM. For auxin induced depletion experiments, strains were grown in YEPD supplemented with 138 μL glacial acetic acid for each 1 L YEPD. The auxin analogue indole-3-acetic acid (IAA, Sigma-Aldrich) was used at a concentration of 500 μM.

Mean cell volume measurements

Sample cultures were subjected to mild sonication with a tip sonicator to break up cell clumps and 0.1 mL of culture was diluted 1:100 with Isoton II Diluent (Beckman Coulter). Cell volume was measured on a Beckman Multisizer 3 Coulter Counter to produce a histogram of the population's cell volumes. Values above the half-maximal cell count were used to calculate the mean cell volume of the culture.

Protein and ribosome quantification

Protein and ribosome concentrations were quantified using a quantitative ribosome purification method as described in Terhorst et al., 2020 (Terhorst et al., 2020). In short, 50 mL of sample culture were collected by centrifugation (300 rpm, 5 min) and pellets were flash frozen in liquid N_2. After resuspension in 30 mL lysis buffer (20 mM Hepes pH 7.4, 100 mM potassium acetate, 2 mM magnesium acetate, 3 mM DTT, 0.5 mg/mL zymolyase, protease inhibitor (Roche, 11836170001)), cells were lysed with a French Press and lysates were cleared by centrifugation at 19′000 rpm for 20 min at 4 °C. Total protein concentration in the lysate ([Protein]) was determined by Bradford Assay (Biorad, 5000006).

15 mL of a 30% sucrose solution in lysis buffer were added to a ultracentrifugation tube and pre-chilled before addition of 10 mL cell lysate on top. Intact ribosomes were spun down into the sucrose cushion at 50,000 rpm for 4 h at 4°C. After removal of the supernatant pellets were air dried and resuspended in 1 mL lysis buffer. RNA concentration in the sucrose cushion, which corresponds to the concentration of isolated ribosomes ([Ribosome]), was measured on a Nanodrop (absorbance at A260 nm). [Ribosome]/[Protein] was calculated, and values were normalized to those of the *WT* cycling samples at each time point and subsequently $\log_2$ transformed. Error bars represent standard deviation from the mean of experimental replicates.

TMT proteomics

TMT Proteomics was performed essentially as described in Rose et al., 2016 (Rose et al., 2016). 50mL of sample culture were collected by centrifugation (300 rpm, 5 min), and pellets were flash frozen in liquid N_2. Cells were resuspended in 0.5 mL lysis buffer (8M Urea, 200 mM EPPS pH8.5, protease inhibitor (Roche, #11836170001)) and lysed through 9 rounds of bead beating (1 mL ceramic beads, Biospec 11079105z) on a FastPrep (Level 6, 45s pulse, 4°C). Tubes were pierced with a hot needle and centrifuged at 14,000xg for 10 min at 4°C to collect the lysate. Protein concentration in the lysate was measured by BCA Assay (Thermo Fisher Scientific, #22662).

Proteins were reduced with 10 mM DTT (Sigma, 1h, 56°C) and subsequently with 55 mM iodoacetamide (Sigma, 1h, 25°C, dark). Digestion was performed using modified trypsin at an enzyme: substrate ration of 1:50 in (Promega) in 100 mM ammonium bicarbonate (pH 8.9) overnight at 25°C and reactions were quenched in 5% formic acid (Fluka). Samples were desalted with Pierce Peptide Desalting Spin Columns (Thermo Fisher Science, # 89852). TMT labeling (10plex, Thermo) was performed as described by the manufacturer: Samples were dissolved in 100 mM triethylammonium bicarbonate (pH 8.5) and mixed with the respective TMT reagent dissolved in 41 μL anhydrous acetonitrile for 1 h at RT. Labelled samples were combined prior to drying *via* vacuum centrifugation.

Reverse phase HPLC (Thero Easy nLC1000) was performed on a precolumn (6 cm of 10 μm C18) and a self-pack 5 μm tip analytical column (12 cm of 5 μm C18). Samples were injected on a QExactive HF-X mass spectrometer (Thermo) operated in data-dependent mode (Full scan parameters: resolution of 70,000 across 350–2000 m/*z*, AGC $3e^6$, maximum IT 50 ms). The top 15 precursor ions of each cycle were further analyzed with MS/MS (NCE of 24, dynamic exclusion of 30 s). Raw data

files were searched using Proteome Discoverer (Thermo) and Mascot (version 2.4.1, Matrix Science). TMT data was normalized to the median of each TMT channel and only peptides with Mascot scores of ≥25 and isolation interference of ≤30 were included.

[RP] was the sum of the isotopic abundances for all 40S ribosomal proteins, 60S ribosomal proteins, and 60S acidic ribosomal proteins with Total Peptide (TotPep) values greater than 2 and Unique Peptide (UniPep) greater than 1. [Total Protein] was the sum of isotopic abundances for all proteins with Total Peptide (TotPep) values greater than 2 and Unique Peptide (UniPep) greater than 1. [RP]/[Protein] values were normalized to the 1-h time point in each experiment and subsequently $\log_2$ transformed. The TMT data is summarized in Supplementary Table S1.

GEM diffusion measurements

GEM diffusion measurements were essentially performed as described in Delarue et al., 2018 (Delarue et al., 2018). *WT* and *cdc-ts* strains expressing 40 nM-GEMs were imaged using a TIRF Nikon TI eclipse microscope equipped with a scMOS camera with a ×100 objective at a frame rate of 100 images per second for a total of 4 s. Particles were tracked using Mosaic (FIJI). Time averaged mean square displacement (MSD) curves were calculated for each trajectory and apparent diffusion coefficients were determined at a short timescale (<100 ms) as described (Delarue et al., 2018).

RNASeq

RNASeq was performed as described in Terhorst et al., 2020 (Terhorst et al., 2020). 5mL samples were spun down, washed with DEPC water and snap frozen in liquid N_2. RNA was purified using an RNeasy kit (Qiagen) according to the manufacturers instructions. Libraries were prepared using Illumina Truseq followed by Roche KAPA. For the *cdc28-13* arrest, stationary phase, and Rapamycin treatment (Figure 3) total RNA was sequenced while for all other samples mRNA was enriched to increase sequencing depth. Sequencing was performed on an Illumina HiSeq 2000. The RNA Seq data is summarized in Supplementary Table S2.

Data processing and single-sample Gene Set Enrichment Analysis (ssGSEA)

Reads form raw RNA Seq data were aligned to the *S. cerevisiae* transcriptome using STAR (Dobin et al., 2013). RSEM (Li and Dewey, 2011) was used to quantify gene expression. TPM values were calculated, offset by +1, and $\log_2$ transformed (Subramanian et al., 2005) (Terhorst et al., 2020) iESR and rESR gene sets were defined based on Gasch et al., 2000 (Gasch et al., 2000) and ssGSEA projections were calculated as described in Tarca et al., 2013 (Tarca et al., 2013). The ssGSEA method computes an enrichment value for a gene set from a gene expression sample by ranking genes using absolute expression level, rank normalizing the data and calculating scores for genes in the gene set and genes not in the gene set using the Empirical Cumulative Distribution Function (ECDF). The ssGSEA enrichment value for a gene set is then computed from the difference between "set" and "non-set" ECDF scores. While the parental GSEA method quantifies coordinated regulation of a gene set between experimental conditions, ssGSEA projections assess coordinated regulation of a gene set relative to non-set genes within a single sample.

Cell viability measurements

1 mL samples of culture were diluted 1:100 diluted with Isoton II Diluent (Beckman Coulter) and used to determine cell concentration of the culture using a Beckman Multisizer 3 Coulter Counter. 300 cells were plated on YEPD agar plates and grown at 25°C until colonies appeared, approximately 3–5 days. Colonies were counted by hand, and values were normalized to the 2-h time point of each experiment.

Data availability statement

The original contributions presented in the study are publicly available. This data can be found here: The RNA-Seq data presented in the study are deposited in the Gene Expression Omnibus (GEO) database, accession no GSE221908. The TMT-prroteomics data are deposited to the ETH Research Collection, DOI: https://doi.org/10.3929/ethz-b-000602269.

Author contributions

AA, AT, and AS conceived project and experiments. AT, AS, GN, TS, and LH conducted experiments and performed data analysis. CW performed transcriptome data analysis. AT and GN wrote and revised manuscript.

Funding

This work was supported by NIH grants CA206157 and GM118066 to AA who was an investigator of the Howard Hughes Medical Institute, the Paul F. Glenn Center for Biology of Aging Research at MIT, and the Ludwig Center at MIT. LH was funded by NIH R01 GM132447 and R37 CA240765. TS was funded by DFG Project 417630603. CW partially supported by Cancer Center Support (core) Grant P30-CA14051 from the NCI to the Barbara K. Ostrom (1978) Bioinformatics and Computing Core Facility of the Swanson Biotechnology Center. GN was funded by Eccellenza Grant PCEFP3_187003 from SNSF. Open access funding provided by ETH Zurich.

Acknowledgments

We thank Frank Solomon, Monica Boselli, Alexi Goranov, and Summer Morrill for comments, the MIT BioMicroCenter for RNA-Seq, the MIT Swanson Biotechnology Center for proteomics, and Amy Ikui for exciting discussions about our results. This work is based off thesis work in Terhorst et al., 2021 (Terhorst A. L., 2021). This manuscript has been released as a preprint at bioRxiv as Terhorst et al. (2021). This article is dedicated to the memory of the late Angelika Amon.

Conflict of interest

The authors declare that the research was conducted in the absence of any commercial or financial relationships that could be construed as a potential conflict of interest.

Publisher's note

All claims expressed in this article are solely those of the authors and do not necessarily represent those of their affiliated organizations, or those of the publisher, the editors and the reviewers. Any product that may be evaluated in this article, or claim that may be made by its manufacturer, is not guaranteed or endorsed by the publisher.

Supplementary material

The Supplementary Material for this article can be found online at: https://www.frontiersin.org/articles/10.3389/fcell.2023.1118766/full#supplementary-material

References

Ballensiefen, W., and Schmitt, H. D. (1997). Periplasmic Bar1 protease of *Saccharomyces cerevisiae* is active before reaching its extracellular destination. *Eur. J. Biochem.* 247 (1), 142–147. doi:10.1111/j.1432-1033.1997.00142.x

Barbie, D. A., Tamayo, P., Boehm, J. S., Kim, S. Y., Moody, S. E., Dunn, I. F., et al. (2009). Systematic RNA interference reveals that oncogenic KRAS-driven cancers require TBK1. *Nature* 462 (7269), 108–112. doi:10.1038/nature08460

Bardwell, L. (2004). A walk-through of the yeast mating pheromone response pathway. *Peptides* 25, 1465–1476.

Brauer, M. J., Huttenhower, C., Airoldi, E. M., Rosenstein, R., Matese, J. C., Gresham, D., et al. (2008). Coordination of growth rate, cell cycle, stress response, and metabolic activity in yeast. *Mol. Biol. Cell* 19 (1), 352–367. doi:10.1091/mbc.e07-08-0779

Cadart, C., Monnier, S., Grilli, J., Sáez, P. J., Srivastava, N., Attia, R., et al. (2018). Size control in mammalian cells involves modulation of both growth rate and cell cycle duration. *Nat. Commun.* 9 (1), 3275. doi:10.1038/s41467-018-05393-0

Chasman, D., Ho, Y., Berry, D. B., Nemec, C. M., MacGilvray, M. E., Hose, J., et al. (2014). Pathway connectivity and signaling coordination in the yeast stress-activated signaling network. *Mol. Syst. Biol.* 10 (11), 759. doi:10.15252/msb.20145120

Conrad, M., Schothorst, J., Kankipati, H. N., Zeebroeck, G. V., Rubio-Texeira, M., and Thevelein, J. M. (2014). Nutrient sensing and signaling in the yeast *Saccharomyces cerevisiae*. *FEMS Microbiol. Rev.* 38 (2), 254–299. doi:10.1111/1574-6976.12065

Crozier, L., Foy, R., Mouery, B. L., Whitaker, R. H., Corno, A., Spanos, C., et al. (2022). CDK4/6 inhibitors induce replication stress to cause long-term cell cycle withdrawal. *EMBO J.* 41 (6), 1085999–e108620. doi:10.15252/embj.2021108599

Dechant, R., and Peter, M. (2008). Nutrient signals driving cell growth. *Curr. Opin. Cell Biol.* 20 (6), 678–687. doi:10.1016/j.ceb.2008.09.009

Delarue, M., Brittingham, G. P., Pfeffer, S., Surovtsev, I. V., Pinglay, S., Kennedy, K. J., et al. (2018). mTORC1 controls phase separation and the biophysical properties of the cytoplasm by tuning crowding. *Cell* 174 (2), 338–349.e20. doi:10.1016/j.cell.2018.05.042

Demidenko, Z. N., and Blagosklonny, M. V. (2008). Growth stimulation leads to cellular senescence when the cell cycle is blocked. *Cell Cycle* 7 (21), 3355–3361. doi:10.4161/cc.7.21.6919

Dobin, A., Davis, C. A., Schlesinger, F., Drenkow, J., Zaleski, C., Jha, S., et al. (2013). Star: Ultrafast universal RNA-seq aligner. *Bioinformatics* 29 (1), 15–21. doi:10.1093/bioinformatics/bts635

Elliott, B., and Futcher, B. (1993). Stress resistance of yeast cells is largely independent of cell cycle phase. *Yeast* 9 (1), 33–42. doi:10.1002/yea.320090105

Fingar, D. C., Salama, S., Tsou, C., Harlow, E., and Blenis, J. (2002). Mammalian cell size is controlled by mTOR and its downstream targets S6K1 and 4EBP1/eIF4E. *Genes Dev.* 16 (12), 1472–1487. doi:10.1101/gad.995802

Gasch, A. P., Spellman, P. T., Kao, C. M., et al. (2000). Genomic expression programs in the response of yeast cells to environmental changes. *Mol. Biol. Cell* 11 (12), 4241–4257. doi:10.1091/mbc.11.12.4241

Ginzberg, M. B., Chang, N., D'Souza, H., Patel, N., Kafri, R., Kirschner, M. W., et al. (2018). Cell size sensing in animal cells coordinates anabolic growth rates and cell cycle progression to maintain cell size uniformity. *Curr. Biol.* 7 (8), e26957–R278. doi:10.7554/eLife.26957

Godin, M., Delgado, F. F., Son, S., Grover, W. H., Bryan, A. K., Tzur, A., et al. (2010). Using buoyant mass to measure the growth of single cells. *Nat. Methods* 7 (5), 387–390. doi:10.1038/nmeth.1452

González, A., and Hall, M. N. (2017). Nutrient sensing and TOR signaling in yeast and mammals. *EMBO J.* 36 (4), 397–408. doi:10.15252/embj.201696010

Goranov, A. I., Cook, M., Ricicova, M., Ben-Ari, G., Gonzalez, C., Hansen, C., et al. (2009). The rate of cell growth is governed by cell cycle stage. *Genes Dev.* 23 (12), 1408–1422. doi:10.1101/gad.1777309

Goranov, A. I., Gulati, A., Dephoure, N., Takahara, T., Maeda, T., Gygi, S. P., et al. (2013). Changes in cell morphology are coordinated with cell growth through the TORC1 pathway. *Curr. Biol.* 23, 1269–1279. doi:10.1016/j.cub.2013.05.035

Guan, Q., Haroon, S., Bravo, D. G., Will, J. L., and Gasch, A. P. (2012). Cellular memory of acquired stress resistance in *Saccharomyces cerevisiae*. *Genetics* 192 (2), 495–505. doi:10.1534/genetics.112.143016

Hartwell, L. H., Culotti, J., and Reid, B. (1970). Genetic control of the cell-division cycle in yeast, I. Detection of mutants. *Proc. Natl. Acad. Sci.* 66 (2), 352–359. doi:10.1073/pnas.66.2.352

Ho, Y. H., and Gasch, A. P. (2015). Exploiting the yeast stress-activated signaling network to inform on stress biology and disease signaling. *Curr. Genet.* 61 (4), 503–511. doi:10.1007/s00294-015-0491-0

Ho, Y. H., Shishkova, E., Hose, J., Coon, J. J., and Gasch, A. P. (2018). Decoupling yeast cell division and stress defense implicates mRNA repression in translational reallocation during stress. *Curr. Biol.* 28, 2673–2680.e4. doi:10.1016/j.cub.2018.06.044

Johnston, G. C., Pringle, J. R., and Hartwell, L. H. (1977). Coordination of growth with cell division in the yeast *Saccharomyces cerevisiae*. *Exp. Cell Res.* 105 (1), 79–98. doi:10.1016/0014-4827(77)90154-9

Jorgensen, P., and Tyers, M. (2004). How cells coordinate growth and division. *Curr. Biol.* 14 (23), R1014–R1027. doi:10.1016/j.cub.2004.11.027

Kane, A. J., Brennan, C. M., Xu, A. E., Solís, E. J., Terhorst, A., Denic, V., et al. (2021). Cell adaptation to aneuploidy by the environmental stress response dampens induction of the cytosolic unfolded-protein response. *Mol. Biol. Cell* 32 (17), 1557–1564. doi:10.1091/mbc.E21-03-0104

Lanz, M. C., Zatulovskiy, E., Swaffer, M. P., Zhang, L., Ilerten, I., Zhang, S., et al. (2022). Increasing cell size remodels the proteome and promotes senescence. *Mol. Cell* 82 (17), 3255–3269.e8. doi:10.1016/j.molcel.2022.07.017

Li, B., and Dewey, C. N. (2011). Rsem: Accurate transcript quantification from RNA-seq data with or without a reference genome. *BMC Bioinforma.* 12, 323. doi:10.1186/1471-2105-12-323

Liu, X., Yan, J., and Kirschner, M. W. (2022). *Beyond G1/S regulation: How cell size homeostasis is tightly controlled throughout the cell cycle?* bioRxiv.

Lloyd, A. C. (2013). The regulation of cell size. *Cell* 154 (6), 1194–1205. doi:10.1016/j.cell.2013.08.053

Lu, C., Brauer, M. J., and Botstein, D. (2009). Slow growth induces heat-shock resistance in normal and respiratory-deficient yeast. *Mol. Biol. Cell* 20 (3), 891–903. doi:10.1091/mbc.e08-08-0852

Marion, R. M., Regev, A., Segal, E., Barash, Y., Koller, D., Friedman, N., et al. (2004). Sfp1 is a stress-and nutrient-sensitive regulator of ribosomal protein gene expression. [Internet]. 2004. Available from www.pnas.orgcgidoi10.1073pnas.0405353101.

Metzl-Raz, E., Kafri, M., Yaakov, G., Soifer, I., Gurvich, Y., and Barkai, N. (2017). Principles of cellular resource allocation revealed by condition-dependent proteome profiling. *Elife* 6, e28034. doi:10.7554/eLife.28034

Miles, S., Li, L., Davison, J., and Breeden, L. L. (2013). Xbp1 directs global repression of budding yeast transcription during the transition to quiescence and is important for the longevity and reversibility of the quiescent state. *PLoS Genet.* 9 (10), e1003854. doi:10.1371/journal.pgen.1003854

Miles, S., Li, L. H., Melville, Z., and Breeden, L. L. (2019). Ssd1 and the cell wall integrity pathway promote entry, maintenance, and recovery from quiescence in budding yeast. *Mol. Biol. Cell* 30 (17), 2205–2217. doi:10.1091/mbc.E19-04-0190

Morawska, M., and Ulrich, H. D. (2013). An expanded tool kit for the auxin-inducible degron system in budding yeast. *Yeast* 30 (9), 341–351. doi:10.1002/yea.2967

Moreno-Torres, M., Jaquenoud, M., and de Virgilio, C. (2015). TORC1 controls G 1 - S cell cycle transition in yeast via Mpk1 and the greatwall kinase pathway. *Nat. Commun.* 6, 8256. doi:10.1038/ncomms9256

Nasmyth, K. (1993). Control of the yeast cell cycle by the Cdc28 protein kinase. *Curr. Opin. Cell Biol.* 5 (2), 166–179. doi:10.1016/0955-0674(93)90099-c

Neurohr, G. E., Terry, R. L., Lengefeld, J., Bonney, M., Brittingham, G. P., Moretto, F., et al. (2019). Excessive cell growth causes cytoplasm dilution and contributes to senescence. *Cell* 176 (5), 1083–1097.e18. doi:10.1016/j.cell.2019.01.018

Nishimura, K., Fukagawa, T., Takisawa, H., Kakimoto, T., and Kanemaki, M. (2009). An auxin-based degron system for the rapid depletion of proteins in nonplant cells. *Nat. Methods* 6 (12), 917–922. doi:10.1038/nmeth.1401

O'Duibhir, E., Lijnzaad, P., Benschop, J. J., Lenstra, T. L., Leenen, D., Groot Koerkamp, M. J., et al. (2014). Cell cycle population effects in perturbation studies. *Mol. Syst. Biol.* 10 (6), 732. doi:10.15252/msb.20145172

Persson, L. B., Ambati, V. S., and Brandman, O. (2020). Cellular control of viscosity counters changes in temperature and energy availability. *Cell* 183, 1572–1585.e16. doi:10.1016/j.cell.2020.10.017

Rose, C. M., Isasa, M., Ordureau, A., Prado, M. A., Beausoleil, S. A., Jedrychowski, M. P., et al. (2016). Highly multiplexed quantitative mass spectrometry analysis of ubiquitylomes. *Cell Syst.* 3 (4), 395–403.e4. doi:10.1016/j.cels.2016.08.009

Sheltzer, J. M., Torres, E. M., Dunham, M. J., and Amon, A. (2012). Transcriptional consequences of aneuploidy. *Proc. Natl. Acad. Sci.* 109 (31), 12644–12649. doi:10.1073/pnas.1209227109

Subramanian, A., Tamayo, P., Mootha, V. K., Mukherjee, S., Ebert, B. L., Gillette, M. A., et al. (2005). Gene set enrichment analysis: A knowledge-based approach for interpreting genome-wide expression profiles. *Proc. Natl. Acad. Sci. U. S. A.* 102 (43), 15545–15550. doi:10.1073/pnas.0506580102

Tarca, A. L., Bhatti, G., and Romero, R. (2013). A comparison of gene set analysis methods in terms of sensitivity, prioritization and specificity. *PLoS One* 8 (11), e79217. doi:10.1371/journal.pone.0079217

Terhorst, A., Sandikci, A., Keller, A., Whittaker, C. A., Dunham, M. J., and Amon, A. (2020). The environmental stress response causes ribosome loss in aneuploid yeast cells. *Proc. Natl. Acad. Sci. U. S. A.* 117 (29), 17031–17040. doi:10.1073/pnas.2005648117

Terhorst, A., Sandikci, A., Neurohr, G. E., Whittaker, C. A., Szórádi, T., Holt, L. J., et al. (2021). The environmental stress response regulates ribosome content in cell cycle-arrested *S. cerevisiae*. bioRxiv. 2021;2021.05.14.444167.

Terhorst, A. L. (2021). *The role of the environmental stress response in aneuploid and cell cycle-arrested budding yeast*. PhD Thesis [Internet]. 2021;1–23. Available from: https://dspace.mit.edu/handle/1721.1/142697.

Toda, T., Cameron, S., Sass, P., Zoller, M., Scott, J. D., McMullen, B., et al. (1987). Cloning and characterization of BCY1, a locus encoding a regulatory subunit of the cyclic AMP-dependent protein kinase in *Saccharomyces cerevisiae*. *Mol. Cell Biol.* 7 (4), 1371–1377. doi:10.1128/mcb.7.4.1371-1377.1987

Turner, J. J., Ewald, J. C., and Skotheim, J. M. (2012). Cell size control in yeast. *Curr. Biol.* 22 (9), R350–R359. doi:10.1016/j.cub.2012.02.041

Verghese, J., Abrams, J., Wang, Y., and Morano, K. A. (2012). Biology of the heat shock response and protein chaperones: Budding yeast (*Saccharomyces cerevisiae*) as a model system. *Microbiol. Mol. Biol. Rev.* 76 (2), 115–158. doi:10.1128/MMBR.05018-11

Visintin, R., and Amon, A. (2001). Regulation of the mitotic exit protein kinases CDc15 and Dbf2. *Mol. Biol. Cell* 12 (10), 2961–2974. doi:10.1091/mbc.12.10.2961

Visintin, R., Prinz, S., and Amon, A. (1979). CDC20 and CDH1: A family of substrate-specific activators of APC-dependent proteolysis. *Science* 278 (5337), 460–463. doi:10.1126/science.278.5337.460

Warner, J. R. (1999). The economics of ribosome biosynthesis in yeast. *Trends Biochem. Sci.* 24 (11), 437–440. doi:10.1016/s0968-0004(99)01460-7

Yang, J., Dungrawala, H., Hua, H., Manukyan, A., Abraham, L., Lane, W., et al. (2011). Cell size and growth rate are major determinants of replicative lifespan. *Cell Cycle* 10 (1), 144–155. doi:10.4161/cc.10.1.14455

Zakhartsev, M., and Reuss, M. (2018). Cell size and morphological properties of yeast *Saccharomyces cerevisiae* in relation to growth temperature. *FEMS Yeast Res.* 18 (6), 1–16. doi:10.1093/femsyr/foy052

Zatulovskiy, E., Lanz, M. C., Zhang, S., McCarthy, F., Elias, J. E., and Skotheim, J. M. (2022). Delineation of proteome changes driven by cell size and growth rate. *Front. Cell Dev. Biol.* 10, 980721–980814. doi:10.3389/fcell.2022.980721

Zhurinsky, J., Leonhard, K., Watt, S., Marguerat, S., Bähler, J., and Nurse, P. (2010). A coordinated global control over cellular transcription. *Curr. Biol.* 20 (22), 2010–2015. doi:10.1016/j.cub.2010.10.002

Frontiers in
Cell and Developmental Biology

Explores the fundamental biological processes of life, covering intracellular and extracellular dynamics.

The world's most cited developmental biology journal, advancing our understanding of the fundamental processes of life. It explores a wide spectrum of cell and developmental biology, covering intracellular and extracellular dynamics.

Discover the latest Research Topics

See more →

Frontiers

Avenue du Tribunal-Fédéral 34
1005 Lausanne, Switzerland
frontiersin.org

Contact us

+41 (0)21 510 17 00
frontiersin.org/about/contact